OPTICAL AND INFRARED LASERS

Final Report
December 1, 1972 to March 31, 1978

To:

National Aeronautics and Space Administration
Goddard Space Flight Center
Greenbeld, Maryland 20771

NASA Research Grant NGL 22-009-741
M.I.T. Project OSP 80711

From:

Professor Ali Javan
Department of Physics
Massachusetts Institute of Technology
Cambridge, Massachusetts 02139

1 August 1978

MASSACHUSETTS INSTITUTE OF TECHNOLOGY
DEPARTMENT OF PHYSICS
CAMBRIDGE. MASSACHUSETTS 02139

August 8, 1978

N78-28437

NASA Scientific and Technical Information
Facility
P.O. Box 8757
Baltimore/Washington International Airport
Maryland 21240

Gentlemen:

In compliance with the requirements of NASA Grant No. NGR 22-009-741, we submit two copies of the Final Technical Report covering the period December 1, 1972 to March 31, 1978.

If you should need further information, please let me know.

Sincerely yours,

A. Javan

Ali Javan
Francis W. Davis Professor of Physics

Enclosures

cc: N. McAvoy
G. Wiseman
D. Herlehy

Case File

Table of Contents

Papers appear in the order listed below

Table of Contents continued --

11. H.P. Grieneisen, J. Goldhar, and N.A. Kurnit, Observation of Zero-Degree Pulse Propagation in a Resonant Medium, Proceedings of the 3rd Rochester Conference on Coherent and Quantum Optics, edited by L. Mandel and E. Wolf, Plenum Press 1973.

12. R.M. Osgood, Jr. and A. Javan, Measurement of Vibration-Vibration Energy Transfer Time in HF Gas, Published in Appl. Phys. Letters.

13. Measurement of V-V Transfer Rate from HF v = 3 Using Simultaneous Optical Pumping on the HF v = 2 → 1 and v = 1 → 0 bands, Published in Appl. Phys. Lett.

14. N. Skribanowitz, M.J. Kelly and M.S. Feld, A New Laser Technique for the Identification of Molecular Transitions, Published in Phys. Rev. A.

15. F. Keilmann, R.L. Sheffield, M.S. Feld and A. Javan, Optical Isolation using a Doppler-Broadened Molecular Absorber, Appl. Phys. Lett., 23, 612 (1973).

16. J.G. Small, Infrared Frequency Synthesis and Precision Spectroscopy.

This final report consists of selected papers describing research work performed in the MIT Optical and Infrared Laser Laboratory with the support of NASA Research Grant NGL 22-009-741.

1. D. Seligson, M. Ducloy, J.R.R. Leite,
A. Sanchez and M.S. Feld

Quantum Mechanical Features of Optically Pumped CW FIR Lasers

J. of Quantum Electronics, QE-13, 468 (1977)

Quantum Mechanical Features of Optically Pumped CW FIR Lasers

D. SELIGSON, MARTIAL DUCLOY, J. R. R. LEITE, A. SANCHEZ, AND M. S. FELD

Abstract—Quantum mechanical predictions for the gain of an optically pumped CW FIR laser are presented for cases in which one or both of the pump and FIR transitions are pressure or Doppler broadened. The results are compared to those based on the rate equation model. Some of the quantum mechanical predictions are verified in CH_3OH.

Manuscript received February 4, 1977. This work was supported in part by the U.S. Army Research Office (Durham), the National Aeronautics and Space Administration, the Universidade Federal de Pernambuco and the CNPq-Brazil under grants to one of the authors (J. R. R. L.), and an Alfred P. Sloan Fellowship (M.S.F.).

D. Seligson, J. R. R. Leite, A. Sanchez, and M. S. Feld are with the Department of Physics and the Spectroscopy Laboratory, Massachusetts Institute of Technology, Cambridge, MA 02139.

M. Ducloy was with the Department of Physics and the Spectroscopy Laboratory, Massachusetts Institute of Technology, Cambridge, MA 02139. He is now with the Laboratoire de Physique des Lasers, Université Paris Nord, Villetaneuse, France.

GENERATION of far infrared (FIR) laser radiation by means of optical pumping of molecules has received increasing attention over the past few years [1]. Analysis of the optical pumping process is usually based on rate equation (RE) treatments [2]. Such treatments neglect important contributions to the FIR gain due to multiple quantum processes and modulation of the time-dependent wave function. From the quantum-mechanical (QM) point of view an optically pumped laser can be considered as a coupled three-level system interacting with applied radiation fields. It is well known that in such systems Raman-type processes [3] play an impor-

 Annals No. 706QE026

tant role. For example, double quantum transitions can occur in which a molecule initially in the ground state undergoes a coherent transition to the lower level of the FIR transition by simultaneously absorbing a pump photon and emitting a FIR photon. Such processes can modify the gain and, in some cases, give rise to directional anisotropy in the FIR laser emission [3], [4]. Accordingly, a complete understanding of the quantum mechanical features makes it possible to optimize the output characteristics of such lasers. For example, in one case [5] it has been possible to achieve gain and laser oscillation in the absence of population inversion. The way in which Raman-type processes manifest themselves depends on whether one or both of the coupled transitions are pressure or Doppler broadened. In Sections I–III the predictions of the QM treatment for the gain of an optically pumped laser are discussed for the various cases. Section IV presents some FIR laser experiments in which QM features, not predicted by rate equations, are observed.

The theoretical model [6] considers a three-level system composed of a pump transition, 2–0, center frequency ω_2, coupled to a FIR transition, 0–1, center frequency ω_1, via the common level, 0 (Fig. 1). It is assumed that in the absence of the pump laser only the ground state, level 2, is populated (total population n_2). The pump field, E_2, at frequency Ω_2, can be arbitrarily large, but the field E_1, frequency Ω_1, generated at the 0–1 transition is considered to be weak [7]. Different relaxation rates (γ's) are included in the theory: population decay ($\gamma_0, \gamma_1, \gamma_2$), polarization decay ($\gamma_{01}, \gamma_{02}$), and decay of the Raman coherence (γ_{12}). The quantity of interest is the gain induced at the 0–1 transition by a weak probe field E_1 propagating either parallel or antiparallel to E_2. Let $W(v)$ be the normalized velocity distribution of molecules with velocity component v along the propagation direction of the fields:

$$W(v) = \frac{1}{u\sqrt{\pi}} \exp -(v/u)^2, \quad u^2 = 2kT/M$$

(u = thermal velocity, M = molecular mass). The probe field gain is then given by [8]

$$G(\Omega_1) = G_0 \beta^2 \operatorname{Im} \gamma_{10} \int \left[\frac{L_2 - 2R\gamma_{20}/\gamma_0}{AB}\right] W(v)\, \alpha v, \quad (1)$$

where

$$G_0 = 4\pi \frac{\omega_1}{c} \frac{\mu_1^2}{\hbar} \frac{N_2}{\gamma_{10}},$$

$$\beta = \mu_2 E_2/(2\hbar),$$

$$L_1 = \Delta_1' + i\gamma_{10},$$

$$L_2 = -\Delta_2' + i\gamma_{20},$$

$$R = (\Delta_1' - \Delta_2') - i\gamma_{21},$$

$$A = |L_2|^2 + 4\beta^2\gamma_{20}^2/(\gamma_0\gamma_2),$$

$$B = -RL_1^* + \beta^2,$$

$$\Delta_j' = \Omega_j' - \omega_j, \quad j = 1, 2,$$

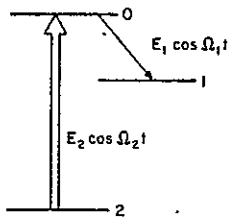

Fig. 1. Three-level system used to describe an optically pumped FIR laser. The pump field resonates with the 2–0 transition, molecular center frequency ω_2. The FIR laser emission occurs at the 0–1 transition, molecular center frequency ω_1.

$$\Omega_1' = \Omega_1 - k_1 v,$$

$$\Omega_2' = \Omega_2 - \epsilon k_2 v,$$

$$k_j = \Omega_j/c.$$

The frequencies Ω_1' and Ω_2' are those seen by the molecules in their rest frames and are Doppler shifted by $k_1 v$ and $\epsilon k_2 v$, respectively. For copropagating (counterpropagating) beams we have $\epsilon = +1 (\epsilon = -1)$. Depending on whether pump and probe transitions are pressure or Doppler broadened, any of the cases described in the following three sections can occur.

I. Homogeneously Broadened Systems (High-Pressure Regime)

When both transitions are pressure broadened ($\gamma \gg k_{1,2} u$) the velocity dependence at both pump and probe frequencies may be neglected (i.e., $\Omega_1' = \Omega_1$, $\Omega_2' = \Omega_2$), so the factor in brackets in (1) becomes velocity independent and the remaining integration over $W(v)$ gives unity. In this case the gain curve reverts to the well-known result of microwave–microwave and microwave–RF double resonance experiments. For simplicity, let us inspect the case in which all relaxation rates are equal. Equation (1) can be written in the following form, first given by Javan [9]:

$$G = G_0 \frac{\gamma^2\beta^2}{2a^2} \left\{\frac{1}{2}\left[\frac{1}{\gamma^2 + (a+b)^2} + \frac{1}{\gamma^2 + (a-b)^2}\right] + \frac{(a^2 - b^2)(2a^2 + \gamma^2) - \gamma^4}{(4a^2 + \gamma^2)[\gamma^2 + (a+b)^2][\gamma^2 + (a-b)^2]}\right\}, \quad (2)$$

where

$$G_0 = 4\pi \frac{\omega_1}{c} \frac{\mu_1^2}{\hbar} \frac{N_2}{\gamma},$$

$$a = (\Delta_2^2 + 4\beta^2)^{1/2}/2,$$

$$b = \Delta_2/2 - \Delta_1,$$

and

$$\Delta_j = \Omega_j - \omega_j.$$

The first two terms give rise to a doublet with resonant frequencies at

$$\Omega_1(\pm) = \omega_1 + \tfrac{1}{2}[\Delta_2 \pm (\Delta_2^2 + 4\beta^2)^{1/2}].$$

The third term, which is due to interference originating from overlap of the components of the doublet, is important only at low intensities ($\beta \ll \gamma$), when the splitting is small. For very large intensities ($\beta \gg \gamma, \Delta_2$) the doublet separation is 2β.

This splitting is a manifestation of the dynamical Stark effect (Autler-Townes effect).

Let us first analyze the gain expression for the case of resonant pumping ($\Delta_2 = 0$), where G is always largest. At low intensities a peak gain of $3G_0\beta^2/\gamma^2$ occurs at $\Delta_1 = 0$. The peak gain increases with increasing pump intensity, reaching a maximum value $G_0/3$ for $\beta = \gamma/2$. At a slightly higher intensity ($\beta = 5\gamma/7$) the line begins to split. As β continues to increase the splitting increases, and for $\beta \gg \gamma$ the peak gain at each doublet component approaches a limiting value $G_0/4$.

For off-resonance pumping ($\Delta_2 \gg \beta \gg \gamma$) the gain curve is again in the form of a doublet with peaks of equal magnitude $G_0\beta^2/\Delta_2^2$ occurring at $\Delta_1 = 0$ and $\Delta_1 = \Delta_2$.

The corresponding expression in the RE limit can be obtained from (1) by setting $\gamma_{12} \to \infty$, which has the effect of completely destroying the Raman coherence, i.e., no double quantum processes can then occur. Setting all other decay rates equal we then obtain

$$G_{RE} = G_0 \frac{2\beta^2\gamma^2}{(\Delta_1^2 + \gamma^2)(\Delta_2^2 + \gamma^2 + 4\beta^2)}.$$

In contrast to (2), this expression is always a Lorentzian function of Δ_1 of width 2γ (FWHM), which has a peak value at $\Delta_1 = \Delta_2 = 0$ of magnitude

$$G_0 \frac{2\beta^2}{\gamma^2 + 4\beta^2}.$$

Therefore, for weak pumping the RE predicts a peak gain $2G_0\beta^2/\gamma^2$, somewhat smaller than the QM result. For strong saturation the RE limit predicts no splitting and a peak gain that is twice as large as that of each doublet component.

II. Systems in Which Only the Pump Transition is Doppler Broadened

This is the case in which the Doppler effect at the FIR frequency is negligible compared to the pressure-broadened linewidth, but the pump transition is still Doppler broadened ($k_1 u \ll \gamma \ll k_2 u$). Therefore, in the velocity integration of (1) the $k_1 v$ velocity dependence may be neglected ($\Omega_1' = \Omega_1$, $\Omega_2' = \Omega_2 - \epsilon k_2 v$). This gives

$$G(\Delta_1) = G_0' \frac{2\beta^2}{\gamma_0 Q} \cdot \mathrm{Re}\left[\frac{\gamma_{21} + \gamma_{20}Q - \gamma_0(Q-1)/2 + i\Delta_1}{\beta^2 + (i\Delta_1 + \gamma_{10})(i\Delta_1 + \gamma_{21} + \gamma_{20}Q)}\right], \quad (3)$$

with

$$G_0' = 4\pi \frac{\omega_1}{c} \frac{\mu_1^2}{\hbar} \frac{N_2 \exp[-(\Delta_2/k_2 u)^2]}{k_2 u/\sqrt{\pi}},$$

and saturation parameter

$$Q = [1 + 4\beta^2/\gamma_0\gamma_2]^{1/2}.$$

When phase changing collisions are absent [i.e., for $\gamma_{ij} = (\gamma_i + \gamma_j)/2$] the numerator becomes a factor of the denominator, and the line shape becomes a Lorentzian of width $\gamma_1 + \gamma_0 Q$ (FWHM).

The RE approximation corresponds, again, to setting $\gamma_{12} = \infty$ in (3). For weak pump intensities the RE limit agrees with the QM result but not for an intense pump, where the RE predicts an emission line that does not power broaden (FWHM = $2\gamma_{01}$), and whose peak gain increases as β/γ. In contrast, for large β/γ the QM expression, (3), predicts that the gain reaches a limiting value $G_0'(2\gamma_{20}/\gamma_0 - 1)$. This behavior is a direct consequence of the occurrence of two quantum transitions. Notice also the absence of dynamical Stark splitting, which vanishes in the velocity integration.

When the pump field becomes so intense that $\beta \doteq k_2 u$ the Doppler shift at the 2–0 transition is no longer important, and the system reverts to the homogeneously broadened case of Section I.

III. Fully Doppler-Broadened Systems

The fully Doppler-broadened limit has been studied extensively over the past few years [6]. In this case $\gamma \ll k_{1,2} u$, and so the Doppler shift at both transitions is important. This gives rise to a directional anisotropy in the gain. The integration can be performed analytically in the limit $\beta^2 \ll \gamma(ku)$. Complete expressions may be found in [10].

For weak pump intensity and no dephasing collisions the emission line shape is a Lorentzian, narrower in the forward direction ($\epsilon = +1$) than in the backward direction ($\epsilon = -1$), and is centered at frequency $\Omega_1^0(\epsilon) = \omega_1(1 + \epsilon\Delta_2/\omega_2)$. The respective linewidths (FWHM) are

$$\gamma(\epsilon) = \gamma_1 + \gamma_0 + (\gamma_2 - \epsilon\gamma_0)\omega_1/\omega_2. \quad (4)$$

The peak gain, located at frequency $\Omega_1^0(\epsilon)$ for $\epsilon = \pm 1$, is given by

$$G(\epsilon) = 4G_0'\beta^2/[\gamma_0\gamma(\epsilon)]. \quad (5)$$

Note that the gain in the forward direction exceeds that in the backward direction [$G(+) > G(-)$], and that because $\gamma(+)\,G(+) = \gamma(-)\,G(-)$ the "areas" under the two Lorentzians are equal. The gain anisotropy has made it possible to construct a unidirectional optically pumped laser amplifier in a ring cavity configuration [11].

The gain anisotropy $G(+)/G(-)$ increases with the ratio ω_1/ω_2. In the case when all the γ's are equal

$$G(+)/G(-) = 1 + \omega_1/\omega_2. \quad (6)$$

In the limit of $\omega_1/\omega_2 \ll 1$

$$G(+) \simeq G(-) \simeq 2G_0'\beta^2/\gamma^2,$$

and the anisotropy disappears.

For large pump intensities ($ku > \beta > \gamma$) the anisotropy between forward and backward emission line shapes becomes even more pronounced. The backward emission line shape remains Lorentzian, with a linewidth $\gamma_1 + Q[\gamma_0 + (\gamma_2 + \gamma_0)\cdot\omega_1/\omega_2]$ (FWHM). Accordingly, for large β/γ the backward gain profile power broadens. At the same time its peak value approaches a limiting value

$$G_0'\gamma_2/[\gamma_0 + (\gamma_2 + \gamma_0)\omega_1/\omega_2].$$

In contrast, at large pump intensities the forward emission line shape splits symmetrically into two components separated by

$4\beta[\omega_1(\omega_2 - \omega_1)]^{1/2}$. The splitting of this doublet is maximum for $\omega_1 = \omega_2/2$. This splitting is another manifestation of the dynamic Stark effect, discussed in Section I, which is preserved in the fully Doppler-broadened limit when E_1 and E_2 are copropagating. Note, however, that although the splitting increases linearly with β, as in the pressure-broadened case, its magnitude is different. In contrast to the counterpropagating case, the peak gain of each component does not saturate with increasing pump intensity, but instead continues to increase $\propto (\beta/\gamma)^{1/2}$ up to the point $\beta \sim ku$, where the system is no longer Doppler broadened and the gain saturates, as described in Section I.

In comparison with the above results, the RE approach in the fully Doppler-broadened limit predicts identical Lorentzian gain profiles centered at $\Omega_1^0(\pm)$. There is no forward–backward anisotropy, since Raman-type processes are neglected [3]. For weak pump intensities the gain curves are identical to the backward gain curve of the QM case. For large pump intensities the Lorentzians power broaden. In the case of no dephasing collisions the linewidths are $\gamma_1 + \gamma_0 + Q(\gamma_0 + \gamma_2)\,\omega_1/\omega_2$ (FWHM), somewhat narrower than the $\epsilon = -1$ QM linewidth. With increasing pump intensity the peak gain (for both $\epsilon = \pm 1$) approaches the limiting value $G_0'(\omega_2/\omega_1)\,\gamma_2/(\gamma_2 + \gamma_0)$, which is larger than that of the $\epsilon = -1$ QM peak gain, but smaller than the gain peaks of the $\epsilon = +1$ doublet.

IV. Experiments

We have studied the emission characteristics of an optically pumped FIR system which is fully Doppler broadened. Two types of experiments will be described. In the first a weak tunable field is used to probe the gain line shape at the FIR transition in an optically pumped external cell. Subsequent experiments study the frequency characteristics of the output of an optically pumped FIR laser. In this case the laser field itself serves as the probe.

In the gain line shape studies a CH_3OH sample cell was pumped with a CO_2 laser and probed with the radiation from a FIR CH_3OH laser. The CO_2 laser, capable of delivering 12 W CW at 9.7 μm, had a 1-m discharge and used a diffraction grating for line selection. Power was coupled out of the cavity via the zeroth diffraction order. The frequency of the CO_2 laser could be controlled by adjusting the voltage of a PZT attached to the end cavity mirror.

Most of the CO_2 laser power was used to pump the FIR laser. The FIR laser cavity was of the waveguide type with two flat mirrors, one of which was mounted on a second PZT. The FIR cavity modes could be tuned by adjusting the PZT voltage. The CO_2 pump beam was focused inside the FIR cavity through a 2-mm-diam hole in one of the mirrors. This hole also served to couple out the FIR radiation. The FIR cavity was filled with CH_3OH in the pressure range 50–500 mtorr. Using different CO_2 pump lines, CW FIR radiation at several wavelengths could be generated [1]. The experiments reported below studied the FIR emission of the 70.5-μm line, [$P(34)$ 9.7-μm CO_2 pump].

In the external cell experiments about 1 W of the CO_2 laser power was split off from the main beam and sent unfocused to pump a 60-cm cell filled with low-pressure (<100 mtorr) CH_3OH (Fig. 2). The collimated output of the FIR laser, aligned to coincide with the CO_2 beam, was used to probe the gain at the coupled transition of the CH_3OH sample cell in the forward direction. A TPX filter placed after the sample cell was used to reject the pump beam and transmit the FIR signal. A He-cooled InGe detector was used to detect the FIR radiation. The CO_2 laser was chopped at 100 Hz, and synchronous detection was used to measure the gain.

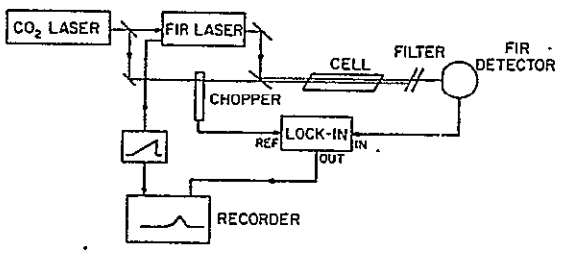

Fig. 2. Experimental setup for studying the CH_3OH FIR gain induced in an external, optically pumped sample cell.

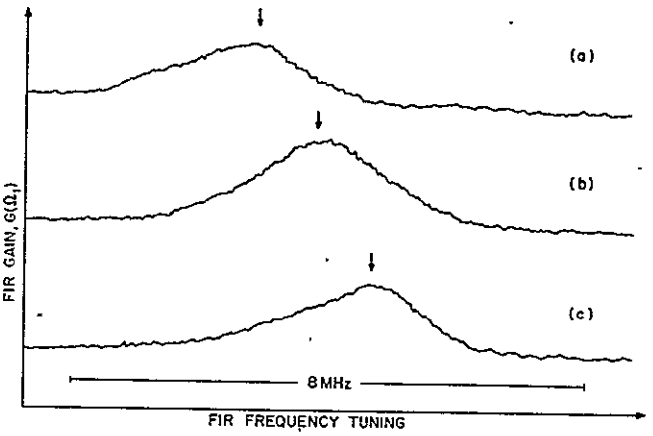

Fig. 3. Observed FIR gain profiles. Lock-in amplifier output versus FIR probe frequency is shown. In traces (a), (b), (c) the frequency setting of the CO_2 pump laser is successively incremented by 7 MHz.

Fig. 3 shows the output of the lock-in detector as the FIR frequency is swept. The sample cell pressure was 50 mtorr. In gain profiles (a), (b), and (c) the CO_2 pump frequency was successively increased by increments of 7 MHz. The distortion in the line shapes is due to the power change of the probe laser (operated at 300 mtorr) as it is tuned over its ~10-MHz range. The gain profiles are found to be 2.4-MHz wide (FWHM). Power broadening was negligible at the available pumping power, so that if we assume $\gamma_1 = \gamma_0 = \gamma$ in (4) (with $\epsilon = \pm 1$) we obtain $\gamma = 24(\pm 6)$ MHz/torr. Under these experimental conditions a peak FIR gain of 5 percent/m was measured.

The forward–backward gain anisotropy is one of the most interesting predictions of the QM treatment in the fully Doppler-broadened limit. Equation (5) predicts a higher gain in the forward direction than in the backward direction, the gain anisotropy ratio being $1 + \omega_1/\omega_2$, (6). For the 70-μm FIR transition $\omega_1 = 0.08\omega_2$, yielding a small anisotropy ratio which would be difficult to observe in forward/backward probe experiments. Instead, the gain anisotropy was investigated by studying the tuning characteristics of the FIR laser itself, because near threshold the power output is very sensi-

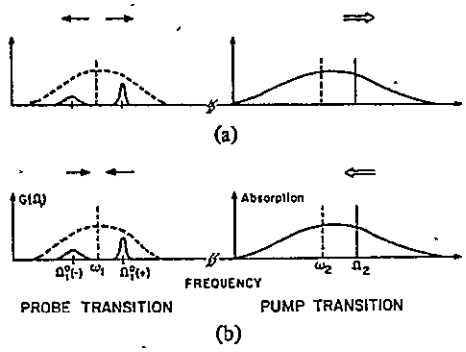

Fig. 4. Frequency profile of FIR gain induced by a standing-wave pump field. The dashed lines show the Doppler profile of the 0–1 transition. (a) and (b) show the gain contributions from the right- and left-propagating traveling wave components of the standing wave field. Peaks occur at $\Omega_1^0(\pm) = \omega_1 \pm \Delta_2\omega_1/\omega_2$. Note that in both (a) and (b) for $\Delta_2 > 0$ ($\Delta_2 < 0$) the emission component above (below) ω_1 has higher gain.

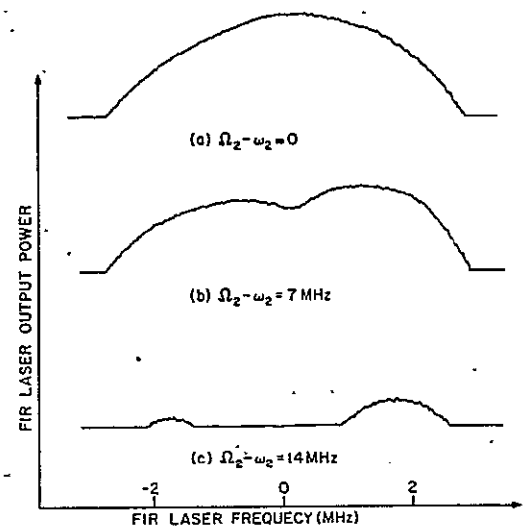

Fig. 5. FIR laser output tuning curve. Laser output intensity versus cavity tuning is shown. (a) on-resonance pumping ($\Delta_2 = 0$); (b) $\Delta_2 =$ 7 MHz; (c) $\Delta_2 = 14$ MHz.

tive to small changes in gain. In these experiments the FIR laser was operated in the low-pressure (80 mtorr) range. In order to resolve the forward and backward emission line shapes the pump laser was detuned from the center of the CH_3OH transition. It is important to realize that the gain anisotropy, usually described for the traveling wave pump field, is not destroyed when the pump field is in the form of a standing wave, as is the case in our FIR cavity (Fig. 4). If the pump laser is set at the high- (low-) frequency side of the CH_3OH absorbing transition, the high- (low-) frequency component of the FIR emission line shape should exhibit higher gain, and this gain asymmetry should give rise to a corresponding asymmetry in the FIR laser output as the FIR cavity is tuned.

This is verified in the experimental results of Fig. 5: when the pump is tuned to the center of the absorbing transition ($\Delta_2 = 0$) 1) forward and backward line shapes overlap, giving rise to a single symmetrical profile of the FIR laser output tuning curve. For a pump frequency detuning of $\Delta_2 = 7$ MHz 2) the components begin to split and the gain asymmetry becomes apparent. With increased detuning 3) the splitting becomes larger and both peaks decrease in magnitude, but the backward peak decreases more rapidly since its gain is closer to oscillation threshold. Eventually only the forward emission component has enough gain for laser oscillation.

Similar effects have been observed in the visible in a three-level system in neon in which the common level (level 0) is lowest in energy [12].

Further experiments to explore the QM features of optically pumped CH_3OH FIR lasers are in progress. Studies are planned using transitions having shorter FIR wavelengths, where the gain anisotropy is more pronounced. Cases (1) and (2) will be studied by going to higher pressures and using longer FIR wavelengths ($\lambda \sim 500\ \mu$m). Studies of the transient behavior of the FIR emission, obtained when the pump laser is suddenly turned on or off, are also under way.

Acknowledgment

We would like to thank J. Mickey and C. Duda for their help in the experiments, and W. Ryan for expert technical assistance.

References

[1] T. Y. Chang, "Optically pumped submillimeter-wave sources," *IEEE Trans. Microwave Theory Tech.*, vol MTT-22, p. 983, 1974.
[2] See, for example, T. A. DeTemple and E. Danielewicz, "Continuous-wave CH_3F waveguide laser at 496 μm: Theory and experiment," *IEEE J. Quantum Electron.*, vol. QE-12, p. 40, 1976.
[3] M. S. Feld, "Laser saturation spectroscopy in coupled Doppler-broadened systems: How to find a needle in a haystack," in *Fundamental and Applied Laser Physics*, M. S. Feld, A. Javan, and N. A. Kurnit, Ed. New York, Wiley, 1973; p. 369.
[4] V. P. Chebotayev, "Three-level laser spectroscopy," in *Topics in Applied Physics*, vol. 13, K. Shimoda, Ed. New York: Springer, 1976, p. 201.
[5] N. Skribanowitz, I. P. Herman, and M. S. Feld, "Laser oscillation and anisotropic gain in the $1 \rightarrow 0$ vibrational band of optically pumped HF gas," *Appl. Phys. Lett.*, vol. 21, p. 466, 1972 For the case of off-resonant pumping, see the recent work of T. Y Chang and J. D. McGee, "Off-resonant infrared laser action in NH_3 and C_2Hy without population inversion," *Appl. Phys. Lett.*, vol. 29, p. 725, 1976.
[6] See reviews [3] and [4] and references therein.
[7] The case of strong FIR fields (E_1) has recently been analyzed for a coupled homogeneously broadened system by R. J. Temkin, "Rate equations and theory of optically-pumped submillimeter lasers," in *Conf. Dig. Second Int. Conf. and Winter School on Submillimeter Waves and their Applications*, Puerto Rico, 1976, p. 43; and R. L. Panock and R. J Temkin, "Interaction of two laser fields with a three level molecular system," this issue, pp. 425–434.
[8] M. S. Feld and A. Javan, "Laser-induced line narrowing effects in coupled Doppler-broadened transitions," *Phys. Rev.*, vol. 177, p. 540, 1969.
[9] A. Javan, "Theory of a three-level maser," *Phys. Rev.*, vol. 107, p. 1579, 1957.
[10] B. J. Feldman and M. S Feld, "Laser induced line-narrowing effects in coupled Doppler-broadened transitions, II. Standing wave features," *Phys. Rev.*, vol. A5, p. 899, 1972.
[11] N. Skribanowitz, M. S. Feld, R. E. Francke, M. J. Kelly, and A. Javan, "Possibility of a unidirectional laser amplifier produced by monochromatic optical pumping of a coupled Doppler-broadened transition," *Appl. Phys. Lett.*, vol. 19, p. 161, 1971; N. Skribanowitz, I. P. Herman, R. M. Osgood, Jr., M S. Feld, and A. Javan, "Anisotropic ultra-high gain emission observed in rotational transitions in optically pumped HF gas," *Appl Phys. Lett.*, vol. 20, p. 428, 1972.
[12] I. M. Beterov and V. P. Chebotayev, "Three level gas lasers," *JETP Lett.*, vol. 9, p. 127, 1969.

R. E. McNair, S.F. Fulghum, G.W. Flynn,
M.S. Feld

Energy Storage and Vibrational Heating in CH_3F Following Intense Laser Excitation

Chem. Phys. Lett. 48, 241 (1977)

ENERGY STORAGE AND VIBRATIONAL HEATING IN CH_3F FOLLOWING INTENSE LASER EXCITATION

R.E. McNAIR*, S.F. FULGHUM, G.W. FLYNN**, M.S. FELD‡
Physics Department and Spectroscopy Laboratory, Massachusetts Institute of Technology, Cambridge, Massachusetts 02139, USA

and

B.J. FELDMAN
Los Alamos Scientific Laboratory, Los Alamos, New Mexico 87545, USA

Received 15 March 1977

Fundamental relations for energy storage among the modes of a polyatomic molecule are derived in terms of γ_{VV}, the V–V collision parameter and the energy flow path. A new method is introduced for making absolute measurements of vibrational energy.

This paper explores energy absorption and energy transfer induced by vibrational (V–V) collisions following intense laser excitation‡‡. A theoretical model is derived which predicts that under appropriate conditions several quanta per molecule can be absorbed in vibrational energy. This is confirmed using a pulsed CO_2 laser to vibrationally heat $^{13}CH_3F$. In addition, we directly measure the energy stored in the vibrational modes and show that a steady state exists. These findings are basic to the use of molecular gases as energy storage media. Furthermore, a complete knowledge of the energy distribution of vibrationally hot but rotationally cold gases opens interesting possibilities for achieving laser oscillation and for studying chemical reactions in excited vibrational states.

Consider an intense pulse of laser radiation resonantly interacting with one of the ground state ($v = 0 \rightarrow 1$) rotational–vibrational transitions of a diatomic molecular gas. When the laser pulse time (τ_P) is long compared to the rotational bottleneck time (τ_B), the entire rotational manifold of the $v = 1$ state can be populated‡. If τ_P is short compared to the characteristic V–V collision time (τ_{VV}), the energy flow into the system will be limited by the condition that not more than half of the ground state population can be transferred into the $v = 1$ vibrational state. However, if $\tau_P \gg \tau_{VV}$ additional energy can flow into the system. This comes about because the normal V–V processes as they occur in thermal equilibrium are unbalanced by the presence of the intense laser field. The laser continually acts to equalize the $v = 0$ and $v = 1$ level populations, and resonant V–V processes can then lead to additional vibrational heating. For example, consider the process in which two molecules in the $v = 1$ state collide to produce a $v = 2$ molecule and a $v = 0$ molecule. The $v = 2$ molecules thus created will be carried up the vibrational ladder by subsequent

* Present address: Hughes Research Laboratory, Malibu, California, USA.

** John Simon Guggenheim Memorial Fellow 1974–75; permanent address: Department of Chemistry, Columbia University, New York City, New York, USA.

‡ Alfred P. Sloan Fellow.

‡‡ Many energy transfer and relaxation studies have been made using weak laser excitation. See for example, ref. [1] and references therein.

‡ $\tau_B = \tau_R/f$, with τ_R the rotational thermalization time, and f the fractional population of the lower level of the laser transition. Letokhov and Makarov [2] have considered the regime where $\tau_B \gg \tau_{VV}$. See also ref. [3].

11<

V–V collisions. The molecules transferred to the $v = 0$ level unbalance the population equality of the $v = 0$ and $v = 1$ states. However, the laser maintains this equality, thereby bringing additional energy into the system. This build-up of stored vibrational energy can continue until V–T relaxation (characteristic time τ_{VT}) sets in.

The theoretical model assumes: (1) $\tau_B \ll \tau_P$, (2) $\tau_P \ll \tau_{VT}$ (to prevent thermal heating) and (3) a pulse sufficiently intense to equalize $v = 0$ and 1 level populations for molecules of all velocities. Assuming resonant binary V–V processes, and dipole–dipole collisions in the harmonic oscillator approximation, the vibrational heating of a diatomic molecule can be described by coupled rate equations of the form[‡]

$$\mathrm{d}\mathcal{P}_v/\mathrm{d}t + \tfrac{1}{2}\gamma_{VV}\sum_{v'=0}^{\infty}\{[(v+1)v' + v(v'+1)]\,\mathcal{P}_v\,\mathcal{P}_{v'} - vv'\,\mathcal{P}_{v-1}\,\mathcal{P}_{v'} - (v+1)(v'+1)\,\mathcal{P}_{v+1}\,\mathcal{P}_{v'}\} \quad (1)$$

$$= \sigma I(\mathcal{P}_0 - \mathcal{P}_1)(\delta_{v,1} - \delta_{v,0}), \quad v = 0, 1, 2, \ldots .$$

Here $\mathcal{P}_v$ is the fraction of molecules in the vth level, γ_{VV} is the V–V rate constant ($\tau_{VV} \approx \gamma_{VV}^{-1}$). The right-hand side of eq. (1) describes the pumping of the $v = 0 \rightarrow 1$ transition (absorption cross section σ) by a laser field of photon flux I. For full saturation of the laser transition $\dot{\mathcal{P}}_0 \approx \dot{\mathcal{P}}_1$ and we assume that a quasi-equilibrium is established among states $v \geqslant 1$ having an effective temperature which increases with time. The number of quanta per molecule, ϵ, is then

$$\epsilon = \sum v\mathcal{P}_v = (1 - \mathcal{P}_1)^2/\mathcal{P}_1 . \quad (2a)$$

Using eq. (1) and initial conditions $\mathcal{P}_0(0) = \mathcal{P}_1(0) = 1/2$, $\mathcal{P}_1(t)$ is then given by

$$1/\mathcal{P}_1^2 + 4\ln(2\mathcal{P}_1) = 4 + \gamma_{VV}t , \quad (2b)$$

from which $\epsilon(t)$ can be obtained. Computer solutions of eq. (1) agree with eqs. (2) and confirm that an effective temperature is established [5].

In polyatomic molecules, where other modes are present, the energy absorption process is modified by V–V cross-over collisions, which lead to energy transfer to other modes. However, when the $v = 1$ level of a closely coupled mode, ν_b, is at least $\approx kT$ above that of the mode being pumped, ν_a (as in the CH_3F experiments), a temperature relationship [eq. (5), below] is rapidly established between the modes *during* the pumping process, and the number of quanta within the modes, ϵ_a and ϵ_b, increases with $\epsilon_a \gg \epsilon_b$. As a result, the *net* vibrational energy deposited in a polyatomic molecule is very nearly *the same* as in the diatomic case, so that eqs. (2) still hold, with $\epsilon = \epsilon_a + \epsilon_b$ and γ_{VV} being the V–V rate constant of the mode being pumped. Computer calculations [5] confirm these findings. As seen below, eqs. (2) give good agreement with the data.

The 9.65 μm P(32) CO_2 laser line falls within the Doppler width of the ν_3 ($v = 0 \rightarrow 1$) R(4, 3) transition of $^{13}CH_3F$. The large transition matrix element leads to full saturation at moderate laser intensities, and $\tau_R \ll \tau_{VV} \ll \tau_{VT}$ [1]. Spontaneous emission from several modes is readily observable, providing a means of observing stored vibrational energy. Laser pulse durations were typically 2–4 μs. Pulse energies (<0.25 J) were kept well below the threshold for collisionless absorption [6], but sufficiently high to ensure complete saturation of the $^{13}CH_3F$ Doppler profile.

In the energy absorption experiments the laser beam traversed an 18 cm CH_3F sample cell. Incident and transmitted pulse energies were monitored with calibrated Au : Ge detectors. Given the energy absorbed by the sample and the beam volume, the number of CO_2 quanta absorbed per molecule, $\epsilon(P)$, can be obtained as a function of the $^{13}CH_3F$ pressure, P (fig. 1a). For $P < 5$ torr $\epsilon(P)$ rose monotonically, reaching a maximum of 2.6 quanta. At higher pressures it slowly decreased due to incomplete laser saturation over the cell length. A best fit to $\epsilon(P)$, obtained from eqs. (2), gives a value of $\gamma_{VV} = 0.8 \pm 0.2\ \mu s^{-1}\ \mathrm{torr}^{-1}$. This result agrees with Earl and Ronn's value [7] of $1.2 \pm 0.3\ \mu s^{-1}\ \mathrm{torr}^{-1}$, measured via laser fluorescence, and confirms that eq. (2) is a good approximation for predicting energy absorption in a polyatomic.

If a rotational bottleneck [2,3] is present it can be eliminated by adding a buffer gas which reduces τ_R. In CH_3F, however, no bottleneck is present, as evidenced by the fact that the energy absorbed did not change when up to 500 torr of argon was added to a fixed amount of CH_3F.

To establish that for times $\ll \tau_{VT}$ the absorbed energy resides in the vibrational degrees of freedom, the time evolution of the fluorescence from the 9.6 μm

[‡] The left-hand side of this equation is given by Shuler [4].

12<

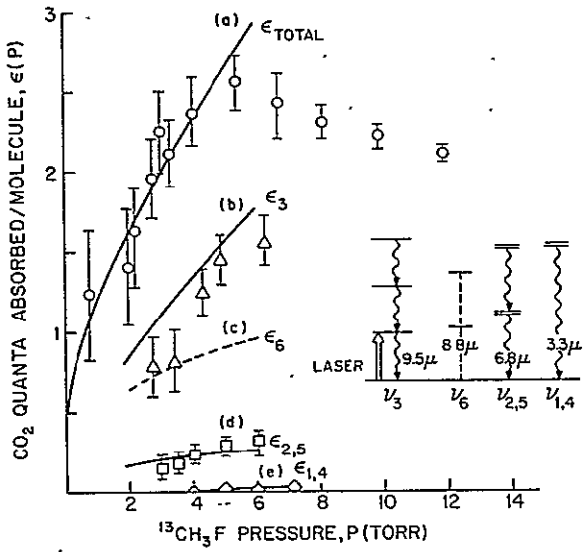

Fig. 1. CO_2 quanta stored versus pressure. (a) Total quanta stored. The theoretical fit gives $\gamma_{VV} = 0.8 \pm 0.2\ \mu s^{-1}\ torr^{-1}$. (b–e) Quanta stored in ν_n. The curves were calculated from (a). The insert shows relevant vibrational levels.

C–F stretch mode (ν_3) was monitored by a Cu : Ge detector. In the pressure range of the experiments the fluorescence signal was always in the form of a rapid rise, governed by the duration of the laser pulse, followed by a long ($\approx$ ms) decay, determined by the V–T relaxation processes. The 3.3 μm C–H stretch (ν_1, ν_4) and 6.8 μm bend (ν_2, ν_5) fluorescence bands exhibited the same temporal behavior as ν_3. This indicates fast intermode V–V transfer rates, and that soon after the laser pulse terminates a vibrational steady state among the modes is established.

Since the absorbed energy is distributed among all the modes, it is important to determine how much is stored in each. However, absolute measurement of fluorescence intensities would be difficult and imprecise. A new technique, which utilizes the fact that a steady state is rapidly established among the vibrational modes, was employed to measure the energy stored in ν_3. In this technique the peak fluorescence is first observed after it passes through an *empty* "cold gas filter" cell to give $I(0)$. Then, methyl fluoride gas at room temperature is introduced into this cell to remove the $v = 1 \rightarrow 0$, giving $I(0) - I_{10}$. This "cold" (room temperature) gas is an ideal filter for the $v = 1 \rightarrow 0$ fluorescence, since the absorption band matches the emission frequencies line for line, and the small anharmonicity (18 cm^{-1}) is sufficient to prevent absorption of ν_3 fluorescence from higher lying levels*. Describing the vibrational level populations by a Boltzmann distribution at temperature T_3 ($T_3 >$ room temperature), and assuming harmonic oscillator transition moment matrix elements, we obtain

$$I_{10}/I(0) = (1+\epsilon_3)^{-2}, \quad \epsilon_3 = [\exp(\hbar\omega_3/kT_3) - 1]^{-1}, \tag{3}$$

where ω_3 is the ν_3 frequency. The measured ratio $I_{10}/I(0)$ determines ϵ_3, the number of quanta stored in ν_3.

In practice, care must be taken in obtaining the ratio $I_{10}/I(0)$. The $v = 1 \rightarrow 0$ emission occurs over the entire rotational manifold. The intense emission lines are absorbed strongly; conversely, the weak emission lines are absorbed weakly. As a result the curve of transmitted intensity $I(P')$ versus cold gas filter pressure, P' has a long tail rather than a sharp cut-off. One finds

$$I(P')/I(0) = 1 + [I_{10}/I(0)]\,[\chi(P') - 1], \tag{4a}$$

where $\chi(P')$ is a function of the symmetric top matrix elements and absorption coefficients. For a cold gas filter cell of length L containing Doppler-broadened CH_3F, $\chi(P')$ is closely approximated by

$$\chi(P') = 0.567\ e^{-0.614P'L} + 0.331\ e^{-0.145P'L} + 0.102\ e^{-0.019P'L}. \tag{4b}$$

Fig. 2 shows the transmitted fluorescence intensity as a function of cold gas filter pressure for several values of sample cell pressure. In each case the solid line gives a best fit to the theoretical expression for $I(P')/I(0)$ [eq. (4)], from which ϵ_3 is obtained [eq. (3)]. Note that with increasing *sample* cell pressure, P, $I(P')$ falls off more slowly, indicating increased population of the upper vibrational states and thus higher T_3.

The observed values of ϵ_3 at various pressures are given in fig. 1b. Note that 40–50% of the total energy (fig. 1a) resides in ν_3. Since τ_{VT} is long the remaining energy must be shared among other modes.

In order to determine more precisely the partitioning of energy, the vibrational energies ϵ_n of the $\nu_{2,5}$

* Pressures of both sample and cold gas filter cells were kept below 10 torr to avoid overlap of lines due to excessive pressure broadening.

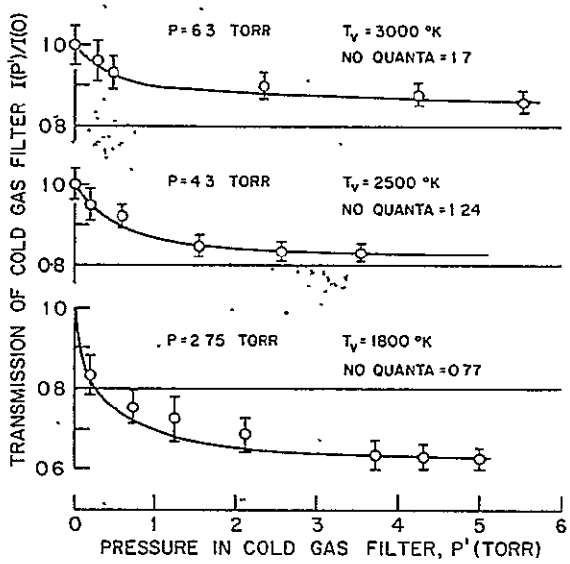

Fig. 2. Cold gas filter measurements. The theoretical fits give the temperature of the ν_3 mode.

and $\nu_{1,4}$ modes were also measured. (ϵ_6 was too weak to measure.) This was done by taking ratios of the corresponding fluorescence intensities to that of ν_3. Knowing the ratios of the mode frequencies and transition moments, and the detector efficiency, ϵ_n could then be obtained in terms of ϵ_3 (fig. 1). Cold gas filter experiments performed on the $\nu_{1,4}$ fluorescence, which are less accurate because of its weak transition moment, establish a firm upper bound for $\epsilon_{1,4}$ which agrees with fig. 1.

The steady state partitioning of energy among the modes may be determined from a knowledge of the path by which energy is transferred among the modes. The temperature of two modes, energies E_a and E_b, in vibrational equilibrium are related by [8]

$$E_a/T_a - E_b/T_b = (E_a - E_b)/T\,, \qquad (5)$$

with T the kinetic temperature. Therefore, by assuming a dominant energy flow path, eq. (5) can be successively applied to each pair of modes collisionally coupled in the energy flow process. The smooth curves of figs. 1b–1e were obtained from eq. (5) using the theoretical curve of fig. 1a and the energy flow path of ref. [9]. The agreement with the experimental points is indicative of the accuracy of our absolute measurements of vibrational temperatures, and supports the energy flow assignments [9]. No other path assignments led to good agreement with the data.

In conclusion, this is the first time that the energy storage and partitioning of a highly excited polyatomic have been measured. The confirmation of the simple prediction of laser induced vibrational heating [eq. (2)] and subsequent vibrational energy redistribution shows that these relationships can be applied with confidence in other molecules. Finally, a comparison of the present results with weak excitation experiments [9] strongly suggests that the dominant path for vibrational energy redistribution does not change in CH_3F for vibrational excitation up to ≈7 kcal/mole.

The authors wish to thank Rick Forber, Vladik Letokhov, Bill Ryan, Howard Schlossberg and Ramesh Sharma for useful discussions and Ali Javan for his support and encouragement.

References

[1] E. Weitz and G.W. Flynn, Ann. Rev. Phys. Chem. 27 (1973) 81.
[2] V.S. Letokhov and A.A. Makarov, Soviet Phys. JETP 36 (1973) 1091.
[3] B.J. Feldman, IEEE J. Quantum Electron. QE-9 (1973) 1070.
[4] K.E. Shuler, J. Chem. Phys. 32 (1960) 1692.
[5] R.E. McNair, R. Forber, S.F. Fulghum, G.W. Flynn, B.J. Feldman and M.S. Feld, to be published.
[6] R.V. Ambartzumian, V.S. Letokhov, E.A. Ryabov and N.V. Chekalin, JETP Letters 20 (1975) 275; J.L. Lyman, R.J. Jensen, J. Rink, C.P. Robinson and S.D. Rockwood, Appl. Phys. Letters 27 (1975) 87.
[7] B.L. Earl and A.M. Ronn, Chem. Phys. Letters 39 (1976) 95.
[8] C.E. Treanor, J.W. Rich and R.G. Rehm, J. Chem. Phys. 48 (1968) 1798.
[9] I. Shamah and G.W. Flynn, J. Chem. Phys., to be published.

14<

3. R.E. McNair, R. Forber, S.F. Fulghum, G.W. Flynn, M. S. Feld and B. J. Feldman

Energy Absorption and Vibrational Excitation by Intense Laser Pulses

(To be Published)

ENERGY ABSORPTION AND VIBRATIONAL EXCITATION BY INTENSE LASER PULSES

R. E. McNair,* R. Forber, S. F. Fulghum, G. W. Flynn,# M. S. Feld

Department of Physics and Spectroscopy Laboratory

Massachusetts Institute of Technology

Cambridge, Massachusetts 02139

B. J. Feldman

Los Alamos Scientific Laboratory

Los Alamos, New Mexico 87545

ABSTRACT

Theoretical and experimental studies are made of the energy flow into and among the vibrational degrees of freedom of polyatomic molecules due to V-V collisions following intense laser excitation. Simple ~~closed form~~ expressions are derived for predicting the energy extracted by diatomic and some polyatomic molecules from a saturating laser pulse. A new method for measuring the energy stored in the vibrational degrees of freedom is introduced and a model for predicting the steady state partitioning of energy in polyatomics is applied to CH_3F.

---

*Present address: Hughes Research Laboratories, Malibu, California 90265

#Present address: Department of Chemistry, Columbia University, New York, NY

I. INTRODUCTION

The interaction of intense laser fields with molecular systems and the subsequent inter-molecular processes is an area of great interest among physicists and chemists. The laser has become an excellent tool for probing the flow of energy within the internal degrees of freedom of a molecule, and it provides a powerful method for obtaining high levels of excitation. Conversely, the increased knowledge of energy absorption, transfer, and relaxation processes in molecules has led to new and improved lasers, with many more possibilities ahead.

Very little is known about the detailed kinetics involved in the energy absorption process in molecules, nor has the redistribution of absorbed energy among the vibrational degrees of freedom of polyatomics been fully understood. Because of the spectroscopic complexities and the lack of information on interaction potentials, collisional rate constants and energy flow mechanisms, polyatomic molecules have not been investigated as thoroughly as some diatomics.

This paper presents a detailed theoretical and experimental study of energy absorption and transfer in a polyatomic molecule from intense resonant laser pulses in the regime where the energy flow is determined by V-V collisions. This is different from the studies of Letokhov and others,( )

which are concerned with collisionless cascade excitations characteristic of shorter, more intense laser pulses.

The theoretical work investigates both a single mode oscillator and one with two collisionally-coupled modes. We use the collisional rate equations for vibrational energy transfer, as in the works of Shuler and others,( ) with the addition of two important features: (1) a laser pumping term, and (2) the assumption of a quasi-equilibrium among the vibrational levels not directly connected to the laser field, which provides a relationship between the populations of all the levels. In the case of a single mode oscillator, simple expressions are derived for predicting the energy absorbed during the laser excitation. The addition of one other vibrational mode, collisionally coupled to the first, is considered in some detail. A general formula is derived and discussed in relation to the one mode case; it is found that the influence of the second mode on the absorption process dramatically depends on its energy spacing relative to the spacing on the energy absorbing mode. Numerical solutions of the population rate of change equations are used to justify the quasi-equilibrium assumptions, and the agreement with theory is quite good.

The experimental work studies the absorption of the P(32) line of CO_2 by $^{13}CH_3F$, and the subsequent energy transfer among the modes of the molecule. Fitting the single mode model to the measured absorption leads to a determination of γ_{VV}, the VV collision rate constant for the ν_3 mode. In addition,

the partitioning of the absorbed energy among the several vibrational modes is determined by means of a technique for measuring the absolute energy stored in a particular mode. This technique, which involves the use of a "cold gas" filter, is described in detail. Knowledge of the partitioning of energy then allows confirmation of a specific flow path for the transfer of energy between the modes of CH_3F.

Interest in laser development, laser induced chemical reactions, and chemical lasers requires a detailed understanding of the molecular processes involved. The rate constants and paths of energy flow during and after excitation govern the gain, power outputs, reaction rates, mode specific excitation, etc. Once the transient mechanisms of energy absorption and transfer are understood, a vast set of applications await them. It is hoped that the present work contributes to that understanding.

Some of the concepts and data presented here are outlined in Reference . A detailed treatment is given here.

II. THEORY

A. Introduction

Consider the interaction of a resonant laser pulse of carrier frequency ω and duration τ_p with a particular rotational-vibrational transition from the ground vibrational state of a

molecule to its first excited vibrational state (Fig. 1a). The amount of energy the molecule can absorb depends on τ_p. As τ_p is increased three distinct regimes can be considered.

1) When τ_p is short compared to the rotational relaxation time, τ_{RR}, then only the fractional population Z_J of molecules in the particular rotational state J of the ground vibrational state can be excited. Therefore, if the pulse is intense enough( ) to saturate the transition then only the energy $\frac{1}{2}Z_J\hbar\omega$ can be absorbed by the molecule on the average.

2) When τ_p is on the order of τ_{RR}/Z_J then the rotational populations of both the upper and lower vibrational states have time to reach a new equilibrium during the laser pulse. In this case the total population in the upper and lower vibrational states can equalize, and the average energy absorbed by the molecule is $\frac{1}{2}\hbar\omega$.

3) When τ_p is longer than the characteristic time for vibrational-vibrational energy exchanging collisions, τ_{VV}, and both times are longer than τ_{RR}/Z_J then additional energy can be absorbed and stored by the molecule as vibrational energy.( ) When this condition is satisfied the rotational structure becomes unimportant and the system reduces to that of a simple vibrational oscillator. This last regime is the subject

of this work.

For example consider the process in which two molecules in the v = 1 state collide and exchange energy, producing one molecule in the v = 2 state and one of the v = 0 state. The result is that energy has been carried up the vibrational ladder and a molecule has been returned to the ground state where it can again absorb energy from the laser. Energy will continue to be absorbed through processes of this kind, until the laser pulse length becomes comparable to τ_{VT}, the characteristic time for translational energy transfer. Thus, under appropriate conditions many quanta can be stored as vibrational energy.

This process is analyzed theoretically in the following sections. Section II.B. treats the case of a molecule with only one vibrational mode, as in a diatomic molecule. In Section II.C. the addition of another vibrational mode is considered, in an attempt to obtain an understanding of the vibrational energy absorption process in a polyatomic molecule such as CH_3F. Computer results will be used throughout to verify the analytical results and check the assumptions. A treatment of the conditions necessary for ignoring the rotational structure is given in the Appendix.

B. One Mode Model

If we denote P_v as the probability of a molecule being in state v, where the density in state v is $N_v = P_v N$ (N is the

total number density of molecules in the system), the rate equations describing the interaction of the laser with the oscillator system may be written as

$$\frac{dP_0}{dt} = \left(\frac{\partial P_0}{\partial t}\right)_c - \gamma_p (P_0 - P_1)$$

$$\frac{dP_1}{dt} = \left(\frac{\partial P_1}{\partial t}\right)_c + \gamma_p (P_0 - P_1) \qquad (1)$$

$$\frac{dP_v}{dt} = \left(\frac{\partial P_v}{\partial t}\right)_c \qquad v \geq 2$$

where $(\partial P_v/\partial t)_c$ is the contribution due to V-V collisions and γ_p is the effective rate constant describing the energy flow into the system due to stimulated emission and collisions. [The expression for γ_p is given in Eq. (A-15) of the Appendix.] This expression assumes that the laser pulse duration is sufficient so that the rotational structure can be ignored (the conditions are given in the Appendix), and that the laser intensity is such as to only couple to the $v = 0 \rightarrow 1$ vibrational transition, collisionless multiple photon absorption processes being negligible. Relaxation due to VT processes is also assumed to be unimportant, as in the case when $\tau_p \ll \tau_{VT}$. The treatment will be generalized to include VT processes below.

If we assume resonant binary V V processes, and dipole-dipole collisions in the harmonic oscillator approximation, the process has a probability rate Therefore, the collision part of the coupled rate equations can be written as( )

$$\left(\frac{\partial P_v}{\partial t}\right)_c = \frac{\gamma_{VV}}{2} \sum_{v'=0}^{\infty} \Big\{ (v+1)v' \left[P_{v+1} P_{v'-1} - P_v P_{v'} \right] + (v'+1)v \left[P_{v-1} P_{v'+1} - P_v P_{v'} \right] \Big\} . \qquad (2)$$

Here γ_{VV} is defined such that for an isolated three level system (v = 0,1,2),

$$\frac{dP_1}{dt} = \left.\frac{\partial P_1}{\partial t}\right)_c = 2\gamma_{VV}\left(P_2 P_0 - P_1 P_1\right) \quad ,$$

where γ_{VV} is the characteristic "up the ladder" collision rate.( ) Equation (2) may be simplified by using the condition of number conservation

$$\sum_{v=0}^{\infty} P_v = 1 \quad , \tag{3}$$

and noting that the mean number of quanta stored in an oscillator is given by

$$\epsilon = \sum_{v=0}^{\infty} v P_v = \frac{\text{vibrational energy}/\hbar\omega}{\text{molecule}} \quad . \tag{4}$$

Thus,

$$\left.\frac{\partial P_v}{\partial t}\right)_c = \frac{\gamma_{VV}}{2}\left\{-\left[(2v+1)\epsilon + v\right]P_v + v\epsilon P_{v-1} + (v+1)(\epsilon+1)P_{v+1}\right\} . \tag{5}$$

We now wish to examine the problem in the limit in which the laser saturates the v = 0→1 transition( ) such that

$$\frac{dP_0}{dt} \simeq \frac{dP_1}{dt} \quad . \tag{6}$$

That is, the time rate of change of levels 0 and 1 are locked together, so that if one changes the other follows. Therefore, using Eqs. (1)

$$P_0 - P_1 = \frac{1}{2\gamma_p}\left[\left(\frac{\partial P_0}{\partial t}\right)_c - \left(\frac{\partial P_1}{\partial t}\right)_c \right] \quad .$$

Thus, it can be seen from Eq. (5) that P_0-P_1 is at most of order $\gamma_{VV}/2\gamma_p$. So, if

$$\gamma_{VV} << 2\gamma_p \quad , \tag{7}$$

then

$$P_0 \simeq P_1 \quad . \tag{8}$$

Accordingly, (7) is a sufficient condition for equalizing the populations of the v = 0 and v = 1 levels for all time, and thus insures (8) and (6). Note, however, that we must allow the product $\gamma_p(P_0-P_1)$ to be non-zero, but as yet unspecified.

Let us now find an expression for the time rate of change of vibrational energy per molecule. Taking the derivative of Eq. (4) and using Eqs. (1)

$$\dot{\epsilon} = \sum_{v=0}^{\infty} v \frac{dP_v}{dt} = \sum_{v=0}^{\infty} v \left(\frac{\partial P_v}{\partial t}\right)_c + \gamma_p(P_0 - P_1) \quad .$$

Substituting Eq. (5) one obtains $\sum_0^\infty v \left(\frac{\partial P_v}{\partial t}\right)_c \equiv 0$, as expected, since energy is conserved in the collisions in this model.

Thus,

$$\dot{\epsilon} = \gamma_p (P_0 - P_1) \quad , \tag{9}$$

and the rate equations become

$$\dot{P}_0 = \left(\frac{\partial P_0}{\partial t}\right)_c - \dot{\epsilon} \quad , \tag{10a}$$

$$\dot{P}_1 = \left(\frac{\partial P_1}{\partial t}\right)_c + \dot{\epsilon} \quad , \tag{10b}$$

$$\dot{P}_v = \left(\frac{\partial P_v}{\partial t}\right)_c \qquad v \geq 2 \quad . \tag{10c}$$

The $\dot{\epsilon}$ term may be considered as a perturbation, not necessarily small, on the usual collisional relaxation. The VV processes attempt to drive all the populations to a Boltzmann equilibrium,( ) but the $\dot{\epsilon}$ term offsets the process by maintaining nearly equal populations in v = 0 and v = 1. As a result, VV collisions pump molecules to higher vibtational levels, with the laser supplying the necessary energy. Using Eqs. (5) and (10) with $P_0 = P_1$ and $\dot{P}_0 = \dot{P}_1$

$$\dot{\epsilon} = \frac{\gamma_{VV}}{2} P_1 \sim \dot{P}_1 \quad . \tag{11}$$

This equation gives ϵ once $P_1(t)$ is known. Conversely, $P_1(t)$ can be found once ϵ is specified as a function of t or P_1. The fact is, $\dot{\epsilon} = \gamma_p(P_0 - P_1)$ is an unspecified parameter other than the requirement $P_0(t) \simeq P_1(t)$.

This difficulty can be overcome by taking advantage of the fact that the vibrational levels $v \geq 2$ are all in

25<

equilibrium with respect to the v = 1 level. This can be understood in the following way. With $P_0 = P_1$ the tendency of the collision terms in Eqs. (10a) and (10b) is to increase P_0 and decrease P_1 [cf. Eq. (2)]. However, the $\dot{\epsilon}$ terms in these two expressions oppose these changes and sufficiently retards the relaxation of these two levels so that they can be considered slowly varying on the VV time scale.( ) The remainder of the levels then come into equilibrium with the v = 1 level in a time $1/\gamma_{vv}$. Thus, the vibrational populations can be described by an effective temperature in the form

$$P_0 = P_1 \equiv P$$
$$P_v = P\, e^{-(v-1)\theta} \quad , \qquad (12)$$

where $\theta = \hbar\omega/kT_v$, with T_v being the time-dependent effective vibrational temperature of the v = 1→∞ vibrational levels relative to the v = 1 level. This assumed time dependent quasi-equilibrium distribution is verified by computer solutions of Eqs. (1) and (2). Figure compares the distribution of Eq. (12) with the rate equation predictions for a value of $\gamma_p/\gamma_{vv} \cong 100$. As can be seen, the overall agreement is excellent. The small discrepancies are inconsequential, since ε(t) is determined by a sum over the P_v's and is not very sensitive to individual values.

Substituting (12) into (3) and (4), and solving for ε in terms of P

$$\epsilon = (1-P)^2/P \quad , \qquad (13)$$

26

and

$$\dot{\epsilon} = -\frac{1-P^2}{P^2}\dot{P} \qquad (14)$$

This gives an independent expression for $\dot{\epsilon}(P)$, as desired. Equating the two expressions for $\dot{\epsilon}$, (11) and (14), one obtains a differential equation for P

$$\dot{P}\left[2 - \frac{1}{P^2}\right] = \frac{\gamma_{VV}}{2} P \quad , \qquad (15)$$

which can be easily integrated subject to the relevant boundary conditions. Since the laser saturates the v = 0→1 transition on a time scale substantially shorter than the characteristic VV time [see Eq. (7)], the appropriate boundary conditions are

$$P(t=0) = P_1(t=0) = P_0(t=0) = \frac{1}{2} \quad . \qquad (16)$$

Thus

$$\frac{1}{P^2} + 4\ln 2P = \gamma_{VV}\tau_p + 4 \quad . \qquad (17)$$

This simple expression, together with Eq. (13), determines the number of quanta per molecule absorbed. Note that ε is entirely determined by the product of the VV rate constant and the laser pulse duration, which is roughly the number of V-V collisions occurring during the laser pulse. Neither the laser intensity

nor any other parameters enter in. Values of $\epsilon(t)$ predicted by Eqs. (17) and (13) are in precise agreement with computer solutions of the coupled rate equations (1,2) (Fig.).

This solution has interesting forms for the limiting values of $\gamma_{VV}\tau_p$. For $\gamma_{VV}\tau_p \ll 1$, $P(\gamma_{VV}\tau_p)$ doesn't change much from its initial value and

$$\epsilon \simeq \frac{1}{2} + \frac{3}{8}\gamma_{vv}\tau_p \qquad (18a)$$

Thus, in the initial part of the pulse the energy stored increases linearly with time. In the other extreme, when $\gamma_{VV}\tau_p \gg 1$, $P(\gamma_{VV}\tau_p) \ll 1$ and consequently

$$\epsilon \simeq \sqrt{\gamma_{vv}\tau_p} \qquad (18b)$$

This expresses the fact that the energy absorption becomes more like a random walk ($\gamma_{VV}\tau_p$ = number of VV collisions), since higher states are populated and energy can flow down the vibrational ladder, as well as up. Furthermore, in these two limits

$$\dot{P}_0 \simeq \dot{P}_1 \simeq -\frac{1}{8}\gamma_{vv} \quad , \quad \gamma_{vv}t \ll 1$$

$$\dot{P}_0 \simeq \dot{P}_1 \simeq -\frac{1}{2(\gamma_{vv}t)^{3/2}}\gamma_{vv} \quad , \quad \gamma_{vv}t \gg 1$$

so that P_0 and P_1 do change at a rate substantially slower than the charateristic VV rate, γ_{VV}, which is consistent with assumption (12).

28<

According to the results so far, any desired amount of

of laser energy can be transferred to the molecule by using a laser pulse of sufficiently long duration. In actuality, vibration-to-translation (VT) relaxation processes place an upper limit on the maximum amount of stored energy. For pulses exceeding τ_{VT}, the VT relaxation time, some of the stored vibrational energy will be converted to translational energy. Thus, for $\tau_p \sim \tau_{VT}$ the amount of stored vibrational energy reaches a limiting value.

To include the influence of VT processes one must include this interaction in the rate equations. For this the term

$$\gamma_{VT}\left[(v+1)\left(P_{v+1} - \eta P_v\right) - v\left(P_v - \eta P_{v-1}\right)\right]$$

must be added to each of Eqs. (1), where $\gamma_{VT} = \tau_{VT}^{-1}$ is the VT relaxation rate( ) and η is given by $\eta = e^{-\hbar\omega/kT}$, as is necessary for detailed balancing.( ) In this case Eq. (9) becomes

$$\dot{\epsilon} + \gamma_{VT}\left(\epsilon - \eta(\epsilon+1)\right) = \gamma_p\left(P_0 - P_1\right) .$$

using the expression for the laser pumping term in the revised Eqs. (1), with $P_0 = P_1$ and $\dot{P}_0 = \dot{P}_1$, and the expressions for ϵ and $\dot{\epsilon}$ from the temperature assumption [Eqs. (13), (14)], the differential equation for P becomes

---

* When the system comes into thermal equilibrium (i.e. the vibrational temperature equal to kinetic temperature, T) this choice of η causes $\frac{\partial P_V}{\partial t})_{VT\ Coll} \equiv 0$.

$$\dot{P}\left[2-\frac{1}{P^2}\right] = \frac{\gamma_{VV}}{2}P - \gamma_{VT}\left[(1-\eta)\frac{1}{P} - (2-\eta)\right]. \quad (19)$$

This can be integrated with the initial condition, $P(t=0) = 1/2$, as before. For $\eta \ll 1$ and $\gamma_{VV} \gg \gamma_{VT}$ (the usual case) the energy per molecule is

$$\frac{E}{\hbar\omega} = \epsilon(\tau_p) \simeq \sqrt{\frac{\gamma_{VV}}{2\gamma_{VT}}}\left(1 - \frac{1}{2}e^{-2\gamma_{VT}\tau_p}\right), \quad (20)$$

valid for $\tau_p \gtrsim \tau_{VT}$. Thus, for laser pulses longer than a few τ_{VT} the number of quanta per molecule reaches the limiting value $\sqrt{\gamma_{VV}/2\gamma_{VT}}$. Thus, VT processes place an upper limit on the amount of laser energy which can be vibrationally stored in the molecule.

Finally, Eqs. (1) with VT interaction but without the laser (after the laser pulse is terminated) have the expected solution for $t > \tau_p$ $\epsilon(t) = \epsilon_0 + [\epsilon(\tau_p) - \epsilon_0] \exp[-(1-\eta)\gamma_{VT}(t-\tau_p)]$ where $\epsilon_0 \equiv \eta/(1-\eta)$ is the energy of the oscillator system at room temperature.

It should be noted that this model becomes inadequate for cases in which the laser induces substantial population into high lying levels in which there is a significant degree of anharmonicity. This is so because an anharmonic oscillator does not evolve toward equilibrium through a continuous series of Boltzmann-like distributions,( ) hence assumption (12) becomes inadequate. To get an idea of when this effect becomes important assume that the temperature assumption of Eqs. (12) is still approximately valid and notice that Eqs. (3) and (4) for small P lead to

$$P_v \simeq P\, e^{-(v-1)/\epsilon}$$

Thus, if the degree of anharmonicity is not significant up to vibrational level v = 10, for instance, then the model remains valid for energy absorption of up to 4 or 5 photons. After that anharmonicity effects such as bottlenecking, Trainor pumping, etc.( ) may become important.

III. ENERGY ABSORPTION IN METHYL FLUORIDE (CH_3F)

A. Relevant Properties

The energy absorption from an intense laser pulse and subsequent vibrational partioning, induced by vibrational collisions, have been studied in methyl fluoride. This molecule was chosen because of several features which make it well suited for our studies. The attractive features of methyl fluoride are: (a) A strong $C^{13}H_3F$ absorption resonance coincides with a strong CO_2 laser line[3,9], (b) in methyl fluoride the relaxation processes obey the relations $\tau_{V-T} \ll \tau_{V-V} \ll \tau_{R-R}$[19], (c) its energy flow path and kinetics in the low excitation regime has been well established, and (d) fluorescence observed from emission by the vibrational modes make it possible to study partitioning of the vibrational energy after the laser excitation process is completed.

Strong fluorescence from the C-F stretch mode, ν_3 near 9.6 μm, and the C-H stretch, ν_1 and ν_4 near 3.4 μm, have been observed.[3] Weaker but observable emissions also have been reported from the bending modes, ν_2 and ν_5, near 6.8 μm and the methyl rock mode, ν_6 near 8.8 μm.[4] (ν_1, ν_5, and ν_6 are all doubly degenerate modes)

These fluorescing modes have provided much information about relaxation processes in methyl fluoride. The rotational relaxation time in methyl fluoride, measured from pressure broadening data, was reported to be 8×10^{-9} sec.[15] τ_{V-V} and τ_{V-T} have been determined from laser induced fluorescence techniques with reported values of 0.83 μsec-torr[19] and 1.69 msec-torr[3], respectively.

B. Experiment

The 9.65 μm P(32) TEA CO_2 laser line falls within 25 MHz of the ν_3 ($V = 0 \rightarrow 1$) R(4,3) transition of $^{13}CH_3F$. Laser pulses were typically 2-3 μsec duration with energies ≤ 0.25 Joules, small enough to avoid appreciable absorption by collisionless processes,[16,17] but sufficiently large to ensure complete saturation of the Doppler profile. Single mode output of the grating coupled laser oscillator was ensured by placing apertures inside the cavity. Care was taken to avoid mode locking which could produce ambiguities in the data analysis. The long pulses, necessary to insure many V-V collisions during the laser excitation process, were obtained by ajusting the nitrogen content of the laser gas mixture.

The laser output, collimated to a 6 mm spotsize, was passed through an 18 cm glass absorption cell. A KCl beam splitter was placed in front of the cell to sample a portion of the incident beam for monitoring. Both the sample beam and the transmitted beam were scattered off coarse aluminum surfaces to avoid the viewing of hot spots by two Au:Ge detectors whose outputs were integrated by an RC circuit and viewed on a dual beam oscilloscope. A Scientech 362 energy-power meter was used to calibrate the detectors and establish their linearity. Gas samples used were 90% $^{13}CH_3F$ and 10% $^{12}CH_3F$ from Merk, Sharp, and Dohme of Canada. The appropriate factors for the isotopic purities used were included in all analysis.

The volume of the interaction region was carefully estimated to within 10%. The number of CO_2 quanta absorbed, ξ, was obtained by measuring the amount of energy absorbed from the laser beam and

33<

dividing by the number of molecules in the interaction region.

The data points of Figure 5F2 give the measured number of CO_2 quanta absorbed vs $^{13}CH_3F$ pressure. As can be seen, $\bar{\varepsilon}$ rises monotonically up to a value of 2.6 quanta absorbed at 6.0 torr, at which point it starts to decrease. This decline is due to absorption of the laser pulse as it transverses the gas sample. As explained in the previous section, the condition, $I > (\hbar\omega/\sigma_{abs})\gamma_{VV}$, must be satisfied in order for efficient vibrational heating to occur. At higher pressure, however, sufficient attenuation occurs so that the laser intensity is reduced below this value before the end of the sample cell, leading to a reduction in V-V heating efficiency.[5] The use of a shorter cell would not have permitted sufficient observable absorption for accurate measurements below 3.0 torr.

The data was analyzed using the model discussed in Section III. The assumptions made in the derivation,

$$\tau_{RR} < \tau_{VV} < \tau_p < \tau_{VT},$$

are all satisfied in CH_3F. As explained in Section II, analytical result of eq. 15 should be accurate to within 20%; accordingly, this simple expression was used. Taking the experimental value of laser pulse duration, $\tau_p \simeq 3$ μsec, eq. 15 was fit to the data points of figure 5F2 by varying the single parameter γ_{V-V}. The best fit (solid curve of figure 5F2) resulted in a value of $\gamma_{VV} = 0.8 \pm 0.2$ μsec^{-1} torr^{-1}. No significant improvement in fit could be gained by using the two mode computer model of Section II. The principle sources of error in the quoted value are uncertainity in the beam volume and fluctuations of the laser pulse amplitude.

34<

This value is within experimental error of the Earl and Ronn[19] value of 1.2 ±.3 μsec^{-1} $torr^{-1}$ measured using laser induced fluorescence techniques.

As explained earlier, efficient VV heating can only occur in the absence of a rotational bottleneck. The necessary condition, derived in the Appendix, is $\tau_B = \frac{\tau_R}{Z_R} << \tau_{V-V}$.

However, if this inequality is not satisfied by the pure absorbing gas, a buffer gas can be added to decrease τ_R, hence, τ_B. To test for the presence of a bottleneck, energy absorption experiments were performed at a fixed CH_3F pressure, 5.0 torr, while different amounts of argon was added up to 500 torr. Argon was chosen because this heavy inert atom should leave the V-V rate unaffected but should increase the rotational collision rate, τ_R, without appreciably deactivating the level populations via V-T processes.

The pressure broadening of CH_3F by argon was estimated to be ~ 3 MHz/torr, by comparison of pressure broadening data in references [20, 21, 29, 30]. The CH_3F self broadening is 40 MHz/torr,[15] thus, 500 torr of argon would broaden the 200 MHz CH_3F lines to 1700 MHz. This represents a factor seven increase in the rotational collision time given by

$$\tau_{R-R} = 1/\pi\Delta\nu$$

where $\Delta\nu$ is the linewidth (FWHM). This gives $\tau_{R-R} \sim 0.18$ nsec at 500 torr argon, more than sufficient to remove any potential bottleneck. However, the transmitted intensity vs. argon pressure indicates no detectable increase in the energy absorbed as argon was added.

35

← We could then conclude that in pure CH_3F, no rotational bottleneck is present under our experimental conditions. These results also suggest the absence of multiple photon or other non v=0→1 absorption in CH_3F.[5] The condition for efficient laser pumping is by equation (1).

$$\tau_B = \tau_{R-R}/Z_{JK} \ll \tau_{V-V}$$

where τ_B is the rotational bottleneck time and Z_{JK} the fraction of molecules in any (J,K) state. Using τ_{R-R} = 8 nsec at 1.0 torr and Z_{JK} = .0073 for the R(4,3) transition, we find τ_B = 1.1 μsec or $\tau_B \gtrsim \tau_{V-V}$ and, therefore, the existence of a bottleneck. This conflict with experimental observations suggest that maybe τ_{R-R} is inaccurate due to the J-dependence of the pressure broadening. Also, the unequal distribution of population among the (J,K) states with a large concentration in the K = 3, 6, 9... states can shorten the number of collisions necessary for transfer of molecules into the (J = 4, K = 3) state for pumping. Nevertheless, experiment establishes the absence of bottleneck effects, and to resolve this discrepancy, ~~requires~~ a more careful examination of the parameter τ_{R-R} and how it is used here is required.

IV. Energy Distribution in CH_3F

To establish that for times $<<\tau_{vt}$ the absorbed energy resides in the vibrational degrees of freedom, the time evolution of the fluorescence from the 9.6 μm C-F stretch mode (ν_3) was monitored by a Cu:Ge detector. (Fig SF3) In the pressure range of the experiments the fluorescence was always in the form of a rapid rise, governed by the duration of the laser pulse, followed by a long (~ ms) decay, determined by the V-T relaxation processes. The 3.3 m C-H stretch (ν_1,ν_4) and 6.8 μm bend (ν_2,ν_5) fluorescence bands exhibited the same temporal behavior as ν_3. (Fig SF3) This indicates fast intermode V-V rates and that a vibrational steady state among the modes is reached soon after the laser pulse terminates.

A. Cold Gas Filter Analysis of Mode Temperature

Since the absorbed energy is distributed among all the vibrational modes, it is important to determine how much is stored in each. Absolute measurements of fluorescence intensities from each mode could provide this information but such are difficult and imprecise. A new technique, which utilizes the fact that a steady state is rapidly established among the vibrational modes, was used to measure the energy stored in the ν_3 mode. In this technique the peak fluourescence is first observed after it passes through an empty "cold gas filter" cell to give I(0). Then, methyl fluoride gas at room temperature

is introduced into this cell to remove the $\nu = 1 \rightarrow \nu = 0$ component of the fluorescence, giving $I(0)-I_{10}$. This "cold" gas (room temperature) is an ideal filter for the $\nu = 1 \rightarrow \nu = 0$ fluorescence since its absorption frequencies match the emission frequencies line for line, and only the vibrational ground state is significantly populated. The small anharmonicity (18 cm^{-1}) is sufficient to prevent the absorption of ν_3 fluorescence from higher lying levels.

The ratio $\frac{I(0)-I_{10}}{I(0)}$ is an easily measured quantity which determines the vibrational temperature or energy content of the mode in question. At higher temperatures more of the fluorescence arises from higher lying vibrational states and the ratio tends to unity. At lower temperatures the fluorescence is primarily I_{10} and the ratio tends to zero.

Describing the vibrational level populations of the ν_3 mode, vibrational frequency ν_3, by a Boltzmann distribution at temperature T_3, the fluorescence intensity arisng from a particular vibrational transition is

$$I_{v,v-1} \propto |\mu|^2_{v,v-1} e^{-v\beta_3}\left(1-e^{-\beta_3}\right) \qquad (1)$$

where $\beta_3 = \frac{h\omega_3}{kT_3}$. $I_{v',\,v-1}$ is the net fluorescence intensity summed over the individual rotational quantum numbers J,K. Thus $|\mu|^2_{v,v-1}$ is the vibrational transition moment and the re-

maining factor is proportional to the total population of level v. Assuming harmonic oscillator transition moment matrix elements $|\mu|^2_{v,v-1} = v|\mu|^2_{1,0}$ the ratio becomes

$$\frac{I(0)-I_{10}}{I(0)} = 1-(1-e^{-\beta_3})^2 = 1-(1+\epsilon_3)^{-2} \qquad (2)$$

where ϵ_3 is the number of vibrational quanta stored in ν_3.

This equation is valid when the I_{10} component is completely removed by the cold gas filter. In practice, however, several problems are incurred in achieving this. The v = 1 to v = 0 fluorescence is composed of many rotational-vibrational lines. The intense emission lines are absorbed strongly; conversely, the weak emission lines are absorbed weakly. A similar effect occurs because each rotational-vibrational line is Doppler broadened and the wings of its profile are absorbed more slowly than its line center. As a result the curve of transmitted intensity I(P') versus cold gas filter pressure P' is not a single exponential but instead has a long tail.

In principle all of I_{10} can be filtered out by increasing the optical absorption length, proportional to P'L' in the Doppler regime. However, signal is lost to solid angle if L', the filter cell length, is made too long. Furthmore, if the pressure P' is increased too much, the I_{10} absorption lines may be pressure broadened sufficiently to overlap rotational-

vibrational lines of higher vibrational transitions. To avoid these problems the dependence of I_{10} on P'L' was determined by considering the absorption of each individual rotational-vibrational emission line and summing over J,K.

The spontaneous emission intensity of an individual line (J,K J'K') is determined by the population of its upper state and its matrix element. Both are functions of the rotational quantum numbers. Similarly, its absorption by the cold gas filter is dependent on the matrix element and the population difference between its upper and lower states. Neglecting for the moment the non-zero linewidths of the rotational-vibrational transitions, we have

$$I_{10}(P'L') \propto \sum_{PQR} \sum_{JK} N_{JK} |\mu|^2_{JK-J'K'} \, e^{-\alpha_{JK-J'K'} P'L'} \qquad (3)$$

with absorption coefficient

$$\alpha_{JK-J'K'} = C' |\mu|^2_{JK-J'K'} (N_{JK} - N_{J'K'}) \qquad (4)$$

where C' is a known constant. Here N_{JK} and $N_{J'K'}$ are the populations in the upper and lower states, respectively (including statistical weighting factors for nuclear spin and K degeneracy) and $|\mu|^2_{JK-J'K'}$ is the matrix element for the branch considered (P,Q,R).[21] The value for the transition dipole moment, necessary for calculating $\mu_{JK-J'K'}$ was deter-

mined from known absorption coefficients.[15] The effects of Doppler broadening (non-zero linewidth) are included by replacing the single exponential $e^{-\alpha_{JK-J'K'}P'L'}$ in Eq. ( ) by $\sum_{n=0}^{\infty}\left(-\alpha_{JK-J'K'}P'L'\right)^n/n!\sqrt{n+1}$. This function is readily derived by considering the absorption of a Doppler broadened line by a gas whose absorption coefficient is also Doppler broadened [similar considerations are found in Ref. ( )].

This numerical procedure establishes an expression for the transmitted intensity as a function of P'L'. To facilitate data analysis this generated curve was approximated by a three exponential fit, $\chi(P'L') = 0.567\exp(-0.614P'L') + 0.331\exp(-0.145P'L') + 0.102\exp(-0.019$ so that

$$I_{10}(P'L') = I_{10}(0)\chi(P'L') \tag{5}$$

Equation ( ) can thus be modified to include the dependence on P'L'.

$$\frac{I(P'L')}{I(0)} = \frac{I(0) - I_{10} + I_{10}(P'L')}{I(0)} = 1 - (1+\epsilon_3)^{-2}\left[1 - \chi(P'L')\right] \tag{6}$$

In the data analysis, the parameter ϵ_3 of Eq. (6) was varied until the resulting theoretical curve matched the experimental data (Fig. 8).

In the experiments (Fig. SF1 6) a 0.25J CO_2 laser beam, 0.6 cm diameter, was passed through a fluorescence cell de-

signed for viewing emission at right angles to the beam. Noise from laser scatter, most of which is off the exit window, was minimized by locating the exit window far from the side window (Fig. SF1). Since $^{13}CH_3F$ is a strong absorber, the scattered radiation was completely absorbed in the long optical path between the two windows. To minimize reabsorption of the fluorescence by unexcited gas it is important to keep the laser beam close to the side window. Recessing the side window into the cell reduced this distance to only 2 mm. The 6 mm beam diameter was sufficiently small so that absorption of fluorescence in the excited region was unimportant. The side light emission from this fluorescence cell was passed through an 8 cm cold gas filter. The transmitted intensity was focused onto a Cu:Ge detector whose output was displayed on an oscilloscope.

Figure SF4 shows the experimental data and the theoretical fits for various fluorescence cell pressures, P. As can be seen, at higher pressures, P, and thus higher VV rates, the number of quanta found in ν_3 increases as expected. However, this represents only 40-50% of the total energy absorbed by the molecule. The remaining energy is transferred to the other vibrational modes through VV cross-over collisions.

B. Energy Distribution and Flow Paths

The VV cross over collisions which transfer energy from ν_3 to the other vibrational modes have rates about 1/10 of the VV rate within the ν_3 mode.[19] As explained above, the VT relaxation rate is slow enough to allow all of the modes to reach a vibrational equilibrium, with each mode at a different vibrational temperature.

Measuring the temperatures of modes other than ν_3 by the cold gas filter method is generally not practical because of the weaker absorption coefficients characteristic of these modes.

For these modes, I_{10} can only be absorbed out by increasing P'L' to the point where the signal to noise and pressure broadening limitations are significant. A cold gas filter measurement on both (ν_1,ν_4) and (ν_2,ν_5) was only able to give an upper bound to the energies (ν_1,ν_4) which agrees with Fig. 4. Once the temperature of ν_3 is established by the CGF method, however, relative fluorescence intensities can be used to determine the temperatures of the other modes.

The fluorescence intensity due to a particular vibrational transition in a mode of frequency ω is

$$I_{v,v-1} \propto \omega^4 v |\mu|_{10}^2 n_0 e^{-v\beta} \qquad (7)$$

where n_0 is the population of the vibrational ground state.

The integrated absorption "strengths", α, for each mode, which are tabulated in the literature allow us to replace μ_{10}^2 in the equation since

$$\alpha = \frac{n_0 4\pi^2 \omega}{\hbar c} \mu_{10}^2 \quad (8)$$

Summing over all v yields the total flourescence intensity for the mode.

$$I \propto \omega^3 \alpha e^{-\beta}(1-e^{-\beta})^2 \quad (9)$$

Therefore, from measurements of I_B/I_A, the ratio of the fluorescence intensities of two modes, A and B, the vibrational temperature of mode B can be obtained from the known temperature of mode A via

$$e^{-\beta_B}(1-e^{-\beta_B})^{-2} = \frac{I_B}{I_A}\left(\frac{\omega_A}{\omega_B}\right)^3 \frac{\alpha_A}{\alpha_B} e^{-\beta_A}(1-e^{-\beta_A})^{-2} \quad (10)$$

Once the temperature is known, of course, the energy stored in the mode ε_B is also known [Eq. ( )].

This method was applied to the degenerate modes ν_2 and ν_5 at 6.8 μm and degenerate modes ν_1 and ν_4 at 3.4 μm. The fluorescence from the ν_6 mode at 8.8 μm was too weak to measure. The (ν_1,ν_4) fluorescence was isolated with an infrasil quartz filter and the ν_2,ν_5 fluorescence with a wide bandpass dielectric filter. The ν_3 flourescence, which served

as the reference intensity was isolated by a dielectric filter which passed long wavelengths. In establishing the relative vibrational temperatures with Eq. ( ), the tabulated values of integrated absorption coefficients of Ref. 24 were used. These values agree with the absorption spectra given in Refs. 25,26. In the analysis (ν_2,ν_5) was considered to be triply degenerate since the doubly degenerate ν_5 is only 4 cm^{-1} below ν_2. Likewise, (ν_1,ν_4) was treated as triply degenerate since doubly degenerate ν_4 is 15 cm^{-1} above ν_1. Conributions to the 3 μm fluorescence from the Fermi mixed (ν_2,ν_5) state were neglected because of its relatively weak intensity.[27]

The results of these measurements are shown as data points in Fig. 4. $\varepsilon_{2,5}$ and $\varepsilon_{1,4}$ are the sums of all the consistent degenerate modes' energies. Although ε_6 was not measured, it could be estimated theoretically (as discussed below). Thus, we have experimentally established that for times $<<VT$, all of the absorbed energy is partitioned among the vibrational degrees of freedom. This result also establishes the internal consistency of the absorption, cold gas filter, and relative fluorescence techniques.

Given a knowledge of the energy flow paths between equilibrating vibrational modes, and the total amount of energy absorbed, the distribution of this energy among the modes can

be circulated theoretically. Since we have measured these energies experimentally we can choose between various possible flow paths on the basis of how well they fit the data. The solid curves, (b), (c), (d) and (e) of Fig. 4 are theoretical fits assuming a model given below.

The path below, Path 1, used to calculate the curves in Fig. 4, has been shown by Flynn and coworkers (23 to be the dominant path in the weak excitation regime.

Path 1

(1) $(\nu_3) + (0) \rightleftarrows (\nu_6) + (0) - 147\ cm^{-1}$

(2) $(\nu_6) + (0) \rightleftarrows (\nu_2,\nu_5) + (0) - 275\ cm^{-1}$

(3) $2(\nu_2,\nu_5) \rightleftarrows (2\nu_2,2\nu_5) + (0) - 68\ cm^{-1}$

(4) $(2\nu_2,2\nu_5) + (0) \rightleftarrows (\nu_1,\nu_4) + (0) + 103\ cm^{-1}$

where, for instance, $(2\nu_2,2\nu_5)$ represents a single molecule with two quanta in mode ν_2 and two quanta in mode ν_5 and (0), a molecule in the vibrational ground state.

The temperatures, T_A and T_B, of two different modes in vibrational equilibrium with each other are related by

$$\frac{\omega_A}{T_A} - \frac{\omega_B}{T_B} = \frac{(\omega_A-\omega_B)}{T} \qquad (11)$$

where the ω's are the vibrational frequencies and T is the kinetic temperature. Applying Eq. ( ), for example, to the two modes ν_3 and ν_6 held in vibrational equilibrium with each other by reaction (1) in Path 1 we find

46

$$T_6 = \omega_6 \left[\frac{2\pi c\,(147 cm^{-1})}{300°K} + \frac{\omega_3}{T_3} \right]^{-1}$$

which for $T_3 = 2000^{\circ}$ K gives $T_6 = 1180^{\circ}$ K. Similarly from this T_6 and reaction (2), $T_{2,5}$ can be calculated and so on. From these temperatures we can relate a particular distribution of energy among the modes to the total vibrational energy of a molecule. Curves (b), (c), (d), and (e) were determined in this fashion from the total energy curve (a) which itself was a theoretical fit to the data assuming a particular γ_{VV}.

The good agreement of these curves with the experimental data in Fig. 4 argues well for the validity of Path 1. A possible alternative path, Path 2 below, was shown not to agree with the experimental results.

Path 2

(1) $(\nu_3) + (\nu_3) \rightleftarrows (2\nu_3) + (0) +$

(2) $(2\nu_3) + (\nu_3) \rightleftarrows (3\nu_3) + (0) +$

(3) $(3\nu_3) + (0) \rightleftarrows (\nu_1, \nu_4) + (0) + 16 \text{ cm}^{-1}$

For example, small energy defect of reaction 3 would indicate $T_{14} = 2000.4^{\circ}$ K. or $\varepsilon_{14} = .13$ for a T_3 of 2000° K. This is much greater than the measured $\varepsilon_{1,4}$.

DRAWINGS FOR PAPER

I HAVE MARKED ALL FIGURE REFERENCES IN THESE SECTIONS AS SF1, SF2, SF3, SF-

FIGURE SF 1

YOU WILL HAVE TO ASSIGN AN ABSOLUTE NUMBER WHEN YOU PUT YOUR FIGURES IN

ORIGINAL PAGE IS
OF POOR QUALITY

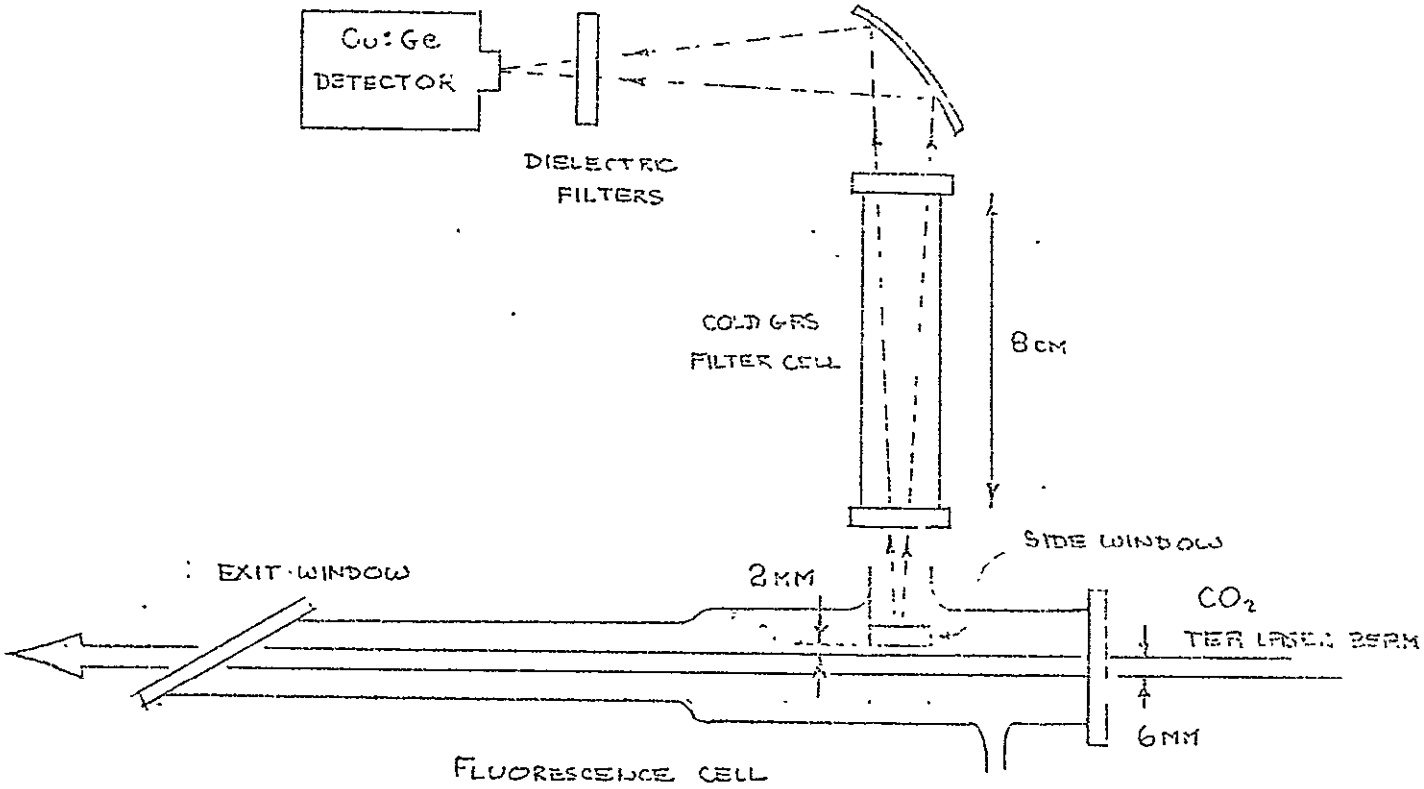

FIG. 6

HERE ARE 5 OF THE 6 DRAWINGS WE CONSIDERED

THE SIXTH IS THE DIAGRAM - THE ABSORPTION EXPERIMENT

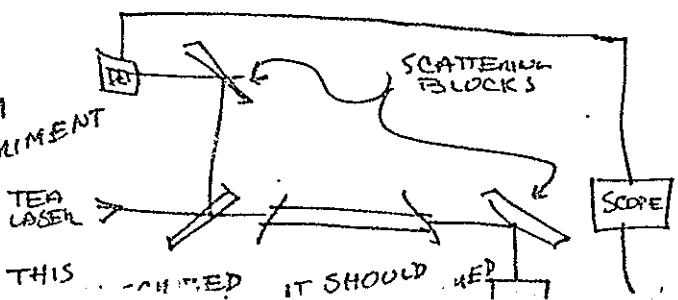

I THINK THIS ... IT SHOULD ...

CUT PAGE

FIGURE SF2.

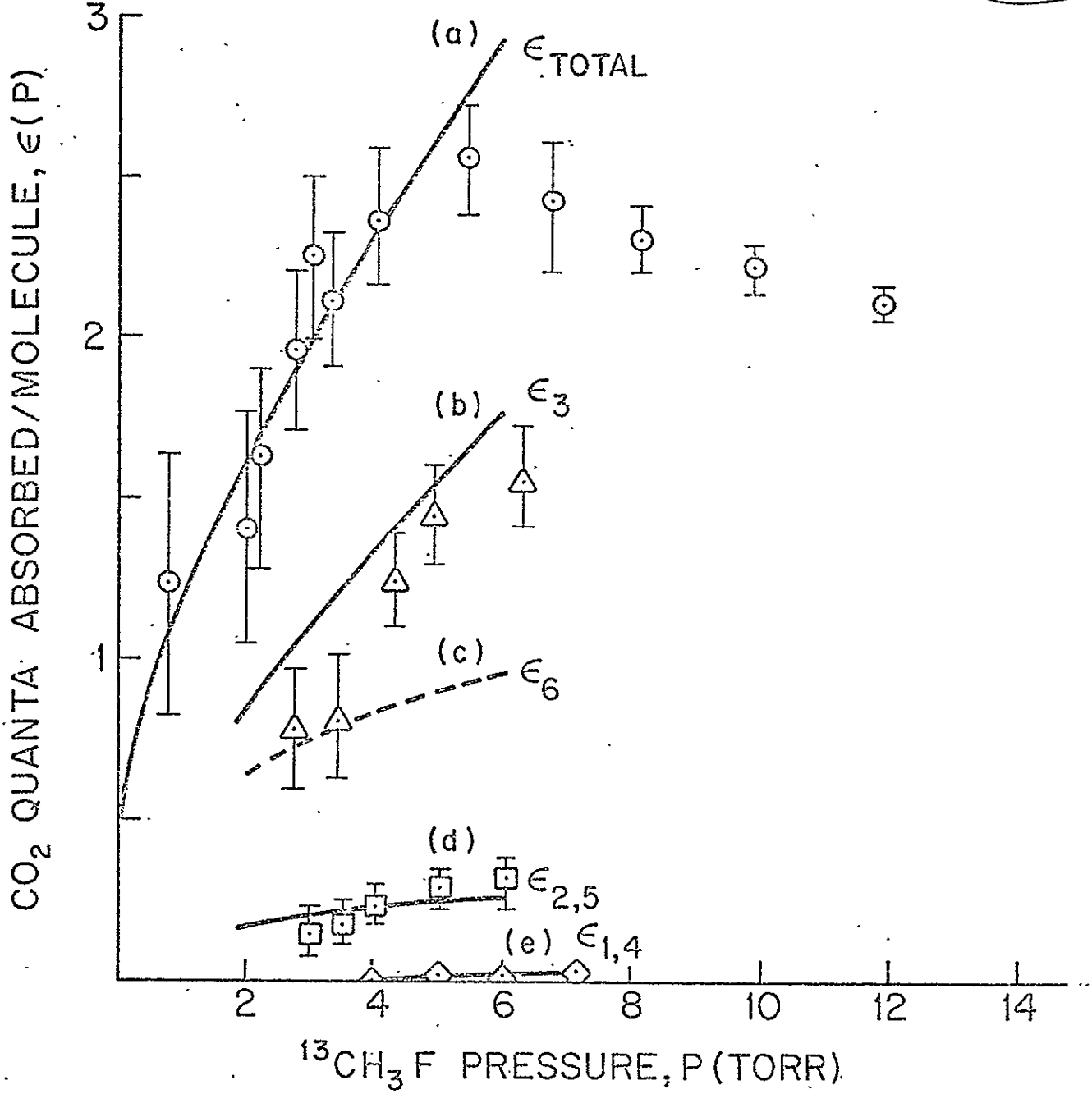

FIGURE SF3

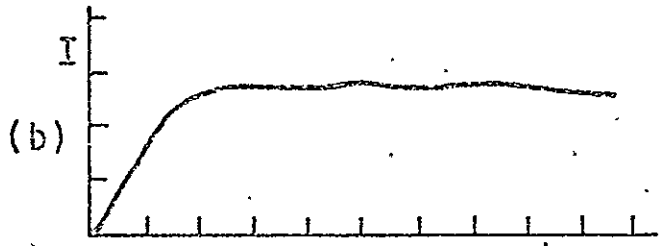

ν_3

— DECREASE SPACES OF COURSE

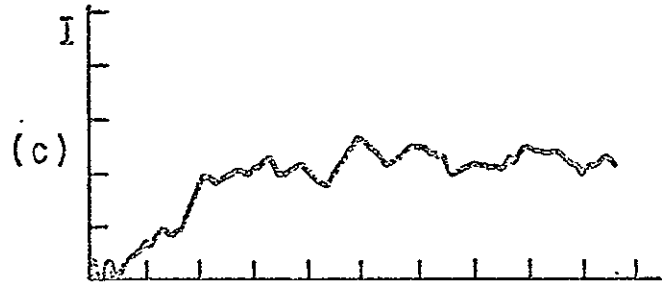

ν_2, ν_5

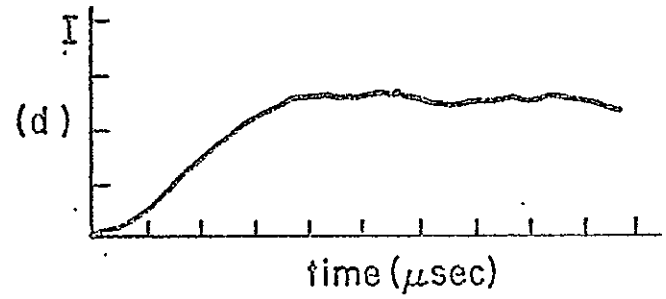

ν_1, ν_4

FIGURE SF4

ORIGINAL PAGE IS
OF POOR QUALITY

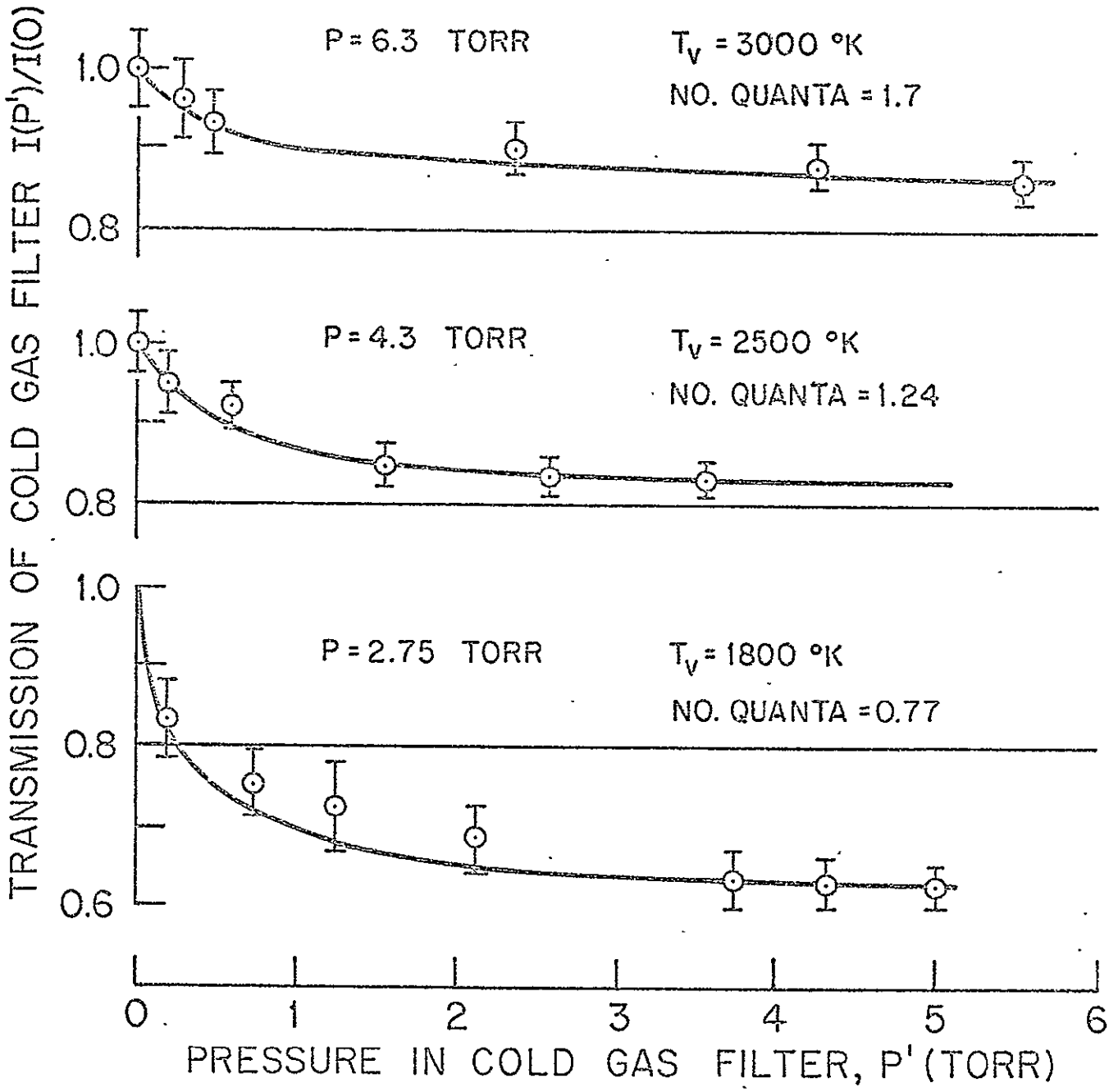

51<

HAVE A GOOD ONE AT 8.8 TORR T_V = 3200 °K 1.7 QUANTA

3.42 TORR 1850 °K .71 QUANTA — SOMETHING LONGER HERE SEE 2.75 TORR

4.95 TORR 2800 °K 1.43 QUANTA

= WHERE E OF $I(P')/I(0)$ MESSED UP ... 1.0 — NO 0.8 ... E IT

CAN TAKE THESE CHT OUT OF THESIS VE TO DRAFTSMAN

CUT PAGE

4. A. Javan and A. Sanchez

Extension of Microwave Detection and Frequency Measuring Technologies into the Optical Region

Proceedings of the Vail Conference, Plenum Press 1973

EXTENSION OF MICROWAVE DETECTION AND FREQUENCY MEASURING TECHNOLOGIES INTO THE OPTICAL REGION

A. Javan and A. Sanchez

Department of Physics

Massachusetts Institute of Technology

Cambridge, Massachusetts

Prepared for

Proceedings of the Vail Conference, 1973

EXTENSION OF MICROWAVE DETECTION AND FREQUENCY MEASURING TECHNOLOGIES INTO THE OPTICAL REGION

A. Javan and A. Sanchez*

Department of Physics, Massachusetts Institute of Technology, Cambridge, Massachusetts

ABSTRACT

Precise frequency measurements in the far-infrared and infrared have made possible highly accurate spectroscopic observations in these regions. This article gives a review of the general properties of the high-speed diode element used in the frequency measurements. Other future applications are discussed in the concluding section.

INTRODUCTION

Conventional spectroscopy in the optical and infrared region is based on precision wavelength measurements which utilize a variety of dispersive methods to compare different wavelengths and accurately determine their ratios. In the microwave region, on the other hand, precision measurements are done by measuring frequencies. In these, two different microwave frequencies, or a microwave and a radio frequency, are compared via frequency mixing in a nonlinear element.

The practical limits in the accuracies of the optical wavelengths measuring methods are set by the dispersive instruments, whose resolving widths are generally broad and considerably exceed the frequency spread of a stable monochromatic laser oscillator. In contrast, the ultimate accuracy of the microwave frequency measuring methods are determined by the fundamental limitation arising from the purity and the frequency stability of the microwave radiation. Because of this, the relative accuracy obtainable in a precision microwave frequency measurement is in general appre-

ciably higher than the relative accuracy of a precise wavelength measurement in the optical region.

The existing wavelength measuring methods have been more than adequate in a wide range of spectroscopic observations where the widths of the optical spectral lines are broad and appreciably exceed the resolving widths of the high-resolution wavelength measuring devices. In these cases, accurate molecular or atomic parameters are obtained by means of observations in which a large number of transitions belonging to the same atomic or molecular species are studied over a broad range of the spectrum.

With the availability of stable monochromatic laser radiation, it has become possible to make high-resolution spectroscopic observations in which optical resonances appear at much reduced linewidths, considerably below the resolution limits of even the best optical wavelength measuring instruments. Early observations followed the advent of gas lasers. These resulted in the discovery of a number of nonlinear radiative processes in which the interaction of monochromatic radiation with an atomic resonance occurs selectively over a narrow region of the atomic velocity distribution, resulting in narrow resonances which are completely free from Doppler broadening.[1] Other approaches, such as the molecular beam method,[2] have also enabled application of monochromatic laser radiation to the observation of narrow resonances whose widths are considerably less than their classical Doppler breadths. Beyond these, in the far-infrared and the long-wavelength region of the infrared, the Doppler breadth of a molecular transition is inherently sufficiently narrow to allow the frequency of a monochromatic source to be tuned to the center of the transition with an accuracy much beyond the capabilities of a high resolution dispersive instrument.[3] The exploitations of these methods in high resolution spectroscopic observations are subjects of our "laser spectroscopy", the topic under review in this Conference. In order to use the potentials of laser spectroscopy in highly accurate observations, with an ultimate accuracy beyond the capabilities offered by classical wavelength measurements, the frequency measuring methods previously used in the microwave region, are introduced into the optical regions. This radically different approach to the art of measurements in optics became possible with the aid of a new optical element which responds to an infrared frequency in much the same way as a microwave diode responds to microwave radiation.[4-9]

In the microwave region, the technology of microwave rectifier-frequency mixer diodes has been the basis for all types of microwave receivers and spectrometers. With the extension of this technology into the optical region, a host of new possibilities have now become available. These include a number of possibilities besides the frequency measuring applications, some of which do not necessarily have an analogue in the microwave region. (See below)

In September of 1971, a review paper was presented (by A. Javan) at the Esfahan Symposium on the topic of modern methods in precision spectroscopy. This review included a summary of the developments at M.I.T. in nonlinear laser spectroscopy and also in the area of extending the microwave frequency measuring methods into the optical regions. Since then, further advances have been made at M.I.T. in both of these areas. In this paper, however, rather than reviewing these recent results[10-13] (which are due to appear in several publications elsewhere), an account will be given of the quantum mechanical mechanism occurring in the high speed diode element which has enabled extension of the microwave frequency measuring methods into the infrared region. This will be done along with a description of the general properties of the diode element. The concluding section will describe several novel possibilities and future applications.

GENERAL PROPERTIES OF THE INFRARED METAL-METAL OXIDE-METAL ELECTRON TUNNELING DIODE

In the high speed diode element, alternating electric currents flowing at infrared frequencies give rise to its general properties as an infrared frequency mixer and rectifier. In addition to the application in precise frequency measurements, the diode has been used to parametrically generate infrared radiation at the mixture frequencies of two applied fields.[14] The nonlinear current-voltage characteristics of the element arises from a quantum mechanical electron tunneling process occurring at its metal-metal oxide-metal junction.

The diode element consists of a thin metallic wire antenna mechanically contacted at its pointed tip to a polished metal post. The thin wire antenna is a few microns in diameter and several infrared wavelengths long. The antenna serves the purpose of coupling the diode to the radiation fields. The pointed tip of the wire antenna has a dimension below 1000 Å (as verified by electron microscope photographs of the tip.) Electron tunneling occurs across a potential barrier formed by thin layers of oxides existing on the surfaces of the two metals in the small area of the junction between the pointed tip and the metal base. The size of this area, along with the thickness and the effective dielectric constant of the oxide layers, determine the capacitive loading, C, of the element across its tunneling junction. As is shown below, in the elements studied the thickness of the barrier potential is below about 10Å. From this it follows that $C \lesssim 10^{-4}$ picofard. Inspection shows that the diode's series resistance, R, is essentially determined by the thin antenna's radiation resistance. From these general considerations, the RC time constant of the diode which limits its high-frequency response, can be approximately estimated to be $RC \lesssim 10^{-14}$ sec.

Quantum mechanical electron tunneling across a potential barrier formed by a thin dielectric in between two metals, has been the subject of extensive studies,[15] with some of the theoretical considerations dating back to the early days of the quantum mechanics. Until now, the experimental studies in this field have been mainly confined to the observations made in the dc and the low frequency regions, in which the I-V characteristics of different types of metal-oxide-metal junctions are explored under varying conditions. These junctions, however, differ in important ways from ours. The contact areas in the previously studied junctions are macroscopic in dimensions, having generally an area of about 1 mm x 1 mm. Because of this, these are low speed junctions. In our elements, the required high speed performance dictates a microscopic size for the contact area, from which several important consequences follow. Considering that the junction resistance is inversely proportional to its area, we note that the barrier thickness in our junctions will have to be thinner than those studied previously; otherwise, the junction resistance will be excessively large. (A reduction in the barrier thickness exponentially lowers the electron tunneling impedance, see below.) From this it follows that at a given voltage drop across the oxide layer, the corresponding electric field is larger in our element. Moreover, at a given bias field, the current density in our junctions can become very large. This can be of particular importance, since we believe that the charges within the dielectric layer arising from the tunneling electron's wave functions inside the classically forbidden region of the barrier potential can contribute cooperatively to the shape of the potential barrier (in a way similar to the role played by the space charge in a vacuum diode.) The charge neutrality in this case is satisfied by the image charge distributions in the two metals, which also cooperatively contribute to the potential barrier. As the junction is biased by an external field, the resultant current (which arises from an imbalance caused by a change in the wave functions of the oppositely traveling electrons inside the barrier) will be accompanied by a change in the overall charge distributions. This will in turn result in a modification of the potential barrier. These types of effects need to be considered in a complete theoretical treatment of the subject.

The nonlinearities of the I-V characteristic give rise to rectification and frequency mixing in the diode. The various orders of frequency mixings are dictated by the derivatives of the I-V characteristic curve, as can be readily seen by considering the Taylor expansion of I versus V around a dc bias voltage, $V=V_o$. For instance, when a radiation field is coupled to the diode, a dc voltage appears across it due to rectification of current flowing through the diode. At a low signal level, this dominantly originates from the second order term in the Taylor expansion of the I-V curve. This term is proportional to the second order

derivative of I versus V. Hence, a plot of the resultant voltage measured versus a simultaneously applied dc bias voltage gives a curve identical to a second-order derivative of the I-V characteristic curve. At the same time, the amplitude of the current component flowing through the diode at the second harmonic of the frequency of the applied field is also due to the same second order term, and hence, it will show a dependence on bias voltage which is again identical to the second-derivative of the I-V characteristic. In general, the current amplitude due to an nth order frequency mixing, measured versus a dc field, follows the nth order derivative curve of the I-V characteristic. (This is true for low level applied ac fields, otherwise, the n + 2, n + 4,... can also contribute to the nth order frequency mixing.)

Fig. 1 gives the observed dc bias field dependence of the amplitude of an infrared frequency current flowing through the diode at the sum (or difference) frequency of a simultaneously applied 10.6-μ radiation field and a microwave field. The synthesis is due to a second-order frequency mixing, (as in the case of second-harmonic generation or the rectification of an ac current resulting in its conversion to dc current.) This synthesis corresponds to currents flowing through the diode at the 1st microwave side-bands on either side of the 10.6-μ frequency. The current amplitude for either side-band will be proportional to I" (V), the second-order derivative of I versus the bias field V. The measurements are made by detecting the infrared radiation emitted from the diode at the 1st microwave side-bands on either sides of the frequency of the 10.6-μ radiation. (See Ref. 14) The detection is done by means of a superheterodyne method. In this case, the detected signal is proportional to the electric field amplitude of the side-band radiation and, hence, proportional to the corresponding diode current responsible for the emitted radiation. Note that this method of detection is phase-sensitive and thus is capable of recognizing a 180° phase-shift which can occur as the polarity of the applied dc bias field is reversed. Accordingly, the measured signal is proportional to the magnitude as well as the algebraic sign of I" (V).

The above observation represents measurements directly performed in the infrared. A measurement of the rectified dc voltage developed across the same diode when subjected to either the 10.6-μ radiation or the microwave radiation alone also shows a dependence on the bias voltage identical to that of Fig. 1. These observations show the intricate relationship of all these processes, and the fact that they are all manifestations of ac currents flowing through the diode at the frequencies of the applied radiation. The nonlinear I-V characteristic distorts the current waveform, resulting in the rectification and the frequency mixing.

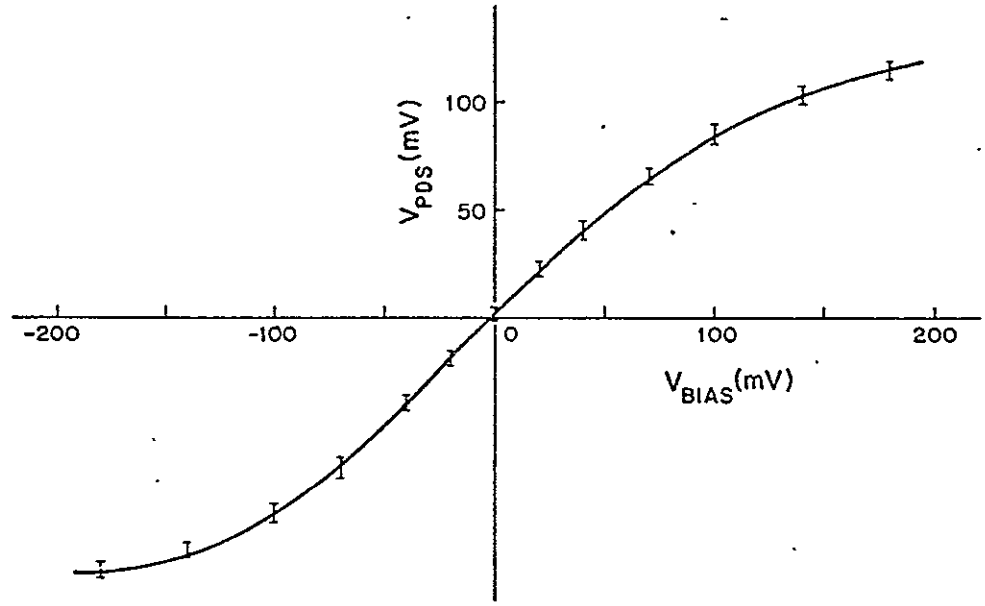

Fig. 1. Bias voltage dependence of the amplitude of an infrared frequency current, synthesized in the diode as a result of a second order mixing.

Fig. 2 shows another frequency mixing example observed at an infrared frequency. This figure gives the bias field dependence of an infrared frequency current flowing through the diode arising from a third order frequency mixing process. The diode is simultaneously subject to 10.6-μ and microwave radiation. In this case, the emitted radiation at the second microwave side-band on either sides of the frequency of the 10.6-μ radiation is detected in an external detector. (See Ref. 14). As in the previous case, the detection is done by means of a superheterodyne method, which gives a signal proportional to the amplitude of the detected side-band radiation, and hence, as before, the infrared frequency diode current responsible for the radiation. Fig. 2 gives the dependence of the detected signal on a dc bias field applied to the diode. This curve represents the third-order derivative of the I-V characteristic curve. In fact, it also agrees with the bias field dependence of a signal observed across the same diode due to a third order frequency mixing process in which both of the applied fields are in the microwave regions (see below).

Measurements of the 3rd-order derivative given in Fig. 2 is performed on a different diode than that used in determining the

2nd-order derivative curve given in Fig. 1. Note that the tunneling contacts in both diodes correspond to I-V characteristic curves which are somewhat asymmetrical with respect to the origin. However, the asymmetry is more pronounced in the Fig. 2 diode than that of Fig. 1.

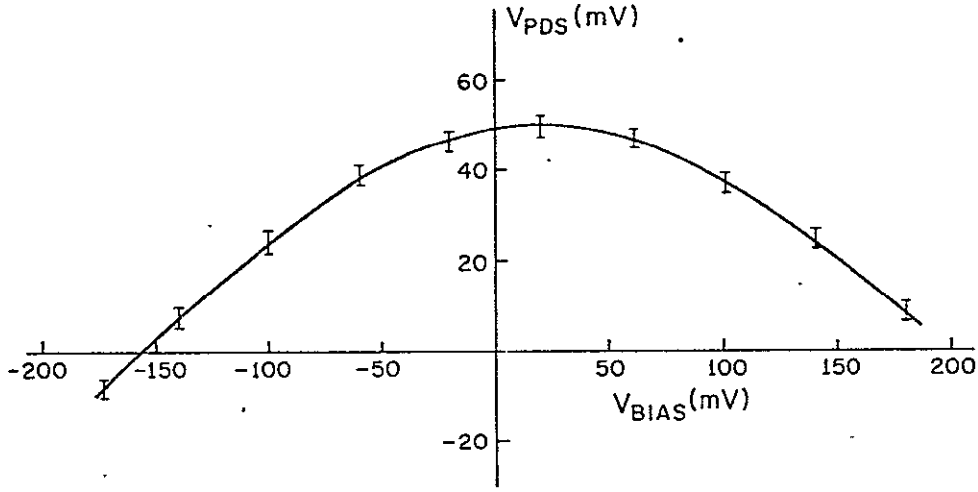

Fig. 2. Bias voltage dependence of the amplitude of an infrared frequency current, synthesized in the diode as a result of a third order mixing.

The similarity of the microwave frequency mixing curves and those obtained at the infrared frequencies show that in the elements studied there are no observable dispersive effects. (There are a number of dispersive possibilities which can be expected to become observable under appropriate conditions. These include effects when hν becomes comparable to the barrier height.)

Observation of a high-order frequency mixing signal versus a bias-field is a convenient method of obtaining high-order derivatives of the I-V characteristic curve. Because of the broadband characteristics, the measurements can be more conveniently performed at a microwave or rf frequency. In addition to information on barrier thickness and height, comparison of these high order derivatives with theory can give additional useful information, particularly in regard to the shape of the potential barrier. The latter is a topic which has not been given sufficient attention in the previous studies.

Fig. 3 gives the observed derivatives up to the 6th order of the I-V characteristics. These have been obtained in the same

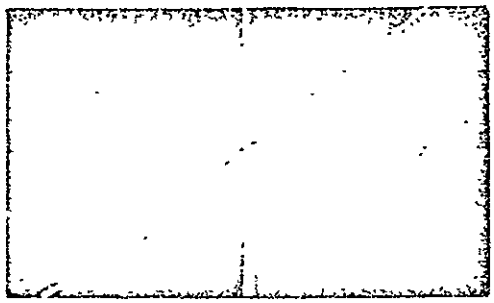

Vertical I (mA): 1/cm

Horizontal V_b (mV): 50/cm

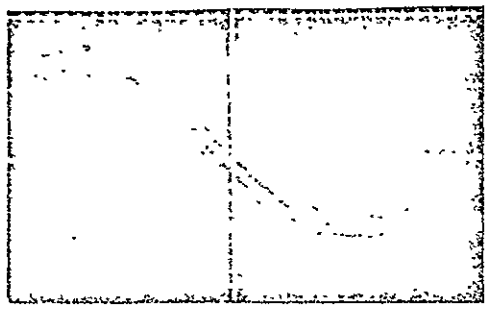

$\frac{\partial^4 I}{\partial V^4}\left(\frac{\mu amps}{(mV)^4}\right)$: 10^{-6}/cm

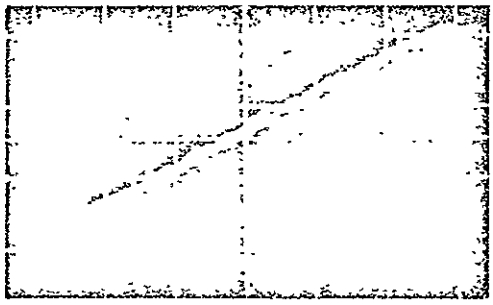

$\frac{\partial^2 I}{\partial V^2}\left(\frac{\mu amps}{(mV)^2}\right)$: 3×10^{-3}/cm

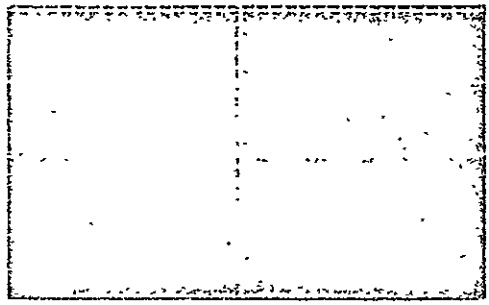

$\frac{\partial^5 I}{\partial V^5}\left(\frac{\mu amps}{(mV)^5}\right)$: 10^{-8}/cm

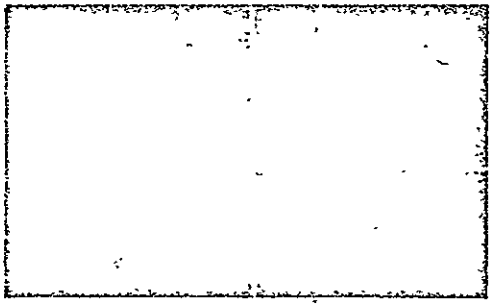

$\frac{\partial^3 I}{\partial V^3}\left(\frac{\mu amps}{(mV)^3}\right)$: 3×10^{-5}/cm

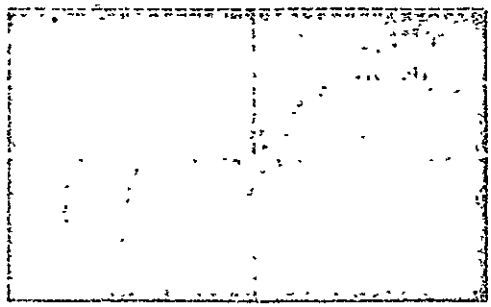

$\frac{\partial^6 I}{\partial V^6}\left(\frac{\mu amps}{(mV)^6}\right)$: 10^{-10}/cm

Fig. 3. Experimental I-V characteristic of the MOM diode and its different Nth order derivatives (up the sixth order).

diode element by means of a frequency mixing procedure performed in the microwave region: The element is subjected to the outputs of two S-band microwave klystrons (tunable from 2 to 4 GHz) at frequencies ν_1 and ν_2. The two microwave frequencies are tuned to obtain a 40 MHz beat signal due to a frequency mixing of a type in which $m_1\nu_1 + m_2\nu_2 = \nu_{IF}$, where m_1 and m_2 are positive or negative integers and ν_{IF} is the IF frequency. The order of frequency mixing is given by $|m_1| + |m_2|$. The 40 MHz beat note is observed by feeding the signal across the diode to a fixed frequency narrow-band IF. By tuning the ν_1 and ν_2 frequencies, signals due to different orders of frequency mixing can be observed in the same diode and studied in sufficient detail over a period of several hours, during which time the diode characteristic remains unchanged. The studies are made by observing the dependence of the 40 MHz beat notes versus a varying dc bias field applied to the diode. A phase sensitive detector is used to obtain a signal proportional to the amplitude of the 40 MHz beat note (rather than its square obtainable with a square law detector.) This is done in order to obtain information on the sign as well as the amplitude of the observed beat note versus the dc bias field. In the phase sensitive system, the reference signal is obtained by simultaneously performing the same frequency mixing experiment in a separate frequency-mixer consisting of an ordinary silicon diode. The resultant 40 MHz IF signal provides the reference used in a 40 MHz lock-in amplifier whose signal channel is subjected to the 40 MHz beat note across the high speed tunneling element.[16]

A. CLASSIFICATION OF THE OBSERVED CHARACTERISTICS

As is expected, due to the local inhomogeneity of the metal base and the non-uniformity of its surface, the exact shape of the I-V characteristic is found to vary appreciably as the process of mechanically contacting the wire antenna to the metal post is repeated. In fact, for the same diode element, several types of I-V characteristics corresponding to different types of barrier shapes and heights can be obtained by repeatedly breaking the mechanical contact and attempting new ones. A disadvantage of this is that, once a contact is burned-out or purposely disconnected, it requires several trials in order to reproduce a contact with approximately the same I-V characteristic curve. Because of this, accurate comparisons of different properties of the diode must be done by means of observations performed on the same contact and before a change occurs in its I-V characteristic. Breaking the contact and repeating it a number of times, however, gives an opportunity to conveniently produce junctions corresponding to a varied set of tunneling barriers. This in turn makes it possible to study different types of barriers whose properties are varied and represent different manifestation of the tunneling effect. In general, however, mechanical instability of a junction is trouble-

some and careful measurements require both delicate manipulation and patience. Also, one must guard against spurious signals not related to the electron tunneling process, which can appear across the element and interfere with the measurements (See Ref. 1).

The different types of I-V characteristics observable in the element can be classified as follows. One type consists of anti-symmetric I-V curves for which the current versus voltage closely satisfies the relationship $I(V) = -I(-V)$. In this case, rectification of an applied radiation field can occur only in the presence of a dc bias field since the even order terms in the I-V expansion are all zero at V=0. For the same two metals, a different type of contact can be obtained with a non-symmetrical I-V characteristic around V_o=0. In this case, rectification of an applied radiation field can occur in the absence of a bias voltage. The polarity of the dc rectified voltage, however, is dependent on a specific contact and can reverse its sign as the contact is broken and repeated over again. This can be understood on the basis of the relative values of the effective work functions of the two metals in different contacts.

THEORETICAL DISCUSSIONS

In the previous studies of the large area tunneling junctions, there have been a number of theoretical analyses to explain the observed I-V characteristics.[15] In general, the observed I-V curves are found to be in good agreement with estimates based on reasonable models for the barrier potentials.

The following discussion is intended to give a preliminary account of the application of the existing theory to our explanation of the general features of our observed I-V characteristics and their high-order derivatives.

The theory considers an individual electron with an energy E_x (measured relative to the Fermi energy E_F) moving inside the metal along a direction, x, normal to the plane of the metal-oxide-metal junction. When the electron reaches the junction, it sees a potential barrier higher than its energy E_x; according to quantum mechanics, there is a probability that the electron will tunnel through the barrier. Let us consider this process in the presence of an external field causing a potential difference V to appear between the two metals. From the W.K.B. approximation, the tunneling probability can be written as:

$$P(E_x,V) = \exp\left\{-Q(E_x,V)\right\}$$

where $Q(E_x, V) = 2\frac{\sqrt{2m}}{\hbar}\int_{x_1}^{x_2} \sqrt{\phi(x,V)-E_x}\,dx$

$\phi(x,V)$ is the barrier potential in the presence of the applied voltage, V. It can be written as

$$\phi(x,V) = \phi_o(x) - \frac{x-x_1}{x_2-x_1} eV$$

In this equation, $\phi_o(x)$ is the barrier potential for V=0 and x_1 and x_2 are the classical turning points which satisfy $\phi(x_1,V) = \phi(x_2,V) = E_x$. The thickness of the oxide layer is $L = x_2-x_1$, at the Fermi level (E_x=0), and no bias voltage (V=0).

The net current density can be expressed as the integral

$$J(V) = A \int_{-E_F}^{\infty} dE_x\, P(E_x,V)\, F(E_x,V)$$

where $$A = \frac{4\pi me}{h^3} kT$$

and

$$F(E_x,V) = \ln\frac{1 + \exp(-E_x/kT)}{1 + \exp(-(E_x+eV)/kT)}$$

the function $F(E_x,V)$ accounts for the Fermi-Dirac electron energy electron energy distribution. Inspection shows that the integrand in J peaks near E_x=0, (the Fermi level). In the previous treatments, approximate analytic expressions are obtained by expanding the integrand around E_x=0. The resultant expressions for different barrier heights and thicknesses provide good fits to the experimentally measured J-V characteristics. However, these analytic approximations are not applicable to our junctions where the barrier thickness is considerably less than those of the barriers studied previously. In a thin barrier, electrons with energies appreciably removed from E_x=0 can contribute sizably to the tunneling current.

The integral in equation (1), along with the high-order derivatives of J versus V, can be numerically calculated without resorting to an analytic approximation. This can be done with the aid of a digital computer. Here we give a brief summary of the results for several cases in which Q can be expressed analytically. This considerably simplifies the computer calculations. Specific-

ally the calculations are done for trapezoidal, rectangular, parabolic, and triangular barriers. The parabolic barrier is emphasized below. In this case with

$$\phi_o(x) = 4\phi_m \frac{x}{L}\left(1 - \frac{x}{L}\right) \quad , \quad \phi_m = \phi_o\left(\frac{L}{2}\right)$$

the computer's expression for Q is:

$$Q(E_x,V) = \frac{\pi}{4} \alpha L \sqrt{\phi_m} \left(\left(1 - \frac{V}{4\phi_m}\right)^2 - \frac{E_x}{\phi_m}\right)$$

For a symmetrical barrier, the J-V curve as well as the curves corresponding to the even-order derivatives of J versus V go through the origin and have an inflection at that point (i.e. the Taylor expansion of I versus V will contain only odd powers of V). Let us now consider the behavior of J"(v), the second-derivation of J versus V, for a symmetrical barrier. In this case, in the region close to the origin, J" appears as a nearly straight line, with a slope which varies at increasing values of V. Depending on the shape of the barrier, its thickness and its height, the slope can either increase or decrease when increasing V. An increasing slope versus V corresponds to a positive value for $J_o^{(5)}$ the 5th derivative of J versus V at V=0, while a negative value for $J_o^{(5)}$ gives a decreasing slope. We have inspected this behavior over wide ranges of values for barrier heights and thicknesses. Interestingly, we find that for a rectangular barrier, $J_o^{(5)}$ appears to remain positive for reasonable values of barrier thicknesses and heights, corresponding to an increasing slope for J" versus V. The experimental results show, however, that in our junctions the observed second-derivative curves for symmetrical barriers have a decreasing slope at increasing values of V.[19] In a parabolic barrier, on the other hand, it is possible to find a range of values for the potential heights and thicknesses corresponding to decreasing values of slope versus V. Fig. 4 gives a typical computer calculation. In this figure, in order to emphasize the nonlinear features of J" versus V, a straight line has been subtracted from J" as indicated. This is done so that each curve appears tangent to the V axis at V=0. Note that the curves below the V axis have decreasing slopes at increasing V. (i.e. $J_o^{(5)}<0$).

The above example is mentioned in order to emphasize that high order derivatives of the I-V characteristics can be used to obtain some information on the shape of a potential barrier. From the theory, it is possible to obtain a series of curves for J(V) as well as J"(V) at different values of ϕ_m and L. These curves,

as noted above, are nearly straight lines for small voltages. From the slope of J versus V, a value for the tunneling conductance per unit area, Y, can be found at varying ϕ_m and L. We then note that for given values of ϕ_m and L, the ratio of J"(V)/J(V) is constant at small V's. (Both J" and J are nearly straight lines, as noted above.) We define this parameter as $r(\phi_m,L)=J"(V)/J(V)$.

From the experiments, it is possible to measure the parameters Y and r in a high speed symmetric junction. This can be done, e.g., at a radio frequency where the rf voltage across the junction can be directly measured. The parameter Y can be measured by applying a small dc bias voltage (.01 to 0.1 volts) to the diode and measuring the bias current density. The current density can be obtained from the measured current along with a knowledge of the junction area A. From electron microscope photographs of the tip of wire antenna, A is found to be close to $0.01(\mu)^2$. The parameter r can be measured in the same contact by applying a radio frequency field and measuring the rectified rf current versus the dc bias current. This is done at a fixed (and known) value of the rf voltage amplitude. (Note that r is proportional to v_{rf}^{-2} and is independent of area).

The resistance of the junction varies in different contacts. In a typical low impedance contact of 100 ohms, (corresponding to $Y \approx 1\text{mho}/(\mu)^2$), the measured value of r is found to vary between 2-4 $(\text{volts})^{-2}$.

For a parabolic barrier, a class of curves for r and Y can be found by varying ϕ_m and L. The results show that $Y=1\ \text{mho}/(\mu\text{m})^2$ and r = 3 volts corresponds to ϕ_m = 0.7 ev and L = 6Å. A further result is that these values are not a sensitive function of the barrier shape (as is the sign of the $J^{(5)}$, see above). In fact a rectangular barrier having an effective height the same as the parabolic barrier with ϕ_m = 0.7 volts and L = 6Å, will also give the same values for Y and r. (For definition of effective height see Ref. 17). As noted above, however, a rectangular barrier predicts the incorrect sign for the curvature of J" versus V.

In the face of mechanical instability of the junction, and the difficulties in obtaining reproducible results, the above estimates must be considered to give approximate values for the barrier parameters. These results will yet have to be supported by other independent observations, particularly at cryogenic temperatures.

FUTURE POSSIBILITIES

The observed properties of the high-speed diode element arise from interaction of the tunneling electrons with the thin dielec-

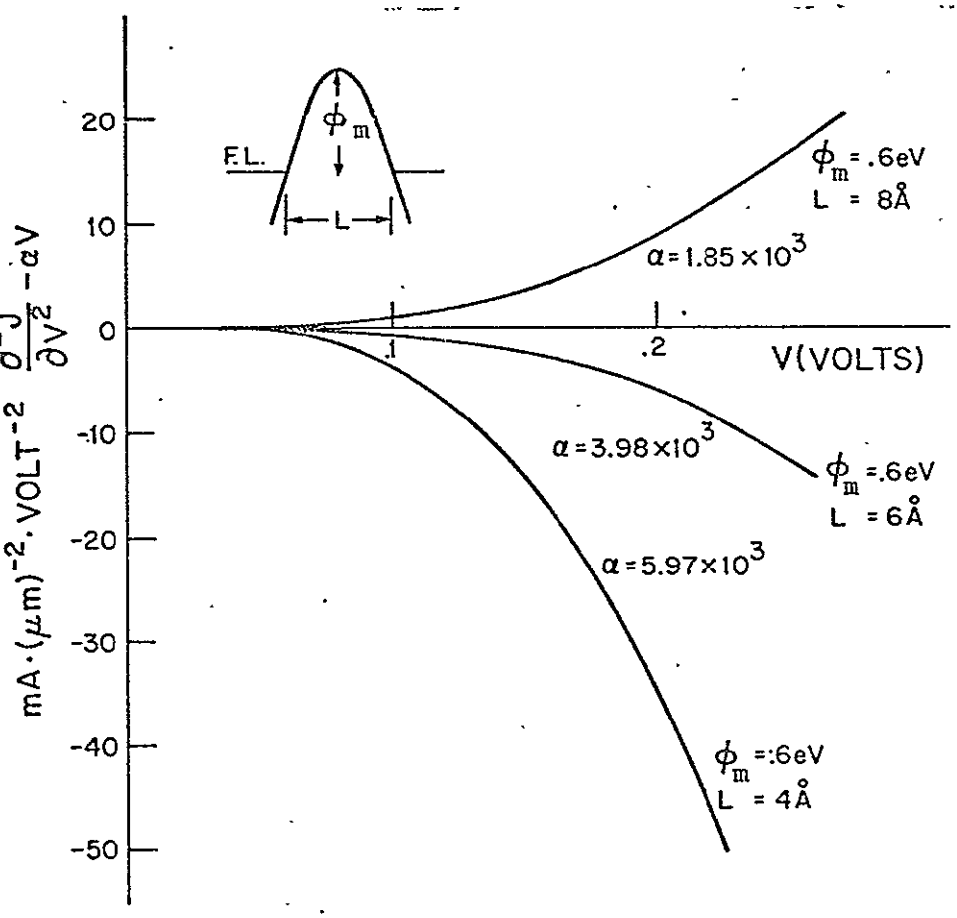

Fig. 4. Theoretical second derivative with respect to V of the J-V characteristic. The shape of the barrier is approximated by a parabola. A straight line, αV, has been subtracted to emphasize the nonlinear features of J".

tric barrier occupying a microscopic volume where the pointed tip of the thin wire antenna touches the metal base. Accordingly, we can generalize our thinking and consider this as a method for making observations on the physical properties of matter occupying a microscopic volume in the region of the point-contact. For instance, this approach can be used as a "micro-probe" for studying surface physics in metals. From previous observations made in large-area metal-to-metal tunneling junctions, it is known that resonant scattering of electrons off the local infrared or far-infrared vibrational modes in the thin dielectric barrier can contribute to the detailed features of the I-V characteristic curve.[18] These have been observed at cryogenic temperatures and appear as changes in the tunneling impedence whose onsets occur at fairly well-defined values of the bias voltages. These voltages correspond to the quantized energies of the vibrational modes

associated with the specific molecular bonds in the dielectric barrier. Our high-speed tunneling junctions will permit these types of observations to be made not only in the dc and the low frequency regions, but also at the far-infrared or the infrared frequencies where the quantized local modes of a barrier can interact resonantly, or in their near-resonant regions, with the ac tunneling current and the applied fields. These will result in dispersive effects, causing phase-shifts and thus introducing inductive or capacitive components in the tunneling impedence. These effects will be nonlinear-functions of the applied fields.

A high speed metal-dielectric-metal tunneling junction can be made via vacuum-deposition of thin films on a substrate. This requires application of methods of microelectronics to achieve the small area junction. These methods will also permit the junction to be integrated with thin film antenna structures for coupling to the radiation field. The deposited antenna length can be designed to be resonant at the wavelength of an applied radiation field. In addition, with microelectronics, it is possible to simultaneously deposit a large number of these types of junctions in a small area of a substrate. The various junctions along with their resonant antenna structures can be placed in a geometrical pattern to form a phased-array configuration.

At the time of the Vail Symposium, promising results were obtained in a series of experiments designed to show the feasibility of achieving a high-speed tunneling junction by means of thin-film vacuum deposition combined with microelectronics. These experiments have been completed by the time of final preparation of this manuscript for publication in the proceedings of the Vail Symposium. The results are described in a manuscript due to appear in publication. The reader is referred to this reference for the details of the experiments and the results.

With the possibility of depositing a large number of high-speed diode elements as noted above, several novel applications appear to be within the range of practical possibilities. These include the possibility of applying a two-dimensional phased-array configuration to obtain in real time a hologram of an image formed on the array. Consider, for example, the image to be formed by laser irradiation of an object. The image can be heterodyned at each junction with radiation from a local oscillator uniformly applied to all the junctions in the array. The local oscillator frequency, if desired, can be shifted by a fixed frequency to obtain a heterodyne signal at a convenient IF. The IF signals across the various junctions will have information on both the amplitudes and the phases of the image at the locations of each junction. These real-time signals can be stored; their Fourier transform, in turn, will reproduce the image holographically. It should also be noted that this proposed method for holographic

imaging in real time, can be applied utilizing any two dimensional array of detector elements whose speeds are sufficiently fast to produce heterodyne signals at the IF frequency. A holographic image in real time is of considerable importance in a number of practical applications, both in the infrared as well as in the visible region. Beside these, superheterodyne imaging offers the advantage of enhanced detection sensitivity. There are a number of variations in this imaging scheme. For instance, the local oscillator used to obtain phase and amplitude information can be chosen to have a frequency widely different from that of the laser which illuminates the object. (In this case, the two laser frequencies can be phased-locked, using a separate frequency multiplier chain, as discussed in Ref. 1.) Another possibility is to use an illuminator laser consisting of two closely spaced frequencies, ν_1 and ν_2. With appropriate frequency components in the reference local oscillator radiation, it is possible to extract phase information (and a corresponding amplitude), at the difference frequency $|\nu_1-\nu_2|$. This will enable holographic imaging at a longer effective wavelength corresponding to interference between the two propagating waves at frequencies ν_1 and ν_2, giving rise to spatial beats.

It is known theoretically that, under special conditions, a tunneling junction can be obtained in a multi-barrier structure (the super-lattice), in which the corresponding I-V characteristic will show regions of negative differential conductivity.[20] A high-speed junction of this type, if achieved, can be integrated with a high frequency L-C tank configuration, to obtain a high-frequency negative impedence oscillator. Inspection shows that, with the available methods of microelectronics, an L-C tank circuit consisting of, e.g., a simple pair of lines, or a more complex configuration, can readily be made whose resonances lie in the far-IR or the IR regions. The major challenge, however, is achievement of the negarive impedence junction.

It is also known theoretically that, instead of a diode, a triode configuration[21] can be envisioned with a control-grid for controlling the current flow in the element. A high-speed junction of this type will have interesting possibilities in novel high frequency device applications.

The above examples are cited in areas other than frequency measurements and spectroscopy. For a review of these and the related topics, see Ref. 1.

* Present address, Air Force Cambridge Research Laboratory
L. G. Hanscom Field, Bedford, Massachusetts

REFERENCES

1. For a review see: A. Javan, Fundamental and Applied Laser Physics, Proceedings of the Esfahan Symposium, edited by M. S. Feld, A. Javan, and N. A. Kurnit, Wiley-Interscience, 1973, Page 295. There are a number of review papers on these and closely related topics in these proceedings.

2. See S. Ezekiel, this volume.

3. See A. Mooradian, this volume.

4. L. O. Hocker, D. R. Sokoloff, V. Daneu, A. Szoke, and A. Javan, Appl. Phys. Letters 12, 401 (1968).

5. V. Daneu, D. R. Sokoloff, A. Sanchez, and A. Javan, Appl. Phys. Letters 15, 398 (1969).

6. D. R. Sokoloff, A. Sanchez, R. M. Osgood, and A. Javan, Appl. Phys. Letters 17, 257 (1970).

7. K. M. Evenson, G. W. Day, J. S. Wells, and L. O. Mullen, Appl. Phys. Letters 20, 133 (1972).

8. K. M. Evenson, this volume.

9. A. Javan, Ref. 1.

10. A. T. Mattick, A. Sanchez, N. A. Kurnit, and A. Javan, Appl. Phys. Letters 23, 675 (1973).

11. F. Keilmann, R. L. Sheffield, M. S. Feld, and A. Javan, Appl. Phys. Letters 23, 612 (1973).

12. J. G. Small, G. M. Elchinger, A. Javan, A. Sanchez, F. J. Bachner, and D. L. Smythe, to be published in March 15 issue of Appl. Phys. Letters.

13. M. Kelly, J. Thomas, J. Monchalin, N. A. Kurnit, and A. Javan, to be published.

14. A. Sanchez, S. K. Singh, and A. Javan, Appl. Phys. Letters, 21, 240 (1972).

15. For review of recent works see for instance, Tunneling Phenomena in Solids, edited by E. Burstein and S. L. Lunquist (Plenum Press, New York, 1969).

16. For detail see, A. Sanchez, Ph. D. Thesis, M.I.T., (1973), unpublished.

17. J. G. Simmons, J. Appl. Phys. 34, 1793 (1963).

18. J. Lambe and R. C. Jaklevic, Phys. Rev. 165, 821 (1968).

19. See also S. M. Farris, T. K. Guftanson, and J. C. Weisner, IEEE J. Quantum Electronics QE-9, 737 (1973).

20. See e.g. R. Tsu and L. Esaki, Appl. Phys. Letters 22, 562 (1973).

21. See e.g. R. H. Davis and H. H. Horack, J. Appl. Phys. 34, 864 (1963).

5. A. Sanchez, S. K. Singh and A. Javan

Generation of Infrared Radiation in a Metal-to-Metal Point Contact Diode at Synthesized Frequencies of Incident Fields; A New High Speed Broad Band Light Modulator

Published in Applied Physics Letters

GENERATION OF INFRARED RADIATION IN A METAL-TO-METAL POINT CONTACT DIODE AT SYNTHESIZED FREQUENCIES OF INCIDENT FIELDS; A NEW HIGH SPEED BROAD BAND LIGHT MODULATOR*

A. Sanchez†* S. K. Singh and A. Javan
Department of Physics
Massachusetts Institute of Technology
Cambridge, Massachusetts 02139

ABSTRACT

This letter reports for the first time the detection of infrared radiation emitted from a metal-to-metal point contact diode at the mixture of the frequencies of the radiation fields applied to the diode.

Published in Applied Physics Letters

The metal-to-metal point contact diode used in this experiment has a nonlinear current-voltage characteristic similar to a radio frequency or microwave diode, but it has a speed of response which is at least as high as the near infrared frequencies. The diode is similar in construction to that used for the first time in an experiment demonstrating its speed of response in the far-infrared,[1] and later in the 9μ and the near-infrared region.[2,3,4] A thin tungsten wire antenna -- several μ in diameter and somewhat less than a mm long -- is mounted at the end of a coaxial cable; its tip is pointed by means of a standard etching technique and contacted mechanically with a nickel post mounted on a differential screw to allow fine adjustment of the point contact. The pointed tip of the thin wire antenna is less than 1000Å in diameter[5] and its contact with the nickel post occurs most likely through a thin oxide layer on the order of several Å thick. The processes occurring in the diode have not been established in great detail, but electron tunneling across the thin oxide layer can be responsible for the nonlinear current-voltage characteristic: As infrared radiation is coupled to the diode's antenna, an alternating voltage at the corresponding frequency is developed across the oxide layer. This gives rise to an alternating current flowing through the diode at the corresponding frequency, but with a distorted wave form due to the nonlinear characteristic. The distorted wave can have an average rectified value as well as current components at high order harmonics of the frequency of the applied infrared field. When two or several radiation fields are coupled to the diode, the total current will contain additional components

at frequencies corresponding to the mixtures, (i.e. sums and differences), of those of the applied fields as well as the mixtures of their various harmonics; this occurs for the mixture frequencies below the diode's high frequency cut-off limit.

The current components at the various harmonics and the frequency mixtures generated in the point contact can excite propagating current waves in the thin wire antenna which can subsequently emit electromagnetic waves at the corresponding frequencies. Until now, however, only the frequency mixtures corresponding to a zero beat note (or a beat note at a convenient IF in the tens of MHz) have been detected directly across the diode in the form of a voltage appearing at the beat frequency. In these experiments, for example, the radiation from two lasers at frequencies $\nu_1 > \nu_2$, the mixture $(\nu_1 - p\nu_2 \pm q\nu_m)$ equals the IF frequency or gives the zero beat, with p and q representing integers larger than or equal to unity.

Here we report for the first time the detection of radiation emitted from the diode due to the current components flowing through it at mixture frequencies lying in the infrared. In the experiment, the output of a CO_2 laser is coupled to the diode together with that of a microwave klystron. The emitted infrared radiation displaced in frequency by the fundamental or the second harmonic of the microwave frequency is detected in a liquid He-cooled Cu:Ge detector. The experiment is of importance in several applications. It provides a new way to study the processes occurring in the diode. Furthermore, it demonstrates a new method to generate frequency tunable radiation at the tunable microwave side-bands of any fixed frequency gas laser oscillating throughout the infrared and the far-

infrared regions. The radiation emitted from the diode is not intense but its magnitude is sufficiently above the noise to make it useful in spectroscopic applications. We are also able to show that the diode can potentially generate detectable radiations at the harmonic frequencies of a number of existing far-infrared or infrared lasers.

In the experiment, the radiation emitted from the diode was observed with a superheterodyne detection system which offered high sensitivity. The CO_2 laser, which had a resonator with a grating for line selection at one end and a mirror mounted on a piezoelectric tuner at the other end, was made to oscillate simultaneously on two adjacent P or R branch transitions. The laser output was coupled to the diode by focusing it onto the diode's tungsten antenna close to its point contact along a direction perpendicular to the antenna. The lens had a 2.5 cm focal distance and produced a spot-size on the antenna of about 100μ diameter. In the first phase of the experiment, the output of a frequency tunable klystron operating in the 52.6 GHz region was fed through a variable attenuator into a wave-guide with an open end; the microwave radiation emitted from the wave-guide was coupled to the diode simply by placing the diode at a distance of about 1 cm from the wave-guide with its wire antenna parallel to the microwave E-field. The total microwave power emitted into free space was determined to be about a few milliwatts, and the total laser output incident on the diode was about a watt.

The emitted radiation from the diode was collected along a direction perpendicular to that of the incident laser radiation and

the antenna with a 1.3 cm focal length lens, which focused it onto the liquid He-cooled Cu:Ge detector placed at a distance of about 50 cm, and in some cases as much as about 2 meters, away from the lens. The Cu:Ge detector package had a speed of response of up to about 100 MHz.

The frequency mixing process described above results in emitted infrared radiation containing frequency components displaced from those of the two incident laser lines by $\pm n\nu_m$, with ν_m the klystron frequency and n representing integer numbers. The dominant components of the emitted signal, however, consists of re-radiated fields at the frequencies of the incident laser lines due to the process of linear scattering from the diode's antenna; in our case, the resultant scattered radiation at the undisplaced frequencies collected by the lens and focused on the Cu:Ge was several milliwatts

The two oscillating laser lines selected for the experiment were the P(14) and P(16) transitions of the CO_2, 9.3 μ band which differ in frequency by δ_o= 52.592 GHz with the P(14) line lying on the high frequency side of the P(16). The klystron frequency was tuned in a region overlapping δ_o. The emitted radiations at the frequency mixtures displaced from the two laser lines by $\pm \nu_m$ was observed by detecting across the Cu:Ge element a beat signal arising from heterodyning of the frequency upshifted P(16) radiation with tne P(14) local oscillator radiation and the downshifted P(14) radiation with the P(16) local oscillator radiation; the corresponding beat frequency for both signals appear at $(\delta-\nu_m)$, where δ is the frequency spacing of the two oscillating laser lines which is close to δ_o and fluctuates near it due to laser detuning effects. The several milli-

watts of scattering radiation incident on the Cu:Ge element at the undisplaced frequencies provided adequate local oscillator powers for the superheterodyne detection.

In the second phase of the experiment, another klystron whose frequency ν_m was tunable in the 26.3 GHz region was used. In this case, the emitted radiation displaced in frequency by $\pm 2\nu_m$ was detected as before, by observing a heterodyne beat signal across the Cu:Ge element at the frequency $(\delta - 2\nu_m)$.

Prior to the experiment, the current-voltage characteristic curve of the metal-to-metal point contact diode and its high order derivatives were studied in detail; the nigher order derivatives are responsible for the various orders of frequency mixings.[6] This study showed that a D.C. bias voltage applied to the diode had a sizeable effect on the various frequency mixing signals. The initial observations were made by mixing in the diode two microwave frequencies in various orders and noting the behavior of the resultant beat signals developed across the diode versus the bias voltage. Similarly, the effect was studied in the far-infrared and infrared regions for several orders of frequency mixing; here we define a mixing of the n^{th} order by the corresponding frequency combinations obtainable from V^n where V is the sum of the applied oscillatory voltages. In the studies we find that in general, the even-order mixing signals have a minimum for the bias voltage, V_o, close to zero; the odd-order mixing signals, on the other hand, are at a maximum for $-V_o$ near zero. For instance, an infrared radiation applied to the diode produces a D.C. voltage across it due to rectification arising from even-order terms in the i-v characteristic; in this case, the rectified voltage is found to increase

sizeably when the bias voltage V_o is applied. This occurs in general for both negative as well as positive V_o. On the other hand, an odd-order mixing signal, e.g. the zero beat (of about several millivolts) observed across the diode when the output of the CO_2 laser oscillating on the two P branch transitions is applied to the diode together with the mixrowave radiation at a frequency $\nu_m \approx \delta$, will diminish in size as V_o is increased. For high order mixing, the beat signal versus V_o show several maxima and minima when $|V_o|$ is increased by as much as a few hundred millivolts. In fact, the curve obtained for mixing of the (n+1) order signal versus V_o resembles closely the derivative of the curve obtained for the n^{th} order mixing, as expected.[6]

From these observations we note that infrared frequency current components flowing through the diode at the first microwave side-bands arise from an even-order mixing, hence, their corresponding amplitudes and the subsequent re-radiated signals should increase in size as a bias voltage is applied. On the other hand, the re-radiation at the second side-bands should have its maximum near $V_o=0$ since they arise from odd-order mixings. Accordingly, provisions were made to apply a varying bias voltage to the metal-to-metal point contact frequency mixing element.

In the experiment, the frequency fluctuations and the drifts of both the laser and the klystron due to thermal and microphonic effects, resulted in sizeable variations of the beat frequency $(\delta-\nu_m)$. Because of this, narrow-banding of the post-detector electronics for enhanced sensitivity required special precautions to eliminate the instabilities of the beat frequency. Enhanced detection sensitivity by narrow-banding aided our initial search for the signal. With the observation of

the signal, however, it was possible to improve its magnitude sizeably so that a broad-band electronic system was adequate in the subsequent observations. We shall first describe the latter: the signal from the Cu:Ge detector was amplified by an amplifier with a band-pass extending from 10 KHz to about 1 MHz and its output displayed on an oscilloscope screen. The klystron frequency was swept in synchronism with the oscilloscope sweep over a range of about several MHz centered at $\nu_m \approx \delta$. The beat signal appeared on the oscilloscope screen as the beat frequency $(\delta - \nu_m)$ was swept through the amplifier band-pass. (See the lower trace in Fig. 1.) The observed signal was improved by rectifying the output of the amplifier and feeding it to the input of a one hundred channel box-car integrator. Each channel had a 2 μsec gate-width and they were switched on consecutively in synchronism with the klystron and the oscilloscope sweep. The upper trace in Fig. 1 is the output of the integrator with a few seconds integration time and a sweep repetition rate of about one KHz.

In agreement with the above, the observed signal increased sizeably as the bias voltage, V_o, was increased; in fact, as a function of V_o, the beat signal followed identically the behavior determined previously for the second order mixing signals.

In our initial search, the following method was used to stabilize the beat frequency $(\delta - \nu_m)$, enabling much improved sensitivity: The klystron frequency was detuned from δ by about 40 MHz. In this case, the third order mixing of the frequencies of the two laser lines and the microwave frequency produced across the diode a beat voltage at 40 MHz. This signal was amplified and fed to a voltage limiter and

then mixed with the output of a stable crystal controlled reference oscillator at 40 MHz; a correction signal was subsequently extracted and fed to the klystron reflector to form a phase-locking loop. The loop caused the klystron frequency to follow the variations in δ so that the beat frequency $(\delta-\nu_m)$ remained the same as the 40 MHz reference oscillator to within one hundredtn of a radian. The 40 MHz beat signal across the diode was sufficiently intense, (about several millivolts), so that even for over one order of magnitude decrease in its intensity, caused e.g. by varying the vias voltage V_o, or by attenuating the microwave power, the performance of the feedback loop remained entirely unaffected.

The elimination of the instability of the beat frequency $(\delta-\nu_m)$ enabled narrow-band detection of the heterodyne signal across the Cu:Ge detector; the detector output was fed to a 40 MHz phase-sensitive amplifier with the 40 MHz crystal controlled oscillator providing the reference signal. Figure 2 shows the block diagram. Figure 3 indicates the dependence of the radiation generated by the diode on the applied bias voltage.

With the 26.3 GHz modulating klystron, the second side-bands correspond to frequency displacements close to δ, enabling observations with the same heterodyne detection schemes described above. We find that for several milliwatts of 26.3 GHz klystron power, the emitted infrared radiation at the second side-band is to within a factor of two the same as that observed previously at the first side-band using the 52.6 GHz klystron. The radiation emitted at the second side-band, however, behaved differently as a function of the applied bias voltage V_o. In this case, the emitted radiation had its maximum

for V_o close to zero. The detailed dependence on V_o was in agreement with our previous determination of the behavior of a third order frequency mixing versus the bias voltage, as described above.

As a function of the incident microwave or klystron power, the zero beat (or the 40 MHz beat) across the diode is found to behave similarly to the dependence of the zero beat (or correspondingly, the 40 MHz beat) across the Cu:Ge element. The relationship between the two signals, (i.e. the heterodyne signal across the Cu:Ge detector on the one hand, and the beat signal developed across the diode on the other), can be used to determine prior to an observation, whether the current flowing through the diode at the synthesized infrared frequency is of sufficient intensity to generate detectable radiation. This relationship shows that the diode is potentially capable of generating detectable radiations at the harmonic frequencies of a number of existing infrared or far-infrared lasers. For example, fifty to one nundred of mW radiation from a 337 μ HCN laser and several mW from a 118 μ H_2O laser coupled to the diode together with tens of mW output of a V-band klystron can readily produce a zero beat across the diode as large as several millivolts; the zero beat is obtained when the klystron frequency, ν_m, is tuned so that $\nu_{118} - 3\nu_{337} + 2\nu_m \approx 0$. Our results show that the corresponding current at the synthesized frequency $(3\nu_{337} - 2\nu_m)$ should be sufficiently large to produce detectable radiation.

In our experiment, the wavefronts of the synthesized and the local oscillator radiations incident on the Cu:Ge were not in exact coincidence: The heterodyne signal across the Cu:Ge was found in general to increase as the aperture of the collecting lens was reduced down to

about 3 mm diameter. A rough calibration gave an estimate of about 5×10^{-11} watts of total radiation emitted at the synthesized frequency. Much improvement can be expected since in our experiment the couplings of both the laser and the microwave radiations to the diode are as yet far from optimum.

Lastly, we note that the slow speed of the Cu:Ge limits the superheterodyne detection to cases where the frequency of the synthesized radiation falls within hundreds of MHz of the local oscillator frequency. However, instead of a Cu:Ge, a metal-to-metal point contact diode used as a detector element would allow, with its fast response and highly nonlinear characteristic, superheterodyne detection of a synthesized radiation at a frequency differing from the local oscillator's by an amount in the microwave region: In this case, in addition to the local oscillator and the synthesized radiations, the detector diode may also be subjected to a microwave radiation at an appropriate difference frequency so that final heterodyne signal across it is observed at a convenient IF frequency, (say in the tens of MHz region).

REFERENCES

1. L. O. Hocker, D. R. Sokoloff, V. Daneu, A. Szoke and A. Javan, Appl. Phys. Letters 12, 401 (1968).

2. V. Daneu, D. Sokoloff, A. Sanchez and A. Javan, Appl. Phys. Letters 15, 398 (1969).

3. D. R. Sokoloff, A. Sanchez, R. M. Osgood, Jr. and A. Javan, Appl. Phys. Letters 17, 257 (1970).

4. K. M. Evenson, G. W. Day, J. S. Wells and L. O. Mullen, Appl. Phys. Letters 20, 133 (1972).

5. See electron microscope photograph of the antenna tip in Ref. 3 which reports absolute frequency measurements in the 5 μ region.

6. The current voltage characteristic curve in the presence of a bias voltage V_o, can be written as $i = \Sigma \frac{1}{n!} \alpha_n V^n$ where α_n is the n^{th} derivative of the characteristic curve evaluated at V_o and (V_o+V) is the total applied voltage; accordingly, the observed variation of an n^{th} order mixing signal as V_o is varied gives closely the dependence of the n^{th} derivative on V_o (since the term in V^n is dominantly responsible for the n^{th} order mixing.)

FIGURE CAPTIONS

Figure 1. The lower oscilloscope trace is the beatnote after band-pass amplifier. The upper is after the integrator.

Figure 2. Block diagram (see text). Switches s_1 and s_2 in position A give the phase-locking of the klystron and the subsequent narrow-band detection system. Position B corresponds to the broadband detection of the zero beat.

Figure 3. Phase-sensitive amplifier output for bias voltage varying at about 10 Hz by about 100 millivolts.

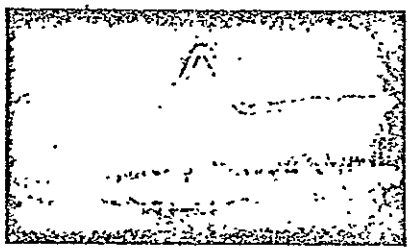

Original. Please return, Sandy, Bugs & Jason

Fig 1.3

L4033

86

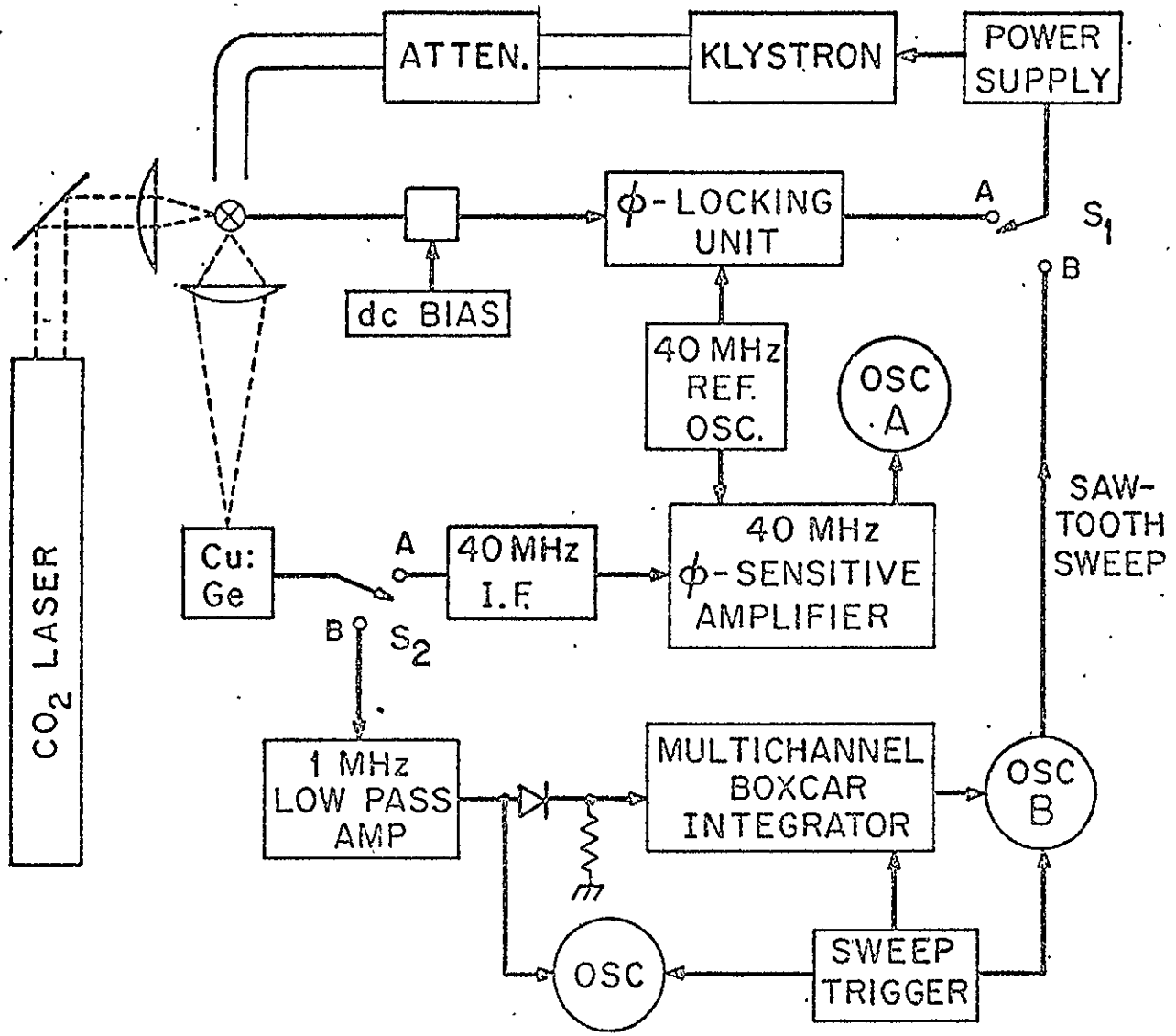
ATTEN.
KLYSTRON
POWER SUPPLY
φ-LOCKING UNIT
A
S1
B
dc BIAS
40 MHz REF. OSC.
OSC A
CO2 LASER
Cu: Ge
A
40 MHz I.F.
40 MHz φ-SENSITIVE AMPLIFIER
SAW-TOOTH SWEEP
B
S2
1 MHz LOW PASS AMP
MULTICHANNEL BOXCAR INTEGRATOR
OSC B
OSC
SWEEP TRIGGER

Fig. 2

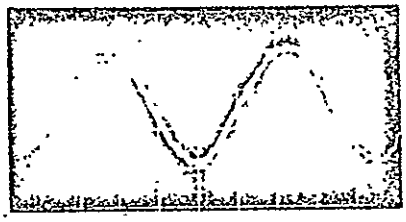

Original, Please Return, Sandy Siegel Rm 1103

Fig 3.03

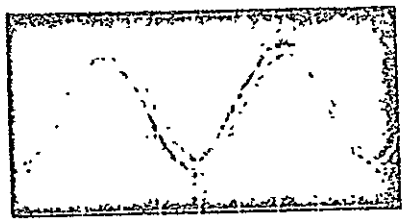

Original. Please Return, Sandy Sieglaff

89<

Fig 3.93

14033

6. T. W. Ducas and A. Javan

Measurement of Microwave Fine Structure in OH Infrared Transitions using Frequency Mixing with Metal-to-Metal Infrared Diodes

J. Chem. Phys. 60, 1677 (1974)

Measurement of microwave fine structure in OH infrared transitions using frequency mixing with metal-to-metal infrared diodes*

T. W. Ducas and A. Javan

Department of Physics, Massachusetts Institute of Technology, Cambridge, Massachusetts 02139
(Received 12 November 1973)

In this letter we report precise measurements of fine structure in OH utilizing an infrared pure rotational OH laser.[1] Frequency mixing with metal–to–metal infrared diodes[2,3] was used to find the precise frequency spacing between laser lines originating from fine structure sublevels of the same rotational level. These frequency spacings lie in the K-band region, and the accuracy of the present measurement is 100 times better than that achieved with conventional infrared techniques.[2]

The OH fine structure consists of the splitting of each rotational level into doublets by the interaction between electron spin and the molecule's angular momentum. Each element of a doublet is split again by the interaction of molecular rotation and electron angular momentum (Λ doubling). Laser lines are observed as closely spaced quartets of $R(K)$ lines: $R_1(K)$, $R_1'(K)$, $R_2(K)$, $R_2'(K)$, where K is the total orbital angular momentum. (The fine structure sublevels are designated by subscripts 1 and 2 for the different spin-doublet components. Primes indicate the Λ-doublet components of higher energy). The pairs of laser transitions used were the $R_1(20)$, $R_2(20)$ and $R_1(21)$, $R_2(21)$ lines ($\sim 14\mu$ wavelength), within the $v=0$ vibrational level of the $^2\Pi$ electronic ground state of OH.

The experimental apparatus included a pulsed helical "pin" transverse laser discharge tube[1] through which O_2, H_2 and SF_6 were flowed with partial pressures of 5.6, 1.4, and 0.9 torr, respectively. The pulses originated from a 0.1μF capacitor bank charged to 15 KV. The laser pulses were 1μ sec wide and the repetition rate was ~1Hz. An internal mirror configuration was used with a cavity 1.5 m long and two 4.25 m radius-of-curvature mirrors. A 2mm hole in one mirror provided output coupling. Laser oscillation occured simultaneously on 44 lines ranging from 12μ to 18μ.

The laser and the pulsing circuit were enclosed in a "Faraday cage" to reduce noise from the circuitry and the laser. The line voltage was taken through an RF filter. These precautions were important because otherwise the radiated noise would be picked up by the point contact diode and would overwhelm the difference frequency measurements.

The laser output was focused onto the point contact diode using a parabolic mirror with a 7 cm focal length. The diode itself consisted of a pointed 1 mil tungsten wire in contact with a polished nickel post. The structure was identical to that described in Ref. 2. Microwave power from an OKI 24V10 K-band klystron was coupled to the diode's infrared antenna by subjecting the diode to the radiation from the open end of a K-band waveguide. Frequency measurements were made to within ±2MHz with a calibrated wavemeter. The output of the diode was sent into an I. F. strip centered at $\nu_{IF}=57$ MHz with a bandwidth of ±3MHz.

The frequencies of two infrared laser lines differing by $\Delta\nu_L$ mix with the klystron output to produce a beat note at $\Delta\nu_L-\nu_K$. Accordingly a beat signal is observed at the output of the IF amplifier when $\Delta\nu_L-\nu_K=\pm\nu_{IF}$.

The laser oscillation on each transition can take place over a frequency range determined by the combined Doppler and pressure-broadened width of the transition. In the pressure and temperature regime at which the OH laser operates, the total width of the transition is about 150 MHz.[4] Since our laser cavity had a mirror-separation of 1.5 m, this indicates that oscillation took place mainly on only a single longitudinal mode. This is confirmed by the observed beat note which fluctuated over many pulses in a range of 40–50 MHz. After repeated runs and statistical analysis, the difference frequencies were established to accuracies of a fraction of the oscillation width:

$$\nu\{R_1(20)-R_2(20)\}=21.500\pm.005\ \text{GHz},$$

and

$$\nu\{R_1(21)-R_2(21)\}=15.26(5)\pm.010\ \text{GHz}.$$

The precision of these difference frequency measurements represents an improvement of better than a factor of 100 over results using a conventional grating monochromator,[1] and a factor 500 over work observing ultraviolet electronic transitions.[5]

The above work has shown the applicability of frequency mixing techniques using the metal–to–metal infrared point contact diode in precision spectroscopic studies of OH. Extension of this work can provide highly accurate measurements of fine structure parameters and the influence of molecular rotation on the splittings.

The authors express their appreciation to Dr. Antonio Sanchez for his valuable suggestions and discussions.

*Work supported by U. S. Army, NASA, and NSF.

[1] T. W. Ducas, L. D. Geoffrion, R. M. Osgood, Jr., and A. Javan, Appl. Phys. Lett. 21, 42 (1972).

[2] V. Daneu, D. Sokoloff, A. Sanchez, and A. Javan, Appl. Phys. Lett. 15, 398 (1969).

[3] A. Javan, Fundamental and Applied Laser Physics, Proc. Esfahan Sym., edited by M. S. Feld, A. Javan and N. A. Kurnit (Wiley, New York, 1973), p. 295.

[4] J. Goldhar, R. M. Osgood, Jr., and A. Javan, Appl. Phys. Lett. 18, 1967 (1971).

[5] G. H. Dieke and H. M. Crosswhite, J. Quant. Spectry. Rad. Transfer 2, 97 (1962).

91

7. A. Sanchez, C.F. Davis, K. C. Liu and A. Javan

The MOM Tunneling Diode: Theoretical Estimate of its Performance at Microwave and Infrared Frequencies

J. Applied Physics (to be published in August 1978)

THE MOM TUNNELING DIODE: THEORETICAL ESTIMATE OF ITS PERFORMANCE AT MICROWAVE AND INFRARED FREQUENCIES*

A. Sanchez, C. F. Davis, Jr., K. C. Liu and A. Javan

Department of Physics
Massachusetts Institute of Technology
Cambridge, Massachusetts 02139

(To be published J. of Appl Phys. Aug. 1978)

ABSTRACT

A theoretical analysis of the metal-oxide-metal (MOM) antenna/diode as detector of microwave and infrared radiation is presented with experimental verification conducted in the far infrared. It is shown that the detectivity at room temperature can be as high as 10^{10} watts^{-1} Hz$^{1/2}$ at frequencies of 10^{14} Hz in the infrared. As a result, design guidelines are obtained for the lithographic fabrication of thin film MOM structures that are to operate in the 10 micron region of the infrared spectrum.

* This work has been supported by the Air Force ARPA and, in part, by NASA and Army Research Office.

I. INTRODUCTION

The metal-oxide-metal diode has been used extensively over the past decade for frequency measurements in the infrared.[1-4] In fact, frequencies up to the 2.0 micron region have been measured.[5] Electron tunneling across an oxide layer separating the sharply tipped tungsten wire from the metal(typically nickel) post, has been recognized as the dominant (nonlinear) conduction mechanism in the dc regime. Previously it has been shown that the conduction mechanism at low frequencies is also responsible for rectification in the 10 micron region.[6] Radiation is coupled from an electromagnetic wave to the nonlinear junction by means of an antenna that in the case of the point contact diode is the tungsten wire.[7,8] Several theoretical analyses of the metal-oxide-metal point contact detector have dealt either with the nonlinearities of the junction[9,10,11] or with the antenna characteristics.[12] These theoretical results are consequently not easy to compare with the measured values of detector characteristics such as responsivity and noise equivalent power. For instance, in the analysis followed by Green[9] and Kwok[10] the junction's nonlinearities are thoroughly discussed but the problem of matching the junction to the antenna is ignored. Other analyses based only on the antenna model[12] predict a frequency dependence of the diode responsivity that is not in good agreement with experimental observations.[13]

In the present paper a model is chosen for the antenna (Section II) where the load contains a capacitive component due to the small contact area. Electron tunneling theory is briefly reviewed in Section III to obtain expressions for the responsivity in the case of a trapezoidal tunneling barrier. The results from these two section are combined in Sections IV and V to yield actual numerical results for optimum expected power conversion efficiency ($\sim 10^{-2}$) and detector NEP at room temperature ($\sim 10^{-10}$ W.Hz$^{-1/2}$). Further, it is seen that the quantum efficiency factor can be as high as 10^{-2} in the 10μ region.

Section VI contains the results of computer calculations that support the validity of the simplified analytical results of the previous two sections.

II. ANTENNA MODEL

The antenna, as a receiver, is represented by an ac voltage source $v\cos\omega t$ with an internal real impedance R_A.
The non-linear resistance, R_D, in parallel with the junction capacitance represents the diode whose series resistance is assumed negligible compared to both R_A and R_D. The effective voltage (see Fig. 1) developed across the diode is

$$v_D = v\,\frac{Z_D}{R_A + Z_D} = v\,\frac{R_D}{R_A + R_D + j\omega R_A R_D C}$$

where Z_D is the parallel combination of R_D with X_C. The junction capacitance, $C = \epsilon_o \epsilon \frac{a}{L}$ is due to the finite contact area, a, and dielectric thickness, L.

C-2

95<

Introducing the "reduced frequency," $q = \omega C R_A$, the "reduced diode resistance," $x = R_D/R_A$ and the "incident power" $P = \frac{v^2}{8R_A}$, then

$$v_D = v \frac{x}{1 + (1 + jq)x}$$

The power dissipated in R_D (effectively the receiver load) is

$$P_r = \frac{|v_D|^2}{2R_D} = 4P \frac{x}{1 + 2x + (1+q^2)x^2} \qquad [1]$$

It is of interest to find the value of the diode resistance that maximizes P_r, the power coupled to the load. The condition $\frac{\partial P_r}{\partial x} = 0$ leads to $x_m^2 = \frac{1}{1 + q^2}$, and then

$$P_r(x_m) = 2P \frac{1}{1 + \sqrt{1+q^2}}$$

At high frequency ($q >> 1$), there is a roll off where $P_r(x_m) \sim q^{-1}$.

In the low frequency regime ($q << 1$), the maximum value of P_r occurs for $R_D = R_A$, ($x = 1$) and is

$$P_r(\max) = P$$

We then say that the antenna is matched to the load. This optimum received power, P, is related to the Poynting Vector, $\overline{S}$, of the incident field.

$$P = \sigma(\theta,\phi)\ |\overline{S}|$$

This relationship defines the effective aperture of the antenna.[14] Calculation of the aperture and antenna impedance for different antenna geometries is a subject that belongs to antenna theory. For certain simple geometries (e.g. dipole), the maximum effective aperture is about $0.1\lambda^2$. (See Section VII a). In what follows, and for reasons that will become evident later, we will want to study the effect on the diode as the radiation frequency is changed. In order to still couple the same power P, we will require that: a) the linear dimensions of the antenna be scaled with the wavelength (that means same R_A, same σ/λ^2); b) the power incident in λ^2 ($=\lambda^2|S|$) also be kept constant. In the case of two lasers of equal power and different frequencies this implies that their beams are focused with the same f number.

III. DIODE MODEL

Electrical conduction between the two metallic electrodes forming the MOM diode is due to electron tunneling through a potential barrier formed by a metal oxide layer on the order of 10 Å or less. This mechanism produces the non-linearities in the I-V characteristic. In order to

97<

calculate the I-V characteristic, we choose a model consisting of a trapezoidal potential barrier with thickness L and heights ϕ_1 and ϕ_2 on each side. The WKB approximation is used[15] to calculate the tunneling probability for an electron that has a certain energy associated with its motion normal to the barrier.

The total current density for an applied voltage V is obtained by integrating the contributions of electrons with all possible energies. This can be done with the help of a computer. However, some analytical approximations[15] allow us to obtain a closed form expression for the I-V characteristic. A series expansion up to V^3 leads to

$$I = \frac{1}{R_D} (V + mV^2 + nV^3)$$

Introducing the average barrier height $\phi_o = \frac{\phi_1 + \phi_2}{2}$, the asymmetry factor $\alpha = \frac{\phi_1 - \phi_2}{\phi_1 + \phi_2}$ and the dimensionless parameter $S = 1.025 L \sqrt{\phi_o}$, where L is given in angstroms and ϕ_o in electron volts, the theory (see Appendix A) gives the following results

$$R_D = \frac{Se^S}{324\phi_o} \quad \frac{1}{a(\mu m^2)} \qquad \text{(a = junction area)} \qquad [2]$$

$$m = \frac{\alpha S}{24\phi_o} \qquad \text{and} \qquad [3]$$

$$n = \frac{1}{6} \left(\frac{S}{4\phi_o}\right)^2 \qquad [4]$$

98<

If a voltage of amplitude $v_D \cos \omega t$ is applied to the diode simultaneously with a bias voltage V_b, there will be a rectified current whose value is

$$i_r = \frac{1}{2} \left. \frac{\partial^2 I}{\partial V^2} \right|_{V_b} \overline{v_D^2 \cos^2 \omega t} = (m + 3nV_b) \frac{v_D^2}{2R_D}$$

$$= (m + 3nV_b) P_r$$

The current responsivity is defined as $\beta_i = \frac{i_r}{P_r}$. In what follows we will consider only the case of the unbiased diode so that β_i

IV. RECTIFICATION AND POWER CONVERSION

a) Rectification

The rectified voltage appearing on the diode (with given parameters α, L, ϕ_o, a) is

$$V_r = R_D \beta_i P_r$$

where P_r is the power delivered by the antenna to the diode (load) Therefore

$$V_r = \beta_i \, 4P \, R_A \, \frac{x^2}{1 + 2x + (1 + q^2) x^2} \qquad [5]$$

99<

It should be noted that both β_i and q are relatively insensitive functions of the barrier thickness, L, while x has an exponential dependence. With that in mind we can see from Eq. (5) that v_r is a monotonically increasing function of x. The limiting value is

$$v_r(x=\infty) = v_o \frac{1}{1 + q^2} \quad \text{where } v_o = 4\beta_i R_A P \qquad [6]$$

Fig. 2 displays the rectified voltage given by Eq. (5) as a function of the reduced resistance x and for various values of the reduced frequency q.

From Eq. (6) we can get some numerical results for a practical case. Consider a barrier with L = 10 Å, ϕ_o = 1ev, α = 0.2 so that S $\approx$ 10 and β_i = m = 1/12 amp/watt. If R_A = 100Ω and q << 1 (frequency below the roll off) we obtain for an incident power P = 1mW that the maximum rectified voltage is about v_o = 30 mV.

b) Power Conversion

An incident power P generates a rectified voltage v_r, according to Eq. (5). The rectified power P_{DC} associated with v_r is given by

$$P_{DC} = \frac{v_r^2}{R_D} = (4\beta_i P)^2 R_A F(x,q) \qquad [7]$$

$$\text{where } F(x,q) = \frac{x^3}{[1 + 2x + (1 + q^2) x^2]^2} \qquad [8]$$

100<

The maximum value of P_{DC} occurs at

$$x_o = \frac{1 + \sqrt{4 + 3q^2}}{1 + q^2} \qquad [9]$$

so that the optimum conversion efficiency η_e is:

$$\eta_e = \frac{P_{DC}(x_o)}{P} = (4\beta_i)^2 P \, R_A \, F(x_o, q) \qquad [10]$$

where $$F(x_o, q) = \frac{\left[1 + \sqrt{4 + 3q^2}\right]^3}{(1 + q^2)\left[q^2 + \left(2 + \sqrt{4 + 3q^2}\right)^2\right]^2} \qquad [11]$$

In Fig. 3 the dependence on the reduced frequency, q, of the optimum reduced diode resistance, x_o, and of the function $F(x_o, q)$ are displayed. For the typical value of $\beta_i = 1/12$ amp/watt used in the previous section η_e/P is also displayed as a function of q in Fig. 3. It should be noted that for frequencies below roll off $\eta_e/P \approx 1$ watt^{-1}.

The maximum power P that can be used in Eq. (10) is determined by the burn out level of the diode. Voltages across the diode on the order of 0.3 volts can already burn the junction (the electric field in the oxide would be on the order of 3×10^6 volts/cm). This would result from a maximum incident power, P, of about 10 mwatts and, therefore, for $q \leq 1$ we would obtain a conversion efficiency of 1%.

101<

It should be remembered, however, that when the diode is driven with such high power levels, the rectified current depends quite strongly on higher order derivatives of the I-V characteristic. The simple model used to calculate the nonlinear I-V characteristic cannot predict the correct behavior of the fourth order derivative. Available experimental data on MOM diodes, however, show that the fourth derivative contribution is already important at V = 0.1 volt.

At frequencies lying in the roll off ($q >> 1$) the conversion efficiency goes as q^{-3} (see Fig. 3). It is, therefore, evident that in order to have good conversion efficiency in the infrared we should reduce the junction area to minimize C and have $q = \omega RC \leq 1$ at the frequency of interest. In what follows we will estimate the junction area a, and barrier thickness, L, to achieve that condition at a given frequency.

At the corner frequency ($q = 1$) and for optimum conversion we have from Eq. (9) that $x_o = \frac{R_D}{R_A} = 1.82$. This together with Eq. (2) gives a condition relating the area, a, and the barrier parameter S,

$$1.82\ R_A = \frac{1}{324}\ \frac{S}{\phi_o}\ \frac{e^S}{a} \qquad [12]$$

A second relation involving S and a is obtained from the

requirement q = 1, so that $2\pi f_c R_A C = 1$ where the junction capacitance, C, is given in farads by

$$C = \epsilon_o \epsilon \frac{a}{L} = .835 \times 10^{-13} \epsilon \frac{a}{L} \qquad [13]$$

with a in $(\mu m)^2$ and L in Å. This second relation can therefore be expressed as

$$a = .177 \times \frac{L}{R_A} \frac{10^{13}}{\epsilon f_c} \qquad [14]$$

From Eqs. (12) and (14) we have that

$$e^S = 103 \sqrt{\phi_o} \frac{10^{13}}{\epsilon f_c} \qquad [15]$$

$$L = \frac{1}{1.025\sqrt{\phi_o}} \ell n \left(103 \sqrt{\phi_o} \frac{10^{13}}{\epsilon f_c}\right) \qquad [16]$$

The results given by Eqs. (14) and (16) are displayed in Fig. 4 for the typical case of $\phi_o = 1$ and $R_A = 100$.

It should be noticed that the values for L in Fig. 4 do not depend on the antenna resistance (see Eq. (16)) while those for contact area, a, are inversely proportional to R_A (Eq. (14)).

Also, since the value of L changes by not more than a factor of 5, so does the current responsivity $\beta_i = \frac{\alpha S}{24\phi_o}$.

The above guidelines are important to consider in the design of high speed MOM junction structures in which, using photolithographic techniques, an antenna is printed[16,17] and integrated with the small area junction.

As the corner frequency of the diode goes up to $f_c = 10^{14}$ Hz we see that the required L and a decrease. The decrease in a, although a difficult technical problem with the present photolithographic techniques could be achieved with some further sophistication (e.g. electron beam lithography). It should be mentioned that areas on the order of .0004 μm^2 can be obtained in a mechanical point contact diode. The reduction in L down to 2.27Å, on the other hand, brings into question the validity of the WKB approximation used in calculating the electron tunneling. The condition for its validity is that this probability ($\sim e^{-S}$) is small compared to unity. Substituting this condition into Eq. (15) requires:

$$f_c << 103 \sqrt{\phi_o} 10^{13} \approx 10^{15}$$

We will not attempt at this point to make any quantitative estimates on the modifications to the model due to the breakdown of the WKB approximation in the optical and near infrared region. In addition, in this frequency region, photon energy is comparable to the barrier height ($\sim$lev) and other interesting effects may set in and dominate the rectification process.[24]

V. DETECTOR PERFORMANCE

Let us consider thermal noise to be the dominant one. Then

$$V_n = \sqrt{4KTR_D\Delta\nu} = \sqrt{4KTR_A\Delta\nu}\,\sqrt{x}$$

Using the rectified voltage given by Eq. (7) we obtain the signal to noise ratio where F(x) is given by Eq. (8).

$$\frac{V_r}{V_n} = \frac{4\beta_i P\sqrt{R_A}}{\sqrt{4KT\Delta\nu}}\,F^{1/2}(x) \qquad [17]$$

The noise equivalent power (NEP) is the value of the power P that gives a unity signal to noise ratio for a bandwidth of $\Delta\nu$ = 1Hz. The inverse of the NEP is known as the detectivity, D, and therefore, is given by

$$D(x) = \frac{4\beta_i\sqrt{R_A}}{\sqrt{4KT}}\,F^{1/2}(x) \qquad [18]$$

With the same considerations that we used previously we can obtain, by optimizing F(x), the barrier thickness that for a given junction area yields the optimum detectivity.

Replacing $F(x_o)$ as given by Eq. (11), we obtain:

$$D = D(x_o) = \frac{4\beta_i\sqrt{R_A}}{\sqrt{4KT}}\,F^{1/2}(x_o) \qquad [19]$$

105

Using $\beta_i = 1/12$, $R_A = 100$ ohms and $T = 300°K$ we obtain

$$D = 2.6 \times 10^{10} F^{1/2}(x_o)$$

The dependence of D on the frequency is given in Fig. 3.

It is of interest to compare the detector responsivity of the MOM diode with those of existing infrared quantum-type detectors. The detection mechanism in the MOM diode arises from rectification of ac currents induced across the junction at infrared frequencies. The mechanism in the second type of detectors arises from generation of free carriers due to absorption of infrared photons. For this type of detectors the current responsivity, β_i, and the quantum efficiency, η_q, are related by

$$\eta_q = \frac{h\nu}{e}\beta_i$$

For comparison purposes let us estimate the quantum efficiency, η_q, of an MOM diode operating, below roll off, in the 10 microns region. The energy $h\nu$ of a photon at this wavelength is about .1 ev and taking the typical responsivity $\beta_i \approx .1$ amp/watt, we get that $\eta_q \approx 10^{-2}$. In the average, there is a transfer of one electron across the barrier for an energy coupled to the diode corresponding to 100 infrared photons. As the frequency increases, so does the quantum efficiency, but remains

below unity everywhere in the infrared. It is this fact that provides the theoretical justification for using the low frequency I-V characteristic in order to estimate the rectification at infrared frequencies.[18]

VI. COMPUTER CALCULATIONS

In order to get the results of the previous sections, approximations were necessary. In Eq. (5), (7), and (18), the values for v_r, P_{DC} and $D(x)$ were optimized by varying the barrier thickness. In one instance the maximum of the rectified power P_{DC} is obtained by maximizing $F(x)$ in Eq. (8). In this approximation the fact that β_i has a linear dependence on S was ignored because $x \sim R_D \sim e^S$ has an exponential dependence. More exact computer calculations have been carried out to check the validity of these approximations. The results will be compared with those of Fig. 3.

Figure 5 shows the calculated detectivities at different frequencies as the barrier thickness is changed. For this calculation it was assumed $R_A = 100$ ohm, and $a = 1\mu m^2$. Eq. (18) was used where $F(x)$ is taken from Eq. (8) and for β_i we take the value of m given by Eq. (3). The important result in Figure 5 is that for each frequency there is a value of the barrier thickness that optimizes the NEP. For a given contact area we have that to each frequency corresponds an optimum NEP leading to the results of Figure 6. These results are very much in agreement with those in Fig. 3, obtained analytically, where $D(x_o)$ is plotted as a function of the frequency q.

In comparing Figure 3 with Figure 6, we would like to comment on two points. In the low frequency region ($q << 1$)

Figure 6 predicts detectivities ranging from 10^{10} to 1.2×10^{10} Watts^{-1} x Hz$^{1/2}$, depending on contact area, while Figure 3 predicts $.85 \times 10^{10}$ independently of the contact area. This is so because the small dependence of β_i on barrier parameters was not taken care of in calculations leading to Figure 3. The second remark is about the roll off region ($q >> 1$). Figure 3 predicts a dependence $D \sim \omega^{-1.5}$ while more exact calculations predict $D \sim \omega^{-1.78}$. Considering the type of approximations involved the agreement is satisfactory.

VII. EXPERIMENTS AND TEST OF THE THEORY

a) Experiments in support of antenna theory

We have measured the efficiency in coupling the radiation from a focused HCN laser beam ($\lambda = 377\ \mu m$, $P_L = 5$ mw) into the antenna/diode and studied the dependence of this efficiency on the diode resistance and focusing angle of the laser beam. A balancing technique is used for measuring the FIR coupled power (Fig. 7). The focused beam and an adjustable amount of rf (at 400 KHz) are coupled alternately to the diode at a rate of 80 Hz so that a null signal is obtained when the rectified signal due to the FIR laser rectification equals that due to the rf.

The, otherwise unknown, AC voltage at FIR frequency induced on the junction equals that of the balancing r f voltage, easily measurable on an oscilloscope. The received laser power, $P_r = v_{AC}^2 / 2R_D$ on the junction can then be measured when a laser beam with total power P_L is focused on the antenna/diode and the dependence of the coupling efficiency, $\eta = P_r/P_L$, on the diode resistance can be studied and compared to the theory (Eq. 1). In the experiment, the antenna is formed by a thin tungsten wire several wavelengths long so that the radiation impedance is predominantly resistive. Also the radius of the point contact ($\simeq 1000$ Å) is sufficiently small that capacitive loading is negligible ($q \ll 1$). The resistance of the diode is varied by adjusting the pressure on the point contact and the coupling efficiency is measured for each value of the resistance. A typical set of experimental results is presented in Fig. 8 and found to agree with the theoretical prediction: $\eta = 4 \eta_o R_A \frac{R_D}{(R_D + R_A)^2}$

In this way, a value of $R_A = 162 \pm 10$ ohm was obtained for the antenna whose radiation pattern was also measured (Fig. 9) by using a previously described technique.[7]

The dependence $\eta_0 (\theta_f)$ on the focusing angle was then investigated. If the focusing angle is much smaller than the width of the first lobe ($\theta_f << \theta_\ell$), the laser radiation appears essentially as a plane wave and the coupling can be described by an effective antenna aperture $\sigma = \frac{\lambda^2}{4\pi} G$ where the gain, G, for $L >> \lambda$ is given by $G = \frac{120}{R_A} \frac{L}{\lambda}$

(See Appendix B). In this regime, ($\theta_f << \theta_\ell$), the efficiency is given by the ratio $\eta_0 \approx \sigma / \pi w_0^2$ (where $2w_0 = \lambda/\theta_f$ is the focused spot diameter). Then $\eta_0 = \sigma / (\pi w_0^2) = \frac{120}{\pi^2 R_A} \frac{L}{\lambda} \theta_f^2$

has a θ_f^2 dependence in agreement with the experimental results in Fig. 10.

The experimental results of Fig. 10 show that for small focusing angles ($\theta_f = D/f$ where f = 12.7 cm. in this case) the efficiency η_0 is in fact proportional to θ_f^2, consistent with the concept of effective aperture. That proportionality constant agrees within a factor of two with the one expected from the theory when in the above expression for η_0 we replace L and R_A by their experimentally measured values. Considering the simplifications involved and uncertainty in our calorimetric laser power measurements, the above agreement is satisfactory. As the focusing angle is increased to a value comparable to the width of the first radiation lobe, the coupling efficiency saturates to about 3%, in agreement again with the theory. (Appendix B) The experiment was repeated for a different antenna length and a proportionally different coupling efficiency (or antenna gain) was observed for small focusing angles. At larger focusing angles, however, the same saturated value of the coupling efficiency is reached.

To confirm that the FIR detection is due to the same mechanism as that of rf detection (i.e. rectification), we checked that the balancing condition remains when a bias, up to about 100 mV, is applied to the diode. (i.e. FIR and rf detection have the same bias dependence.)

A major recent advance has been photolithographic fabrication of a high-speed metal-oxide-metal junction.[16] With a two-stage thin film vacuum evaporation method, a high-speed junction is deposited on a substrate, along with a small antenna integrated to it. We have applied the balancing technique to the study of such a diode junction (integrated to an antenna). Preliminary results show that in some structures the coupling efficiency is as high as 2 or 3%, comparable to that of the mechanical point contact diode.

We should recall that the technique is applicable regardless of the nature of the rectification mechanism as long as it is the same at rf and ir frequencies. For example, we have also fabricated antenna structures where the load is an evaporated micron-sized, thin-film wire without a junction. A weak bolometric response was observed at both frequencies and the best coupling efficiency was found to be around 1%.

b) Experiments in support of tunneling as the rectification mechanism

We have studied the behavior of the point contact diode nonlinearities by observing the bias dependence of the rectified signal when a known amount of rf power is coupled to the diode. These results can be compared with the predications of the tunneling model (Section III) yielding values for the barrier parameters that are found to be reasonable.

The diode's I-V characteristic up to third order can be expressed as:

$$I = \frac{1}{R} (V + mV^2 + nV^3) .$$

Due to these nonlinearities, the rectified voltage, V_r, when an rf voltage V_D coswt is coupled to the diode is given by

$$V_r = (m + 3n\ V_b)\frac{V_D^2}{2}$$

The experimental dependence of V_r on V_b shown in Fig. 11, can be approximated by a straight line in the low bias region. We can then obtain for the 2 K-ohm diode, $m = .16\ V^{-1}$ and $n = 1.81\ V^{-2}$.

Note that these values for m and n, which are independent of the contact area, are in general agreement with those obtained from the tunneling model assuming reasonable values for the barrier parameters.

We can invert equations (2) and (4) to obtain:

$$\phi_o = \frac{1}{4\sqrt{6n}} \cdot \ell n \frac{.324\ R_D a}{4\sqrt{6n}}$$

$$S = 4\phi_o \sqrt{6n}$$

$$L = \frac{4\sqrt{6n\phi_o}}{1.025}$$

By estimating the value of contact area as $a = .1\ \mu m^2$, we can then obtain $\phi_o = .65$ ev and $L = 10.3$ Å which are quite reasonable and change only logrithmically with the estimated area. Furthermore, the value of α according to the theory is given by

$$\alpha = m\sqrt{6/n}$$

which, in the case of Fig. 11, is equal to 0.29 and does not depend on the estimated area.

As the resistance of the diode is lowered by adjusting the pressure of contact, the value for n decreases monotonically. For example; if $R_d = 50$ ohms we get $n = 1.39$ so that $\phi_o = 0.43$ eV and $L = 7.3$ Å. At

these low values of L and ϕ_o, the W.K.B. approximation used in calculating the tunneling probability begins to lose its applicability.

On the other hand, the value of the barrier asymmetry factor can vary over a very wide range for diodes with the same resistance, Some of the other characteristics reported in the literature[6,11,13,20] correspond only to nearly symmetric diodes.

We have shown that in agreement with the theory, the zero bias responsivity, β_i (=m), remains nearly constant as the resistance is varied over two orders of magnitude. This statement was previously made in section IV (a) without experimental support. We have, however, verified Eq. 5 at FIR frequencies (where $q < 1$) by studying the laser rectification as the resistance of the diode "relaxes" continuously and slowly (presumably keeping the same asymmetry factor α) from 10 to few thousand ohms. We were able to fit the result to the expression:

$$V_r = V_o\left(\frac{R_D}{R_D + R_A}\right)^2$$

with two adjustable parameters, V_o and R_A.

This method of determining R_A is, however, more tedious and difficult than the previously described balancing technique, where the changes in R_D need not be continuous.

The authors would like to acknowledge several valuable discussions on this subject with G. Elchinger.

APPENDIX A

The problem of calculating the I-V characteristic of a metal-insulator-metal structure[15,21,22] has been treated by different authors. We will summarize the treatment given in reference 15. However, we should point out that when the I-V characteristic is expanded up to the V^3 term, the same results are obtained from reference 21.

The current is due to quantum mechanical tunneling of electrons through the potential barrier presented by the thin insulating layer. When a voltage V is applied across the junction the barrier shape is $\phi(x,V) = \phi\ (x) - \frac{x}{L}\ eV$. An electron approaching the barrier with an energy E_x in the direction perpendicular to the barrier has a transmition probability given by the WKB approximation

$$P(E_x,V) = e^{-\alpha_e \int_o^L \sqrt{\phi(x,V) - E_x}\ dx}$$

where $\alpha_e = \frac{2\sqrt{2m}}{\hbar} = 1.025\ eV^{-\frac{1}{2}}\text{Å}^{-1}$

carrying out a Taylor expansion:

$\ln p(E_x,V) = -[b_1 + c_1 \varepsilon_x + f_1 \varepsilon_x^2 + \cdots]$ where $\varepsilon_x = \xi_1 - E_x$, and ξ_1 is the Fermi energy in metal 1 and the V dependence appears in the coefficients b_1, c_1, f_1 ---.

The total tunneling current density is obtained by integration over the contribution of electrons with different energies E_x.

$$J(V) = \frac{4\pi m e kT}{h^3} \int_{-\infty}^{+\infty} P(E_x,V)\ F(E_x,V)\ dE_x$$

and $$F = \ln \frac{1 + \exp(-E_x/kT)}{1 + \exp(-(E_x + eV)/kT)}$$

115

It is possible, at this point, to obtain numerical solutions with the help of a computer. However, further approximations will let us obtain analytical solutions. A discussion of the approximations involved in different methods is best discussed in ref. 22. A series expansion of the current density up to the third power of the voltage is then obtained.

$$J = G(T)\,(V + mV^2 + nV^3)$$

$$G(T) = j_0\, e_{10}\, \frac{\pi c_{10} kT}{\sin(\pi c_{10} kT)}$$

$$j_0 = \frac{A\, e^{-b_{10}}}{(c_{10} kT)^2}$$

$$A = \frac{4\pi m_e e (kT)^2}{h^3} = 120\ T^2\ \text{amp} \cdot \text{cm}^{-2}$$

$$m = b_{11} - \frac{c_{10}}{2}$$

$$n = \frac{b_{11}^2}{2} - \frac{c_{10} b_{11}}{2} + \frac{c_{10}^2}{6} - b_{12} = \frac{m^2}{2} + \frac{c_{10}^2}{24} - b_{12}$$

The parameters b_{10}, b_{11}, b_{12} and C_{10} are obtained from

$$b_1 = \alpha_e \int_0^L \sqrt{\phi(x)}\, dx = b_{10} - b_{11} V + b_{12} V^2 - - -$$

and [A1]

$$c_1 = \frac{\alpha_e}{2} \int_0^L \frac{dx}{\sqrt{\phi(x}} = c_{10} + c_{11} V - - - \qquad [A2]$$

For a trapezoidal barrier we have $\phi(x) = \phi_1 - (\phi_1 - \phi_2)\frac{x}{L}$ that when substituted in Eqs. (A3), (A1), and (A2) leads to:

$$b_{10} = S\left(1 - \frac{\alpha^2}{24} + \cdots\right)$$

$$b_{11} = \frac{S}{4\phi_o}\left(1 + \frac{\alpha}{6} + \cdots\right)$$

$$c_{10} = \frac{S}{2\phi_o}\left(1 + \frac{\alpha^2}{8} + \cdots\right)$$

where the parameter S has been introduced

$$S = \alpha_e L \sqrt{\phi_o} = 1.025\ L\sqrt{\phi_o}$$

$$\phi_o = \frac{\phi_1 + \phi_2}{2} \quad \text{and}$$

$$\alpha = \frac{\phi_1 - \phi_2}{\phi_1 + \phi_2} \quad = \text{asymmetry factor}$$

For zero bias and neglecting high powers in α we get the resistance and responsivity of the diode

$$a\,(\mu m^2)\cdot R_D\,(ohms) = \frac{S\,e^S}{324\,\phi_o} = \frac{1}{G\,(ohm^{-1}\cdot\mu m^{-2})}$$

$$m = \frac{\alpha S}{24\phi_o} \quad \text{and}$$

$$n = \frac{1}{6}\left(\frac{S}{4\phi_o}\right)^2$$

APPENDIX B

We shall estimate the efficiency with which power focused from an infrared laser can be coupled to the antenna/diode. Using the reciprocity theorem of antenna theory and considering the antenna as a radiator, we will calculate the fraction, γ, of power radiated under the same solid angle, Ω_o, with which the infrared radiation is focused. The efficiency is

$$\gamma = \frac{1}{4\pi} \int_{\Omega_o} G(\theta, \phi)\, d\Omega$$

where $G(\theta,\phi)$ is the orientation-dependent antenna gain. It is assumed that the load is matched to the antenna. By definition of gain if Ω_o is taken as 4π steradians, then $\gamma = 1$ (all power delivered to antenna is radiated). In the case of a whisker diode, long wire antenna theory applies.[7,8] The gain in the case of a standing wave antenna is[25]

$$G = \frac{30}{R_A \sin^2\theta} \{\cos^2 kL + \cos^2\theta \sin^2 kL + 1 - 2\cos kL \cos(kL\cos\theta) - 2\cos\theta \sin kL \sin(kL\cos\theta)\}$$

where L is the whisker length.

This radiation pattern has a main lobe at a small angle from the antenna. The first null is at: $\theta_\ell = \sqrt{\frac{2\lambda}{L}}$

118

For long antennas ($L >> \lambda$) it can be shown that the maximum gain can be approximated by $G_m \simeq \frac{120}{R_A} \frac{L}{\lambda}$ so that the coupling efficiency when the focusing angle θ_f is comparable with θ_e is $\gamma \simeq \frac{30}{R_A} \frac{1}{\pi}$

For a typical $R_A = 150\,\Omega$ we would get $\gamma = .06$

In principle it is possible to use phased arrays in the same context that it is done in microwaves. A horn antenna or an end-fire phased array would provide coupling efficiencies close to unity.

REFERENCES

1. L.O. Hocker, A. Javan, Phys. Letters 26A, 255 (1968).
2. V. Daneu, D. Sokoloff, A. Sanchez, A. Javan, Appl. Phys. Letts. 15, 398 (1969).
3. D. Sokoloff, A. Sanchez, R.M. Osgood, A. Javan, Appl. Phys. Letts. 17, 257 (1970).
4. K.M. Evenson, J.S. Wells, F.R. Peterson, B.L. Davidson, and G.W. Day, Appl. Phys. Letts. 22, 192 (1973).
5. D.A. Jennings, F.R. Peterson, K.M. Evenson, Appl. Phys. Letts. 26, 510 (1975).
6. A. Sanchez, S.K. Singh, A. Javan, Appl. Phys. Letts. 21, 240 (1972).
7. L. Matarrese, K.M. Evenson, Appl. Phys. Letts. 17, 8 (1970).
8. Bor-long Twu and S. E. Schwarz, Appl. Phys. Letts. 26, 672 (1975).
9. S.J. Green, J. Appl. Phys. 42, 1166 (1971).
10. S.P. Kwok, G.J. Haddad and G. Lobov, J. Appl. Phys. 42, 544 (1971).
11. S.M. Faris, T.K. Gustafson and J.C. Wiesner, IEEE J. Quantum Electronics 7, 737 (1973).
12. C.C. Bradley and G.J. Edwards, IEEE J. Quantum Electronics 7, 548 (1973).
13. E. Sakuma and K.M. Evenson, IEEE J. Quantum Electronics 8, 599 (1974).
14. J.D. Kraus, Antennas, New York: McGraw Hill (1966).
15. R. Stratton, J. Phys. Chem. Solids 23, 1177 (1962).

120

16. J. Small, G.M. Elchinger, A. Javan, A. Sanchez, F.J. Bachner, D.L. Smythe, Appl. Phys. Letters 24, 275 (1974).

17. S.Y. Wang, T. Izawa and T.K. Gustafson, Appl. Phys. Letters 27, 481 (1975).

18. J.R. Tucker, private communication.

19. W. Gandrud, R. Abrams, Appl. Phys. Letters 17, 150 (1970).

20. Bor-long Twu, S.E. Schwarz, Appl. Phys. Letters 25, 595 (1974).

21. J.G. Simmons, J. Appl. Phys. 34, 1793 (1963).

22. T.E. Hartman, J. Appl. Phys. 35, 3283 (1964).

23. Shyh Wang, Appl. Phys. Letters 28, 303 (1976).

24. G. M. Elchinger, A. Sanchez, C. F. Davis, Jr., and A. Javan, J. Appl. Phys. 47, 591 (1976).

25. P. S. Carter, C. W. Hansell, and N. E. Lindenblad, Proc. IRE 19, 1773 (1931).

121

FIGURE CAPTIONS

Figure 1. Equivalent circuit model of the antenna/diode.

Figure 2. Rectified voltage as a function of the diode resistance, $R_D = xR_A$, at frequencies from below ($q<1$) to well above ($q>1$) roll off. The voltage, v_o, is proportional to the incident power, P, and is given by $v_o = 4\beta_i R_A P$.

Figure 3. Several quantities are plotted as a function of the reduced frequency, q. The value x_o is the reduced resistance that optimizes the power conversion. This conversion efficiency is given by η_ϵ/P in Eq. (10). The optimum detectivity, D, is given by Eq. (19). Finally, $F(x_o)$ is given by Eq. (11) appears frequently in the text.

Figure 4. As the operating frequency of the diode increases the junction area, a, and oxide thickness, L, have to be decreased in order to optimize the detectivity of the diode. The resulting current responsivity, β_i, decreases logarithmically.

Figure 5. The detectivity, D, for a junction area of 1 μm^2, is plotted as a function of dielectric thickness, L. The calculation is done on a computer using Eq. (18). It is noticed that for each frequency there is a value of the thickness, L, that optimizes D. In addition, it is seen that as the frequency increases beyond 3×10^{11} Hz, roll off effects are noticeable.

122<

Figure 6. The maxima of the family of curves displayed in Fig. 5 shows how the optimum value of the detectivity depends on the frequency. In this manner we obtain the curve labeled above as a = 1 μm^2 (the area for which Fig. 5 was calculated). Curves for other junction areas are similarly obtained. The optimum thickness at the corner frequencies are displayed above the curves.

Figure 7. Block diagram of the equipment used for establishing an rf level that gives equivalent response to an incident focused laser beam for various measured diode resistances. An adjustable amount of 400 kHz signal is coupled when the chopper blade blocks the laser. The lock-in is nulled by adjusting the amplitude of the rf, which is then measured.

Figure 8. Antenna/diode efficiency is plotted as a function of the diode resistance. The curve was fitted to the data by varying R_A; best fit is 162 Ω. Whisker length is 1.95 mm = 5.8 λ, λ = 337 μm.

Figure 9. The radiation pattern is given for the antenna used in the measurement of Fig. 8. In this case, the pattern for 311 μm is also given.

Figure 10. The antenna/diode efficiency is plotted as a function of iris diameter, D, for = 12.7 cm. It should be noted that saturation at high values of D comes from a combination of approaching the beam diameter and exceeding the width of the first lobe. The proportionality constant, .0035 coincides with the theoretical prediction. However, the experimental value contains an uncertainty of a factor of about two due to power measurements.

123

Fig. 11. The experimentally determined dependence of V_r on V_b is presented. Diode resistance was measured as 2 KΩ and values of m = .16 V^{-1} and n = 1.81 V^{-2} were calculated from this plot.

124<

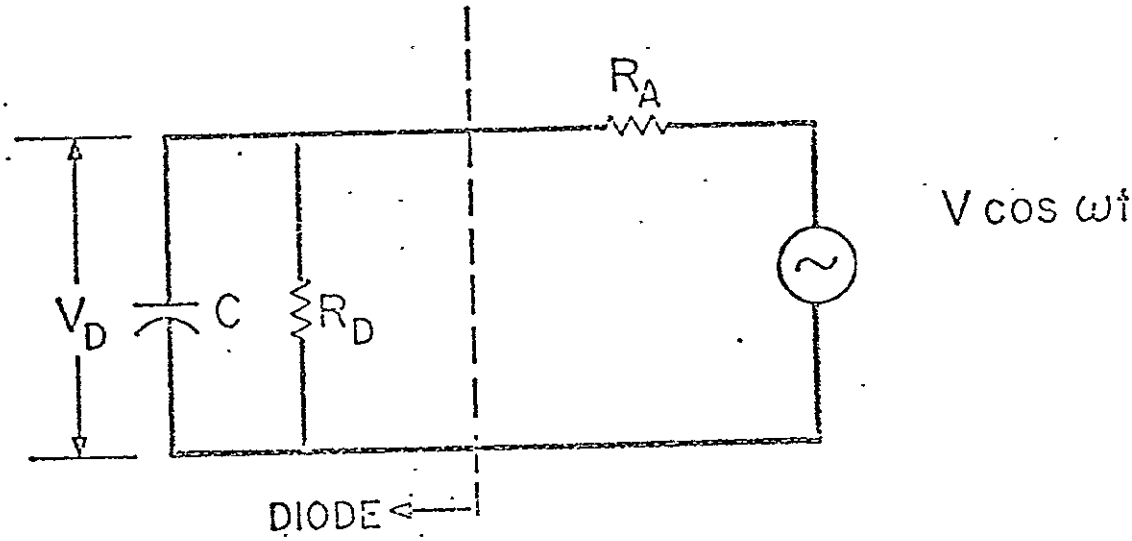

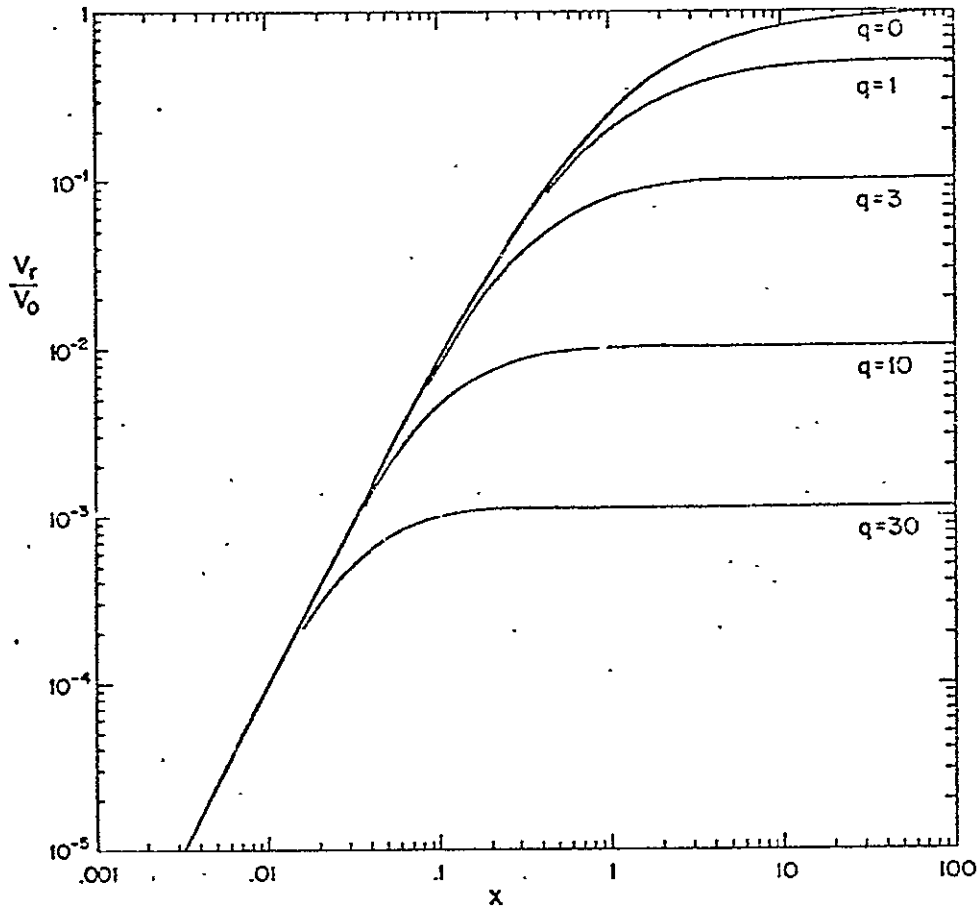

Fig 2 126<

$\eta_e/P(W^{-1})$
$D(W^{-1}Hz^{\frac{1}{2}})$
$F(x_0)$
10^{10}
10^9
10^8
10^7
10^6
.1
.01
.001
.0001
.00001
0
10
1
.1
.01
.001
D
$F(x_0)$
x_0
η_e/P
η_e/P
$F(x_0)$
x_0
D
.01
.1
1
10
100
1000
q
ORIGINAL PAGE IS
OF POOR QUALITY

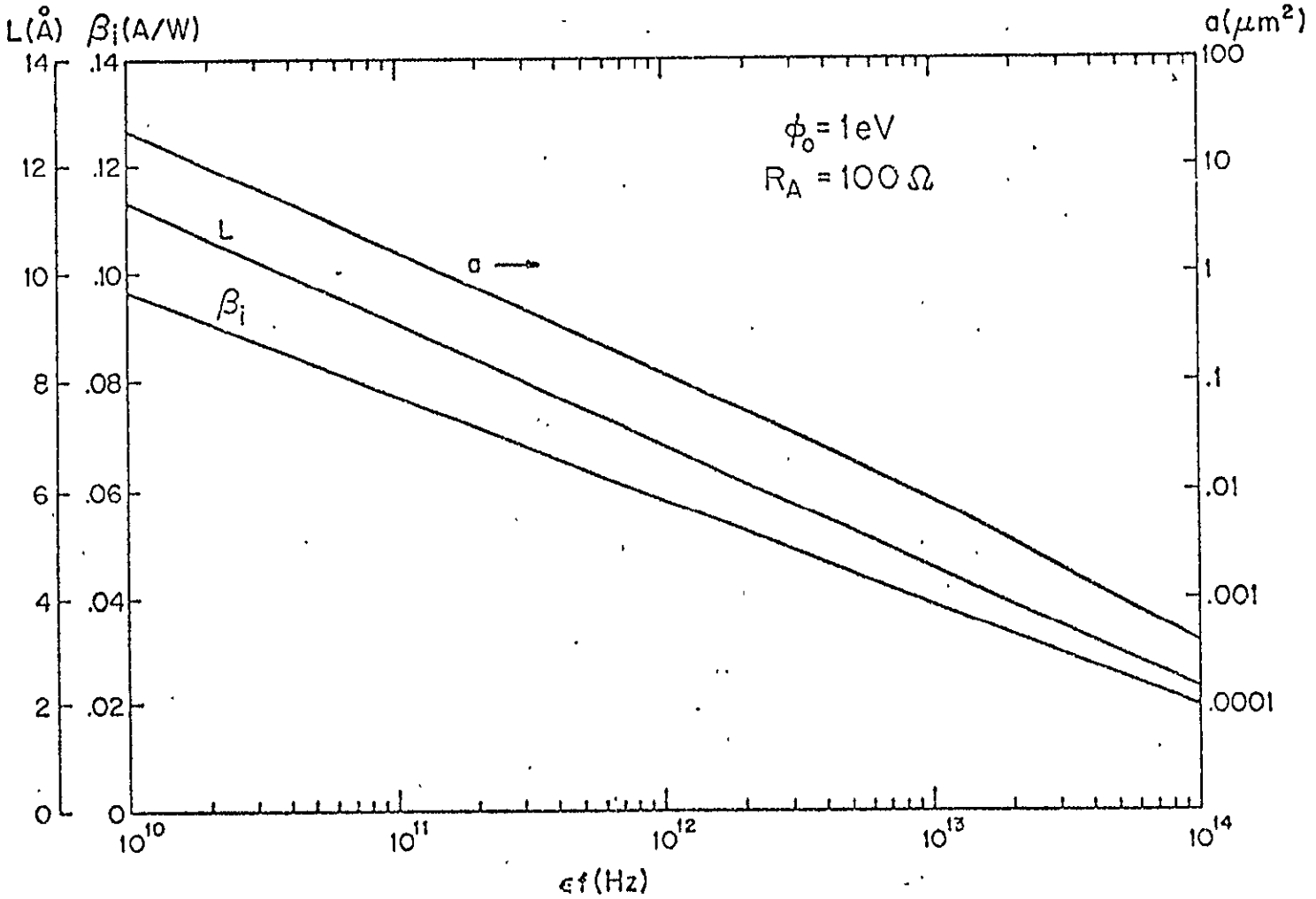
L(Å)
β_i(A/W)
a(μm^2)
ϕ_o = 1eV
R_A = 100 Ω
L
β_i
a
ef(Hz)
14
12
10
8
6
4
2
0
.14
.12
.10
.08
.06
.04
.02
0
100
10
1
.1
.01
.001
.0001
10^{10}
10^{11}
10^{12}
10^{13}
10^{14}

Fig. 7

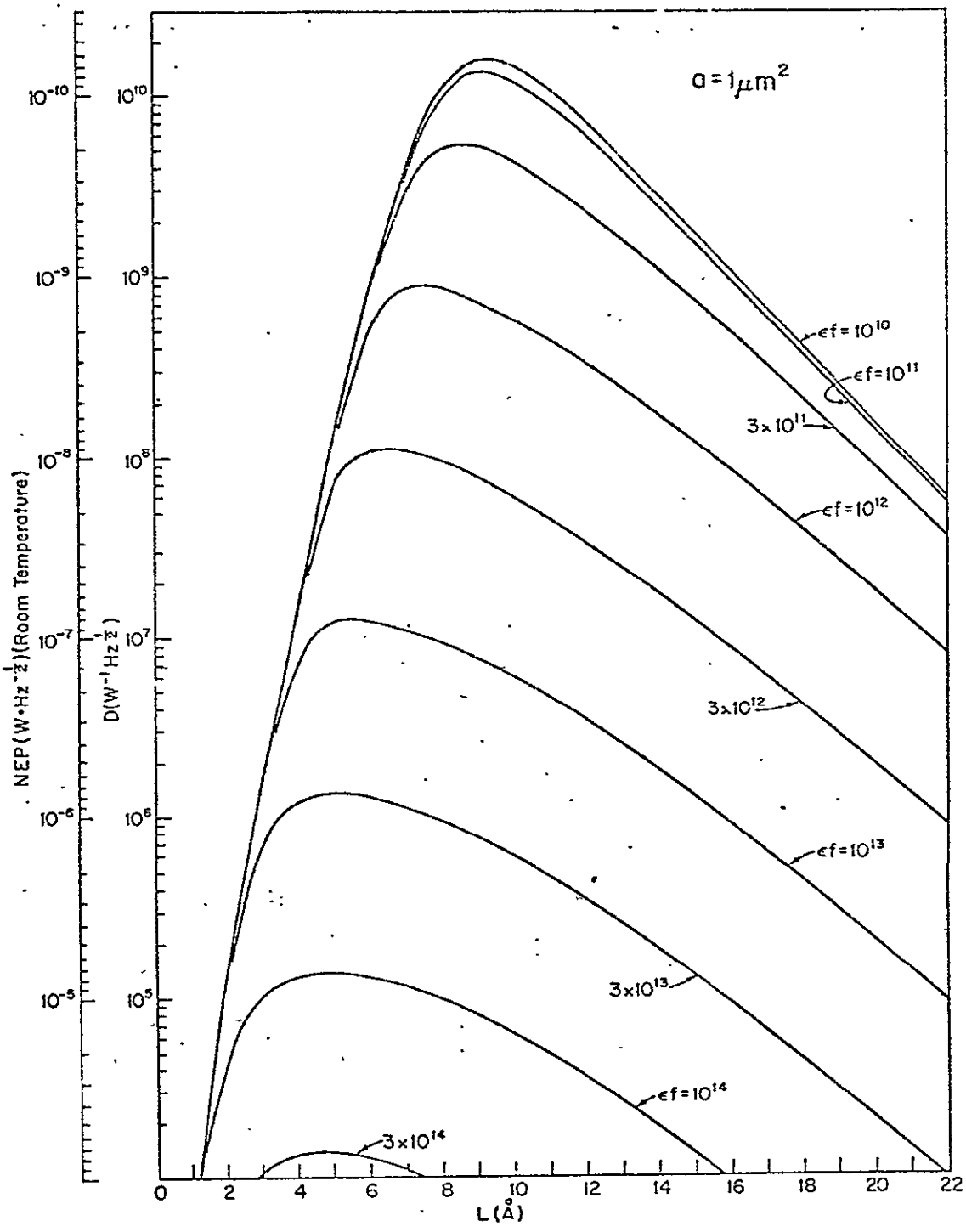

Fig 5

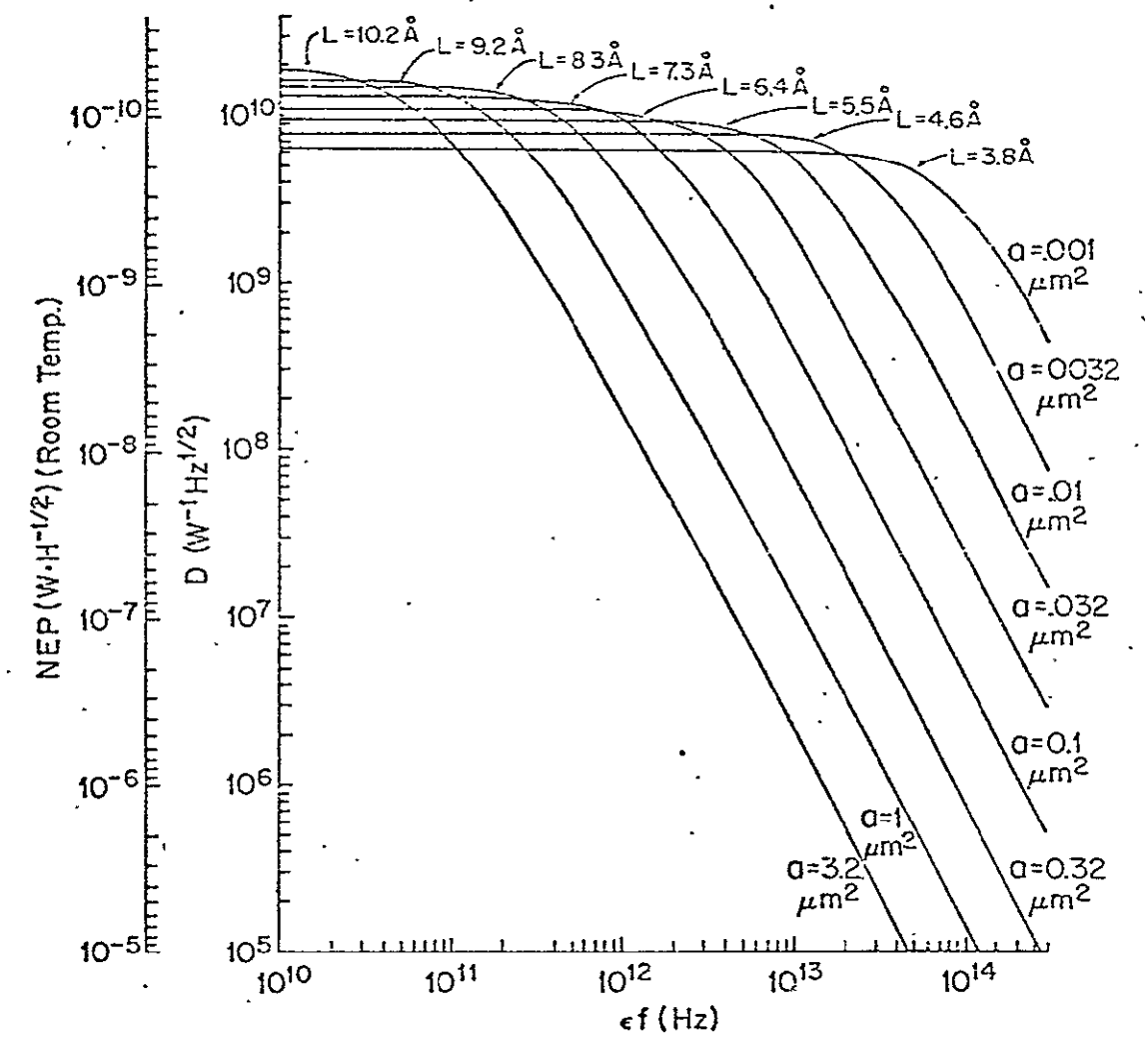
L=10.2Å
L=9.2Å
L=8.3Å
L=7.3Å
L=6.4Å
L=5.5Å
L=4.6Å
L=3.8Å
a=.001 μm²
a=0032 μm²
a=.01 μm²
a=.032 μm²
a=0.1 μm²
a=0.32 μm²
a=1 μm²
a=3.2 μm²
NEP (W·H^-1/2) (Room Temp.)
D (W^-1 Hz^1/2)
10^-10
10^-9
10^-8
10^-7
10^-6
10^-5
10^10
10^9
10^8
10^7
10^6
10^5
10^10
10^11
10^12
10^13
10^14
ef (Hz)

Fig 6

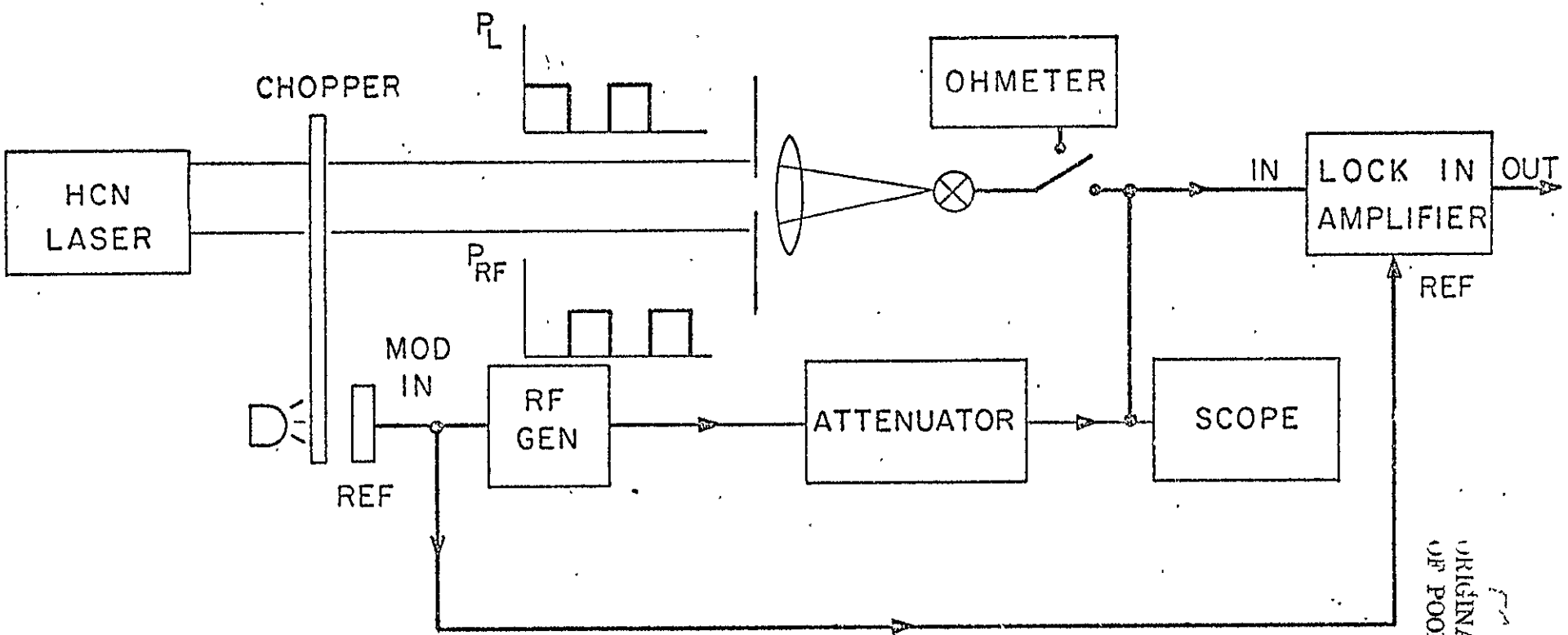

Fig 7

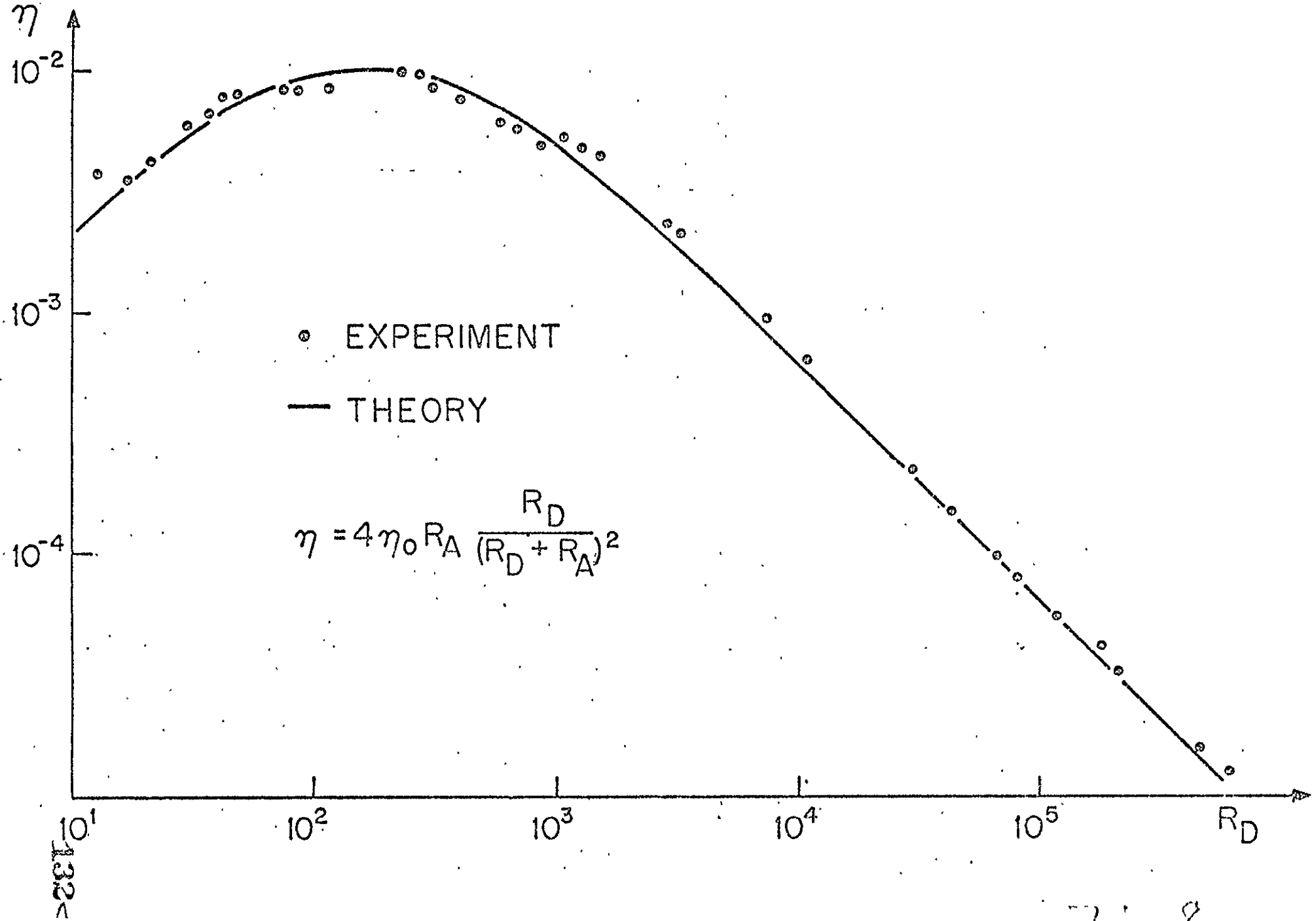
η
10^-2
10^-3
10^-4
EXPERIMENT
THEORY
η = 4 η0 RA (RD / (RD + RA))^2
10^1
10^2
10^3
10^4
10^5
RD
~23 Ω

Fig 8

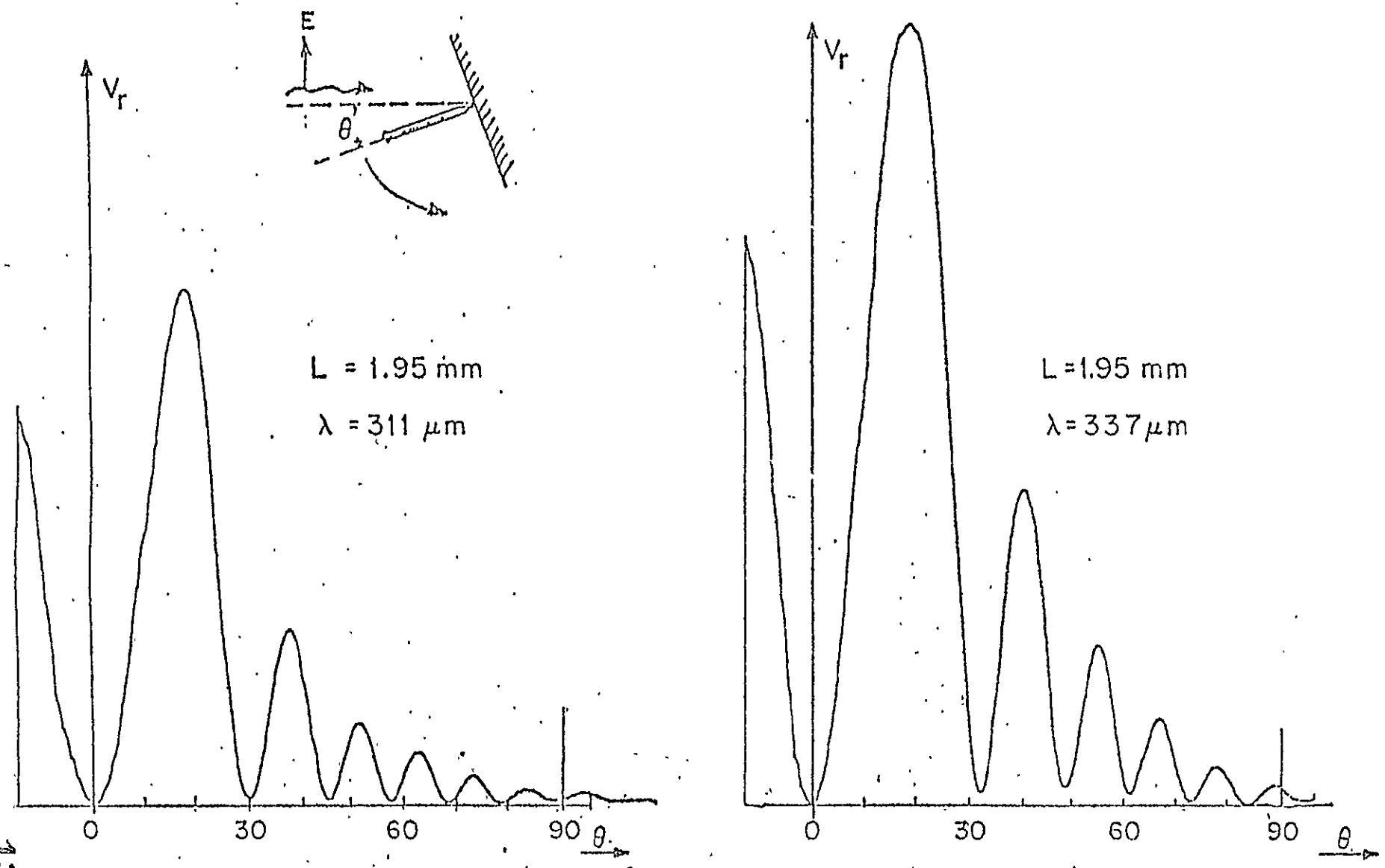

Fig 9

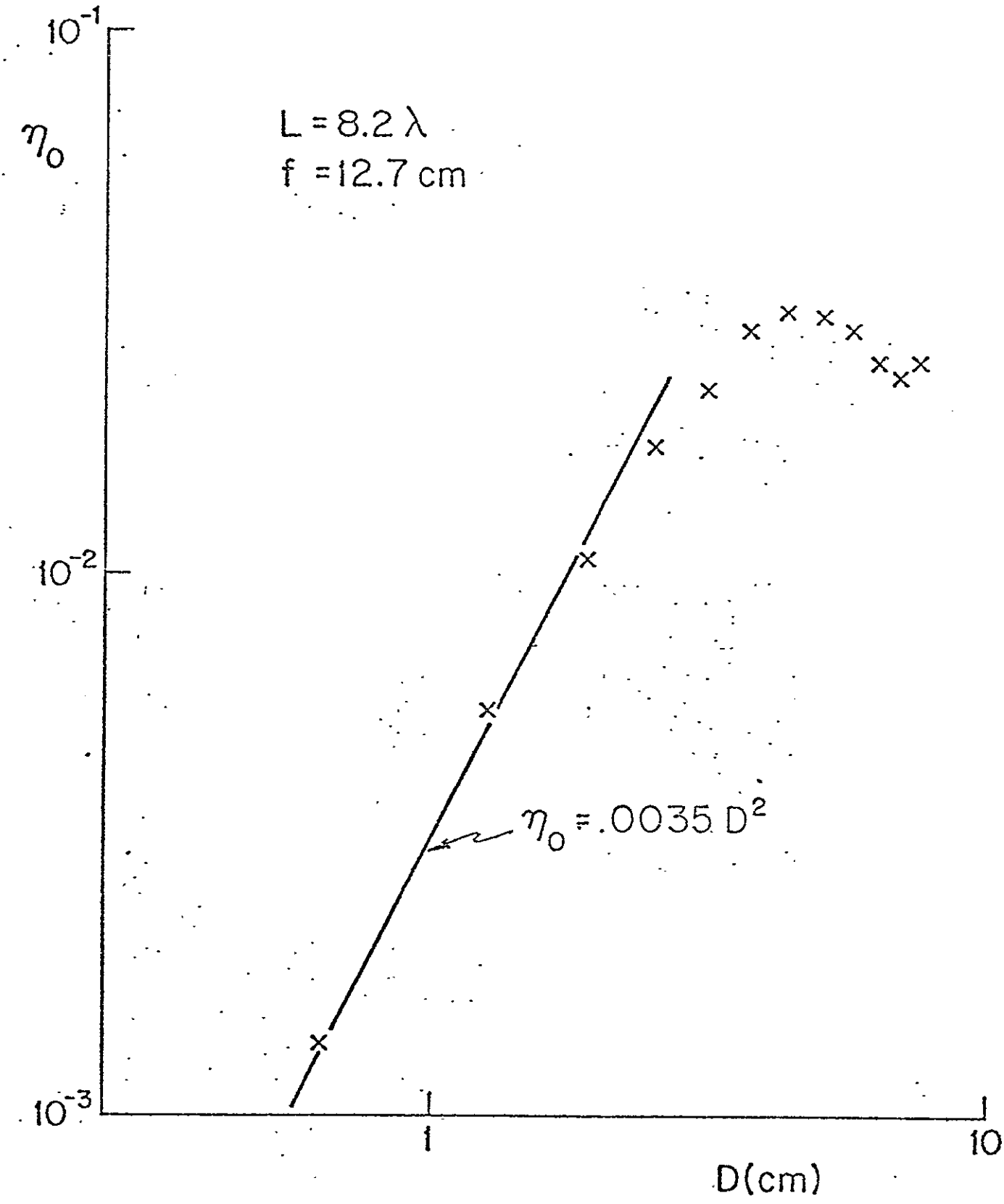

Fig 10

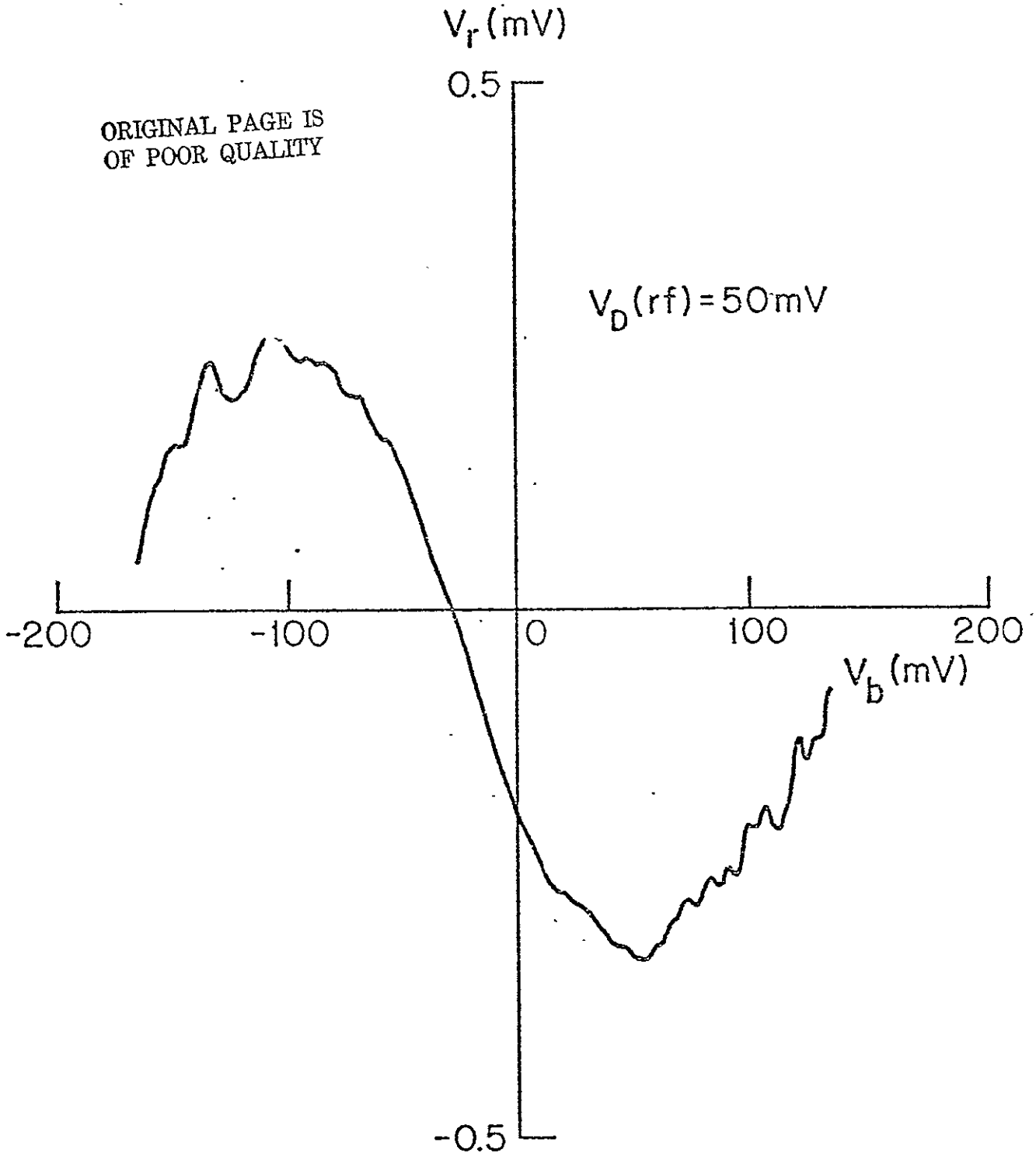

Fig 11

8. T. W. Ducas, L. D. Geoffrion, R. M. Osgood,Jr, and A. Javan

Observation of Laser Oscillation in Pure Rotational Transitions of OH and OD Free Radicals

Published in Appl. Phys. Letters

OBSERVATION OF LASER OSCILLATION IN PURE ROTATIONAL TRANSITIONS OF OH AND OD FREE RADICALS*

T. W. Ducas, L. D. Geoffrion[+], R. M. Osgood, Jr.[‡], and A. Javan

Massachusetts Institute of Technology
Cambridge, Massachusetts 02139

Department of Physics

(Published in Appl. Phys. Letters)

* Research supported by Air Force Cambridge Research Laboratories, Office of Naval Research and National Aeronautics and Space Administration.

+ Preliminary work on this experiment is described in a dissertation presented by L.D.G. to Massachusetts Institute of Technology in partial fulfillment of the requirements for the degree of Master of Science in Physics. Present address: Department of Psychology, Johns Hopkins University, Baltimore, Maryland.

‡ Hertz Foundation Predoctoral Fellow.

ABSTRACT

The first observation is reported of laser oscillation in pure rotational transitions of the OH and OD free radicals. Forty-four lines in OH and seventeen lines in OD have been seen in the 12 to 20 μ region. Transitions were observed within the v=0, 1, 2 vibrational levels of OH and the v=0 vibrational level of OD. Accurate values are calculated for the B and D rotational constants for OD and higher order rotational constants for OH.

Observation of Laser Oscillation in Pure Rotational Transitions of OH and OD Free Radicals

We report the first observation of laser oscillation in pure rotational transitions of the OH and OD free radicals. Forty-four lines in OH and seventeen lines in OD have been seen in the 12 to 20 μ region. Transitions were observed within the v=0,1,2 vibrational levels of OH and the v=0 vibrational level of OD[1]. These levels all belong the the $^2\Pi$ electronic ground state. In this state Λ=1, where Λ is the projection along the internuclear axis of the orbital angular momentum of the unpaired electron.

These pure rotational lasers are of special interest because of the structure of the OH and OD rotational spectra. Each rotational level is actually a doublet due to the interaction of electron spin and the angular momentum of the molecule. Each element of a doublet is split again by the interaction of molecular rotation and electron angular momentum -- Λ doubling[2].

The experimental apparatus consisted of a pulsed discharge tube through which SF_6, H_2, and O_2 were flowed. The pulses originated from a .1 microfarad capacitor bank charged to ∿15 kilovolts. The current pulse was ∿2 μsec wide, and the repetition rate ranged from one to five per second. An internal mirror configuration was used with a cavity 1.5 meters long and a tube diameter of 5 centimeters. The optical arrangement was near confocal using two 4.25 meter radius of curvature mirrors with a 2 millimeter hole in one mirror for output coupling.

The partial pressures of the gases for maximum laser power

were typically 4 Torr SF_6, 2 Torr H_2 and 6 Torr O_2. This held true for bright arc discharges (14-16 kilovolt region) and glow discharges (12-14 kilovolt region) -- both of which produced laser oscillation. It was found that, in particular, the SF_6 and H_2 pressures were critical for laser oscillation.

Laser oscillation was also observed when a transverse discharge tube[3] was placed in the cavity. In this case the dependence on the H_2 and SF_6 pressure was far less critical. When CO_2 was substituted for SF_6, oscillation still occurred in this configuration. This indicates that SF_6 and CO_2 primarily play a role in conditioning the discharge for optimum production of excited OH or OD. The mechanism for this process is most likely a chemical reaction which is as yet undetermined.

Spectral studies of the laser output were performed using a Spex 1400-11 double monochromator. The accuracy of the wavelength measurements of laser lines was better than 1 part in 20,000 for all but the weakest of lines. For these lines the accuracy is better than 1 part in 3000.

Before discussing the measured laser lines, it is useful to describe the rotational structure of OH and OD in more detail (see Figure 1). For clarity, each rotational level is labeled by K, the total orbital angular momentum, $\vec{K} = \vec{\Lambda} + \vec{O}$ where $\vec{\Lambda}$ is defined above, and $\vec{O}$ is the rotational angular momentum of the molecule. The energies of the sublevels corresponding to a given K are designated by F(K). The interaction of electron spin and orbital angular momentum ($\Delta H = A\vec{\Lambda} \cdot \vec{S}$) splits each rotational level into a doublet. In OH and OD the spin-splitting constant, A, is negative, yielding an "inverted" structure where the $J = K - 1/2$ sublevel (energies F(K) with subscript 2)

lies higher than the J=K + 1/2 sublevel (energies F(K) with subscript 1). Each J sublevel is split into a doublet (Λ doubling) by the interaction of molecular rotation and electron angular momentum. The higher components of lambda doublets are labeled with primes (energies $F_1'(K)$ and $F_2'(K)$). Selection rules allow transitions only between similarly labeled sublevels in adjacent rotational levels. [That is, there is no change in spin or in the projection of electron orbital angular momentum onto $\vec{0}$]. Thus, for each pair of rotational levels there is only the quartet of R laser lines as indicated in Figure 1.

The observed laser lines in OH and OD are shown in Tables I and II respectively. The splitting of each rotational level into the four closely spaced levels was manifested in the quartet grouping of laser lines. These quartets were seen for v=0 and v=1 in OH, and v=0 in OD. In OH, lines were observed from R(14) to R(24) with a gap at K=16 and 17.[4] Oscillation occurred simultaneously for all the laser lines observed.

Molecular rotational parameters can be extracted from these observed laser frequencies in a straightforward manner -- without the necessity of detailed analysis of spin-splitting and Λ-doubling[5]. This can be done by noting that the rotational energies E_J are given by:

$$(1) \qquad E_J = \frac{F_2'(J) + F_2(J) + F_1'(J) + F_1(J)}{4}$$

which eliminates the need to know the fine structure of the rotational levels.

The difference between successive rotational energies is:

$$(2) \qquad E_J - E_{J-1} = 2B_{eff}J - 4D_{eff}J^3 + H(6J^5+2J^3) - 8P(J^7+J^5)$$

where B_{eff} is essentially the rotational constant B; D_{eff} represents the influence of centrifugal force; and H and P are higher order terms for the vibrating rotor[5].

Figure 1 has been drawn showing the splittings as sublevels of rotational levels labeled by K. Note that $F_2(K+1)$ and $F_2'(K+1)$ correspond to F_2 and F_2' of J = K+1/2. Also, $F_1(K)$ and $F_1'(K)$ correspond to F_1 and F_1' of the same J. We can combine these facts with Eqs. (1) and (2) to write $E_J - E_{J-1}$ in terms of the laser lines, R(K).

$$(3) \qquad E_J - E_{J-1} = \frac{R_2'(J-1/2) + R_2(J-1/2) + R_1'(J-3/2) + R_1(J-3/2)}{4}$$

For OD, the previous spectroscopic studies[6-9] have been in the ultraviolet region. Our measurements of rotational splittings were more precise than those of the u.v. experiments. This enabled us to arrive at an improved value for D because of the high J's of our laser lines (see Table III).

In OH, previous measurements[10] have also been made in the u.v. region. This work was both more accurate and more extensive than the u.v. data for OD. The accuracy of the measurements reported in Ref. 10 for rotational splittings was lower than that of our measurements, but their wide range of measured lines made it possible to obtain good values for the rotational constants -- especially B and D[5]. The constants derived from their data [Ref. (5)] fit our data quite well. However, we can obtain improved values for the higher order constants by employing the data from Ref. 10 to give the lower order parameters, and the accurate high-J data from the present experiment to obtain the H and P values. In this way, H and P were derived

for v=0, and P was derived for v=1 in OH. (See Table III.)

An interesting insight into collisional coupling comes from noting the relative amplitudes of the lines within a quartet. Those lines originating from levels which are strongly coupled via collision effects can "compete" with each other. In such a situation the lines with higher gain rob energy from those with lower gain and thus have much greater intensity. In OH and OD, competition occurs between the pair of laser lines arising from within each Λ doublet [$R_1(K)$, $R_1'(K)$ and $R_2(K)$, $R_2'(K)$]. $R_1(K)$ and $R_2(K)$ having the higher gain, are usually the more intense lines. However, when lines originate from states of different spin, no competition takes place since collisional coupling is weak between such states. Thus, $R_1(K)$ and $R_2(K)$ generally have comparable amplitudes.

We have been able to resolve completely the spin splittings and Λ-doubling in OH and OD. Analysis of these splittings and their J dependence in the intermediate coupling region of our data is now in progress. In addition, we are investigating the coupling characteristics by introducing a grating into the laser cavity, to prevent competition between laser lines.

Knowledge of the detailed rotational structure of the OH radical is important to studies of the upper atmosphere, as well as to future astrophysical applications. Pure rotational lasers in OH and OD provide the basis for analysis of this detailed structure.

We would like to thank L. W. Ryan, Jr. for his expert technical assistance.

REFERENCES

1. Several vibration-rotation laser lines in the 3μ region have been observed in the OH free radical. See: A. B. Callear and H. E. Van Den Bergh, Chem. Phys. Letters 8, 17 (1971).

2. G. Herzberg, Molecular Spectra and Molecular Structure, I. Spectra of Diatomic Molecules, 2nd ed. (Van Nostrand, New York, 1950).

3. See for example: A. J. Beaulieu, Appl. Phys. Letters 16, 504 (1970). The transverse discharge "pin" laser tube used in our experiment had an active length of 24 inches.

4. Small traces of water vapor could account for this gap, since water vapor absorbs strongly in this region.

5. See a recent analysis of OH by M. Mizushima, Phys. Rev. A, 5, 143 (1972).

6. M. Ishaq and C. A. Fowler, Proceedings of the Royal Society (London) 159, 110 (1939).

7. M. G. Sastry and K. R. Rao, India Jour. Phys. 15, 27 (1941).

8. H. Oura and M. Ninomiya, Proceedings Phys. Math. Soc. Japan 25, 335 (1943).

9. M. Ishaq, India Jour. Phys. 18, 52 (1944).

10. G. H. Dieke and H. M. Crosswhite, J. Quant. Spectry. Radiative Transfer 2, 97 (1962).

Table I

OH ROTATIONAL LINES

Assignment V	Assignment R(K)	$\nu(cm^{-1})$ Observed	Intensity Arbitrary Units
1	$R_2(14)$	508.91	15.
1	$R_2'(14)$	509.70	1.4
1	$R_1(14)$	510.37	16.
1	$R_1'(14)$	511.32	1.0
2	$R_2(15)$	517.56	2.0
2	$R_1(15)$	518.86	2.1
0	$R_2(14)$	529.72	2.
0	$R_2'(14)$	530.54	3.8
0	$R_1(14)$	531.12	10.
0	$R_1'(14)$	532.26	4.
1	$R_2(15)$	539.62	3.
1	$R_2'(15)$	540.49	.5
1	$R_1(15)$	540.77	7.
1	$R_1'(15)$	541.85	1.5
0	$R_2(18)$	653.04	81.
0	$R_1(18)$	653.86	85.
0	$R_2'(18)$	654.07	8.4
1	$R_2(19)$	654.69	14.1
1	$R_1(19)$	655.48	19.6
1	$R_2(20)$	681.70	42.
0	$R_2(19)$	682.04	97.
1	$R_1(20)$	682.35	5.7
0	$R_1(19)$	682.78	55.
0	$R_2'(19)$	683.07	28.
0	$R_1'(19)$	683.99	112.
1	$R_2(21)$	707.76	98.
1	$R_1(21)$	708.32	141.
0	$R_2(20)$	710.20	325.
0	$R_1(20)$	710.88	337.
0	$R_2'(20)$	711.30	80.
0	$R_1'(20)$	712.08	84.
1	$R_2(22)$	733.04	10.7
1	$R_1(22)$	733.55	15.4
0	$R_2(21)$	737.64	224.
0	$R_1(21)$	738.19	140.
0	$R_2'(21)$	738.68	14.0
0	$R_1'(21)$	739.37	8.4
0	$R_2(22)$	764.03	84.
0	$R_1(22)$	764.59	84.
0	$R_2'(22)$	764.91	.5

[Printer Note: table continued on next page]

0	$R_2(23)$	789.72	14.0
0	$R_1(23)$	790.14	22.4
0	$R_2(24)$	814.43	8.0
0	$R_1(24)$	814.79	14.0

Table II

OD ROTATIONAL LINES

Assignment R(K)	$\nu(cm^{-1})$ Observed	Intensity Arbitrary Units
V = 0		
$R_2(26)$	492.29	2.5
$R_2'(26)$	492.71	.5
$R_1(26)$	492.90	3.0
$R_1'(26)$	493.32	.25
$R_2(27)$	507.52	3.0
$R_2'(27)$	507.73	.5
$R_1(27)$	508.10	4.5
$R_1'(27)$	508.60	1.0
$R_2(28)$	521.88	.5
$R_2'(28)$	522.44	3.5
$R_1(28)$	522.99	2.5
$R_1'(28)$	523.50	.5
$R_2(29)$	536.94	.75
$R_1(29)$	537.55	4.5
$R_1'(29)$	537.92	.25
$R_2(30)$	551.34	.5
$R_1(30)$	551.84	1.0

Table III. Rotational Constants for OH and OD Free Radicals

OD Constants (cm^{-1})

$B = 9.870 \pm .005$ [b]

$D = (4.98 \pm .31) \times 10^{-4}$ [c]

OH Constants (cm^{-1})

v=0	Values from Ref. 5	Present Work
B_{eff}	18.5315	———
D_{eff}	1.9074×10^{-3}	———
H	$(1.4074 \pm .070) \times 10^{-7}$ [d]	$(1.347 \pm .083) \times 10^{-7}$ [e]
P	$(1.23 \pm .31) \times 10^{-11}$ [d]	$(1.04 \pm .37) \times 10^{-11}$ [e]

v=1	Values from Ref. 5	Present Work
B_{eff}	17.8208	———
D_{eff}	1.8696×10^{-3}	———
H	1.3883×10^{-7}	———
P	$(1.68 \pm 1.28) \times 10^{-11}$ [d]	$(1.65 \pm .44) \times 10^{-11}$ [e]

[a] The calculations of the constants are based on the rotational energy expressions of Ref. 5. Note that these expressions differ from those based on less accurate perturbation theory used in Refs. 6 - 10.

[b] $B = B_{eff} + \beta + 3/2D$ where β is extracted from Λ doublet separations. See Reference 5.

[c] $D = D_{eff} + 3/4H$. See Reference 5.

[d] Errors quoted are $\pm$ one standard deviation for a least squares fit to the data from Ref. 10.

[e] The data from Ref. 10 were used to give the lower order para-

meters and the data from the present experiment were used to obtain H and P for v=0 and P for v=1. Errors quoted are ± one standard deviation.

FIGURE CAPTION

Figure 1. Energy level diagram showing rotational levels and the fine structure due to spin splitting and Λ-doubling. [The diagram is not to scale; R(K) - R(K-1) is ∿50 times greater than the Λ-splitting.]

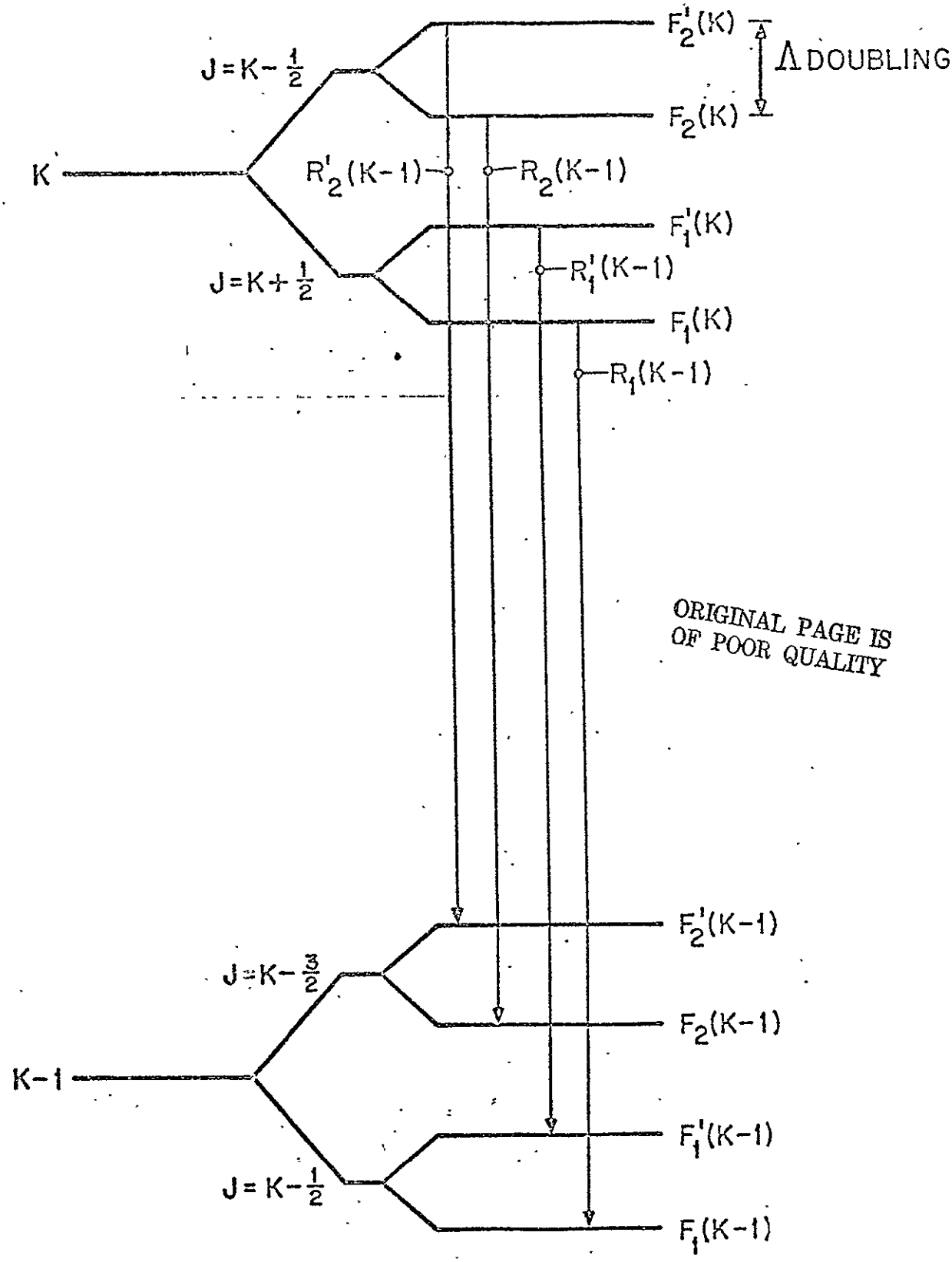

9. H. P. Grieneisen, J. Goldhar, N. A. Kurnit, A. Javan and H. S. Schlossberg

Observation of the Transparency of a Resonant Medium to Zero-Degree Optical Pulses

Published in Appl. Phys. Letters

OBSERVATION OF THE TRANSPARENCY OF A RESONANT MEDIUM TO ZERO-DEGREE OPTICAL PULSES

H.P. Grieneisen[+], J. Goldhar[++], N.A. Kurnit and A. Javan
Department of Physics
Massachusetts Institute of Technology
Cambridge, Mass. 02139

and

H.R. Schlossberg
Air Force Cambridge Research Laboratories
L.G. Hanscom Field
Bedford, Mass. 01730

(Published in Appl. Phys. Letts)

ABSTRACT

Experiments are described in which low intensity laser pulses of zero area ($\int_{-\infty}^{\infty} \mathcal{E}(z,t)dt=0$) are propagated through a degenerate resonantly absorbing medium with greatly reduced absorption. These pulses are constructed either electro-optically or by allowing a nonzero-degree pulse to evolve toward zero area by means of a resonant absorption and reradiation process. We observe the transmission of as much as 65% of the energy of such pulses through a resonant absorber which attenuates the same c.w. laser by $e^{-\alpha L}$, with $\alpha L \approx 20$.

[+] On leave from Universidade Federal do Rio Grande do Sul, Porto Alegre, Brazil. Work done with partial support from Conselho Nacional de Pesquisas, Brazil.

[++] Hertz Foundation Predoctoral Fellow.

The transparency of a resonant absorber to pulses of large "area" $\theta=2n\pi$ (n=1,2...) has been a subject of active experimental[1] and theoretical[2] interest. In an early publication[3] discussing the inhibiting influence of level degeneracy on the transparency of large area pulses, it was noted that zero area pulses can propagate with low loss irrespective of the degeneracy of the resonant transition. Such "zero-degree" pulses result if the pulse envelope undergoes a sign change in such a way that the tipping angle,

$$\theta_m(z,t) = \frac{\mu_m}{h} \int_{-\infty}^{t} \mathcal{E}(z,t)dt$$

goes to zero for $t \to \infty$. Here, $\mathcal{E}(z,t)$ is the envelope of the electric field, $\vec{E} = \hat{\varepsilon}\, \mathcal{E}(z,t)\cos(\omega t-kz)$, and μ_m is the dipole matrix element for the transition involving the m^{th} degenerate sublevel. The area $\theta_m(z,\infty) \equiv \theta_m(z)$ measures the degree of excitation of resonant molecules after passage of the pulse.[4] Recent articles have analyzed additional features of zero-degree pulse propagation.[5-7]

We describe here experiments in which zero-degree pulses have been constructed and propagated through a degenerate resonant absorber with dramatically reduced energy loss. We have also observed the evolution of small area pulses into zero-degree pulses due to a resonant absorption and reradiation process,[7,8] discussed in more detail below. The observations are made in the limit of low pulse intensities corresponding to small tipping angles.

A major requirement for low loss propagation is that the pulse be able to coherently excite and de-excite a molecule in a time short compared to the homogeneous transverse relaxation time, T_2.

For a $2n\pi$ pulse ($n > 1$) the pulse energy must be sufficiently large to induce n complete transitions. Because of this, the required pulse energy (proportional to $1/\tau_{pulse}$) may be excessively large in cases where T_2 is very short. On the other hand, a zero-degree pulse need not induce a complete transition; hence it can propagate with low loss even with small energy.

The latter property is of particular interest for propagation of ultrashort pulses through a homogeneously broadened resonant absorber (for example in the atmosphere). If the absorption line is inhomogeneously broadened, small energy zero-degree pulses will still propagate with low loss provided the pulse envelope changes sign before the molecules can dephase due to the spread in their frequency distribution.[9]

The experimental arrangement is shown in Fig. 1(a). A c.w. laser with an internal mirror and diffraction grating line selector is operated on single P or R branch transitions of CO_2 or N_2O in the 10μ region. The linearly polarized output of the laser is passed through a GaAs electro-optic modulator crystal with its $\vec{E}$ field oriented relative to the crystal axes[10] as shown in Fig. 1(b). The crystal is pulsed with a 5 kV/cm square pulse derived from a pressurized spark gap and RG8/U coaxial cable pulse-forming network. The rise and fall time of the pulse is less than 0.3 nsec and the duration can be varied by changing the length of the charging cable [C in Fig. 1(a)]. In the experiments reported here, pulses of 2 or 6 nsec duration were used. The pulse is propagated over the crystal, which is matched to 50Ω by adjusting the capacitance of the crystal holder.

The voltage pulse can be applied to the crystal a second time with the same or opposite polarity by allowing it to reflect from the end of an open or shorted 50Ω cable [R in Fig. 1(a)] which terminates the crystal. Single pulses are obtained by terminating the cable with a 50Ω resistor. For an incident field $E_o \sin(\omega t - kz)$ polarized as shown, the output in the perpendicular polarization, which is selected by analyzer A, is given by $E_o \cos(\omega t - kz) \sin\Gamma$, where $\Gamma = \pi n_o^3 r_{41} V\ell/\lambda d \approx \pi/8$ is the phase advance or retardation (determined by the sign of the electric field strength V/d) along axes a or b [Fig. 1(b)].[11]

The transparency effect was observed in CO_2, using a 1.5 m heated gas cell, as well as in NH_3. The ν_2[asQ(8,7)] transition of $^{14}NH_3$ is coincident to within 10 MHz of the P(13) 10.6μ N_2O laser line and has a Doppler half-width of 42 MHz.[12,13] The NH_3 absorption coefficient of 0.7 cm^{-1}/torr is considerably larger than in CO_2 and hence allowed detailed studies for many absorption lengths. Figure 2 shows a logarithmic plot of experimental data for the transmission of 0.01 w/cm^2 P(13) 10.6μ N_2O laser pulses through a variable pressure[14] 40 cm NH_3 absorption cell [CI in Fig. 1(a)]. Curve A in Fig. 2(a) shows the transmission of zero-degree pulses with two out-of-phase 2 nsec lobes, which are shorter than $T_2^* = 1/2\pi\Delta\nu \approx 4$ nsec (where $\Delta\nu$ is the Doppler half-width of the absorbing transition). The dashed line shows for comparison the transmission of low intensity c.w. radiation as given by $e^{-\alpha L}$, where α is the linear absorption coefficient and L is the length of the sample cell. At low pressures, the number of absorption lengths, αL, is proportional to pressure since the pressure broadening is small compared to the

Doppler width.[15] The effective absorption coefficient for the zero-degree pulses may be obtained from the logarithmic slope of curve A. By comparison with the c.w. absorption (dashed line), we note that at low pressures the absorption coefficient of the 2 nsec zero-degree pulses is smaller by a factor of more than 25 than the value of 0.7 cm^{-1}/torr. (At pressures above 75μ, corresponding to $\alpha L \approx 2$, the slope in curve A increases slightly indicating an increased absorption; this is believed to be due to a small delay between the two pulses which can result in an interference between the second pulse and the molecular reradiation after the first pulse.)

For a short duration pulse of non-zero area, the absorption coefficient is expected to be smaller than α when its duration is less than T_2^*. In this case, the energy absorbed becomes proportional to the pulse duration rather than the inverse linewidth. For a thin sample ($\alpha L < 1$) this reduction is not as great as for the zero-degree pulse of the same duration. For $\alpha L >> 1$, propagation effects cause the pulse area to evolve toward zero (see below). Curve B in Fig. 2(a) shows the transmission of a pulse of non-zero area consisting of two in-phase 2 nsec pulses. The initial absorption obtained from the slope of this curve is less than the c.w. absorption, but larger by a factor of five than that of the zero-degree pulse. At higher pressures, corresponding to several absorption lengths, this curve begins to flatten out and its slope becomes characteristic of that of a zero-degree pulse.

Similar behavior is seen for 6 nsec zero-degree pulses (curve C) and in-phase pulses (curve D), but these exhibit larger absorption

since the pulse is now longer than T_2^*.

We now turn our attention to the evolution of a non-zero area pulse toward zero. Saturation of the medium is negligible in our experiments since for a pulse of duration τ_p=12 nsec (corresponding to two in-phase 6 nsec pulses), and μ=0.2 Debye,[13] the maximum pulse area is less than 2°. For these small angles, the above results can be quantitatively understood[16] in terms of a linearized theory[7] in which the thin sample absorption is proportional to the overlap of the Fourier spectrum of the pulse with the resonance line. A zero-degree pulse has a Fourier spectrum which is zero on resonance. A similar spectrum, and hence absorption, will also result if a non-zero area pulse whose spectral width is broader than the resonance line is allowed to propagate several absorption lengths. A consideration of linear dispersion shows that the phase relationships of the Fourier components are altered in such a way as to yield a zero-degree pulse.[17] For large tipping angles, the nonlinearity invalidates this analytic description, but we know from the area theorem[1-3] that the pulse area will decay toward zero if it is initially less than π.

The evolution of a small area pulse into a low loss zero-degree pulse can alternately be described in the time domain in the following way:[7,8] As the pulse enters the medium, it excites an oscillating macroscopic polarization which for a resonant absorber is phased so as to radiate a field which adds destructively to the incident field. The polarization continues to radiate after the pulse passes and produces a negatively phased lobe on the trailing edge of $\mathcal{E}(z,t)$. For small absorption ($\alpha z \ll 1$, where z is the penetration depth into

the sample), and in the inhomogeneously broadened limit, the coherent "ringing"[8] of the medium lasts for a time comparable to the inverse spectral width of excited atoms, which is given by the longer of the pulse width τ_p or the inverse inhomogeneous width T_2^*. For a homogeneously broadened line, the coherent ringing time will be given by the transverse relaxation time T_2. In either case, the polarization decays before all of the absorbed energy is coherently reradiated. If $\alpha z > 1$, on the other hand, a sufficiently large fraction of the incident pulse has been absorbed and reradiated into the negative lobe to enable this lobe to extract an appreciable fraction of the absorbed energy. This lobe is further amplified as the pulse propagates so that the pulse area approaches zero with little further loss in pulse energy. Significant pulse reshaping, resulting in the development of a pulse with many lobes, is obtained for $\alpha z >> 1$.[18]

In order to further verify this evolution of small area pulses into zero-degree pulses, a second 40 cm absorption cell (CII) was added in front of the first. With cell CII empty, the transmission of cell CI for 6 nsec and 2 nsec single pulses was measured as a function of pressure and is plotted as the lower curves in Fig. 2(b,c). Cell CII was then filled to pressures corresponding to the absorption marked by the arrows on these curves. The fraction of energy transmitted by CI was again measured as the pressure in CI was varied; the results are plotted on the same graphs. The curve labeled I in each case corresponds to an input pulse which has only partially evolved toward a zero-degree pulse, whereas curve II results from a pulse which has propagated a sufficient number of absorption lengths

to become a good zero-degree pulse. The 6 nsec pulse evolves into one which has an absorption coefficient of only 1/20 that of the c.w.; the 2 nsec into one which has only 1/100. At a pressure of 1 torr, where the c.w. beam is attenuated by $e^{-\alpha L}$ with $\alpha L \approx 20$,[15] 65% of the energy of the 2 nsec pulse which emerges from cell CII is transmitted by cell CI.

It should be noted that at pressures sufficiently high that collision broadening becomes larger than the Doppler width, the dashed curve, which represents the c.w. absorption, becomes parallel to the abscissa. In the pressure region where T_2 becomes shorter than the pulse duration, the absorption for all pulses asymptotically approaches the high pressure limit of the dashed curve. At a fixed pressure, the c.w. absorption maintains a constant logarithmic slope as a function of sample length; the zero area pulse would also exhibit a constant but greatly reduced slope.

The use of short pulses from mode-locked lasers should allow the effects described here to be useful for long distance propagation through absorbers with considerably shorter relaxation times. In the case of atmospheric propagation, for example, typical values for pressure broadening range between 1 and 20 MHz/torr. Pulses 10 to 100 times shorter than those utilized here can be expected to result in low loss propagation.

Other aspects of this work which are still the subject of experimental investigation include the study of these effects in the high intensity limit where the nonlinear effects become important, as well as the off-resonance case, and the observation of the actual pulse envelope distortion.

REFERENCES

1. S. L. McCall and E. L. Hahn, Phys. Rev. Letters 18, 908 (1967); H. M. Gibbs and R. E. Slusher, Phys. Rev. A5, 1634 (1972).

2. S. L. McCall and E. L. Hahn, Phys. Rev. 183, 457 (1969).

3. C. K. Rhodes, A. Szöke and A. Javan, Phys. Rev. Letters 21, 1151 (1968).

4. The effect of level degeneracy on coherent excitation has also been observed in an experiment in which the population change was measured by means of the subsequent fluorescence: see H. P. Grieneisen, N. A. Kurnit and A. Szöke, Optics Communications 3, 259 (1971).

5. F. A. Hopf, C. K. Rhodes, G. L. Lamb, Jr. and M. O. Scully, Phys. Rev. A3, 758 (1971).

6. G. L. Lamb, Jr., Rev. Mod. Phys. 43, 99 (1971). This article also gives a comprehensive review of work in the field of ultrashort pulse propagation.

7. M. D. Crisp, Phys. Rev. A1, 1604 (1970).

8. D. C. Burnham and R. Y. Chiao, Phys. Rev. 188, 667 (1969).

9. Large energy zero-degree pulses of specific shapes, related to 4π pulses, are predicted to propagate with low loss without fulfilling this requirement (see Ref. 5,6). Details of the propagation behavior, such as the pulse reshaping, will be different for these large intensity pulses. Loss of energy from the lower intensity wings of the beam profile may also introduce instabilities.

10. S. Namba, J. Opt. Soc. Am. 51, 76 (1961).

11. The voltage applied to the crystal actually consists of a train

of double pulses separated by the 100 nsec round trip time to the spark gap, since the pulse is again reflected there. Although the effects reported here could be seen with such pulse trains, we present only data taken by using a boxcar integrator with a 30 nsec gate to select the first pair of pulses from the output of the Cu:Ge detector.

12. F. Shimizu, J. Chem. Phys. 52, 3572 (1970); Appl. Phys. Letters 16, 368 (1970).

13. T. Shimizu and T. Oka, Phys. Rev. A2, 1177 (1970).

14. The curves in Fig. 2 were measured as a continuous function of pressure. The points correspond to pressures at which the Pirani pressure gauge was calibrated, by means of a McCleod gauge at pressures above 150 mTorr and by means of the c.w. absorption at lower pressures.

15. The pressure broadening of $\sim$ 25 MHz/torr (see Ref. 12) does not become significant until pressures exceed several hundred mTorr.

16. Cf. Fig. 5 or Ref. 7. A more detailed analysis of these results will be presented elsewhere.

17. It should be noted that regardless of the continuous changes in pulse envelope, the carrier frequency remains unshifted if the laser frequency coincides with the center of a symmetrically shaped absorption line (see Ref. 6,7).

18. This behavior has also been described in terms of the superradiant decay of an N particle system excited by a propagating pulse. See, for example, F. T. Arecchi and E. Courtens, Phys. Rev. A2, 1730 (1970); R. Friedberg and S. R. Hartmann, Physics Letters 37A, 285 (1971).

FIGURE CAPTIONS

Figure 1 (a) Schematic of experimental apparatus. Cell CII is in place only as described in text. The integrated output of the detector (D) is recorded as a function of pressure in cell CI.

(b) Orientation of GaAs modulator.

Figure 2 Transmission of N_2O laser energy through resonant NH_3 absorber as function of pressure. Dashed lines give c.w. absorption.

(a) Transmission through cell CI only for: (A) 2 nsec zero-degree pulses, (B) 2 nsec in-phase pulses, (C) 6 nsec zero-degree pulses, and (D) 6 nsec in-phase pulses.

(b) Transmission of single 6 nsec pulses through cell CI with cell CII filled at fixed pressures to give absorption indicated by arrows on lower curve.

(c) Same as (b), for single 2 nsec pulses.

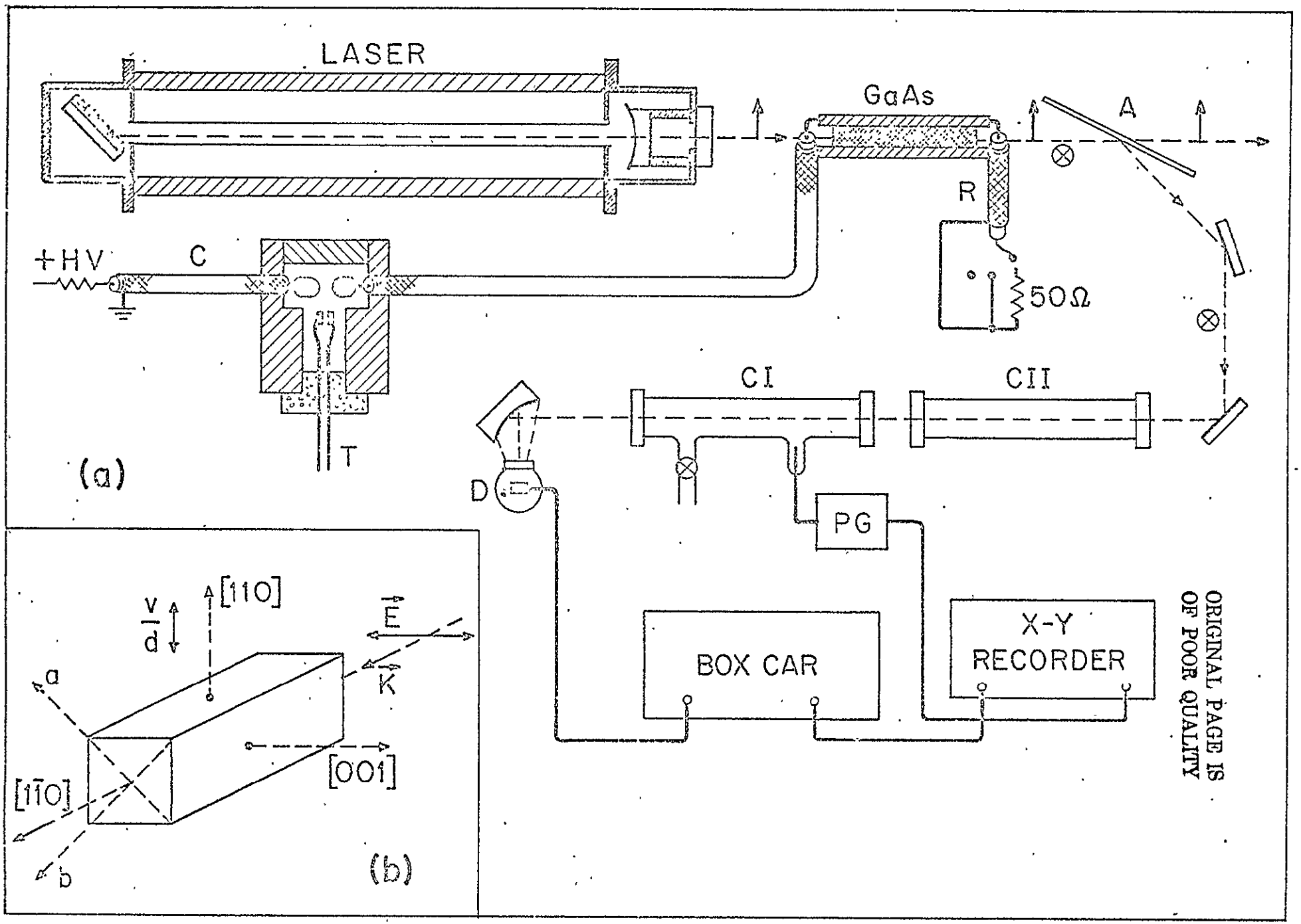
LASER
GaAs
A
R
+HV
C
50Ω
CI
CII
(a)
T
D
PG
BOX CAR
X-Y
RECORDER
ORIGINAL PAGE IS
OF POOR QUALITY
v/d
[110]
E
K
a
[001]
[1$\bar{1}$0]
b
(b)

Fig. 1

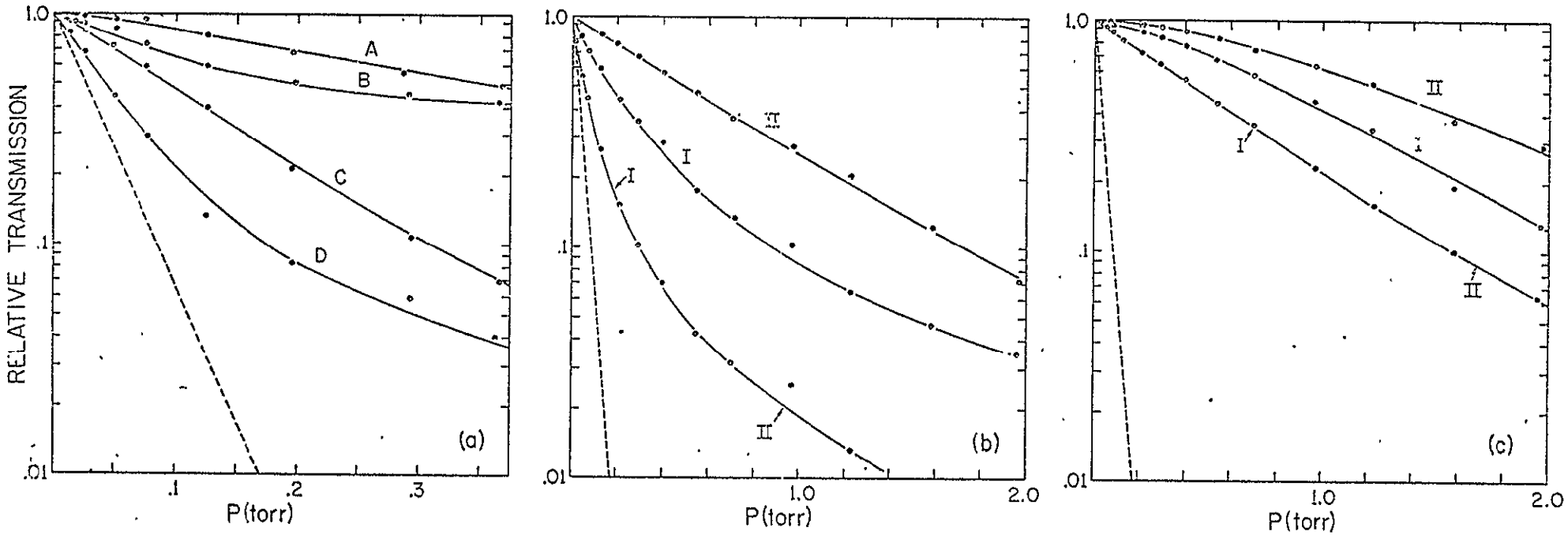

Fig.2

10. N. Skribanowitz, I. P. Herman, R. M. Osgood, Jr., M.S. Feld and A. Javan

Anistropic Ultra-High Gain Emission Observed in Rotational Transitions in Optically Pumped HF Gas

Published in Appl. Phys. Letters

ANISOTROPIC ULTRA-HIGH GAIN EMISSION OBSERVED IN ROTATIONAL TRANSITIONS IN OPTICALLY PUMPED HF GAS

N. Skribanowitz, I. P. Herman, R. M. Osgood, Jr., M. S. Feld and A. Javan

Department of Physics
Massachusetts Institute of Technology
Cambridge, Massachusetts 02139

(Published Appl. Phys. Lett.)

ABSTRACT

Gain and laser oscillations are obtained on rotational transitions of the first excited vibrational state of HF gas at room temperature, resonantly pumped by the 2.7μ lines of a pulsed HF laser. Pumping the P-branch transitions connecting the ground and first excited vibrational states produces gain at the coupled rotational transitions at 36, 42, 51, 84 and 126 μ. The gain exhibits directional properties characteristic of a unidirectional amplifier predicted by a recent theory. The incremental gains of these lines is very large, in excess of 1 per cm, and the lines oscillate easily without mirrors ("superradiance").

This letter reports observation of gain and laser oscillations in rotational transitions of the first excited vibrational state of pure HF gas at room temperature, pumped by the 2.7μ lines of a pulsed HF laser. The gain shows anisotropy characteristic of a unidirectional amplifier predicted by a recent theory[1]. The gain in these lines is enormous and they oscillate easily without mirrors ("superradiance").

Laser oscillations of rotational lines in excited vibrational molecular states have been produced in other gases by optical pumping from the ground vibrational state[2]. The present study also makes use of optical pumping, but the emitted radiation shows unidirectional features not obtained before. These features are caused by the traveling wave pumping of Doppler-broadened transitions. The ultra-high gain of these lines in HF facilitates the observation of the effects.

The HF sample cell was pumped in a single pass by one of the 2.7μ $P_1(J)$ lines of an HF laser, where the notation $P_1(J)$ indicates P-branch transitions connecting the ground and first vibrational states of HF: $(v,J) = (1, J-1) \rightarrow (0,J)$. Gain was observed at the coupled rotational transition $(1,J-1) \rightarrow (1,J-2)$ in the excited vibrational state [Fig. 1(a)]. These transitions fall in the far-infrared (36 - 126μ).

The pump laser was a helical transverse discharge HF "pin" laser using a mixture of SF_6 and H_2[3,4]. The laser cavity consisted of a 2μ diffraction grating and a gold-coated sapphire flat. Individual $P_1(J)$ laser lines could be selected by tuning the grating. Power was coupled out through a 4.5 mm diameter hole in the gold-

coating of the flat. The output pulses typically had a length of one microsecond and a peak power of 3-4 kW as measured with an Epley thermopile.

The absorption cell and the HF gas handling system were made of Monel metal. The cell was 12 cm long with an inner diameter of 12 mm, and had silicon Brewster windows. The windows were coated with a thin layer of Halocarbon standard stopcock grease to prevent degradation due to HF corrosion. Each window had a transmission of approximately 65% in the wavelength range of interest.

The HF gas was purified several times by freezing it at liquid nitrogen temperature and then pumping on it with a diffusion pump. To eliminate water vapor contamination the HF was kept in a Monel cold trap maintained at -30°C to -40°C by an ethyl alcohol - water slush. The absorption cell was filled with HF to an appropriate pressure and then isolated from the rest of the system. The pressure was ascertained from the linear attenuation of the pump beam, suitably attenuated using filters. Pressures ranged from 50 mTorr to 6 Torr depending upon the line studied.

The far-infrared lines were detected with a helium cooled In-Ge detector. The pump lines were filtered out using a thin sheet of black polyethylene. A monochromator with a 135μ grating was used to determine the wavelengths of the rotational lines.

The observed rotational lines are given in Table I. None of these lines have been observed before[5]. All of the lines were strong and easily detectable except for the 63.4u line, which is strongly absorbed by atmospheric water vapor. The lines all oscillated without external mirrors[6]. This implies very high gains

since the absorption cell is only 12 cm long. The output powers were estimated from the detector calibration to be in the mW range.

The intensity of the lines depends strongly on pressure. This is due to a trade-off between the number of atoms available and the extent of saturation. At low pressures the saturation is high but the number of atoms is low, whereas at high pressures the reverse is true. This implies an optimum pressure for a given pump power. For all of the observed lines the optimum pressure was found to be such that approximately 50 - 75% of the pump beam was absorbed[8]. These pressures ranged from approximately 50 mTorr for the $P_1(3)$ and $P_1(4)$ pump lines to about 6 Torr for the $P_1(8)$ line. This large variation is due to the fact that the absorption coefficients of the pump transitions change by two orders of magnitude going from $P_1(3)$ to $P_1(8)$.

The unidirectional theory[1] predicts larger gain in the forward direction (i.e. parallel to the propagation direction of the 2.7μ pump field) than in the backward direction. The gain anisotropy was first studied by comparing the intensities of the radiation emitted by the sample cell in the forward and backward directions under high-gain conditions where regenerative feedback (mirrors) was unnecessary. The intensities in the forward direction were found to be 5 to 10 times larger than those in the backward direction[9].

To further investigate the gain asymmetry we placed the sample cell in a ring cavity[10] consisting of two gold-coated mirrors of radii of curvature 8 m and 1.5 m, respectively, and a BaF_2, KBr or NaCl flat, depending on the far-infrared line studied (Fig. 2).

The pump power was coupled in through the flat, which is transparent in the near-infrared and highly reflective and also opaque (Reststrahlen bands) in the far-infrared, thus serving to decouple the gain cell from the optics associated with the pump laser. The cavity was about 1 meter long. About 1% of the far-infrared power was coupled out by means of a saran-wrap beam splitter. The forward and backward intensities were studied separately. In each case the cavity length was tuned to give maximum output power. The maximum power emitted in the forward direction was found to be 40 to 400 times larger than the maximum backward power. In the ring configuration the intensity was very stable, whereas in an open system the intensity fluctuated strongly from one pulse to the next.

In another test the pump laser intensity was attenuated by a factor of 15 (peak power ~200 watts) using absorbing glass plates. Under these conditions the ring cavity oscillated only in a direction parallel to the pump beam. No signal could be detected traveling in the opposite direction. However, the forward signal was close to threshold and not very stable. This is consistent with the theoretical expectations discussed below.

A brief account of the unidirectional effect may be useful. A normally absorbing transition can be brought into the amplifying phase by resonantly pumping a coupled absorbing transition with an intense monochromatic field [Fig. 1(a)]. If both transitions are Doppler-broadened the gain occurs over a narrow frequency interval determined by the homogeneously broadened linewidth (e.g. due to collisions). It was pointed out in Ref. 1 that if the pump field

is in the form of a traveling wave, gain at the coupled transition for waves traveling in the forward direction occurs at one frequency, whereas the gain in the backward direction appears at a different frequency, symmetrically located on the opposite side of the Doppler profile [Fig. 1(b)]. The frequency separation between forward and backward gain regions is proportional to the detuning of the pump field from the line center of the pump transition, and if the pump frequency is tuned close to line center, forward and backward gain regions overlap. An important feature of this effect (independent of whether or not the gain regions overlap) is that the gain in the forward direction is larger than that in the backward direction. This asymmetry arises from the well known width difference between forward and backward change signals observed in laser-induced line-narrowing experiments[11,12]. The difference in gain can be very large. This explanation accounts for the forward-backward intensity asymmetry observed in the experiments described above.

In applying these considerations to HF an important fact must be noted. Goldhar, et al[3] have found that a transversely excited HF laser always oscillates within a range of less than 70 MHz about line center. It is therefore expected that in our experiments the forward and backward gain regions should overlap. To verify this the single pass output, either forward or backward, was reflected back through the cell by means of a BaF_2 flat placed normal to the pump beam. (BaF_2 was used to prevent the pump laser beam from being reflected back and, hence, producing a standing wave, which would eliminate unidirectional features.) Under these conditions the output intensity was considerably larger and much more stable than in the single pass configuration. In fact, the double pass

arrangement enabled the observation of signals which could not be detected otherwise. The fact that the output intensities in the single pass configuration fluctuated considerably from pulse to pulse, even though the output from the pump laser was fairly stable, indicates spurious feedback due, for example, to back scattering from dust particles or windows or backward Rayleigh scattering in the air[6,7].

A rough estimate of the gains of these lines can be made from the observation that in the ring cavity configuration, where a gain of about 1 per pass is needed to overcome losses, the threshold power is approximately 200 W. Therefore, at normal operating powers (3 - 4 kW) the gain coefficient should be 15 to 20 times larger, leading to an incremental gain of over 1/cm. The theoretically predicted values are consistent with these estimates.

Only qualitative agreement between theory[1,13] and experiment can be expected at present since the theory assumes a monochromatic pump field interacting with fully Doppler-broadened transitions. The frequency purity of pulsed HF "pin" lasers is notoriously poor[3]. Frequency chirping and mode jumping may occur during a pulse due, in part, to changes in the refractive index of the plasma during the discharge pulse. Furthermore, the unidirectional effect is expected to decrease for the shorter wavelength lines (36 - 50μ), which oscillate best at sample cell pressures where the collision broadened width is beginning to become comparable to the Doppler width. However, the longer wavelength transitions are fully Doppler-broadened at optimum pressures.

Laser oscillation on one rotational transition can, in principle,

produce cascade oscillations on other transitions lower down in the rotational ladder, especially if the laser oscillation saturates the rotational transition. However, our far-infrared lines are too weak to saturate their transitions, and cascading has not been observed.

In our studies $P_1(J)$ lines were used to pump the excited state rotational transitions. The $R_1(J)$ lines near 2.4μ [$(v,J) = (1,J+1) \rightarrow (0,J)$] are also produced by our HF laser, but at powers about 10 times smaller. In view of the low thresholds observed, the $R_1(J)$ lines can probably also be used as pump fields. Pumping of the $R_1(J)$ transitions also opens the possibility of observing unidirectional emission of $P_1(J)$ lines near 2.7μ.

It is interesting to note that for amplification observed at wavelengths longer than 50u, kT at room temperature exceeds the quantum energy hν, hence the output signals are triggered by thermal radiation. An attempt was made to observe this effect by placing a globar heat source at the amplifier input. Unfortunately, spurious feedback as described earlier caused considerable fluctuations in the output signal, thus masking the effect. Further studies are currently under way.

We would like to thank Professor E. V. George for giving us the design for the helical HF pin laser, and Thomas C. Rounds, Richard Mendelsohn and Charles J. Murrey for measuring the far-infrared transmission of various materials and for supplying us

with a black polyethylene filter. Special thanks go to L. W. Ryan, Jr. and to A. Erikson for valuable technical assistance and advice.

REFERENCES

1. N. Skribanowitz, M. S. Feld, R. E. Francke, M. J. Kelly and A. Javan, Appl. Phys. Letters 19, 161 (1971).

2. See, for example, T. Y. Chang, T. J. Bridges and E. G. Burkhardt, Appl. Phys. Letters 17, 249 (1970); 17, 357 (1970); and T. Shimizu and T. Oka, Phys. Rev. 2A, 1177 (1970).

3. J. Goldhar, R. M. Osgood, Jr., and A. Javan, Appl. Phys. Letters 18, 167 (1971).

4. D. R. Wood, E. G. Burkhardt, M. A. Pollack and T. J. Bridges, Appl. Phys. Letters 18, 112 (1971).

5. T. F. Deutch [Appl. Phys. Letters 11, 18 (1967)] has observed laser oscillations arising from rotational transitions in the same band using a pulsed discharge in a 2 m cavity. His lines originate from levels having much higher J values.

6. There are indications that in this configuration non-resonant feedback due to scattering, e.g. from the cell windows or from air, influences the observed output, hence, the assumption of single pass gain may not be valid. For a discussion of non-resonant feedback see Ref. 7.

7. R. V. Ambartsumyan, N. G. Basov, P. G. Kryukov and V. S. Letokhov, Soviet Phys. JETP 24, 481 (1967) [J. Exptl. Theoret. Phys. (U.S.S.R.) 51, 724 (1966)]; R. V. Ambartsumyan, S. P. Bazhulin, N. G. Basov and V. S. Letokhov, Soviet Phys. JETP 31, 234 (1970) [J. Exptl. Theoret. Phys. (U.S.S.R.) 58, 441 (1970)].

8. Note that this figure refers to saturated absorption, as opposed to the linear absorption used to measure the pressure.

9. It might be argued that this asymmetry is due in part to the fact that the gain at the entrance of the cell is larger than at the exit, since the pump beam is attenuated by about 50% in

traversing the cell. But note that spatial variations in gain can cause a forward - backward asymmetry only if saturation occurs. This is not the case for our system, as can be ascertained from the observed output powers.

10. Note that a ring cavity decouples forward and backward traveling waves and, at the same time, eliminates the question of spatial gain variations since the cell is traversed many times by the far-infrared radiation.

11. M. S. Feld and A. Javan, Phys. Rev. 177, 540 (1969).

12. When the pump transition is highly saturated, the gain profile in the forward direction shows additional structure. These effects are discussed in Ref. 13.

13. B. J. Feldman and M. S. Feld, Phys. Rev. (Feb., 1972), and N. Skribanowitz, M. J. Kelly and M. S. Feld, J. Mol. Spectroscopy, to be published.

TABLE I

Pump Transition		Coupled Transition (v=1 excited state)	
Designation*	Wavelength	$J_{Upper} \rightarrow J_{Lower}$	Wavelength
$P_1(3)$	2.608μ	2 → 1	126.5μ
$P_1(4)$	2.639μ	3 → 2	84.4μ
$P_1(5)$	2.672μ	4 → 3	63.4μ
$P_1(6)$	2.707μ	5 → 4	50.8μ
$P_1(7)$	2.744μ	6 → 5	42.4μ
$P_1(8)$	2.782μ	7 → 6	36.5μ

*$P_1(J)$ signifies the (v=1,J-1) → (v=0,J) transition.

FIGURE CAPTIONS

Fig. 1 a) Energy level diagram. The level (v,J) has vibrational quantum number v and rotational angular momentum quantum number J.

b) Gain profile of an HF rotational transition, resonantly pumped at a coupled vibrational transition. The gain in the forward and backward directions occurs over narrow frequency intervals symmetrically located about line center. Note that the gain in the forward direction is larger than that in the backward direction.

Fig. 2 Ring laser cavity configuration. Forward (backward) far-infrared output power is coupled out of the cavity when the beam splitter is in position a(b).

11. H. P. Grieneisen, J. Goldhar and N. A. Kurnit

Observation of Zero-Degree Pulse Propagation in a Resonant Medium

Proceedings of the 3rd Rochester Conference on Coherent and Quantum Optics, edited by L. Mandel and E. Wolf, Plenum Press 1973

Published in Proceedings of the 3rd, Rochester Conference on Coherence and Quantum Optics, edited by L. Mandel and E. Wolf, Plenum Press 1973.

OBSERVATION OF ZERO-DEGREE PULSE PROPAGATION IN A RESONANT MEDIUM*

H.P. Grieneisen†, J. Goldhar††, and N.A. Kurnit

Massachusetts Institute of Technology, Cambridge, Mass.

Experiments have recently been described[1] in which zero-degree optical pulses[2-5] have been generated and propagated through a resonantly absorbing medium with reduced absorption loss. We briefly review this experiment here and discuss the conditions for low loss propagation. We also describe some initial studies of the evolution of the pulse envelope and discuss the physics underlying this process.

The propagation of a coherent pulse through a resonant medium can be conveniently described by means of the coupled Bloch and Maxwell equations utilized for the discussion of self-induced transparency[6]. For an incident field $\underline{E} = \hat{\epsilon}\,\mathcal{E}(z,t)\cos(\omega t - kz)$, where $\mathcal{E}(z,t)$ is an envelope which varies slowly on a time scale of $1/\omega$ or a spatial scale of λ, the propagation of the pulse envelope is described, in the case of an absorber which has a symmetric distribution $g(\Delta\omega)$ about the laser frequency, by the reduced wave equation[6]:

* Work supported by Air Force Cambridge Research Laboratories, Office of Naval Research and National Aeronautics and Space Administration.

† On leave from Universidade Federal do Rio Grande do Sul, Porto Alegre, Brazil. Work done with partial support from Conselho Nacional de Pesquisas, Brazil..

†† Hertz Foundation predoctoral fellow.

$$\frac{\partial \mathcal{E}}{\partial z} + \frac{\eta}{c}\frac{\partial \mathcal{E}}{\partial t} = -\frac{2\pi N\mu\omega}{\eta c}\int_{-\infty}^{\infty} g(\Delta\omega)\, v(z,t,\Delta\omega)\, d(\Delta\omega) \qquad (1)$$

Here N and η are the number of resonant atoms/unit volume and background refractive index, respectively, and $v(z,t,\Delta\omega)$ is a component of the Bloch vector $(u,v,-w)$ of an atom with resonant frequency $\omega+\Delta\omega$ whose motion in a reference frame rotating about the $\hat{w}$ axis at the laser frequency is given by:

$$\frac{du}{dt} = \Delta\omega v - u/T_2' \qquad (2a)$$

$$\frac{dv}{dt} = -\Delta\omega u - (\mu \mathcal{E}/\hbar)w - v/T_2' \qquad (2b)$$

$$\frac{dw}{dt} = (\mu \mathcal{E}/\hbar)v - (w-w_{eq})/T_1 \qquad (2c)$$

The in-phase and out-of-phase components of the polarization contributed by an atom detuned by frequency $\Delta\omega$ are given by $\mu u(\Delta\omega)$ and $\mu v(\Delta\omega)$, where μ is the component of the transition matrix element along $\hat{\epsilon}$; $w = \rho_{aa} - \rho_{bb}$ is the population difference between excited and ground state.

If the relaxation times T_1, T_2' are long compared to the pulse duration, the excitation of resonant atoms is determined solely by the integral of the field envelope, since (2b,c) can be integrated to give

$$v(z,t,0) = \sin\phi(z,t) \qquad (3a)$$

$$w(z,t,0) = -\cos\phi(z,t) \qquad (3b)$$

where

$$\phi(z,t) = \frac{\mu}{\hbar}\int_{-\infty}^{t} \mathcal{E}(z,t)dt \qquad (4)$$

The Bloch vector for resonant atoms is turned through the angle ϕ. The pulse "area"[6]

$$\theta(z) = \lim_{t\to\infty} \phi(z,t) \qquad (5)$$

measures the degree of excitation of resonant atoms after passage

of the pulse. A pulse whose envelope $\mathcal{E}(z,t)$ has one or more sign changes can have zero area without having zero energy. Such "zero-degree"[2] pulses leave resonant molecules unexcited and thus can propagate with reduced energy loss. It was pointed out in Ref. 2 that this is true even in the presence of level degeneracy, which has an inhibiting influence on the self-induced transparency of $2n\pi$ pulses with $n \geq 1$, since sublevels with different transition matrix elements are then left with different degrees of excitation.

In these experiments[1], the output of a low intensity cw CO_2 or N_2O laser is passed through a GaAs crystal oriented for amplitude modulation. A voltage pulse derived from a charged 50Ω cable and triggered spark gap[7] is propagated over the crystal and produces elliptically polarized light from the linearly polarized laser output. The perpendicular component of this is reflected from a germanium Brewster plate which normally transmits the laser output, and is then passed through an absorption cell. The voltage pulse may be applied to the crystal a second time with either the same or opposite polarity by reflecting it from the open or shorted end of a 50Ω cable which terminates the crystal mount. Reversing the polarity of the pulse produces a 180° phase change in the electric field component reflected by the Brewster plate. This field is proportional to $\sin\Gamma$, where $\pm\Gamma$ ($\approx\pi/8$ in these experiments) is the phase advance or retardation produced along the fast or slow axis of of the modulator crystal.

Figure 1 shows a CO_2 laser pulse generated with a 2 nsec voltage pulse as observed with a Ge:Cu detector and displayed on a Tektronix oscilloscope with a 1S1 sampling plug-in unit. For the purpose of this figure, a quarter wave plate has been added in front of the modulator, so that the pulses are observed superimposed on a large cw background. In the top trace, two pulses of opposite polarity are applied to the crystal, resulting in opposite changes in the intensity reaching the detector; in the lower trace the second voltage pulse is applied to the crystal with the same polarity as the first. This method gives a reasonable representation of the pulse envelope since the intensity reaching the detector is proportional to $1 + \sin 2\Gamma$. For observation of the pulse envelope evolution, it will be desirable to send a cw beam along a separate path and recombine it with the pulse on the detector.

Measurements of the pulse energy transmitted through an absorption cell were performed with both a CO_2 laser and heated CO_2 absorber and an N_2O laser and NH_3 absorber. The latter permitted measurements over many absorption lengths, since the NH_3 ν_2 [as Q(8,7)] transition is coincident to within 10 MHz of the N_2O P (13) transition, and has an absorption coefficient of 0.7 cm^{-1} and Doppler half-width $\Delta\nu$ = 42 MHz[8]. The transmission of 2 nsec and 6 nsec zero-degree and in-phase pulses is shown in Fig. 2 as a function of NH_3 pressure in a 40 cm

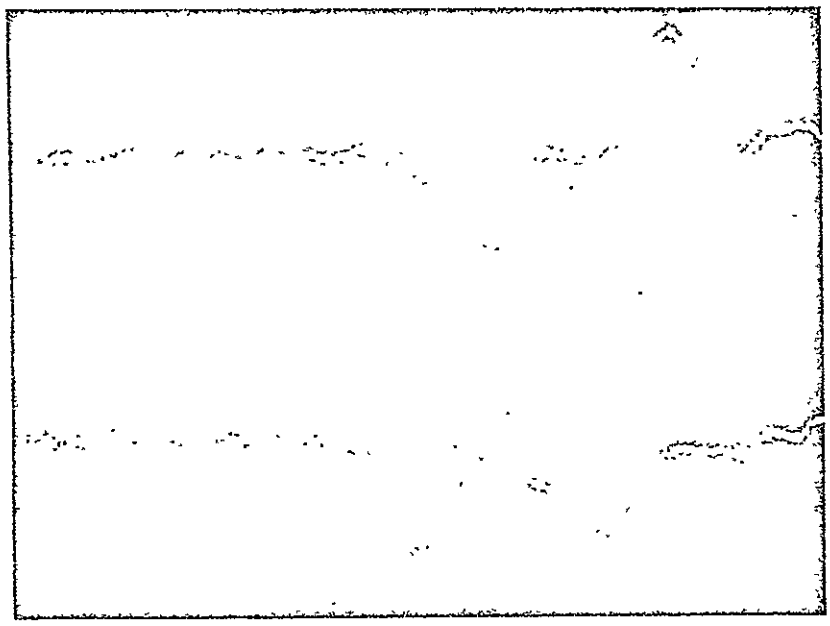

Fig. 1 Pulse observed by Ge:Cu detector with $\lambda/4$ plate in front of modulator (see text). Top: Zero-degree pulse obtained by applying out-of-phase pulses to modulator. Bottom: In-phase pulses applied to modulator. Time scale is 2 nsec/div.

absorption cell. The dashed line shows the cw absorption for comparison. Curve A shows the absorption of a zero-degree pulse formed from two out-of-phase 2 nsec pulses, as in the top trace of Fig. 1. At low pressures, the number of absorption lengths is proportional to pressure, and the absorption coefficient may be obtained from the logarithmic slope of the absorption versus pressure. The dashed curve shows the cw absorption for comparison. Curve B shows the absorption of two 2 nsec in-phase pulses as in the bottom trace of Fig. 1. These pulses show an initial absorption coefficient some five times higher than the corresponding zero-degree pulse, but still a factor of five smaller than the cw absorption.

The latter result is of course to be expected from a consideration of the overlap of the Fourier components of the pulse with the resonance line. In the small angle regime in which these experiments have been carried out ($\phi \leq 2^\circ$), the atomic response may be

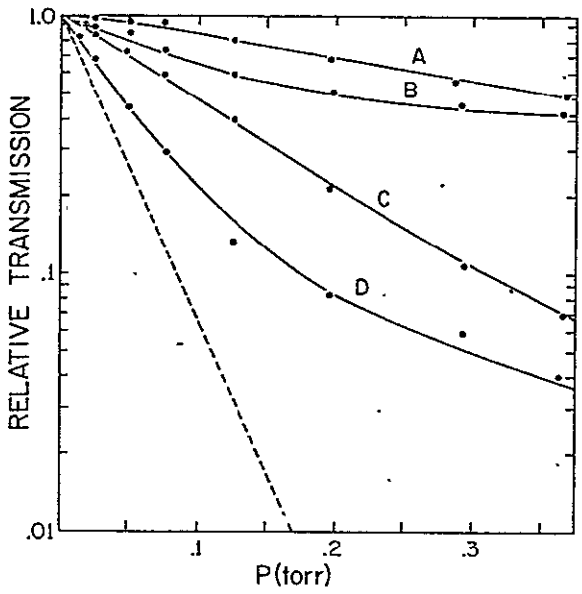

Fig. 2 Transmission of N_2O laser energy through resonant NH_3 absorber as function of pressure, for (A) 2 nsec zero-degree pulses, (B) 2 nsec in-phase pulses, (C) 6 nsec zero-degree pulses, and (D) 6 nsec in-phase pulses. Dashed line gives cw absorption.

approximated by a harmonic oscillator. The pulse evolution may then be described by a linearized theory[5], in which the absorption and dispersion of each Fourier component can be considered independently. A zero-degree pulse has a Fourier spectrum which is zero on resonance (i.e., resonant atoms are left in their initial state after passage of the pulse). Hence, if the resonance line is narrower than the inverse pulse-width, which determines the width of the hole in the Fourier spectrum, very little energy will be extracted from the pulse.

Curves C and D of Fig. 2 show the effect of lengthening the pulse-width to 6 nsec, which is longer than the inhomogeneous relaxation time $T_2^* = 1/2\pi\Delta\nu_D \simeq 4$ nsec. Both zero-degree (C) and in-phase (D) pulses show correspondingly increased absorption, with the zero-degree pulses exhibiting about 1/2 the absorption coefficient of the in-phase pulses. As the pulse lengths are made longer, the absorption for both zero-degree and in-phase pulses approach the cw limit, in this small angle regime. This is not necessarily true in

the nonlinear regime, since particular pulse shapes, related to 4π pulses, are predicted to give small attention even for pulses long compared to T_2^* [3,4].

A few general conclusions can be reached regarding the energy absorbed without considering the detailed pulse shape. If one multiplies Eq.(1) on both sides by $\frac{nc}{4\pi}\mathcal{E}(z,t)$ and integrates over time from $-\infty$ to $+\infty$, one obtains

$$\frac{ds(z)}{dz} = -\frac{N\mu\omega}{2}\int_{-\infty}^{\infty} g(\Delta\omega)d(\Delta\omega)\int_{-\infty}^{\infty}\mathcal{E}(z,t)v(\Delta\omega,z,t)dt \qquad (6)$$

where

$$s(z) = \frac{nc}{8\pi}\int_{-\infty}^{\infty}\mathcal{E}^2(z,t)dt$$

is the pulse energy/unit area. If the pulse duration $\tau = (\int|\mathcal{E}(z,t)|dt)^2/\int\mathcal{E}^2(z,t)dt$ is sufficiently short that the pulse spectrum is broad compared to the resonance line ($\tau<<T_2',T_2^*$), all of the atoms respond resonantly and obey Eq.(3). From Eq.(4), we have $\mathcal{E}(z,t) = (\hbar/\mu)\,\partial\phi/\partial t$, which, when substituted in Eq.(6) together with (3a), yields

$$\frac{\partial s(z)}{\partial z} = -N\hbar\omega(1-\cos\theta(z))/2 \quad . \qquad (7)$$

The right-hand side is just the energy remaining in the atomic system. The angle θ obeys the area theorem[6]

$$\frac{d\theta(z)}{dz} = -\frac{1}{2}\alpha\sin\theta(z) \qquad (8)$$

where $\alpha = 4\pi N\mu^2\omega T_2^*/\hbar nc$ is the small signal linear absorption coefficient of the medium (cf. Eq.(12) below), assuming $T_2^* << T_2'$.

This implies that $\theta(z)$ will approach some multiple n=0,1,2... of 2π after a number of absorption lengths α^{-1}. Once this occurs, no further energy will be absorbed in the narrow line limit, according to (7). The initial absorption will itself be very small if $\tau<<T_2^*$. For example, for a small area square pulse of duration $\tau<<T_2^*$, Eq.(7) reduces to

$$\frac{ds(z)}{dz} = -\alpha\left(\frac{\tau}{2T_2^*}\right)s(z) \qquad (9)$$

As this pulse propagates, its area decays according to (8), primarily due to the development of a negative lobe which follows the pulse, as will be discussed in more detail below. This negative tail, which can be termed free induction decay[10], superradiance[11], or fluorescent ringing[12], extracts energy from the resonantly excited atoms and grows until it is able to return resonant atoms to the ground state. The reduction in absorption coefficient as this pulse develops into a zero-degree pulse, is evident in curves B and D of Fig. 2. After several absorption lengths, the absorption coefficient begins to approach a value comparable to the initial absorption obtained for zero-degree pulses. Experiments in which the output of one absorption cell was used as the input to another clearly show this behavior[1].

In the small angle regime, this reduction in the absorption coefficient is simply seen to result from the attenuation of resonant Fourier components. It has been shown by Crisp[5,13] that a Fourier domain analysis which accounts for the dispersion as well as absorption of each Fourier component predicts the development of an initially negative tail which oscillates in sign after the pulse propagates many absorption lengths, in agreement with the conclusions of Ref. 12. This analysis also yields the small angle form of the area theorem (Eq.(8)), valid for arbitrary ratio of τ to T_2' and T_2^*.

If the line is not narrow compared to the pulse spectrum, the energy absorbed depends not only on the area, as implied by (7), but on the pulse shape as well. In this more general case, the solution of Eq.(2) for v can be written as integral equation[14,5]:

$$v(z,t,\Delta\omega) = \int_{-\infty}^{t} \exp[(-t+t'')/T_2'] \cos[\Delta\omega(t-t'')] \times \frac{\mu \mathcal{E}(z,t'')}{\hbar} w(z,t'',\Delta\omega)dt'' \qquad (10)$$

Substituting this in (6), and letting t' = t-t'', we have

$$\frac{ds(z)}{dz} = -\frac{N\mu\omega}{2} \int_{-\infty}^{\infty} g(\Delta\omega)\, d(\Delta\omega) \int_{-\infty}^{\infty} dt\, \mathcal{E}(z,t) \int_{0}^{\infty} dt' \exp(-t'/T_2') \cos\Delta\omega t' \times \frac{\mu \mathcal{E}(z,t-t')}{\hbar} w(z,t-t',\Delta\omega) \qquad (11)$$

This is not particularly useful unless the solution for w is known; however, a few general conclusions can be drawn. If w is not appreciably altered during the pulse and T_2' or T_2^* is short, the factor

of $\exp(-t'/T_2')$ or $\cos\Delta\omega t'$ acts to limit the contribution of the t' integral to small values of t'. The energy absorbed then depends only on values of $\mathcal{E}(z,t)$ at closely spaced times. If $\mathcal{E}(z,t)$ and $\mathcal{E}(z,t-t')$ are different in sign, we have emission rather than absorption of energy. For long relaxation times, this averaging is performed over the whole pulse, and can give as much emission as absorption. For short relaxation times, there is little memory in the system of previous values of the field. If we assume in this limit that $\mathcal{E}(z,t-t') \cong \mathcal{E}(z,t)$, for all t' which contribute significantly to (11), we have by first performing the $\Delta\omega$ integral and then the t' integral

$$\frac{ds(z)}{dz} = -\frac{4\pi N\mu^2\omega T_2}{\hbar nc}\, s(z) \equiv -\alpha s(z) \tag{12}$$

where, for convenience, we have taken a Lorentzian frequency distribution,

$$g(\Delta\omega) = \frac{1}{\pi T_2^*[(\Delta\omega)^2 + 1/T_2^{*2}]} \tag{13}$$

and have put $1/T_2 = 1/T_2' + 1/T_2^*$.

In the case of large area pulses, w can deviate significantly from its steady state value, and even change sign, resulting in emission during part of a pulse without the pulse envelope changing sign, as, for example, for 2π pulses. Unlike the linear regime considered above, the effects of homogeneous and inhomogeneous broadening are very different. If $T_2'<<\tau$, the population will not be appreciably altered except for very intense fields. If, on the other hand, $T_2^*<<\tau<<T_2'$, complete inversion of resonant atoms can still be achieved, and frequency groups near resonance can be left highly excited. Figure 3 shows the population $\rho_{aa}(\Delta\omega) = (1+w(0,\tau,\Delta\omega))/2$ excited at the input face of a sample, calculated for a square pulse of duration $\tau<<T_2'$, with and without a 180° phase change in the middle, for several values of θ. The energy absorbed per unit area in a thin slab is obtained by multiplying this curve by $N\hbar\omega\Delta z g(\Delta\omega)$ and integrating over frequency. Even for pulses as large as $\pi/2$ followed by $\pm\pi/2$, the spectrum of excited atoms strongly resembles the power spectrum of the pulse, which it must reduce to in the small-angle limit. For want of a better term, we shall call this the Bloch spectrum of the pulse. As the pulse intensity is increased further, the nature of the Bloch spectrum changes considerably. Lobes far from resonance become enhanced, and those near resonance can be suppressed. A zero-degree pulse composed of two π pulses can show considerably more absorption than the corresponding 2π

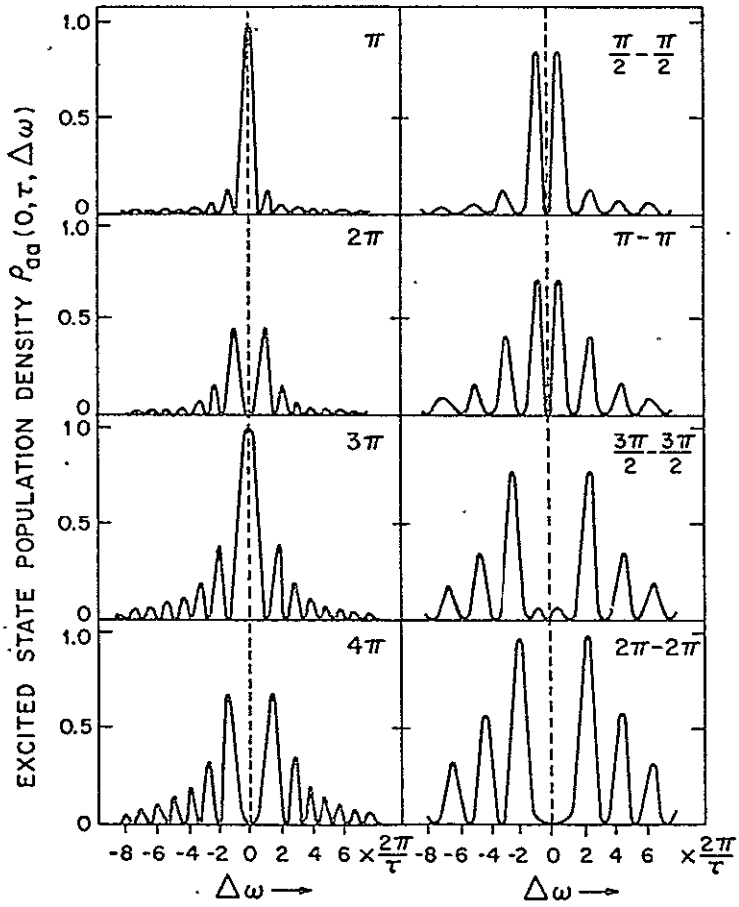

Fig. 3 Excited state population density produced in a thin slab by a short square pulse of duration τ, with and without a 180° phase change at $\tau/2$, as a function of the detuning of the atomic frequency from the frequency of the applied field. Total population change is obtained by multiplying by $g(\Delta\omega)$ and integrating over frequency. Pulse areas are indicated in the figure.

pulse (for a broad line). When the area of each pulse is increased to $3\pi/2$, the zero-degree pulse has a Bloch spectrum which is small over a considerably wider range of frequencies near resonance than the power spectrum of the pulse. Thus, small attenuation can be expected in this case, even for the square pulses considered here, provided the resonance line is narrower than the hole in the Bloch spectrum. More complex pulse shapes have been proposed[3,4] which give better transmission characteristics.

The energy absorbed at distances further into the sample will depend on the modification of the pulse shape by the intervening sample. In general, this is a complicated problem, requiring computer solution of Eqs.(1,2). Analytic solutions have been obtained in the linear regime for a number of pulse shapes[5]. Rather than reviewing such calculations in detail, we shall try to motivate some of our remarks concerning the pulse evolution by considering the effect of a thin slab of sample. The change in pulse shape is due not only to the energy absorbed during the input pulse, but also to the re-radiation by the polarization left in the medium after the pulse passes. The latter is particularly important when $\tau<T_2^*$, since the medium can "ring"[12] for a time T_2. In the nonlinear regime, it can be important even if $\tau>T_2^*$, as is evidenced by the phenomenon of edge echoes[15] in NMR. Here, contributions from near-resonant atoms can give rise to a large polarization at a time $\sim\tau$ after a pulse of duration τ.

Consider a pulse incident on a slab of thickness Δz. The field at $z' = z + \Delta z$ and $t' = t + \frac{\eta}{c}\Delta z$ is related to the field at z,t by

$$\mathcal{E}(z',t') = \mathcal{E}(z,t) + \left(\frac{\partial \mathcal{E}(z,t)}{\partial z} + \frac{\eta}{c}\frac{\partial \mathcal{E}(z,t)}{\partial t}\right)\Delta z$$

$$= \mathcal{E}(z,t) - \frac{2\pi N\mu\omega}{\eta c}\Delta z \int_{-\infty}^{\infty} g(\Delta\omega)v(z,t,\Delta\omega)d(\Delta\omega) \qquad (14)$$

according to Eq.(1). The polarization excited by a square input pulse[16] with amplitude $\mathcal{E}_0$ and duration τ applied at $t = 0$ is, by (2) with $T_2' = \infty$:

$$v(z,t,\Delta\omega) = \frac{\Omega\sin\left[\left(\Omega^2+(\Delta\omega)^2\right)^{\frac{1}{2}}\tau\right]}{\left(\Omega^2+(\Delta\omega)^2\right)^{\frac{1}{2}}}\cos\left(\Delta\omega(t-\tau)\right)$$

$$- \frac{2\Omega\Delta\omega}{\Omega^2+(\Delta\omega)^2}\sin^2\left[\frac{\left(\Omega^2+(\Delta\omega)^2\right)^{\frac{1}{2}}\tau}{2}\right]\sin\Delta\omega(t-\tau) \qquad (15)$$

where $\Omega = \mu\,\mathcal{E}_0/\hbar$. The second term is responsible for the edge echo mentioned above. In the narrow line limit, $\tau<<T_2^*$, (13),(15) yield

$$\langle v(z,t,\Delta\omega)\rangle = \int_{-\infty}^{\infty} g(\Delta\omega)v(z,t,\Delta\omega)d(\Delta\omega) \cong \sin(\Omega\tau)\exp[-(t-\tau/2)/T_2^*] \qquad (16)$$

to first order in τ/T_2^*. The field is then, from (14), for $t>\tau$,

$$\mathcal{E}(z',t') = -\frac{2\pi N\mu\omega}{\eta c}\,\Delta z\,\sin\theta(z)\,\exp[(-t+\tau/2)/T_2^*] \qquad (17)$$

The field radiated after the pulse thus decays exponentially with time constant T_2 for a sample sufficiently thin that (14) does not have to be iterated. Its sign is negative with respect to the incident field since the radiated field must tend to cancel the incident field during the pulse, for $\theta<\pi$. The area of this tail is obtained by multiplying (17) by $\mu/\hbar$ and integrating from τ to ∞:

$$\theta_{tail}(z') \cong -\frac{2\pi N\mu^2\omega}{\hbar\eta c}\,\Delta z\,\sin\theta(z)\,(T_2^*-\tau/2) \qquad (18)$$

During the input pulse, the polarization is given approximately by

$$\langle v(z,t)\rangle \cong \sin(\Omega t)\,\exp(-t/2T_2^*) \qquad (19)$$

(cf. Eq. (16) with $\tau = t$). The field during the pulse is, from (14) and (19),

$$\mathcal{E}(z',t') = \mathcal{E}_0 - \frac{2\pi N\mu\omega}{\eta c}\,\Delta z\,\sin(\Omega t)\,\exp(-t/2T_2^*) \qquad (20)$$

The area during the time τ when the incident field is present is, for $\tau<<T_2^*$,

$$\theta_{pulse}(z') \cong \theta(z) - \frac{2\pi N\mu^2\omega}{\hbar\eta c}\,\Delta z\left(\frac{1-\cos\theta(z)}{\Omega}\right) \qquad (21)$$

For small θ, this reduces to

$$\theta_{pulse}(z') = \theta(z) - \frac{2\pi N\mu^2\omega}{\hbar\eta c}\left(\frac{\tau}{2}\right)\theta(z)\Delta z \qquad (22)$$

Adding this to the small angle form of (18) yields

$$\theta(z') = \theta(z) - \frac{2\pi N\mu^2\omega}{\hbar\eta c}\,T_2^*\,\theta(z)\Delta z \qquad (23)$$

in agreement with the small angle form of (8). We see that, although the area theorem is generally applied in the case of $\tau >> T_2^*$, it is still well obeyed in the limit $\tau << T_2^*$, but the major contribution to the change in area comes from the tail of the pulse.

It might be thought that (16) should contain a term which accounts for radiation damping[17], since, as noted previously, the re-radiation which follows the excitation pulse can be considered to be "superradiant"[11] emission. In order to examine the connection between this pulse-propagation problem and superradiance in more detail, let us calculate the amounts of energy absorbed and re-radiated. The energy incident in our square-input pulse is given by

$$s(z) = \frac{\eta c}{8\pi} \int_0^\infty \mathcal{E}^2(z,t)dt = \frac{\eta c}{8\pi} \mathcal{E}_0^2 \tau \qquad (24)$$

while the energy reaching $z' = z + \Delta z$ is obtained by substituting in (24) $\mathcal{E}(z',t')$ from (20), for $t<\tau$, and from (17) for $t>\tau$. Dropping terms second order in τ/T_2^*, this yields

$$s(z') - s(z) \cong -\frac{4\pi N\mu\omega}{\eta c} \Delta z \left(\frac{\eta c}{8\pi}\right) \mathcal{E}_0 \left(\frac{1-\cos\theta(z)}{\Omega}\right)$$

$$+ \frac{4\pi^2 N^2 \mu^2 \omega^2}{\eta^2 c^2} T_2^* (\Delta z)^2 \left(\frac{\eta c}{8\pi}\right) \sin^2\theta(z) \qquad (25)$$

For small area pulses, this may be written

$$\Delta s(z) = -\alpha \Delta z \left(\frac{\tau}{2T_2^*}\right) s(z) + (\alpha \Delta z)^2 \frac{\tau}{8T_2^*} s(z) \qquad (26)$$

The first term in (25) or (26) represents the energy absorbed from the input pulse; the second term is the energy radiated in the tail. Although the tail accounts for most of the change in area of the pulse, the re-radiated energy is a small fraction of the energy absorbed unless $\alpha \Delta z \geq 1$. But (25) is not valid in this limit since the field in (17) and (20) should properly be modified to account for the changing pulse shape and area[18].

The superradiance approximation[19] treats all of the atoms in the slab of thickness Δz and area A as radiating identically, with an initial radiation rate $I = \frac{\eta c}{8\pi} \mathcal{E}^2 A$, given according to (17), by

$$I = \frac{\eta c}{8\pi}\left(\frac{4\pi^2 N^2 \mu^2 \omega^2}{\eta^2 c^2}\Delta z^2 A\right)\sin^2\theta \qquad (27)$$

In terms of the number $n = NA\Delta z$ of atoms in the slab, this may be written

$$I = \frac{n^2}{4}\sin^2\theta\left(\frac{\hbar\omega}{T_1}\right)\left(\frac{3}{8\pi\eta^2}\frac{\lambda^2}{A}\right)$$

$$= n\hbar\omega\sin^2\theta\left(\frac{1}{T_s}\right) \qquad (28)$$

where $1/T_1 = 4\eta\mu^2\omega^3/3\hbar c^3$ is the spontaneous emission rate, and

$$\frac{1}{T_s} = \frac{3}{32\pi\eta^2}\, n\frac{\lambda^2}{A}\left(\frac{1}{T_1}\right) \qquad (29)$$

is the superradiant decay rate[11,20]. Within the approximation that atoms in the front of the sample do not appreciably alter the field seen by atoms at larger depths in the sample, i.e., $\alpha\Delta z \ll 1$, we thus obtain the enhanced decay rate characteristic of superradiant emission. From the derivation of this result, it is evident that this is only an approximation to the differential equation (1) governing the pulse propagation. As the pulse propagates through the sample, the field radiated by the atoms in the first small thickness produces a negatively phased field which drives atoms further in the sample back toward the ground state. This field grows with increasing z, initially according to Eq.(17), and hence can more and more rapidly extract the energy from the population excited by the first part of the pulse. The time T_s characterizes the re-radiation at a given distance in the medium. Burnham and Chiao[12] have given an analytic expression for the field radiated after a small area δ-function pulse,

$$\theta = \frac{\mu}{\hbar}\,\mathcal{E}_0\,\tau\delta\left(t' - \frac{\eta}{c}z\right),\quad \tau \ll T_2, T_s$$

which, as modified by Crisp[13] to include relaxation, may be written

$$\mathcal{E}(z,t) = -\mathcal{E}_0\frac{\tau}{\tau_R}\,\frac{J_1\left[z(t/\tau_R)^{\frac{1}{2}}\right]}{(t/\tau_R)^{\frac{1}{2}}}\,\exp(-t/T_2) \qquad (30)$$

where $t = t' - \frac{n}{c} z$ is the time measured from the passage of the input pulse, J_1 is the first order Bessel function, and τ_R is given by[21]

$$\frac{1}{\tau_R} = \frac{2\pi N \mu^2 \omega}{\hbar n c} z = \frac{\alpha z}{2T_2} = \frac{4}{T_s} \tag{31}$$

Equation(30) describes an envelope which oscillates in sign as a function of the retarded time t, as indicated in Fig. 4, the first zero occurring at $t = 3.7\tau_R \simeq T_s$. Unless $T_s \leq T_2$, which according

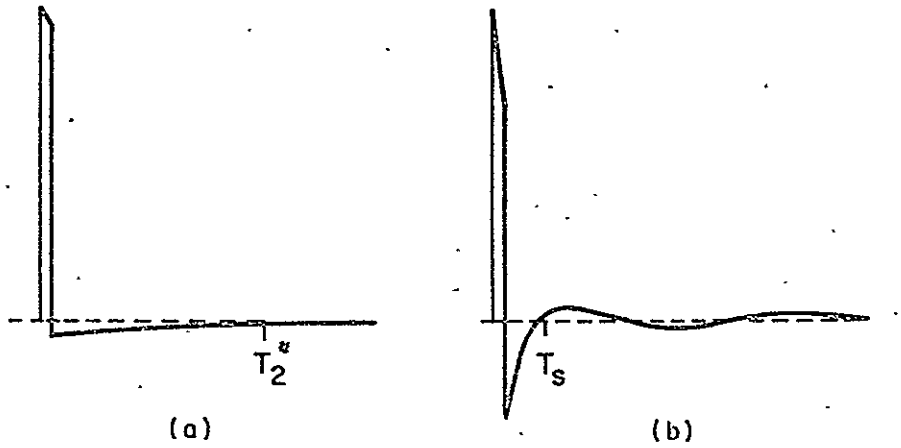

Fig. 4 Evolution of a nearly δ-function input pulse for (a) $\alpha z \ll 1$, (b) $\alpha z \gg 1$.

to (31) implies $\alpha z \geq 8$[22], the factor of $\exp(-t/T_2)$ in (30) will cause the field envelope to decay to zero before it reverses sign. For increasing z, the sign reversal, which arises from an oscillation of the energy between the field and the atomic system, becomes correspondingly faster.

Equation(30) may also be written[13]

$$\mathcal{E}(z,t) = -\mathcal{E}_0 \tau \left(\frac{\alpha z}{2tT_2}\right)^{\frac{1}{2}} J_1\left[2\left(\frac{\alpha z t}{2T_2}\right)^{\frac{1}{2}}\right] \exp(-t/T_2) \tag{32}$$

If J_1 is expanded as a power series, the first two terms yield

$$\mathcal{E}(z,t) \simeq -\mathcal{E}_0 \frac{\tau}{2T_2} \exp(-t/T_2)\ \alpha z\left(1-\frac{\alpha z}{4T_2}t\right) \qquad (33)$$

The first term agrees with the small angle form of (17) and predicts a re-radiated field whose peak grows linearly with αz. The second term governs the decrease of the field for small t. The field decays with an initial slope of $(1/T_2)(1+\alpha z/4) = 1/T_2 + 2/T_S$. For pulses not short compared to T_2 and T_S, the distortion within the input pulse must also be considered[5].

A preliminary observation of this pulse envelope distortion is shown in Fig. 5. Unfortunately, some ringing is present due to

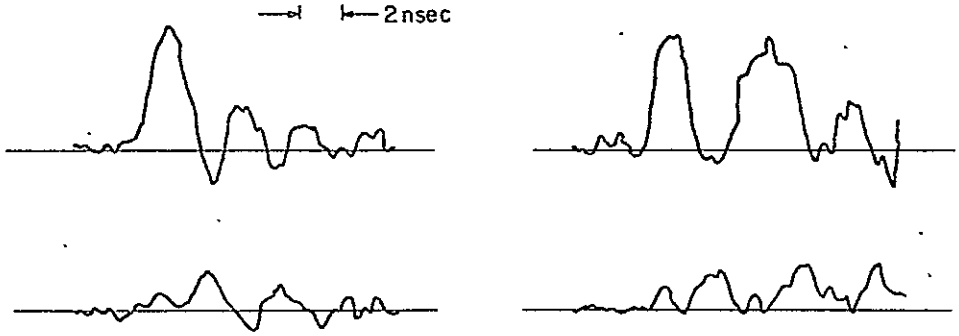

Fig. 5 (a) Top: 2 nsec N_2O laser input pulse (partially obscured by ringing in amplifier). Bottom: same pulse after traversing 15 absorption lengths of NH_3. (b) Top: zero-degree input pulse formed from two 2 nsec pulses. Bottom: same pulse after traversing 15 absorption lengths of NH_3. A baseline subtraction has been made in order to cancel rf noise from the spark gap.

an amplifier which was needed in order to display the N_2O laser pulses of 10 mw intensity. This spurious electronic ringing attenuates linearly with the signal, however, whereas it can be clearly seen from Fig. 5a that if a single 2 nsec pulse (top trace) is passed through a resonant NH_3 absorber with $\alpha z=15$, the output of the absorber (bottom trace) shows a second peak which has grown to be larger than the (attenuated) first peak. In Fig. 5b, a zero-degree pulse is shown. The first pulse again has a double peaked structure after passing through the absorber. There is some evidence that a secondary lobe which is forming in the tail of the first pulse partially interferes with the second input pulse, due

12. R. M. Osgood, Jr. and A. Javan

Measurement of Vibration-Vibration Energy Transfer Time in HF Gas

Published in Appl. Phys. Letters

to a small delay between the two pulses. For a large number of absorption lengths, computer calculations show that this can result in increased absorption for such zero-degree pulses. Some indications of this behavior have been observed[23] and will be discussed elsewhere.

Experiments are in progress to obtain clearer observations of the pulse evolution and to extend these observations to the nonlinear regime where analytic solutions are not available. Also of interest is the propagation behavior in the off-resonance case. These techniques promise to be useful for studying pulse evolution in both absorbing and amplifying media and may find applications in long distance pulse propagation.

Acknowledgments

We wish to thank A. Javan and H.R. Schlossberg for their encouragement and collaboration during the course of these experiments. We also wish to acknowledge numerous stimulating discussions with A. Szöke, M.S. Feld and Y.C. Cho.

References

1. H.P. Grieneisen, J. Goldhar, N.A. Kurnit, A. Javan and H.R. Schlossberg, Bull. Am. Phys. Soc. *17*, 681 (1972), and Appl. Phys. Letters *21*, 559 (1972).
2. C.K. Rhodes, A. Szöke and A. Javan, Phys. Rev. Letters *21*, 1151 (1968).
3. F.A. Hopf, C.K. Rhodes, G.L. Lamb, Jr., and M.O. Scully, Phys. Rev. *A3*, 758 (1971).
4. G.L. Lamb, Jr., *Proceedings of the VII International Quantum Electronics Conference*, to be published; see also G.L. Lamb, Jr., Rev. Mod. Phys. *43*, 99 (1971).
5. M.D. Crisp, Phys. Rev. *A1*, 1604 (1970).
6. S.L. McCall and E.L. Hahn, Phys. Rev. Letters *18*, 908 (1967); Phys. Rev. *183*, 457 (1969); see also H.M. Gibbs and R.E. Slusher, Phys. Rev. *A5*, 1634 (1972).
7. R.C. Fletcher, Rev. Sci. Instr. *20*, 861 (1949).
8. F. Shimizu, J. Chem. Phys. *52*, 3572 (1970); Appl. Phys. Letters *16*, 368 (1970); T. Shimizu and T. Oka, Phys. Rev. *A2*, 1177 (1970).

9. The more general case of level degeneracy can be treated as in Ref. 2.

10. A. Abragam, *Principles of Nuclear Magnetism* (Oxford University Press, London, 1961) Ch. II, III.

11. R.H. Dicke, Phys. Rev. *93*, 99 (1954).

12. D.C. Burnham and R.Y. Chiao, Phys. Rev. *188*, 667 (1969).

13. M.D. Crisp, Opt. Commun. *4*, 199 (1971).

14. F.A. Hopf and M.O. Scully, Phys. Rev. *179*, 399 (1969).

15. A.L. Bloom, Phys. Rev. *98*, 1105 (1955); see also Ref. 14.

16. A square pulse formally violates the slowly varying envelope approximation made for Eq.(1). The pulse can be turned on and off sufficiently slowly to make (1) applicable without appreciably affecting (15).

17. A.M. Ponte Goncalves, A. Tallet and R. Lefebvre, Phys. Rev. *188*, 576 (1969); Phys. Rev. *A1*, 1472 (1970); see also A. Compaan and I.D. Abella, Phys. Rev. Letters *27*, 23 (1971).

18. Similar conclusions have been emphasized by E.L. Hahn, N.S. Shiren and S.L. McCall, Phys. Letters *37A*, 265 (1971); R. Friedberg and S.R. Hartmann, Phys. Letters *37A*, 285 (1971) and *38A*, 227 (1972); R.H. Picard and C.R. Willis, Phys. Letters *37A*, 301 (1971).

19. R.H. Dicke, Ref. 11 and in *Quantum Electronics III*, eds. N. Bloembergen and P. Grivet (Columbia University Press, New York, 1964) Vol. 1, p. 35; N.E. Rehler and J.H. Eberly, Phys. Rev. *A3*, 1735 (1971); R. Bonifacio, P. Schwendimann and F. Haake, Phys. Rev. *A4*, 302 and 854 (1971); see also Y.C. Cho, N.A. Kurnit, and R. Gilmore, in these Proceedings, p. 755.

20. F.T. Arecchi and E. Courtens, Phys. Rev. *A2*, 1730 (1970), as modified by Friedberg and Hartmann, Ref. 18; see also I.D. Abella, N.A. Kurnit and S.R. Hartmann, Phys. Rev. *141*, 391 (1966), Appendix C.

21. In Ref. 12, $1/\tau_R = \omega_p^2 z/4c$, where ω_p is the plasma frequency: classically $\omega_p^2 = 4\pi f N e^2/m$, where f is the oscillator strength; quantum mechanically, $\omega_p^2 = 8\pi N \mu^2 \omega/\hbar$.

22. R. Friedberg and S.R. Hartmann, Ref. 18. In the second of these papers and Optics Commun. *2*, 301 (1970), these authors also consider the effect of the backward wave, which gives rise to a frequency shift. This shift should be small in our experiment.

23. H.P. Grieneisen, Ph.D. Thesis, M.I.T., 1972.

MEASUREMENT OF VIBRATION-VIBRATION ENERGY TRANSFER TIME IN HF GAS

R. M. Osgood, Jr.[+] and A. Javan

Massachusetts Institute of Technology
Cambridge, Massachusetts 02139
Department of Physics

(Published Appl. Phys. Letts.)

P. Sackett

Air Force Cambridge Research Laboratories
L. G. Hanscom Field, Massachusetts

[+] Hertz Foundation Predoctoral Fellow

ABSTRACT

An experimental technique for measuring the vibration-vibration decay rate of the v=2 state in HF gas is described. The technique involves observation of the rise time of the HF v=2 vibrational fluorescence emanating from a gas sample pumped with an HF laser operating on a v=1 → v=0 transition. An analytic model which predicts the temporal behavior of the HF v=1 and v=2 vibrational levels is also described. This model predicts an apparent decay rate of the v=2 fluorescence state which is twice that for v=1. Experimental observation confirms this observation.

Previous measurements of vibrational level lifetimes in gases using the technique of laser-induced fluorescence[1] have been mainly limited to observation of vibration to translation (or rotation) energy decay, or to intermolecular or inter-mode vibration - vibration transfer. In this paper, we report direct measurement of the intra-mode vibration - vibration transfer time in HF. The experiment consisted of pumping a sample cell containing pure HF gas with an HF chemical laser oscillating on a single transition in the v=1 → v=0 band. Spectral resolution of the HF fluorescence then permitted separate observation of the time development for the laser-populated v=1 level and the collisionally-populated v=2 level. The latter arises from the collision of two HF molecules in the v=1 state leading to one molecule in v=1 and the other in the v=0 state. The simplicity of the HF molecule as well as the hierarchy of intramolecular transfer times makes it possible to provide an analytic model for the temporal behavior of the HF vibrational fluorescence. This model indicates that the rise time of the observed v=2 → v=1 fluorescence gives a direct measurement of the vibration - vibration transfer rate, out of v=2; that is, the process HF(v=2)+HF(v=0) → 2HF(v=1). In addition, it shows that the population of v=2 is proportional to its rate of production and hence to the population in the v=1 state squared. As a result the apparent decay rate of our observed v=2 fluorescence is twice that for v=1. We find good agreement between these predictions and the results of the time resolved fluorescence experiments.

The experimental apparatus employed is illustrated by Fig. 1. A helical HF "pin" laser, utilizing an intracavity grating to obtain

single line operation, was used as the source[2]. Peak laser power for the pump transition used in this experiment, P(4) of the v=1 → v=0 band, was several kW with a pulse width of about 0.5 μsec. The HF sample cell was located 2 meters from the laser along an optical path defined by two irises. This positioning allowed substantial spatial filtering of the pump radiation so as to discriminate against unwanted superradiant laser lines.

The HF handling system consisted of a Kel-F distillation chamber for purification of commercial grade HF[3], and an all-monel valving manifold. Purification of the HF was accomplished by using the distillation techniques described by Airey and Fried[3]. Specific conductivity measurements of the HF samples prior to usage showed the H_2O content to be less than 50 ppm. The fluorescence cell was of 1" diameter monel tubing with sapphire brewster windows and viewing ports. Pressure measurements were made with an HF-resistant capacitance manometer, which was clearly sensitive to pressures as low as 3 millitorr. For pressures above 150 millitorr, the uncertainty in pressure measurement was about ± 10 millitorr; below 150 millitorr, the uncertainty was about ± 3 millitorr. Frequent recalibrations of the manometer against a mercury Macleod gauge were made during the course of the experiment. All measurements were made under static (non-flowing) conditions, and pressure readings were taken before and after each fluorescence observation.

Fluorescent output from the cell was taken through a side window, and converted to an f/6 converging beam using a BaF_2 lens. The fluorescence signal was then detected after passage through a Bausch and Lomb 0.5 meter monochromator or through a 10 cm HF absorption cell

(which served as a filter for the v=1 → v=0 fluorescence) or a combination of both. A liquid N_2 cooled InSb detector with a FET preamp was used to detect the fluorescence signal. The measured response time of this system was about 0.5 μseconds. Over the pressure range of interest, the signal to noise ratio was excellent (greater than 5), thus making signal averaging unnecessary. In general, both the monochromator and filter were used to separate the v=2 → v=1 fluorescence from that of v=1 → v=0. Because of the difference in intensity of the two bands at low HF pressures, the monochromator alone was sufficient to isolate v=1 → v=0 fluorescence in the non-overlapping regions of the spectrum. Resolution into single transitions was possible, although with a definite sacrifice in signal to noise ratio. After the preliminary investigation for this work was complete, experimentation with the monochromator-filter cell combination showed that the v=2 → v=1 fluorescence could be measured separately by using the filter cell alone (filled to about 30 Torr of HF). Fluorescence decay from v=1 → v=0 was measured by using the unfiltered signal and observing the signal at sufficiently long times (see below). These techniques allowed for the excellent signal to noise ratio mentioned earlier.

In order to understand the temporal behavior of the fluorescence, one must consider the relevant rate equations.

$$\frac{dN_1}{dt} = -N_1N_0\sigma v - 2N_1N_1\Sigma v + 2N_0N_2\Sigma v \qquad (1)$$

$$\frac{dN_2}{dt} = N_2N_0\sigma' v - N_0N_2\Sigma v - N_1N_1\Sigma v \qquad (2)$$

where v = the molecular rms velocity

$N_{0,1,2}$ = population in the ground, first, second vibrational state

Σ = cross section for vibration - vibration energy transfer, corresponding to the process $2HF(v=1) \rightarrow HF(v=0) + HF(v=2)$

σ, σ' = cross sections for vibration to translation (or rotational) energy transfer for the first and second vibrational levels

and with initial conditions

$$N_1 = N_1^0 \quad \text{and}$$

$$N_2 = 0$$

Notice that we assume that the rotational equilibration time is much faster than any of the vibrational times used above. The supporting evidence for this is described below. The above equations are a set of coupled inhomogeneous nonlinear differential equations whose solution can be simplified by the fact that at any given time $N_2 << N_1 << N_0$, an assumption valid under our experimental conditions (see below). This allows one to linearize the equations and obtain a useful approximate result.

After linearization the solutions to the above equations are found to be

$$N_1 = N_1^0 \, e^{-\gamma T} \tag{3}$$

$$N_2 = \frac{(N_1^0)^2 \, e^{-2\gamma T}}{N_0 (1+\sigma'/\Sigma)} \left(1-e^{-[\Gamma-2\gamma]T}\right) \tag{4}$$

where

$$\gamma = \sigma N_0 v$$

$$\Gamma = (\Sigma + \sigma') N_0 v$$

The adoption of the gamma notation at this point allows one to include in γ any de-excitation due to diffusion of excited HF to the cell walls[4]. As shown in Eqs. (3) and (4), the temporal behavior consists of the sum of a rising exponential, whose time constant is a function of the vibration - vibration collisional decay of N_2; and a decaying exponential whose time constant is twice the vibrational decay of N_1. An actual oscilloscope trace of the v=2 fluorescence is given in Fig. 2. Notice that Γ is approximately a factor of 10 greater than γ.

To test the above model, measurements were made of the pressure dependence of the fluorescent decay rates for v=1 and v=2 levels. As for all measurements reported in this paper, the fluorescing medium consisted of pure HF nominally at 290°K. The results of this measurement, as displayed in Fig. 3, show that over the pressure range of interest the decay rate of v=2 is twice that of v=1. The errors shown in Fig. 3 reflect chiefly the difficulties in reading oscilloscope traces; careful measurements at several selected pressures using the monochromator-filter combination showed that the factor was 2 to within 10%. That the curves in Fig. 3 do not pass through zero, and, in fact, have a slight upward curvature at their low pressure end, indicates the expected importance of diffusion of vibrationally excited HF molecules to the cell wall at low pressures. However, for our tube diameter diffusion is not so pronounced as found in

studies with other gases, because of the comparatively large magnitude of the collisional de-excitation coefficient[4]. Because of diffusion, the best estimate of the collisional relaxation rate is obtained from measurements in the high pressure region. The collisional decay rate is found to be 5.2×10^4 sec^{-1} $Torr^{-1}$. This value agrees closely with that reported by Stephens and Cool[5] for HF at 350°K, indicating that the temperature dependence of γ is small[6].

In order to show that laser-induced gas heating had no appreciable effect in our measurement, an experiment was performed identical to that shown in Fig. 3, except that the sample cell always contained an additional 16 Torr of argon[3,7]. The contribution to γ attributable to HF-HF collisions was identical to that found in the pure HF experiment. The effect of argon on the total decay rate was to eliminate the diffusion contribution and to add a small decay rate due to HF-Ar collisions.

In measuring Γ, a convenient method is to use the time, T_m, at which the maximum signal intensity occurs for the v=2 fluorescence. This can be derived from Eq. (4) to be

$$T_m = \frac{1}{\Gamma} \ln\left(\frac{2\gamma}{\Gamma - 2\gamma}\right) \quad . \tag{6}$$

In the region of measurement where the diffusion contribution is negligible, the expression in the logarithm is independent of pressure, and hence, T_m is inversely proportional to Γ. This expression can be simplified by realizing $\Gamma > 2\gamma$, and hence

$$T_m \simeq \frac{1}{\Gamma} \ln \frac{2\gamma}{\Gamma} \tag{7}$$

Fig. 4 presents the results of the measurement of Γ using the measurement of the T_m and 2γ, and relation 7. There one finds $\Gamma = 6.6 \times 10^5$ sec^{-1} $Torr^{-1}$. It is important to recall from Eq. 2 that Γ represents the total decay out of the v=2 level. It therefore includes the combined effects of diffusion, V-T (or V-R) transfer and the vibration - vibration (V-V) transfer represented by HF(v=2) → HF(v=0) → HF(v=1). However, the predominant contribution to Γ will be from V-V transfer[8] because the V-T decay rate of v=2 will be of the same order as that for v=1, and because, for pressures above 100 mTorr, the decay rate, due to diffusion, is even smaller than V-T relaxation. Note, however, that at low pressures, < 40 mTorr in a cell of the type used above, relaxation of v=2 due to diffusion would be appreciable, and the corresponding value of Γ is no longer a good estimate of the V-V transfer rate.

Experimental proof of the assumption of rapid rotational relaxation was obtained by pumping the HF sample with the P(1) v=1 → v=0 laser transition, and observing the delay of fluorescence from the P(6) transition. Only at 30 μ pressure could a measurable, approximately 5 μ sec delay, be observed. Thus, the rotational transfer time is approximately one order of magnitude faster than Γ, a value expected from pressure broadening measurements[6]. The proof that, under our experimental condition, the approximation $N_0 >> N_1 >> N_2$ is valid, was obtained by two separate techniques. First, the fluorescent intensity for N_2 and N_1 was measured to be 1/15 at 50 μ pressure; thus implying a ratio of N_2/N_1 (and from Eq. (4), N_1N_0) of 1/30 from consideration of the ratio of radiative lifetimes for the two states. Second, it was found that the temporal behavior of the v=2 →

v=1 fluorescence at a given pressure was unchanged by a five-fold decrease in the incident laser power. This observation is consistent with the linearization of the Eqs. (2) and (3), as described above.

In conclusion, the above measurements can be applied to the other hydrogen halide gases, HBr, HCl, and HI. Each of these molecules has been observed to lase strongly on a ground state transition, and each possesses the structural similarity to HF, i.e. large rotational and vibrational spacing, which made the above experiment so uniquely adapted to HF. Also, our results have a direct relevance to the inversion and relaxation phenomena occurring in HF chemical laser processes which at present are not completely understood.

We gratefully acknowledge the following people for their contributions to this work: Professor Michael Feld and Nikolaus Skribanowitz for many timely discussions on HF laser experimentation; Professor Victor George for kindly providing excellent design drawings for the Faraday cage (used to shield laser discharge noise) and the helical pin laser tube; and Mr. Stephen Fried for a detailed discussion of the HF handling techniques. We also thank Mr. L. W. Ryan, Jr. for his valuable technical contributions.

REFERENCES

1. L. Hocker, M. Kovacs, C. Rhodes, G. Flynn, and A. Javan, Phys. Rev. Letters 17, 233 (1966).

2. See for example J. Goldhar, R. M. Osgood, Jr., A. Javan, Appl. Phys. Letters 18, 167 (1971).

3. J. R. Airey and S. Fried, Chem. Phys. Letters 8, 23 (1971), and Arco Research Final Report for Army Contract DAAH01-68-C-2144.

4. Since the contribution to γ from diffusion has an inverse pressure dependency, this contribution is dominant only at low pressures. In this work the pressure for which the pressure contribution to γ was 50% was about 100 mTorr. A detailed description of diffusion in CO_2 gases is provided in M. A. Kovacs, Ph.D. thesis, Department of Physics, M.I.T., unpublished. An abbreviated published version is M. Kovacs, D. Ramachandra Rao, and A. Javan, J. Chem. Phys. 48, 3339 (1968).

5. Ronald R. Stephens and Terrill A. Cool, J. Chem. Phys., to be published.

6. This value is twice as slow as the only other measured decay rate for HF at room temperature (see following reference). Because of a lack of experimental detail provided in this above reference, it is difficult to offer an explanation for this discrepancy. However, for decay measurements above about 300 microns in a typical 1" diameter cell, we find that self absorption by HF molecules in the ground vibrational state can be sufficiently severe that the total fluorescent signal is dominated by the v=2 → v=1 signal. Also, use of an argon bath at 5-40 Torr enhances the absorption of the HF laser radiation (by decreasing the extent of of saturation) and hence increases the ratio of N_2/N_1. Under such conditions the decay of the total fluorescence will not represent v=1 decay rate, γ .

7. J. K. Hancock and W. H. Green, J. Chem. Phys. 5, 2474 (1972).

8. From (2) we note that at T_m $N_2 = \frac{N_1^2}{N_0(1+\sigma'/\Sigma)}$ hence, as assumed, $\Sigma > \sigma'$ $\frac{N_1}{N_0} \approx \frac{N_2}{N_1}$ or $\frac{1}{30}$ as discussed earlier. If, on the other hand, $\sigma' >> \Sigma$ then the v=2 radiation is heavily damped and $\frac{N_1}{N_0} >> \frac{N_2}{N_1} \approx \frac{1}{30}$. We note here only that a figure of $\frac{N_1}{N_0} \approx \frac{1}{30}$ is in good accord with the degree of absorption expected from our laser on the basis of the known HF pressure broadening at 50 μ and the degree of broadening expected from a laser with an intensity as large as ours. Hence the assumption of $\Sigma > \sigma'$ is in accord with experimental observations.

9. G. A. Kuipers, J. Mol. Spect. 2, 75 (1958).

FIGURE CAPTIONS

Fig. 1: Schematic of Apparatus. a. Helical HF laser. b. Monochromator and Detector. c. Filter cell. d. Folding mirror for double pass laser pumping. e. Cell with projecting mirror opposite fluorescent output window. f. Capacitance manometer. g. Cold trapped roughing pump. h. Diffusion pump. i. HF distillation chamber. j. Monel Bellows valve. k. Irises.

Fig. 2: Oscilloscope trace of $\mathring{v}$=2 fluorescence. A 10 cm filter cell at ∿30 Torr was used to eliminate the signal from v=1. Pressure is about millitorr and timebase is 10μsec/cm.

Fig. 3: Plot of measure decay rates of v=2 and v=1 vibrational levels in HF with HF pressure as the independent variable. See text for discussion of pressure error limits. Error limits for time measurement varied. However, 10% is a typical value. Curve fitting was done visually.

Fig. 4: Plot of Γ versus pressure. Eq. (7) was used to calculate Γ from the measured T_m.

I
H
G
J
F
K
E
D
A
C
B

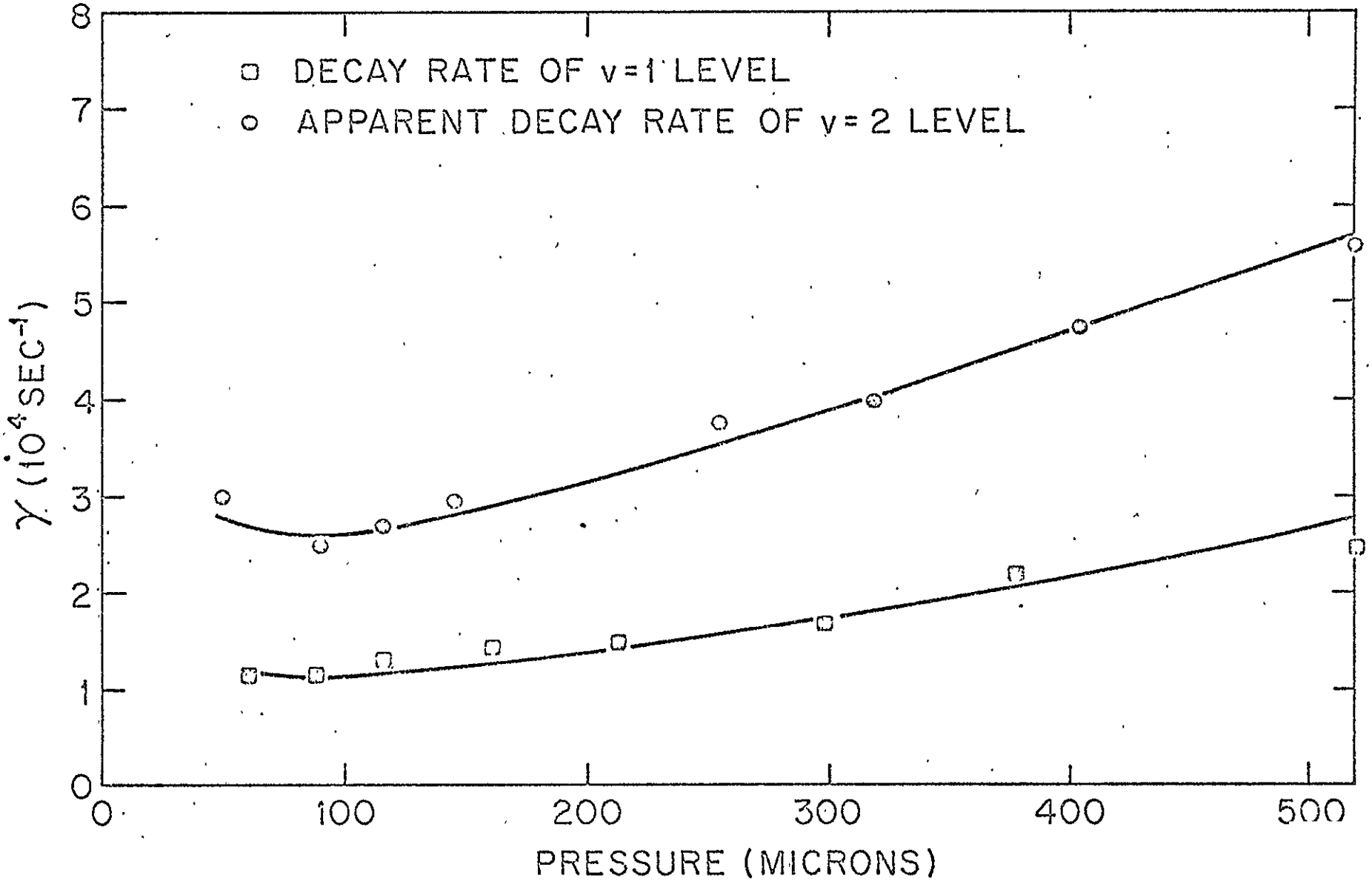
DECAY RATE OF v=1 LEVEL
APPARENT DECAY RATE OF v=2 LEVEL
γ (10⁴SEC⁻¹)
PRESSURE (MICRONS)
0
1
2
3
4
5
6
7
8
0
100
200
300
400
500

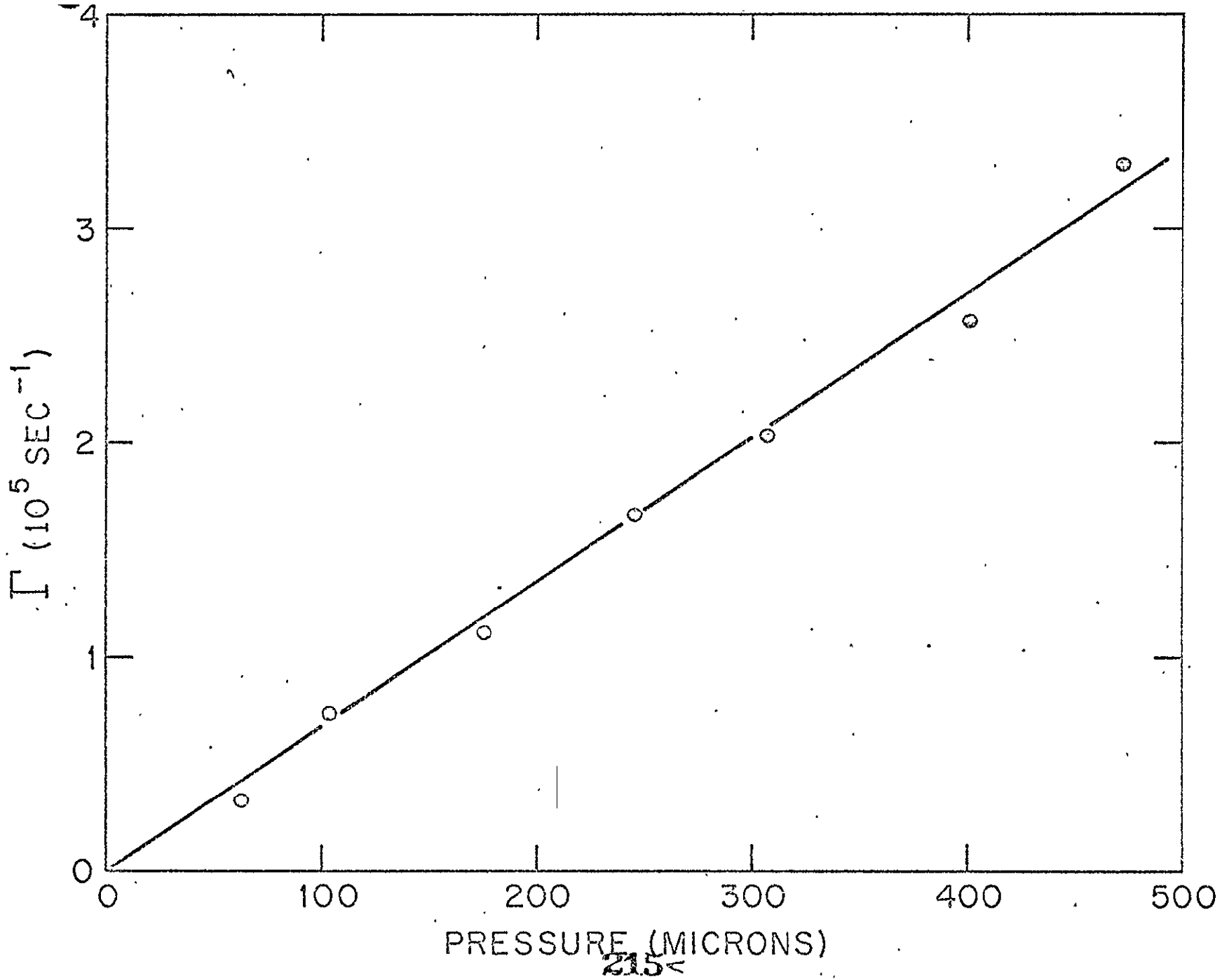
4
3
2
1
0
Γ (10^5 SEC^-1)
0
100
200
300
400
500
PRESSURE (MICRONS)

13. R. M. Osgood, Jr. and A. Javan

Measurement of V-V Transfer Rate from HF v = 3 Using Simultaneous Optical Pumping on the HF v = 2→ 1 and v = 1→ 0 bands

Published in Appl. Phys. Letters

MEASUREMENT OF V-V TRANSFER RATE FROM HF v=3 USING SIMULTANEOUS OPTICAL PUMPING ON THE HF v=2→1 and v=1→0 BANDS

R.M. Osgood, Jr. [†] and A. Javan

Department of Physics
Massachusetts Institute of Technology
Cambridge, Mass. 02139

(Published Appl. Phys. Lett.)

P.B. Sackett

Air Force Cambridge Research Laboratories
L.G. Hanscom Field
Bedford, Mass. 01731

[†] Hertz Foundation predoctoral fellow

ABSTRACT

A measurement of the (predominantly) vibrational to vibrational decay rate of the v=3 level in HF gas yields a value of 1.6×10^{6} sec^{-1} at one torr. The technique utilized was to optically-pump the HF sample with the output of a pulsed HF laser oscillating simultaneously on a line in both the v=2→1 and v=1→0 bands. An analytic description of the time behavior of the v=1, v=2, and v=3 levels using a treatment based on simplified rate equations described.

In a recent publication[1] we reported direct measurement of the vibration-vibration decay rate, Γ_2, out of the second vibrational level in HF, i.e., HF(v=2) + HF(v=0) $\overset{\Gamma_2}{\rightarrow}$ 2HF(v=1). Briefly, this was accomplished by optically pumping a room temperature gaseous HF sample with the output from a pulsed HF chemical laser oscillating with a transition in the v=1→0 band. The laser pulse directly excites the HF v=1 state; population of the v=2 state then results from the collision of two laser excited molecules. By monitoring the vibrational fluorescence from molecules in the v=2 state, we could observe the time dependence of the v=2 population for various gas pressures; and hence, determine the corresponding rate constant, Γ_2/N_0, where N_0 is the number of molecules in the HF ground vibrational state.

In this letter we report an extension of this method which yields the vibration-vibration decay rate Γ_3, out of the HF third vibrational level. In order to provide a sensitive measurement of this decay rate, we used the technique of directly exciting the HF(v=2) state by optically pumping with the output of a pulsed HF laser oscillating simultaneously on one transition in both the v=1→0 and v=2→1 bands. Thus, in analogy with the v=2 state in our previous experiment, the v=3 state is dominantly populated by the reverse of the process, HF(v=3) + HF(v=0) $\overset{\Gamma_3}{\rightarrow}$ HF(v=1) + HF(v=2). Measurement of the rise time of the fluorescence emanating from v=3 can then be used to determine sensitively the rate Γ_3.

In order to clarify our method of measurement, let us consider the rate equations for the states v=2,3 for times after the laser pulse

$$\frac{dN_1}{dT} = - N_1 \gamma_1 \tag{1}$$

$$\frac{dN_2}{dT} = -\Gamma_2 N_2 - \gamma_2 N_2 + \frac{N_1 N_1}{N_0} f_2 \Gamma_2 \tag{2}$$

$$\frac{dN_3}{dT} = - \Gamma_3 N_3 - \gamma_3 N_2 + \frac{N_2 N_1}{N_0} f_3 \Gamma_3 \tag{3}$$

where N_i is the population in the i^{th} vibrational state, Γ_i is V-V decay rate defined above, γ_i is the decay rate of the i^{th} vibrational state due to the process HF(v=i) + HF(v=k) $\xrightarrow{\gamma_i}$ HF(v=i-1) + HF(v=k) (i.e. V-T,R transfer) and f_i are Boltzmann factors arising from the effect of anharmonicity in the detailed balancing of the forward and reverse v-v transfer reactions under investigation ($f_2 \approx 2$, $f_3 \approx 5$). In writing these equations, we have assumed that the initial populations, N_i^0, induced by the laser satisfy the inequality $N_i^0 << N_{i-1}^o$. Under this assumption the equation for N_1 is decoupled from that of N_2 and N_3 and its solution is a simple exponential, as expressed in Eq. 1. Inserting N_1 in Eq. 2 and writing the initial laser-induced population of N_2 as N_2^0, we find:

$$N_2 = \left[\left(\frac{f_2 N_1^{0\,2}}{N_0 (1 - \frac{\gamma_2 - 2\gamma_1}{\Gamma_2})} \right) \left(1 - e^{-(\Gamma_2 + \gamma_2 - 2\gamma_1)T} \right) - N_2^0 e^{-(\Gamma_2 + \gamma_2 - 2\gamma_1)T} \right] e^{-2\gamma_1 T} \tag{4}$$

The time dependence of the v=3 level can now be obtained from (4) after inserting the above expressions for N_1 and N_2 in that equation. This gives a multi-exponential expression for N_3 whose functional

form is dependent on the magnitudes of N_2^0 and N_1^0, and hence on the relative intensities of the v=2→1 and v=1→0 lines in the incident laser pulse. However, considerable simplification of the time dependence of N_2 and N_3 will result if the relative intensities of the two laser lines in the incident laser pulse can be adjusted such that $N_2^0 \approx f_2 N_1^{0\,2}/N_0$. Under this condition, the expression for N_2, Eq. (4), will reduce to a single exponential given by $N_2 = f_2 \frac{N_1^2}{N_0} e^{-2\gamma_1 T}$. The corresponding expression for N_3 will then be

$$N_3 = A\,(1-e^{-(\Gamma_3+\gamma_3-3\gamma_1)T})(e^{-3\gamma_1 T}) \qquad (5)$$

where $A = f_1 f_2 \frac{N_1^{0\,3}}{N_0^2} \left(\frac{1}{1+\frac{(\gamma_3-3\gamma_1)}{\Gamma_3}}\right)$

This expression has a single exponential rise time, with time constant $\Gamma_3+\gamma_3-3\gamma_1$, as well as a decay time of $3\gamma_1 \ll \Gamma_3$. In practice the initial N_2^0 could be adjusted to the appropriate value by varying the intensity of the v=2 → v=1 laser radiation in the incident laser pulse until the fluorescence signal from v=2 showed a single exponential decay starting immediately after the laser pulse. After such an adjustment, detailed analysis of the fluorescence signal from v=3 showed that its time dependence agreed well with that in expression (5).

It may be of interest to note that for $N_2^0 = 0$, i.e. pumping with a v=1→0 line only, the rise time of N_3 is given by two

exponentials with rate constants Γ_2 and Γ_3. Numerical solutions of the rate equation show that for Γ_3 on the order of 1.5 times Γ_2, as is the case in HF, the corresponding magnitude and the shape of the v=3 fluorescence rise is determined primarily by Γ_2 and not by Γ_3. Hence, pumping with a line in the v=1→0 band only is not a desirable method for accurately determining the rate.

The experimental apparatus was similar to that reported in detail in Ref. 1. One essential difference was that the time dependence of population of the v=3 state was observed by detecting the 0.9μm overtone band v=3 → v=0, with an uncooled S-1 photomultiplier. Care was taken to insure that the ratio of the number of excited molecules to the number of ground state molecules was sufficiently small so that the emission from v=4→1 was negligible. Verification of this fact rested upon the single exponential appearance of the decaying part of the 0.9μm fluorescence signal. In addition, because of the rapid rise time in the v=3 fluorescence, it was necessary to shorten the duration of the H_2-SF_6 pulsed HF laser used in the experiment by operating at high H_2/SF_6 ratios. For sample pressures above 350 mTorr, the decay of the v=3 fluorescence was found to be, within experimental error, a factor of three greater than the value reported for the decay of the v=1 state in Ref. 1. This behavior is due to the establishment of vibrational equilibrium at a time longer than the V-V decay time. Accordingly, for $t > 1/\Gamma_i$ we obtain $N_i/N_{i-1} \propto e^{-\omega_0/kT_v}$ where ω_0 is the vibrational energy and T_v is a vibrational "temperature" parameter which decreases in time and approaches room temperature.

(For simplicity, we ignore here the vibrational anharmonicity in the expression for energy.) From this consideration it follows (as shown in Ref. 1 and above) that if $N_1 \propto e^{-\gamma_1 t}$, population densities for N_2 and N_3 decay at rates $2\gamma_1$ and $3\gamma_1$, respectively.

In the pressure region below 250 mTorr, the decay rate of the measured fluorescence from v=3 was found to differ from three times that of the V-T,R decay rate determined in Ref. 1. This may be explained by noting that in this pressure region the molecular diffusion rate across the 5 mm laser beam becomes comparable to the rate of collisional decay of the various vibrational levels.[2] To verify that diffusion was the source of deviation, we note that for diffusion phenomena the magnitude of the component of the decay rate due to diffusion is expected to be inversely proportional to the pressure of a buffer gas such as argon, and to the square of the characteristic length, the beam diameter in this case. Both relationships were found to be valid experimentally.

The measurement of the combined rates $(\Gamma_3+\gamma_3)$, as a function of pressure is displayed in Fig. 1. As mentioned earlier the data for this graph were taken after ascertaining that the relative intensities of the v=2→1 and v=1→0 laser components were adjusted so as to obtain pure single exponential decay of the v=2 fluorescence signal. The method of determining $(\Gamma_3+\gamma_3)$ was similar to that described in Ref. 1; namely, the time of maximum intensity, T_m, for each fluorescence trace was measured, and a formula expressing T_m as a function of $(\Gamma_3+\gamma_3)$ (derived from 5) was used to obtain $(\Gamma_3+\gamma_3)$ for that trace. Note that much of the data in the above

curve was taken in a pressure region where the diffusion effect was unimportant. However, even in the regions of lowest pressure, it was found that the time dependence of the fluorescence could still be fitted fairly accurately with two exponentials as in Eq. (5), except that here the decay rate had to be measured empirically and could not be set equal to $3\gamma_1$. As is seen from Fig. (1), the measured rate constant $\frac{\Gamma_3+\gamma_3}{N_0} = 1.6 \times 10^6$ sec^{-1}torr^{-1} agrees excellently with the observation over a wide range of pressures. This rate of transfer out of N_3 is a factor of 2 greater than the corresponding value measured[1] for N_2.[3,4] We note that it seems reasonable to assume, as for the case of N_2, that this rate is essentially the V-V rate out of the v=3 state, i.e., Γ_3; to attempt to ascribe this high rate to the V=T,R rate of v=3, γ_3, would call for an increase by a factor of 60 over the V-T,R rate of v=1. In addition, under such conditions the loss of quanta to the system through γ_3 would heavily quench the intensity of v=3 fluorescence.

In conclusion, we note here that experimental method and analysis used here are applicable to laser-induced fluorescence experiments with other gases (particularly the other hydrogen halides), and perhaps even polyatomic molecules. Also, a straightforward extension of the above work is to utilize simultaneous pumping with one line in each of the v=3→2, v=2→1, and v=1→0 bands, and thus, enable measurement of the rate, $\Gamma_4+\gamma_4$. Such an experiment is currently underway in this laboratory.

The authors are deeply grateful to Professor A. Szöke for

224

many useful and stimulating discussions during the course of this work.

REFERENCES

1. R.M. Osgood, Jr., A. Javan and P.B. Sackett, Appl. Phys. Letters 20, 469 (1972). Note the change in notation between this paper and that of the previous work. $\Gamma_2+\gamma_2$ of this paper equals the Γ of the previous paper. γ_2, as described later, is the V=T,R of the v=2 level.

2. A more detailed study of this diffusion process (which is fundamentally different than the usual diffusion to and quenching at the walls) is presently underway and will be discussed at length elsewhere. In brief, this process may be explained by noting that as molecules in v=2, v=3, etc. diffused out of the region of the laser excitation, they encounter a bath of unexcited (vibrationally "cold") HF molecules. Rapid V-V re-equilibration via V-V collisional decay then causes these highly excited molecules to give up their quanta to molecules formerly in the v=0 state. Thus, while the total number of vibrational quanta is preserved, the total number of molecules in V > 1 is still reduced. Notice that the increase in the population in V=1 is insignificant since $N_1 >> N_2$, N_3, etc.

3. Recalculation of $\Gamma_2+\gamma_2$ using the exact expression for the time of fluorescence peak versus $\Gamma_2+\gamma_2$ gives $\Gamma_2+\gamma_2 = 8 \times 10^5 \text{sec}^{-1}\text{torr}^{-1}$. This is roughly a factor of 20% higher than the value calculated in Ref. 1 on the basis of a more convenient approximate formula.

4. A recent measurement by Airey and Smith [J. Chem. Phys. 57, 1669 (1972)] uses computer analysis of chemiluminescence from an HF-yielding reaction to calculate values for $\frac{\Gamma_2+\gamma_2}{N_0}$ and $\frac{\Gamma_3+\gamma_3}{N_0}$ which are a factor of 0.75 and 0.4, respectively, times the values obtained by our technique. In view of the relatively indirect nature of the technique of Airey and

Smith, the agreement between the two sets of numbers seems good.

FIGURE CAPTION

Figure 1. Plot of $\Gamma_3+\gamma_3$ in sec^{-1} versus HF pressure in millitorr.

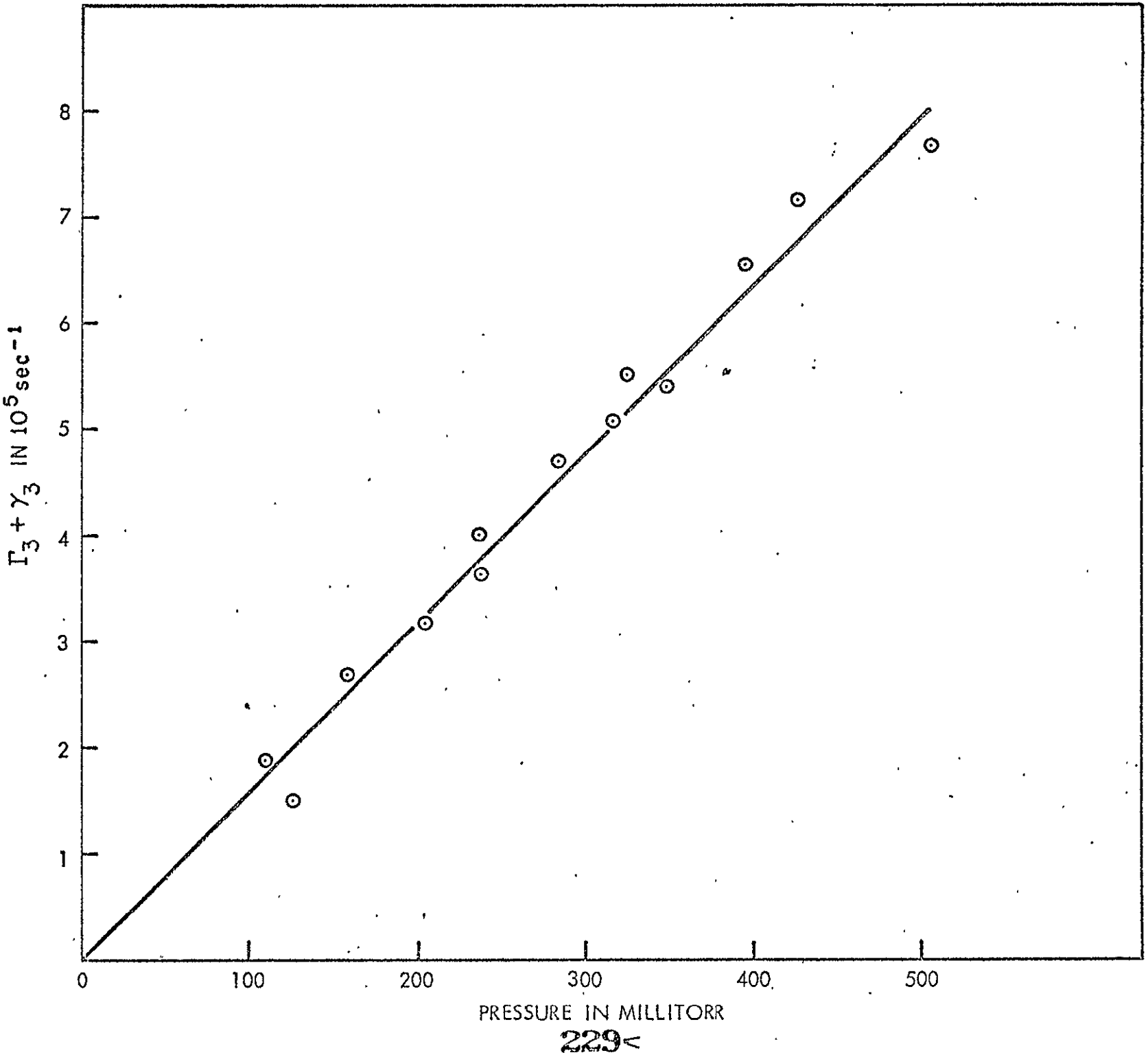
8
7
6
5
4
3
2
1
$\Gamma_3 + \gamma_3$ IN $10^5 sec^{-1}$
0
100
200
300
400
500
PRESSURE IN MILLITORR

14. N. Skribanowitz, M.J. Kelly and M. S. Feld

A New Laser Technique for the Identification of Molecular Transitions

Published in Phys. Rev. A

A NEW LASER TECHNIQUE FOR THE IDENTIFICATION OF MOLECULAR TRANSITIONS*

N. Skribanowitz, M. J. Kelly, and M. S. Feld

Department of Physics

Massachusetts Institute of Technology

Cambridge, Massachusetts 02139

(Published Phys. Rev. A)

* Work supported in part by the National Science Foundation and the National Aeronautics and Space Administration.

ABSTRACT

A laser technique is proposed which may be useful for the assignment of molecular spectra in the visible and infrared regions. The method is based on the resonant interaction of two monochromatic fields with a Doppler-broadened three-level system. Under the appropriate conditions the absorption lineshape of one of the transitions shows a complex structure over a narrow section of the Doppler profile, and for sufficiently high laser power the lineshape splits into a number of narrow peaks. Analysis of the resulting intensity pattern leads to unambiguous assignment of the angular momentum quantum numbers of the three levels involved. A simple set of rules is given to facilitate interpretation of spectra. The lineshapes discussed are also relevant to monochromatic optical pumping of gases and unidirectional laser amplifiers.

I. Introduction

This paper proposes a new method for the determination of J-values of molecular levels using lasers. It is applicable to Doppler-broadened transitions in the infrared, visible, and ultra-violet regions, and it can be used even where Stark and Zeeman effects are absent or very small. In this method one observes the lineshape of a molecular transition as influenced by an intense laser field (called "pump field" in the following) resonating with a coupled transition[1,2]. This lineshape can be probed conveniently by a weak tunable laser field colinear with the pump field [Fig. 1(a)][3]. For a sufficiently intense pump field a number of narrow peaks are superposed on the usual Doppler background [Fig. 1(b)]. The number and relative intensities of these peaks completely specify the J-values of the levels involved. Such lineshapes also occur in the monochromatic optical pumping of gases using high intensity lasers.

II. Qualitative Discussion

Consider a molecular system consisting of a pair of rotational levels in the ground vibrational state and a third rotational level in an excited vibrational state[4]. These levels may be designated by their rotational angular momentum quantum numbers, J_1 and J_2 for the two lower levels and J_0 for the upper level [Fig. 1(a)]. Due to M-degeneracy, each of the levels contains $2J_i + 1$ sublevels specified by their M-values. Both J_1 and J_2 are connected to level J_0 by optical transitions, which are Doppler broadened. The pump field of amplitude E_L at frequency Ω_L resonates at some portion of the Doppler profile of the $J_2 \rightarrow J_0$ transition, centered at frequency ω_2. The

probe field, E_p, of frequency Ω_p, scans the coupled transition $J_1 \rightarrow J_0$, centered at frequency ω_1. The probe field is assumed to be weak and non-saturating, whereas the pump field must strongly saturate its transition.

For the purpose of analysis the axis of quantization of the system is chosen to be parallel to E_L. In this case the pump field induces only transitions having the selection rule $\Delta M = 0$, so that the system may be decomposed conveniently into a number of isolated three-level subsystems of the type $(J_2, M_2) \rightarrow (J_0, M_0) \rightarrow (J_1, M_1)$. Here the arrows denote transitions and (J_i, M_i) specifies a sub-level of level J_i having an M-value equal to M_i. Note that M_i can take on $2J_i+1$ values and that the $\Delta M=0$ selection rule implies that $M_2=M_0$ for all $J_2 \rightarrow J_0$ transitions. The exact details of this decomposition into subsystems, which depends on the J-values of the levels involved and on the relative polarizations of pump and probe fields, are discussed in Section IV.

Consider now one of these subsystems, whose levels shall be designated by 0,1,2 with level 0 being the level common to the two transitions. To be definite, assume that both transitions are in the absorbing phase as they would be, for example, in thermal equilibrium.[5] It is further assumed that the homogeneously broadened widths of the transitions, due e.g. to collisions or radiative decay, are small compared to the Doppler widths. This implies that only molecules whose thermal velocities can Doppler shift the laser frequency into resonance interact strongly with the pump field. Thus, the intense pump field, E_L, which resonates with the $2 \rightarrow 0$ transition, selectively increases the population of the upper level, 0, over a

narrow section of the thermal velocity distribution. The absorption at Ω_p is proportional to the population difference between levels 0 and 1. Therefore, as the probe field is now tuned through the 1-0 transition the increase of population in level 0 manifests itself as a decrease in absorption over a narrow frequency range[6] [Fig. 1(b)]. The center frequency of this decrease in absorption ("change signal"), depends upon the detuning of the pump field from the 2 → 0 center frequency, ω_2. It is given by:

$$\Omega_p^0 = \omega_1 + (\Omega_L - \omega_2) \frac{\omega_1}{\omega_2} \quad . \qquad (1)$$

This follows directly from the Doppler effect. The width of the change signal is of the order of the homogeneously broadened or natural width of the levels involved. It can be considerably narrower than the Doppler width at low pressures (less than 1 Torr); this is the region of interest[8].

As explained in detail below, the shape of the change signal depends on the level populations, the extent of saturation of the 2 → 0 transition due to the pump field, and the frequency ratio of pump and probe transitions. The latter parameter is of particular importance: for $\omega_1/\omega_2 > 1$ the lineshape is a Lorentzian which broadens with increasing saturation. This case is of no interest for the present discussion. However, when $\omega_1/\omega_2 < 1$ the lineshape can deviate considerably from Lorentzian, and for sufficiently large values of the pump field intensity the change signal splits symmetrically into two peaks (Fig. 2). Both the magnitude of the two peaks and their separation increase with increasing values of the parameter,

$$\dot{\beta} = \frac{|\mu_{20}| E_L}{2\hbar} \qquad (2)$$

where μ_{20} is the matrix element connecting levels 2 and 0. This dependence implies in particular, that two subsystems with different matrix elements will exhibit different splittings, everything else being the same (Fig. 3).[9]

The saturation behavior of the molecular system, which is composed of a number of subsystems of the type described above, can now be understood. The absorption lineshape for the $J_1 \rightarrow J_0$ transition is obtained by superposition of the contributions from the individual subsystems. Each subsystem produces a pair of peaks located symmetrically around Ω_p^0, their separation depending on the magnitude of the $(J_2, M) \rightarrow (J_0, M)$ matrix element. These matrix elements depend on the M's and are generally different from one another. Therefore, the total lineshape will show an even number of peaks. This number is completely determined by J_0, J_1 and J_2. The splittings and intensities of the peaks depend on the relative orientations of the pump and probe fields, as well as on the type of transition involved (P, Q, or R-branch). By analyzing the intensity pattern one can readily and unambiguously determine the J-values of the three levels involved. The matrix elements connecting levels 2 and 0 can also be determined if the electric field E_L is known.

III. Exact Expression for Lineshape: Non-degenerate System

In the introduction the lineshape effect was made plausible by considering changes in level populations induced by the strong pump

field. It must be emphasized, however, that the details of the changes in the lineshape of transition $1 \rightarrow 0$ also depend on additional radiative processes, in particular, two-quantum Raman transitions between levels 2 and 1 with level 0 as a resonant intermediate state. It is the inclusion of these coherent effects which produces the splitting in the lineshape, as described above, for the case $\omega_2 > \omega_1$. This splitting is a manifestation of the high frequency Stark effect, and is also known to occur in homogeneously-broadened systems (i.e., in the absence of Doppler broadening)[10]. A detailed theoretical description of this effect for non-degenerate systems has been given recently by Feldman and Feld[2]. The mathematical details of the analysis are of no concern here, and only the results will be discussed in the following.

Let us first summarize the results of Ref. (2) for a non-degenerate three-level system in which, for simplicity, the velocity distributions of all three levels are taken to be Maxwellian at temperature T. Let $I(\Omega_p)$ be the intensity of the weak probe field E_p. The absorption coefficient $\alpha(\Omega_p)$ may be defined, as usual, by the incremental decrease of intensity, ΔI, in a thin sample of thickness Δx:

$$\Delta I = \alpha I \Delta x \qquad (3)$$

In the absence of a pump field ($E_L = 0$), $\alpha(\Omega_p)$ is the usual Doppler-broadened absorption coefficient for a two level system:

$$\alpha_0(\Omega_p) = 4\pi^{3/2} \frac{|\mu_{10}|^2 (N_0 - N_1)}{\hbar u} e^{-\left(\frac{\Omega_p - \omega_1}{k_1 u}\right)^2}, \qquad (4)$$

237<

where μ_{10} is the matrix element connecting levels 1 and 0, N_0 and N_1 are the level population densities in the absence of applied fields; ω_1 is the center frequency of the $1 \to 0$ transition, and k_1 its wave number. Furthermore, $u = (2kT/M)^{1/2}$ is the most probable speed of a molecule, where M is its mass, k the Boltzmann constant, and T the temperature. Note that $k_1 u$ is the Doppler width of the $1 \to 0$ transition in angular frequency units. Note also that for thermal equilibrium N_1 is larger than N_0 and $\alpha_0(\Omega_p)$ has a negative sign, i.e. ΔI is negative, as it should be.

In the presence of the intense pump field, E_L, $\alpha(\Omega_p)$ is equal to $\alpha_0(\Omega_p)$ multiplied by an additional lineshape factor F:[11]

$$\alpha(\Omega_p) = \alpha_0(\Omega_p) \cdot F, \tag{5}$$

where F is given by:

$$F = \mathrm{Im}\left[\frac{T}{Y}\right] + \frac{N_0 - N_2}{N_0 - N_1} \left[\frac{k_1}{k_2}\right]^2 \frac{2\beta^2}{\gamma_0^2 Q} \mathrm{Re}\left[\frac{R}{Y}\right], \tag{6a}$$

$$T = \Omega_p - \Omega_p^0 + \frac{i}{2}\left[\gamma_1 + \gamma_0 + \frac{k_1}{k_2}(\gamma_2 - \gamma_0)\right], \tag{6b}$$

$$Y = [S^2 - T^2]^{1/2} \qquad \text{with } \mathrm{Re}(Y) > 0, \tag{6c}$$

$$S^2 = \frac{4k_1(k_2 - k_1)}{k_2^2}\beta^2, \tag{6d}$$

$$Q^2 = 1 + \frac{4\beta^2}{\gamma_0 \gamma_2}, \tag{6e}$$

$$R = \gamma_0\left[\frac{C_+ + \frac{i}{2}\gamma^2(1-Q)}{C_+ + D_+} - \frac{C_- + \frac{i}{2}\gamma^2(1+Q)}{C_- + D_-}\right], \tag{6f}$$

with $C_{\pm} = T + \frac{i}{2} \frac{k_1}{k_2} [\gamma_0(1\pm Q) - \gamma_2(1\mp Q)]$, (6g)

and $D_{\pm} = -\frac{k_2}{2(k_2-k_1)} (T\pm iY)$. (6h)

Equation (6) has been derived under the assumptions $ku >> \gamma$ and $\beta^2 << \gamma(ku)$ for all k's and γ's. Here k_i is the wavenumber of the $i \to 0$ transition, N_i is the population density of level i in the absence of applied fields, and γ_i is the decay rate of level i, due to, for example, collisions or radiative decay. Ω_p^0 and β are defined in Eqs. (1) and (2), respectively. Note that $\alpha_0(\Omega_p)$ depends only on $|\mu_{10}|$ and F depends only on $|\mu_{20}|$.

In the limit of a vanishing pump field, i.e. $E_L \to 0$, F approaches unity as it should. Further analysis shows that the behavior of F is dominated by Y^{-1}, which appears in both terms of Eq. (6a). In particular, for high saturation the lineshape of F is closely approximated by $|Y|^{-2}$. Note that

$$|Y|^{-2} = \frac{1}{\sqrt{2S\Delta}} \left[\frac{1}{(\Delta-S)^2+(\gamma/2)^2} - \frac{1}{(\Delta+S)^2+(\gamma/2)^2}\right]^{1/2} \quad (7)$$

where

$$\Delta = \Omega_p - \Omega_p^0 \quad , \quad (8a)$$

and

$$\gamma = \gamma_1 + \gamma_0 + \frac{k_1}{k_2} (\gamma_2-\gamma_0) \quad . \quad (8b)$$

This function contains two Lorentzians of width γ which peak at $\Delta = +S$ and $\Delta = -S$, respectively. Since we assume high saturation (i.e. $S/\gamma >> 1$) the Lorentzians are narrow compared to their separation and, therefore, at the peak of one Lorentzian the contribution of the other one to $|Y|^{-2}$ is negligible. Thus, the width (FWHM) of the two peaks of $|Y|^{-2}$ is equal to $\sqrt{3}\,\gamma$. The width of the peaks of F is of the same order. Note that the two Lorentzians merge

as $S \to 0$, i.e. for small pump fields, and the splitting in the line shape disappears.

It is this behavior of $|Y|^{-2}$, and consequently of F, that explains the splitting in the lineshape [Fig. (2)]. For sufficiently large S[12] the splitting between the two peaks is given to a good approximation by:

$$\Delta_0 = 2S \ , \tag{9a}$$

where

$$S = \frac{|\mu_{20}| E_L}{\hbar} \frac{\sqrt{k_1 (k_2 - k_1)}}{k_2} \ , \tag{9b}$$

in angular frequency units. Thus, for a given pump field the splitting is directly proportional to the magnitude of the $2 \to 0$ matrix element.

The height of these peaks is, in general, a complicated function of the parameters. However, for the case of interest, $S >> \gamma$, we can estimate the peak intensities by evaluating Eq. (6) at $\Delta = S$. One finds that

$$F(\Delta=S) \propto \sqrt{\frac{S}{\gamma}} \ , \tag{10}$$

so that the intensity maxima increase as $S^{1/2}$. This fact is useful in interpreting the lineshapes of degenerate systems as shown below.

In summary, the complicated lineshape of Eq. (6) shows a simple behavior for high saturation of the pump transition: The line splits into two narrow resonances of width $\sim\sqrt{3}\,\gamma$ and separation 2S, symmetrically located about Ω_p^0 and having a height proportional to $S^{1/2}$. Therefore, with increasing pump power the splitting increases linearly

and the height increases as the square root of S (Fig. 3). Note that the width of the peaks is not a function of S and does not broaden. This shows that the saturation manifests itself in the splitting of the lineshape and not in the width of its features. This is different from the usual saturation broadening as occurs, e.g., in the case $\omega_1/\omega_2 > 1$ [1].

IV. Extension to Degenerate Systems

To obtain the lineshape $\alpha(\Omega_p)$ for a system composed of three levels having M-degeneracy, one has to sum over the component subsystems. The lineshape for such a system is different for different polarizations of pump and probe fields, but only the relative polarizations are important. Let us assume both fields to be linearly polarized. (Extension of the results to circular polarization is straightforward and will be omitted here.) It is convenient to choose the axis of quantization parallel to E_L, so that only $\Delta M=0$ transitions are induced by the pump field. This greatly simplifies the analysis. The probe field can then be either parallel to E_L (inducing only $\Delta M=0$ transitions) or perpendicular to E_L (selection rule: $\Delta M = \pm 1$). The lineshapes for these two cases are different, as will be shown below.

A. E_L and E_p Have Parallel Polarizations

Both E_L and E_p induce only $\Delta M=0$ transitions. The (J_2, J_0, J_1) three-level system can be decomposed into $2J_0+1$ subsystems of the type

$$(J_2, M) \rightarrow (J_0, M) \rightarrow (J_1, M)$$

[Fig. 4(a)]. Summation is then straightforward:

$$\alpha(\Omega_p) = \sum_{M=-J_0}^{J_0} \alpha_0(\Omega_p, M) \cdot F(M) \qquad (11)$$

Note that $\alpha_0(\Omega_p, M)$,Eq. (4), contains matrix elements of the type

$$\mu_{10}[(J_0, M) \rightarrow (J_2, M)] \ , \qquad (12a)$$

and F(M), Eq.(6), contains matrix elements of the type

$$\mu_{20}[(J_2, M) \rightarrow (J_0, M)] \ . \qquad (12b)$$

The M-dependence of α_0 and F enters only through these matrix elements. The N_i appearing in $\alpha(\Omega_p, M)$ and F(M) should now be interpreted as the population densities of single M-substates in the absence of applied fields.

B. E_L and E_p Have Perpendicular Polarizations

By assumption, the pump field still induces transitions only between sublevels of the same M in levels J_2 and J_0. The probe field, on the other hand, couples sublevels of J_0 of a given M-value to sublevels of J_1 having $M \pm 1$. Thus, the system decomposes into subsystems of the type:

$$(J_2, M) \rightarrow (J_0, M) \rightarrow (J_1, M+1) \ ,$$

and

$$(J_2,\ M) \rightarrow (J_0,\ M) \rightarrow (J_1,\ M-1)\ .$$

As long as the probe field is weak these systems are decoupled and can be considered separately [Fig. 4(b)]. The total lineshape is now given by:

$$\alpha\ (\Omega_p) = \sum_{M=-J_0}^{J_0} \left[\alpha_0(\Omega_p, M+1) + \alpha_0(\Omega_p, M-1)\right] \cdot F(M)\ , \qquad (13)$$

where $\alpha_0(\Omega_p,\ M\pm1)$ contains matrix elements of the type

$$\mu_{10}[(J_0,M) \rightarrow (J_1,M\pm1)]. \qquad (12c)$$

Note that for a given three-level system $(J_2,\ J_0,\ J_1)$ the separations between the peaks are determined only by the pump transition, thus, they are identical for both polarizations. These splittings are given by $F(M)$ and therefore by $|\mu_{20}[(J_2,M) \rightarrow (J_0,M)]|$. Since the latter quantity depends only on the magnitude of M and not on its sign, the lineshape factor F is the same for $+M$ and $-M$. Thus, the pair of peaks for $\pm M$ coincides and instead of $2(2J_0+1)$ peaks there are at most $2(J_0+1)$. The heights of the peaks are different for the two polarizations since the $\alpha_0(\Omega_p,M)$ are different, depending on the ΔM selection rule for the probe transition.

The overall intensity pattern depends on the J-values of the three levels, since the matrix elements [Eq. (12)] depend on the ΔJ selection rules. This fact, and the difference in lineshape for the different relative polarizations of pump and probe fields, enable

unambiguous assignment of the types of transitions involved (P,Q, or R branch) and of the J-values of the three levels.

V. Application to Molecular Systems

To facilitate the interpretation of actual lineshapes it is useful to consolidate the above results in tabular and graphical form. Table I gives the number of peak pairs expected, the relative frequency splitting between peaks of a given pair, and the relative intensities of the components in terms of J_0 and M_0, the quantum numbers of the common level. This table has been constructed using the simple rules summarized at the end of Section III and the considerations of Section IV. From this table the intensity pattern for a given three-level system can be easily constructed.

Typical intensity patterns, obtained using Table I, are given in Fig. 5 for the case $J_0 = 4$. There are nine possible three-level configurations, and for each one there are two different patterns, determined by the relative polarizations of pump and probe fields[13]. The patterns are grouped according to the type of transitions for pump and probe fields. The notation PQ(⊥), for example, denotes a P-branch pump transition, a Q-branch probe transition, and perpendicular relative polarizations of pump and probe fields. The numbers in parenthesis give the J-values of the three levels in the order (J_2, J_0, J_1). For each pattern the value of $|M_0|$ associated with each peak is also indicated.

Each peak in the lineshape is represented by a line of the corresponding intensity, with the largest peak of the two polarizations

for a given (J_2, J_0, J_1) normalized to unity. In reality the peaks are of width $\sim\sqrt{3}\,\gamma$ [Eq. (8b)]. Only relative splittings are shown; the actual splittings are proportional to the field strength E_L of the pump transition [Eq. (9)]. Since the widths of the peaks depend only on pressure and not on the intensity of the pump field, all of the components may be resolved at sufficiently high values of the pump field intensity, or at low enough pressures.

By studying Fig. 5 a number of general conclusions independent of the value of J_0 may be obtained. First, it is evident that all of the patterns are distinct. Secondly, as mentioned above, for a given pump transition the splittings are the same for all types of probe transitions. The splittings between peaks of a given $|M|$ are proportional to $|\mu_{20}[(J_2,M) \rightarrow (J_0,M)]|$. Therefore, for a Q-branch pump transition spacings between adjacent peaks are all equal, since $|\mu_{20}| \propto |M|$. The appearance of this characteristic feature in an actual lineshape is the signature of a Q-branch pump transition. Note that in this case the peaks corresponding to the highest M-value have the greatest splitting. Furthermore, there is no contribution from M=0, since the corresponding matrix-element is zero. For P and R-branch pump transitions $|\mu_{20}| \propto |J^2 - M^2|^{1/2}$; accordingly, the spacings between the peaks are unequal with the low M-values clustered at the outside of the pattern. Therefore, it may be difficult in practice to resolve the peaks belonging to low M-values, particularly for large J-values.

A study of the intensity patterns of Fig. 5 shows that a given pattern is either concave or convex, i.e. the tallest peaks are on

the outside or on the inside of the pattern, respectively. Furthermore, if the pattern is convex for a given relative polarization of pump and probe fields it is concave for the other relative polarization, and vice versa. The concave pattern is always the more intense. Specializing to a Q-branch pump transition and parallel polarization, note that for a Q-branch probe transition the pattern is concave; for a P or R-branch probe transition the pattern is convex. For P and R-branch pump transition the reverse is true; for example, a Q-branch probe gives a convex pattern in this case.

Another clue may be obtained by comparing the number of peaks for the two relative polarizations for a given (J_2, J_0, J_1). In some cases the pattern for perpendicular relative polarization shows more components than the pattern for parallel relative polarization. If, for example, the number of peaks is different for the two relative polarizations a P-branch probe transition is excluded. See Table IA for details.

Illustrative Examples

To give an indication of the lineshape in an actual case we have calculated intensity patterns for NH_3, using a computer to evaluate Eq. (6) in conjunction with Eqs. (11) and (13). In the three-level system chosen the pump transition is the asQ(8,7) line at 928 cm^{-1}, and the probe transition is the saP(9,7) line at 746 cm^{-1}. Both transitions are in the ν_2 vibrational band. This choice was made because the asQ(8,7) transition is known to coincide to within 10 MHz with the P(13) line of the 10.6 μ band of the N_2O laser[14]. The vibrational dipole moment is equal to .238 Debye[15].

A pressure broadening of $1/2\ (\gamma/2\pi) = 26$ MHz Torr^{-1} is assumed[16]. The intensity of the pump laser is taken to be 100 W/cm^2 and an NH_3 pressure of 10 mTorr is assumed.

Graphs of absorption coefficient vs. frequency are plotted in Fig. 6. (In these plots frequencies are given in MHz and not in angular frequency units.) Figure 6(a) shows the contributions of the single M-components for perpendicular relative polarization of pump and probe fields. Note that the curves for $\pm M$ are identical. Notice also that there is considerable overlap between the peaks due to their finite width. Figure 6(b) shows the total lineshape for this polarization. In Fig. 6(c) the total lineshape for the parallel case is shown. The even spacing of the peaks indicates a Q-branch pump transition as explained above [compare with Fig. 5(b)]. The number of pairs of peaks, eight, immediately gives the J-values of levels J_0 and J_2. Since the pattern for perpendicular relative polarization of pump and probe field is concave, and the number of peaks is the same for both polarizations, the probe transition must be P-branch [compare with Figure 5(b)]. Thus, $J_1 = 9$.

As an example of the lineshape produced by a P-branch pump transition, the $P_1(4)$ transition of HF at 2.7μ has been chosen[17]. The probe transition is the $J=3 \rightarrow J=2$ rotational transition ("R-branch") in the first excited vibrational state and has a wavelength of 84μ. The parameters used in the calculation are: $\mu_{vib} = .105$ Debye, $\mu_{rot} = 1.9$ Debye, and $1/2(\gamma/2\pi) = 23$ MHz Torr^{-1}.

Figures 7(a) and (b) show the lineshape for a pump laser power of 5kW/cm^2 at pressures of 3 and 10 mTorr. The pattern is character-

istic of a P-branch pump transition: The peaks have unequal spacings and cluster towards the outside. The pattern for parallel polarization [Fig. 7(a)] has a higher peak intensity, but is has one pair of peaks less than the other polarization. This fact is characteristic of an R-branch probe transition, as a comparison with Fig. 5(a) shows. Note that even at low pressure some of the peaks are barely resolved.

It can be seen from Fig. 7 that in this case the laser induced change signals bring the system into the amplifying phase over the entire linewidth. This is due to the high pump power and the low absorption at 84μ. Large gains and laser oscillations have, in fact, recently been observed on HF rotational transitions in the v=1 band, pumped by the $P_1(J)$ lines of an HF laser. See Ref. (18) for details.

Practical Considerations

Figure 7 points out that in practice it may often be difficult to resolve the low M-components of a system with a P or R-branch pump transition. Nevertheless, the intensity of the overlapping peaks may still give a clue as to the number of components. Similarly, higher pump powers and lower pressures can significantly improve the resolution.

In an actual experiment additional broadening of the peaks may be introduced due to field inhomogeneities of the pump laser output. This comes about because the splitting depends linearly on the pump laser field strength E_L [Eq. (9)] (which is assumed to be the amplitude of a plane wave). Thus, any spatial or temporal variations in E_L tend to decrease the resolution of the pattern. Further broadening

may be introduced by frequency drift and jitter of both the pump and probe lasers. These comments point out the importance of having stable lasers of good beam quality.

Besides the influence of the properties of the pump laser beam on the resolution there are other effects that can decrease the observability of the splittings. These include thermal blooming and convective phenomena in the gas, due to large local heating by the pump beam. Such effects tend to decrease the resolution because they produce a non-uniform intensity profile of the pump beam across the sample. Therefore, it is important to operate under conditions where such effects are minimal.

Another limitation on the applicability of the method described is due to collision effects at higher pressures. The theory discussed here contains a simple relaxation model to take account of de-exciting collisions which determine the homogeneous linewidths of the transitions. In some cases, however, the collisions can also induce additional broadening of the resonances by changing the velocities of the molecules in the excited state (level J_o) without taking them out of this level. This effect tends to spread the velocity distribution of excited molecules, and therefore the lineshapes of interest, thus decreasing resolution. This type of broadening is especially important at higher pressures and should be of little significance at the laser pressures of interest for the present method.

VI. Concluding Discussion

A technique has been proposed which may be useful in the assignment of molecular spectra in the optical-infrared region. The method is based upon the splitting of the laser-induced line-narrowing lineshape which occurs when the appropriate conditions are met. One main prerequisite is an intense optical field which is capable of saturating a Doppler-broadened resonance.

The splitting discussed here is a manifestation of the high frequency Stark effect[10] which is well known in the microwave region where Doppler-broadening is negligible. It is interesting to note that in the pressure-broadened case (e.g. for microwave transitions) this splitting, Δ_m, depends on the detuning, δ, of the pump transition from its line center:

$$\Delta_m = \sqrt{\left(\frac{|\mu_{20}|E_L}{\hbar}\right)^2 + \delta^2} \quad . \tag{14a}$$

In the fully Doppler-broadened case, in contrast, the splitting is independent of detuning and is given by

$$\Delta_0 = \frac{2|\mu_{20}|E_L}{\hbar} \sqrt{\frac{k_1(k_2-k_1)}{k_2}} \quad . \tag{14b}$$

Since in both cases the splitting increases with $|\mu_{20}|E_L$, it follows

that in the optical region when pressure broadening becomes dominant splitting effects due to degeneracy still occur, but the details are somewhat different. Flynn[19] has discussed this type of splitting for the microwave region. To the authors' knowledge such effects have not yet been observed.[20]

It is hoped that the above discussions find useful applications in molecular spectroscopy. The lineshapes given here are also directly relevant to the monochromatic optical pumping of gases, and to unidirectional laser amplifiers of the type which have recently been predicted[7] and observed[18] in the infrared region.

ACKNOWLEDGMENT

We would like to thank Professor Ali Javan for his continued interest and support of this research.

Table I : Lineshape Patterns in Terms of J_0 for Different Types of Transitions

A Number of Pairs of Peaks

Pump		P		Q		R	
Relative Polarization		//	⊥	//	⊥	//	⊥
Probe:	P	J_0+1	J_0+1	J_0	J_0	J_0	J_0
	Q	J_0	J_0+1	J_0	J_0	J_0-1	J_0
	R	J_0	J_0+1	J_0-1	J_0	J_0	J_0

B Relative Spacings Between Peaks of a Given M_0
(Depends only on parameters of pump transition)

Pump Transition	P	Q	R
Relative Spacing	$[(J_0+1)^2-M_0^2]^{1/2}$	M_0	$[J_0^2 - M_0^2]^{1/2}$

C Relative Intensities of Peaks

$$I_{rel} = \begin{cases} 1/2\ A\cdot B & \text{for } M=0 \\ A\cdot B & \text{for } M\neq 0 \end{cases}$$

Type of Transition		P	Q	R
Pump Factor A		$[(J_0+1)^2-M_0^2]^{1/4}$	$M_0^{1/2}$	$[J_0^2-M_0^2]^{1/4}$
Probe factor	B(//)	$(J_0+1)^2 - M_0^2$	M_0^2	$J_0^2 - M_0^2$
	B(⊥)	$\frac{1}{2}[(J_0+1)(J_0+2)+M_0^2]$	$\frac{1}{2}J_0(J_0+1)-M_0^2]$	$\frac{1}{2}[(J_0-1)J_0+M_0^2]$

REFERENCES

1. M. S. Feld and A. Javan, Phys. Rev. 117, 540 (1969).

2. B. J. Feldman and M. S. Feld, Phys. Rev. A 5, 899 (1972).

3. The same lineshapes can also be observed in the absence of a probe field by studying the fluorescence of the coupled transition emitted along the propagation direction of the pump field.

4. The results derived below also hold for three-level systems where the common level is the lowest level (V-configuration) or the intermediate level (cascade system), provided the pump laser has a shorter wavelength than that of the probe field. In a cascade system the lineshapes of interest would appear for a probe field propagating anti-parallel to the pump field. For details see Refs. (1) and (2).

5. The considerations also hold for arbitrary steady state level populations as they would occur, for example, in a gas discharge.

6. For sufficiently strong pump fields one can actually obtain gain for the $J_0 \rightarrow J_1$ transition. For further discussion of this aspect see Ref. (7).

7. N. Skribanowitz, M. S. Feld, R. E. Francke, M. J. Kelly, and A. Javan, Appl. Phys. Letters 19, 161 (1971).

8. The narrowest widths of this type observed to date occur in methane, where they are four orders of magnitude smaller than the Doppler width. R. L. Barger and J. L. Hall, Phys. Rev. Letters 22, 4 (1969).

9. In some cases splitting can occur even for a weakly saturating pump field, but this splitting is small and independent of β. Such an effect has been observed by T. Hansch and P. Toschek, Z. Physik 236, 213 (1970). Also note that for the level scheme under consideration splitting effects only occur for a probe field propagating in a direction parallel to the pump field. For a probe field propagating in the antiparallel direction the change signals always have a Lorentzian lineshape, irrespective of the ratio ω_1/ω_2.[1]

10. A. Javan, Phys. Rev. 107, 1579 (1957).

11. Equation (6) is completely equivalent to Eqs. (52) and (53) of Ref. (2), but the present notation is in a simpler form.

12. Computer evaluations of Eq. (6) indicate that $S/\gamma \approx 4$ is sufficient.

13. In practice the actual number of possibilities is usually much less. For example, the splitting effect only occurs when the wavelength of the pump field is shorter than that of the probe field. Therefore, pumping on a P-branch transition is not possible unless vibrational interband transitions are allowed or the probe field corresponds to a pure rotational transition. Similarly, in many molecular systems Q-branch transitions do not occur.

14. F. Shimizu, J. Chem. Phys. 52, 3572 (1970).

15. D. C. McKean and P. N. Schatz, J. Chem. Phys. 24, 316 (1956).

16. C. H. Townes and A. L. Schawlow, Microwave Spectroscopy, (McGraw-Hill, New York, 1955).

17. The notation $P_1(J)$ denotes the (v=1, J-1) → (v=0, J) transition.

18. N. Skribanowitz, I. P. Herman, R. M. Osgood, Jr., M. S. Feld, and A. Javan, Appl. Phys. Letters 20, 428 (1972).

19. G. W. Flynn, J. Mol. Spec. 28, 1 (1968).

20. In the Doppler-broadened regime additional lineshape distortions can occur near resonance ($\Omega_2=\omega_2$) when the pump field is in the form of a standing wave. For a detailed discussion of these effects, see Ref. (2).

FIGURE CAPTIONS

Fig. 1 (a) Energy level diagram and schematic of experimental arrangement. (b) Doppler profiles of the coupled transitions. The change signal is shown centered at Ω_p^0. The broken line at Ω_L indicates the frequency of the pump laser.

Fig. 2 Lineshape of the change signal for a non-degenerate system vs. Δ, the frequency detuning from Ω_p^0. The inset shows the change signal superimposed on the Doppler background.

Fig. 3 Lineshape of the change signal of a non-degenerate three level system as a function of the parameter S (in MHz) for γ=.52MHz. Notice that in each case the splitting is equal to 2S, and that the linewidth remains constant as S increases. The example shown is the M_0=8 component of the NH_3 system described in Section V.

Fig.4 Decomposition of degenerate three level system into subsystems. (a) E_p parallel to E_L; (b) E_p perpendicular to E_L.

Fig. 5 Intensity patterns for J_0=4. (a) P-branch pump transitions; (b) Q-branch pump transitions; (c) R-branch pump transitions. The notation is explained in Section V.

Fig. 6 Intensity patterns for NH_3. (a) Contributions from individual M-components, for E_p perpendicular to E_L; (b) Total lineshape for part (a); (c) Total lineshape for E_p parallel to E_L. The inset in (a) shows the relevant levels.

Fig. 7 Intensity patterns for HF. The level scheme is shown in the inset. Note that gain rather than absorption is plotted ir this case.

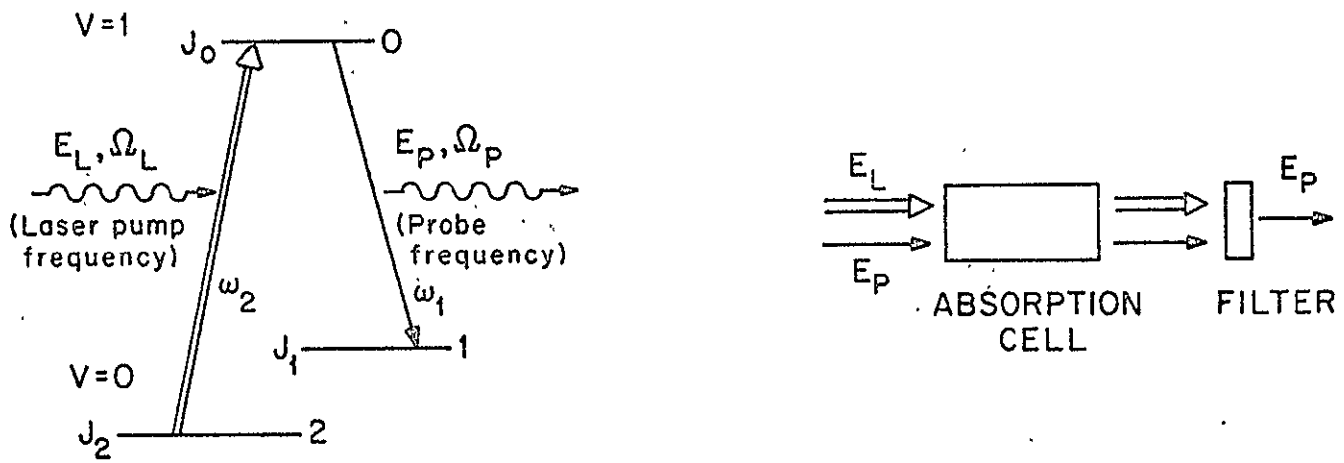
V=1
J_0
0
E_L, Ω_L
(Laser pump frequency)
E_P, Ω_P
(Probe frequency)
ω_2
ω_1
J_1
1
V=0
J_2
2
E_L
E_P
ABSORPTION CELL
E_P
FILTER

(a)

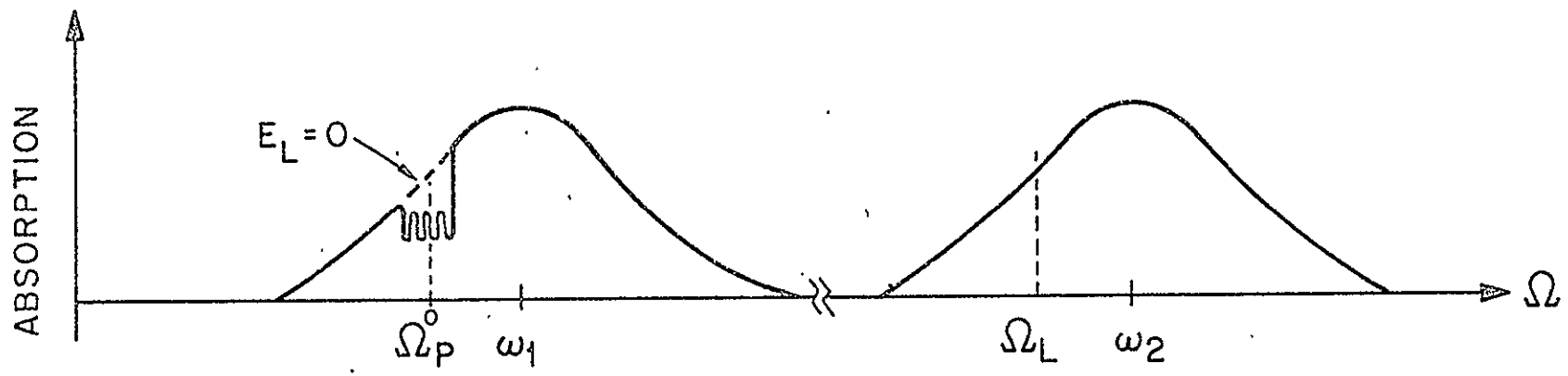
ABSORPTION
$E_L = 0$
Ω_P^0
ω_1
Ω_L
ω_2
Ω

(b)

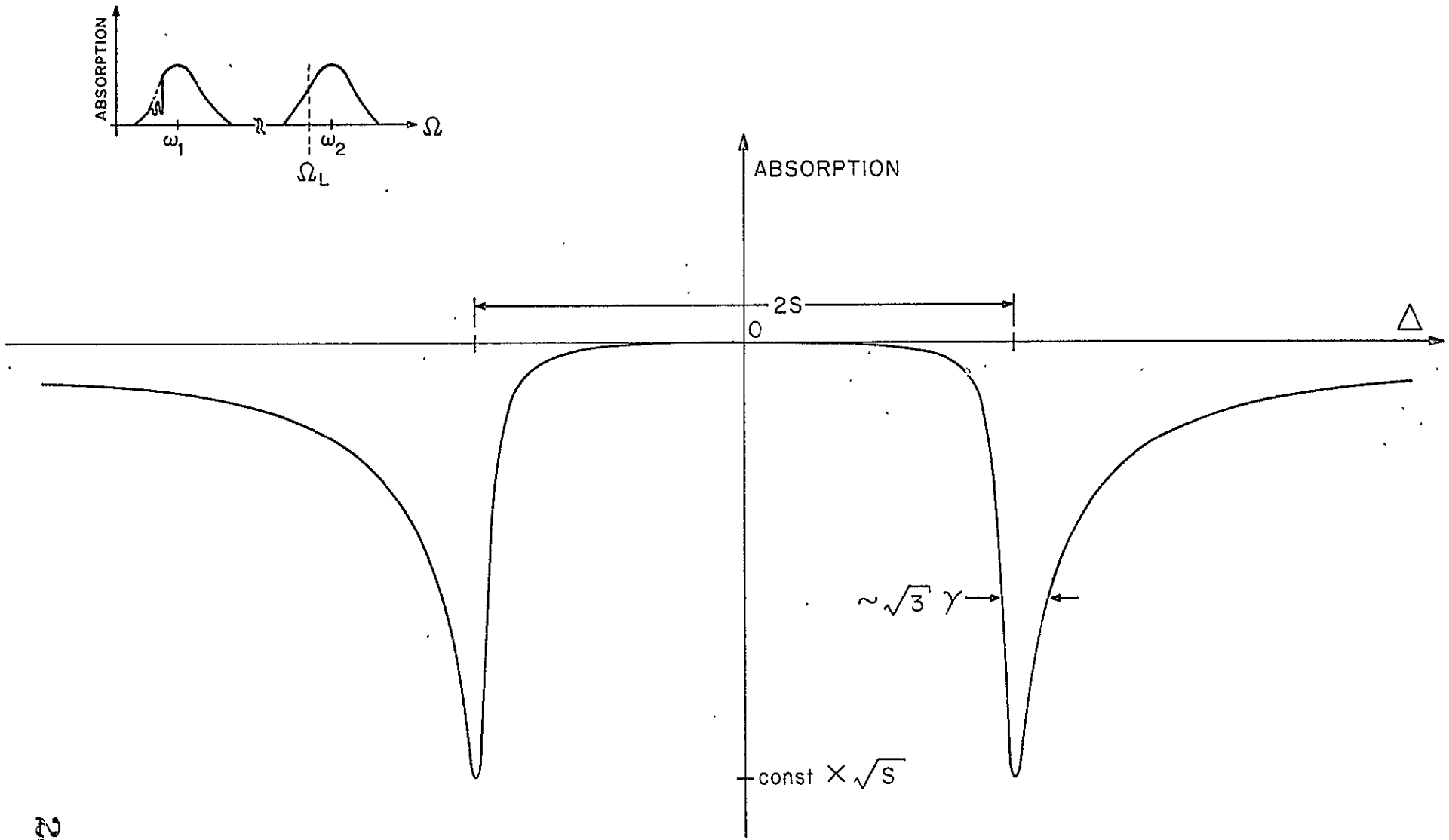
ABSORPTION
ω_1
ω_2
Ω
Ω_L
ABSORPTION
2S
0
Δ
$\sim\sqrt{3}\,\gamma$
const $\times\sqrt{S}$

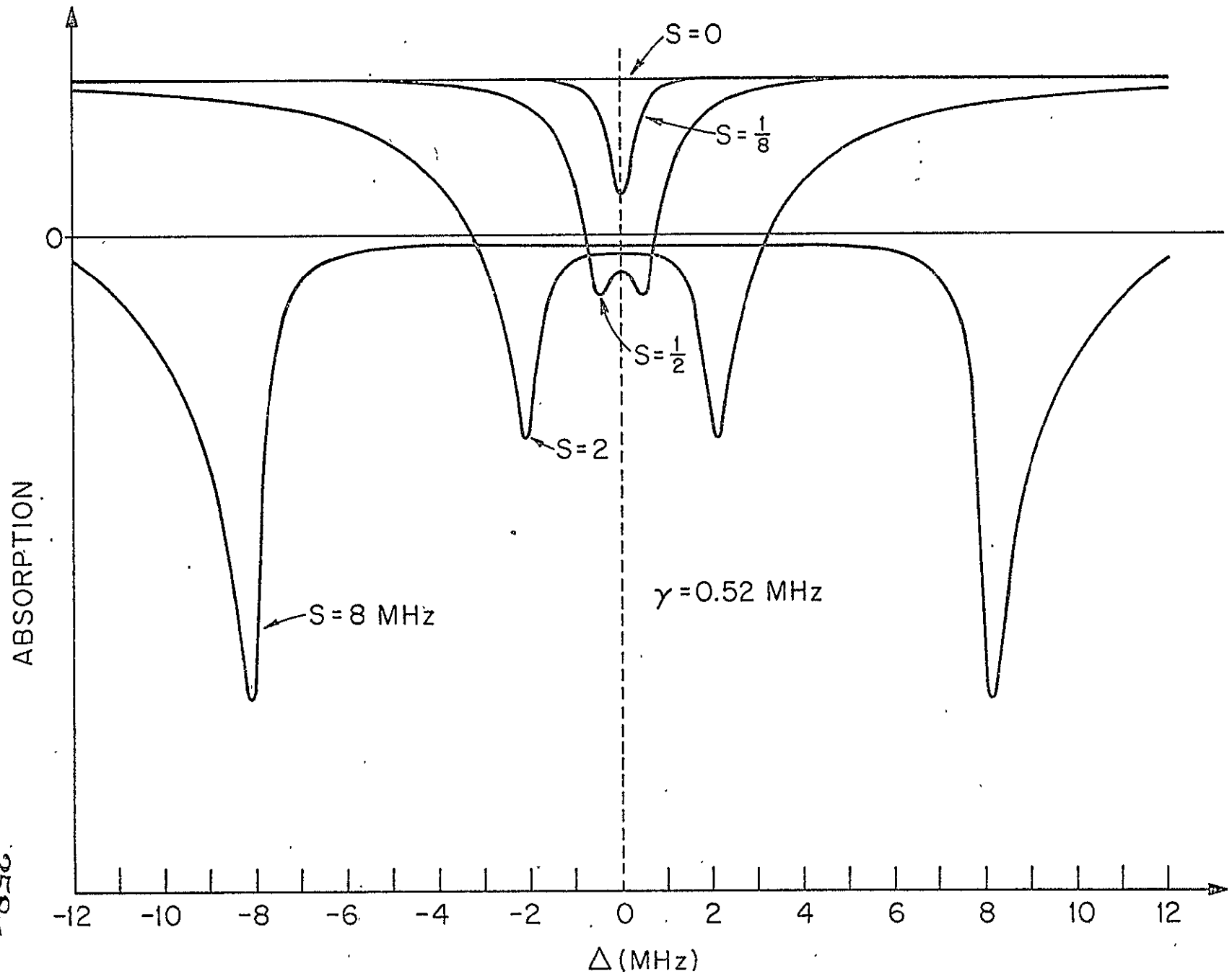
S = 0
S = 1/8
S = 1/2
S = 2
S = 8 MHz
γ = 0.52 MHz
0
ABSORPTION
-12
-10
-8
-6
-4
-2
0
2
4
6
8
10
12
Δ (MHz)

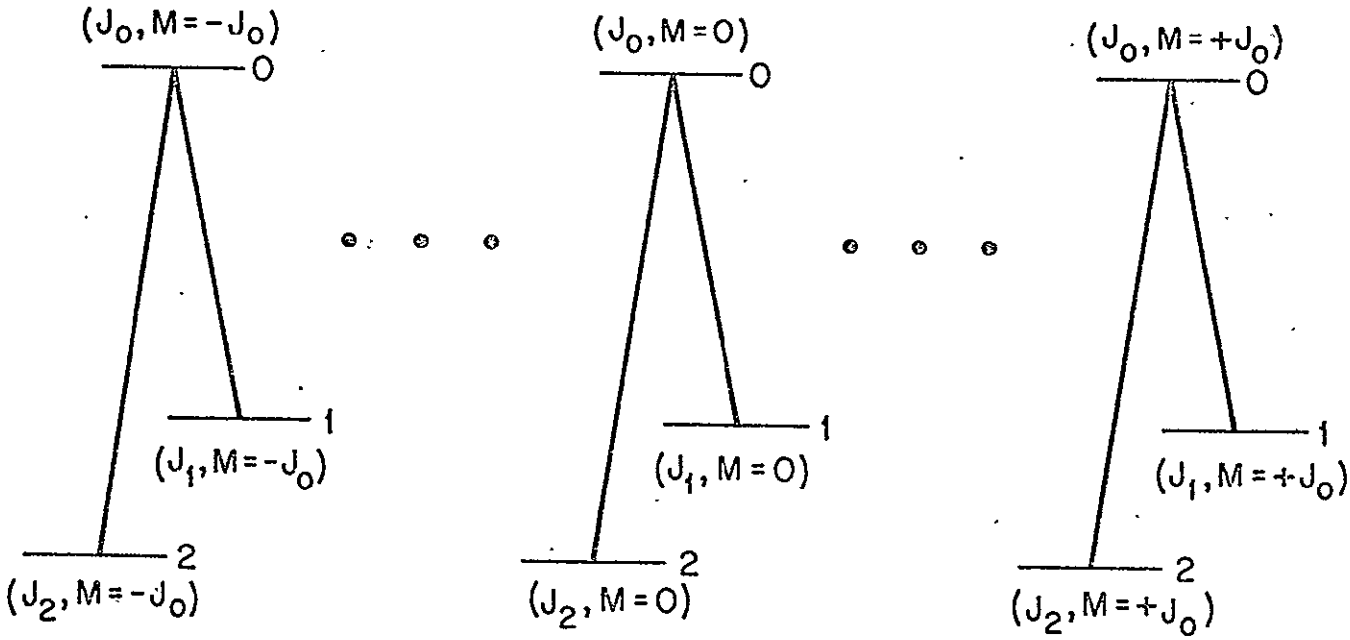
$(J_0, M=-J_0)$
0
1
$(J_1, M=-J_0)$
2
$(J_2, M=-J_0)$
$(J_0, M=0)$
0
1
$(J_1, M=0)$
2
$(J_2, M=0)$
$(J_0, M=+J_0)$
0
1
$(J_1, M=+J_0)$
2
$(J_2, M=+J_0)$

(a)

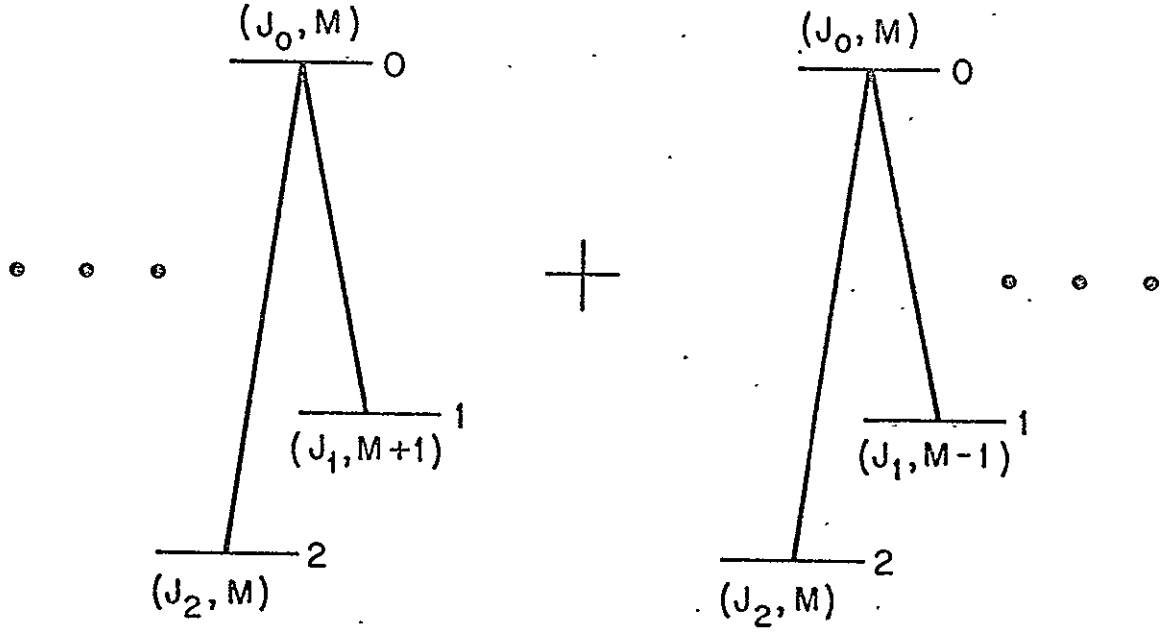
(J_0, M)
0
1
$(J_1, M+1)$
2
(J_2, M)
(J_0, M)
0
1
$(J_1, M-1)$
2
(J_2, M)

(b)

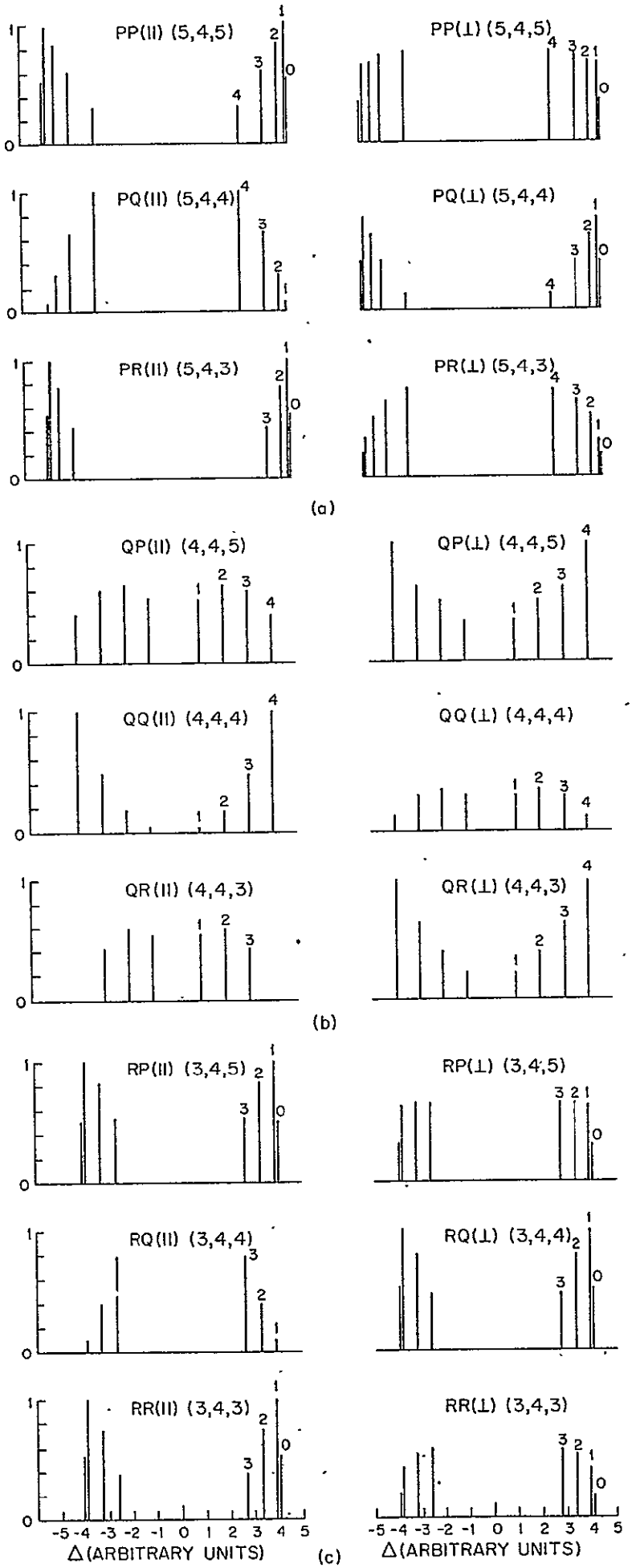
PP(II) (5,4,5)
PP(⊥) (5,4,5)
PQ(II) (5,4,4)
PQ(⊥) (5,4,4)
PR(II) (5,4,3)
PR(⊥) (5,4,3)
(a)
QP(II) (4,4,5)
QP(⊥) (4,4,5)
QQ(II) (4,4,4)
QQ(⊥) (4,4,4)
QR(II) (4,4,3)
QR(⊥) (4,4,3)
(b)
RP(II) (3,4,5)
RP(⊥) (3,4,5)
RQ(II) (3,4,4)
RQ(⊥) (3,4,4)
RR(II) (3,4,3)
RR(⊥) (3,4,3)
-5 -4 -3 -2 -1 0 1 2 3 4 5
Δ(ARBITRARY UNITS)
(c)
-5 -4 -3 -2 -1 0 1 2 3 4 5
Δ(ARBITRARY UNITS)

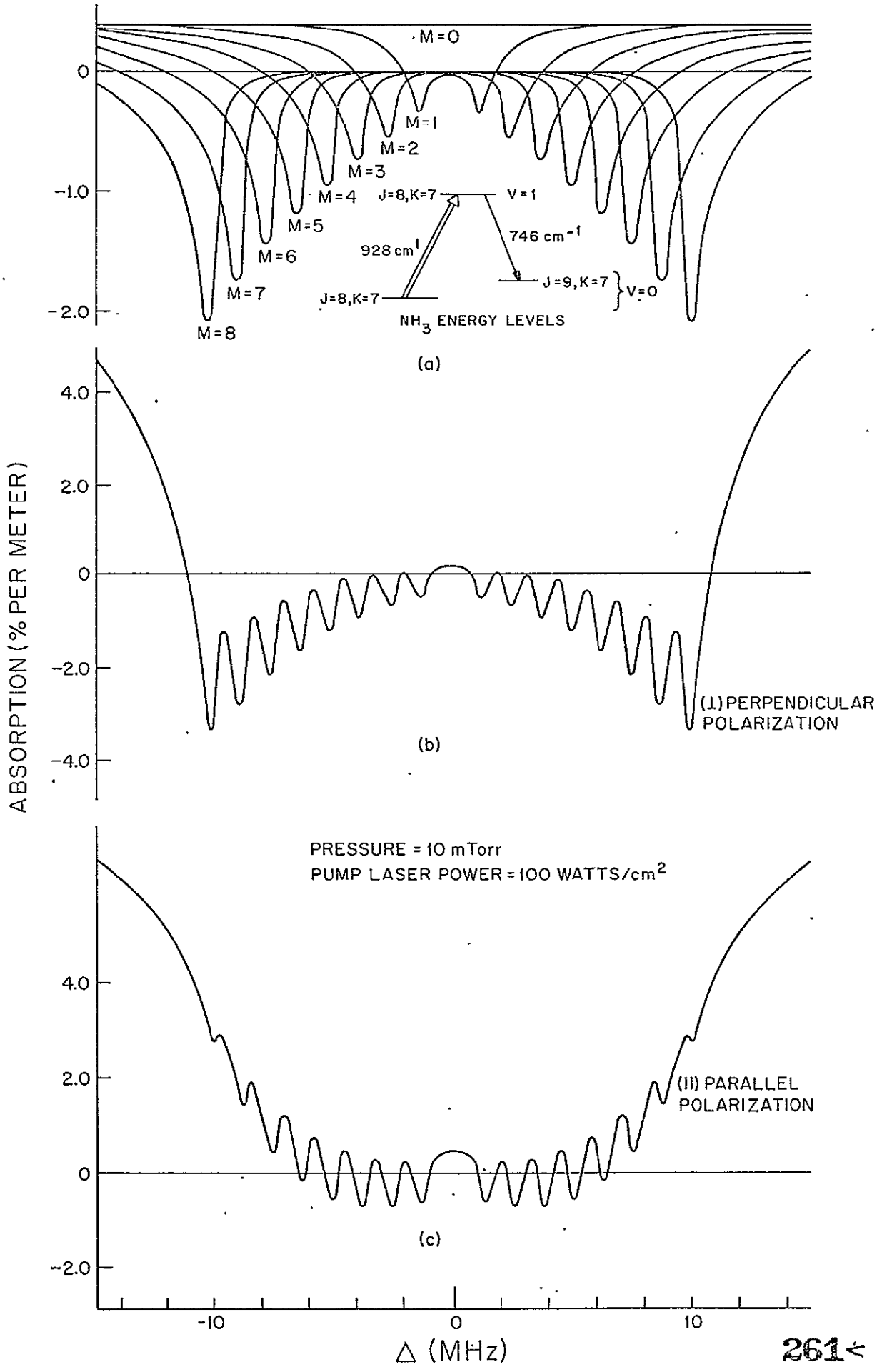
M=0
M=1
M=2
M=3
M=4
M=5
M=6
M=7
M=8
0
-1.0
-2.0
J=8,K=7
V=1
928 cm⁻¹
746 cm⁻¹
J=9,K=7
V=0
J=8,K=7
NH3 ENERGY LEVELS
(a)
4.0
2.0
0
-2.0
-4.0
ABSORPTION (% PER METER)
(⊥) PERPENDICULAR POLARIZATION
(b)
PRESSURE = 10 mTorr
PUMP LASER POWER = 100 WATTS/cm²
4.0
2.0
0
-2.0
(∥) PARALLEL POLARIZATION
(c)
-10
0
10
Δ (MHz)

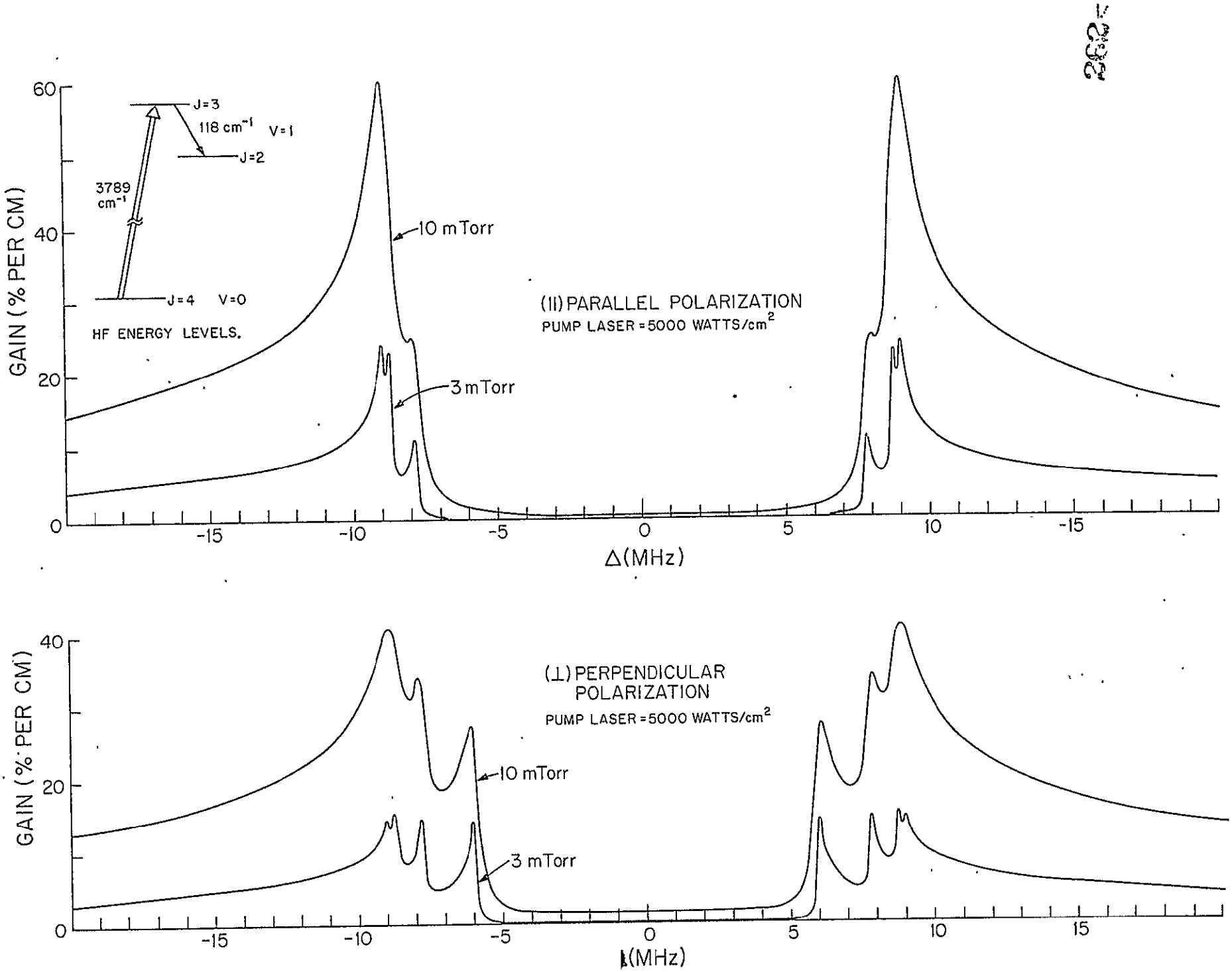
GAIN (% PER CM)
60
40
20
0
J=3
118 cm⁻¹
V=1
J=2
3789 cm⁻¹
J=4
V=0
HF ENERGY LEVELS.
10 m Torr
3 m Torr
(II) PARALLEL POLARIZATION
PUMP LASER = 5000 WATTS/cm²
-15
-10
-5
0
5
10
-15
Δ(MHz)
GAIN (% PER CM)
40
20
0
(⊥) PERPENDICULAR POLARIZATION
PUMP LASER = 5000 WATTS/cm²
10 mTorr
3 mTorr
-15
-10
-5
0
5
10
15
Δ(MHz)

15. F. Keilmann, R. L. Sheffield, M. S. Feld and A. Javan

Optical Isolation using a Doppler-Broadened Molecular Absorber

Appl. Phys. Lett., 23, 612 (1973)

Optical isolation using a Doppler-broadened molecular absorber*

F. Keilmann†, R. L. Sheffield, M. S. Feld‡, and A. Javan

Department of Physics, Massachusetts Institute of Technology, Cambridge, Massachusetts 02139
(Received 27 August 1973)

A new principle for optical isolation based on the saturation of a Doppler-broadened resonance is described. It depends on an initial difference in the power levels of the incident and reflected waves. The technique is demonstrated using an SF_6 absorber to isolate the $P(18)$ line of the CO_2 transition at 10.57 μm.

Protection of a laser oscillator from external reflections can be of great importance where high stability is required. This is the case, for example, in precision measurements such as interferometry and saturation spectroscopy, where only very small frequency fluctuations can be tolerated. We describe here a new principle for optical isolation[1] based on the velocity dependence of the saturation occurring in a low-pressure Doppler-broadened absorber.[2]

Consider a monochromatic beam of laser radiation propagating through a resonant absorber. If the beam is sufficiently intense, molecules will be transferred from the absorber's ground state to its upper state faster than can be made up for by relaxation, thus reducing the population difference ΔN between the upper and lower states. The absorption coefficient is proportional to ΔN. Accordingly, for an intense laser field the medium can become essentially transparent, even though for a weak field it is opaque. In the intermediate range the over-all transmission through the medium can be a sharply changing function of the input intensity.

For a Doppler-broadened medium, however, this population saturation only affects a small portion of the available molecules. Consider a monochromatic wave of wave vector k and frequency ω_L, travelling through a cell containing a Doppler-broadened absorbing gas with center frequency ω_a [Fig. 1(a)]. In the laboratory frame the resonant frequency of a molecule moving with velocity v is shifted due to the Doppler effect to a frequency $\omega_A - \mathbf{k}\cdot\mathbf{v}$. Thus, all molecules having velocity component v_z along the propagation direction k experience the same frequency shift $-kv_z$. Accordingly, for an intense laser field offset from the molecular center frequency by an amount $\Delta = \omega_A - \omega_L$, the radiation selectively saturates a narrow section of the molecular velocity distribution centered at $v_z = \Delta/k$. The saturation extends over a range $\sim\gamma/k$, where γ is the homogeneous linewidth determined by collisions, radiative decay, etc. Therefore, the reduction in the population difference occurs only over a narrow portion of the velocity distribution [Fig. 1(b)].

Now suppose that a portion of the light transmitted through the absorption cell is reflected back through the cell in the opposite direction. In this case the field will resonantly couple to molecules with velocity $v_z = -\Delta/k$. Therefore, the reflected light will interact with molecules symmetrically located on the opposite side of the velocity distribution. So if the laser frequency is detuned from the center of the molecular resonance ($|\Delta| > \gamma$), the oppositely directed waves will interact with different groups of molecules.[3] If the incident wave is more intense than the reflected wave it will have a greater over-all transmission through the cell. Therefore, by simply placing an absorber cell between the laser and the source of feedback it is possible to effectively decouple or isolate the laser from the reflected light [Fig. 1(c)]. By appropriate choice of the experimental parameters the isolation factor can be made very large.

To demonstrate the principles described above, the experimental arrangement of Fig. 2(a) is used. The radiation of a cw single-mode CO_2 laser is transmitted through a 205-cm long tube, 25 mm in diameter, filled with SF_6 gas at a low pressure. SF_6 is known to have many coincidences with the 10.6-μm CO_2 laser lines. We chose the $P(18)$ line of CO_2, since within a tuning range of ± 50 MHz there happens to be just one strong SF_6 resonance.[4] The laser cavity consists of a grating reflector and a piezoelectrically movable mirror swept sinusoidally at 60 Hz with a peak-to-peak amplitude of 15 μm, resulting in a display of three cavity modes. The data are taken in the linear part of the sweep. The diameter is about 11 mm, its total power being 1.3 W at line center. The transmitted radiation passes through a 17-cm-long attenuation cell containing propylene at a variable pressure and is then reflected back, thus simulating varying amounts of feedback [Fig. 2(a)]. Transmission in forward and backward directions is simultaneously measured by means of four Ge:Au de-

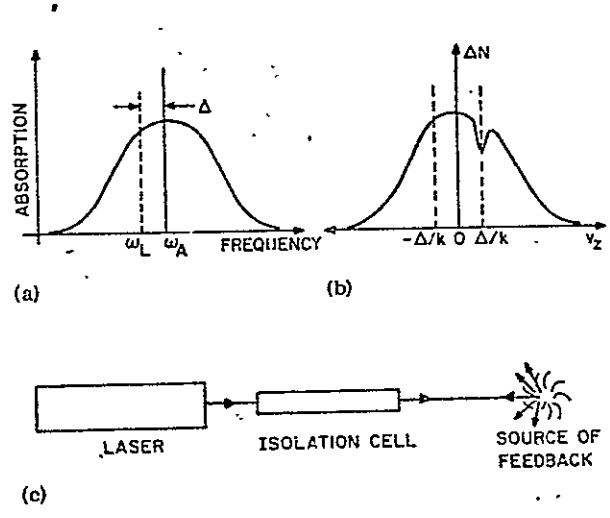

FIG. 1. (a) Doppler-broadened line shape of molecular resonance centered at ω_A; ω_L is the laser frequency. (b) Velocity distribution of molecular population difference, N, showing a depletion at $v_z = \Delta/k$ caused by the strong beam. A weaker beam of same frequency travelling in the opposite direction would cause smaller depletion at $v_z = -\Delta/k$. (c) Schematic diagram of arrangement for isolation. The isolation cell contains the saturable Doppler-broadened absorber.

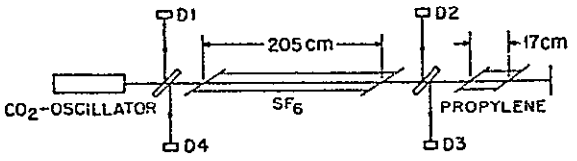

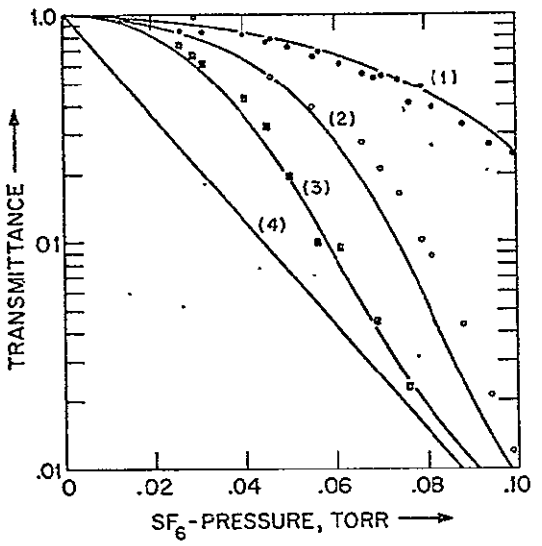

(b)

FIG. 2. (a) Experimental setup for measuring forward and backward transmission simultaneously. The detectors are indicated by D. (b) Simultaneously measured (1) forward and (2, 3) backward transmittances of isolator tube versus SF_6 pressure. (2) and (3) refer to double-pass attenuation factors of propylene cell set to 5 and 28, respectively. The smooth curves represent the theoretical fit. (4) Small-signal transmittance.

tectors, using wedged BaF_2 beamsplitters. A slight misalignment of 2 mrad is necessary to enable measuring the isolation in the high-feedback range. A strong inverted Lamb dip is seen at detector D4, indicating good overlap. It has a width (FWHM) of 3.5 ± 0.5 MHz at 0.05 Torr and is located 7 MHz above the CO_2 line center, in agreement with Goldberg and Yusek.[4] The transmittances are evaluated 14.5 MHz below the SF_6 line center and plotted in Fig. 2(b). They clearly show the isolation effect.

The incremental intensity change of a monochromatic wave of intensity $I(z)$ at position z traversing a section dz of a Doppler-broadened two-level absorber is given by[5]

$$dI = \frac{-\alpha I}{(1 + I/I_s)^{1/2}} dz, \tag{1}$$

where α and I_s are parameters of the specific molecule. α, the small-signal absorption coefficient, is linearly proportional to the pressure. I_s, the saturation intensity, is proportional to γ^2. Therefore, when collisions represent the dominant relaxation mechanism, I_s is a quadratic function of pressure.[6] Henceforth we shall confine ourselves to this region. For particular values of α and I_s, Eq. (1) can be integrated to yield the transmittance $T = I(L)/I(0)$ for a tube of given length L and input intensity $I(0)$.

The data of Fig. 2(b) are fitted to the expression for the transmittance obtained by integrating Eq. (1), taking $I(0)$ to be 2 W/cm^2. Reasonable agreement is obtained for $\alpha = 0.26$ cm^{-1} and $I_s = 7.5$ W/cm^2 at 1 Torr, indicating that the two-level model of Eq. (1) is a reasonable approximation in this case.[5] The small-signal absorption coefficient extrapolated to the CO_2 line center, 0.52 cm^{-1} at 1 Torr, is higher than that measured by Abrams and Dienes.[7]

Once α and I_s have been determined, the calculations can be extended to a wide range of pressures, lengths, and intensities. The appropriate scaling laws follow from the fact that the transmittance only depends on the two parameters $I_s/I(0)$ and αL. One useful relationship which follows is

$$T[p, L, I(0)] = T[\epsilon p, L/\epsilon, \epsilon^2 I(0)], \tag{2}$$

where p is the pressure. With the help of relations such as this, extrapolation of Fig. 2(b) to other systems is possible. In particular, long path lengths and low pressures give the best isolation properties. Note that a long path can be folded into a small space so that isolation factors (i.e., ratios of the transmittance of the incident beam to that of the weak reflected beam) of many orders of magnitude seem feasible. Also note that power broadening can be reduced, if necessary, by expanding the diameter of the laser beam.

The present approach complements the conventional optical isolators. Most commonly, one uses polarization-discriminating devices and circular polarizers[8] or Faraday rotators.[9] These give low forward losses, but the isolation factors are limited to about three orders of magnitude because of critical adjustment requirements. Another type of isolator, in which the frequency of the feedback beam is acousto-optically[10] shifted out of the oscillator bandwidth, is promising but requires efficient high-frequency modulators. Efficient decoupling can also be achieved by means of unidirectional laser amplifiers, recently proposed[11] and demonstrated.[12]

In applying the present technique one should be aware of the restrictions of Refs. 5 and 6. The various interaction bandwidths also limit its applicability. At high pressures, cross relaxation[13] is expected to reduce the isolation even at low intensity levels. Furthemore, if the laser beam is not monochromatic but has a spectral width δ given, for example, by the length of the pulse $\tau = 1/\delta$, cross saturation will significantly reduce the isolation if $\delta \geq 2\pi |\Delta|$. For the SF_6 system used in our experiment at $\Delta = 14.5$ MHz, this implies $\tau \leq 11$ nsec.

The principles described here also may be useful in constructing high-power multistage laser amplifiers, where isolation between stages is necessary to avoid self-oscillation.

The authors are happy to acknowledge the expert technical assistance of L.W. Ryan, Jr.

*Work supported in part by ONR, NASA, and Research Corporation.

†Support by Deutsche Forschungsgemeinschaft is gratefully acknowledged.

‡Alfred P. Sloan Research Fellow.

[1] F. Keilmann, R. Sheffield, M.S. Feld, and A. Javan, IEEE/

265

OSA Conference on Laser Engineering and Applications, Washington, D.C., 1973 (unpublished).

[2]The velocity-dependent saturation of Doppler-broadened resonances can also be utilized to produce unidirectional gain and isolation in a three-level system (Refs. 11 and 12).

[3]When the laser is tuned to the center of the molecular resonance (Lamb-dip condition) oppositely directed waves of the same frequency can interact with the same velocity group of molecules. Consequently, effective isolation cannot be achieved in this case.

[4]M.W. Goldberg and R. Yusek, Appl. Phys. Lett. 17, 349 (1970).

[5]Equation (1) describes a nondegenerate absorber in the fully Doppler-broadened limit, i.e., where the Doppler width $\Delta_D \gg \gamma$ and $\Delta_D \gg \gamma (I/I_s)^{1/2}$ (power broadening).

[6]For a beam diameter of 1 cm, γ will be determined by pressure broadening at pressures above ~10 mTorr. At lower pressures transit time effects and wall collisions become important.

[7]R.L. Abrams and A. Dienes, Appl. Phys. Lett. 14, 238 (1969). The CO_2 laser line in this paper referred to as $P(20)$ is probably $P(18)$.

[8]F.A. Jenkins and H.E. White, *Fundamentals of Optics* (McGraw-Hill, New York, 1957), p. 556.

[9]C.F. Padula and C.G. Young, IEEE J. Quantum Electron. QE-3, 243 (1967).

[10]R.G. Smith, IEEE J. Quantum Electron. QE-9, 545 (1973).

[11]N. Skribanowitz, M.S. Feld, R.E. Francke, M.J. Kelly, and A. Javan, Appl. Phys. Lett. 19, 161 (1971).

[12]N. Skribanowitz, I.P. Herman, R.M. Osgood, Jr., M.S. Feld, and A. Javan, Appl. Phys. Lett. 20, 428 (1972); N. Skribanowitz, I.P. Herman, and M.S. Feld, Appl. Phys. Lett. 21, 466 (1972).

[13]P.W. Smith and T. Hänsch, Phys. Rev. Lett. 26, 740 (1971).

16. J. G. Small

Infrared Frequency Synthesis and Precision Spectroscopy

INFRARED FREQUENCY SYNTHESIS

AND PRECISION SPECTROSCOPY

ABSTRACT

The small contact area metal-dielectric-metal electron tunneling junction has permitted the extension of microwave frequency synthesis technology to infrared frequencies. The mechanically contacted diode has been shown to have a usable upper frequency limit of at least 100 THz. This thesis reports its application to direct frequency measurements of far infrared lasers and to the development of a frequency multiplying chain of lasers which is capable of synthesizing any desired infrared frequency. The laser frequency multiplying chain makes possible a direct comparison between microwave frequency standards and infrared laser frequency sources.

Thin film technology has made possible small contact area printed junctions which also display high speed nonlinearities. Though somewhat slower than the mechanically contacted devices, experimental evidence of frequency synthesis is here presented which demonstrates a frequency response to 1 THz. Observations of high speed rectification further suggest that the upper frequency limit may exceed 30 THz(10μ). Thin film antennas resonant at far infrared frequencies have been integrated with the diodes and exhibit coherent interference in their far field radiation patterns.

An extensive theoretical treatment indicates that a model of electron tunneling through a potential barrier can explain the major features of high speed rectification in the presence of a DC bias current. A negative rectified signal with positive bias voltage corresponds to relatively thick barriers, usually thicker than 10 Angstroms. A positive rectified signal with positive bias voltage occurs

for barriers thinner than about 10 Angstroms, the critical thickness depending upon a simple model of the buildup of electrostatic charge within the dielectric barrier. The explanation of strong curvature in the rectification signals with bias voltage requires a further consideration of current dependent saturation effects and higher order terms in the dependence of the barrier height with bias voltage.

TABLE OF CONTENTS

LIST OF FIGURES AND TABLES

TABLES

FIGURES

Chapter 1

Introduction

1. Review

The infrared (IR) region of the electromagnetic spectrum has long been marginally accessible to experimental study due to a paucity of sources and detectors of IR radiation. It is, however, an area of considerable contemporary interest since a host of molecular bonds have resonant frequencies lying in the decades between 10^{12} and 10^{14} Hertz. Historically, optical techniques, usually relying on bulk effects in materials, have been pushed toward longer wavelengths. More recently from the other end of the spectrum, microwave techniques employing discrete circuit elements have been applied toward shorter wavelengths. Currently, as reported below, the two technologies have met and overlapped in the IR region and are no longer easily distinguishable.

The content of this thesis is: the experimental development of the metal-dielectric-metal point contact (MDM) diode and, particularly, its thin film version; the application of the device as a discrete circuit element to frequency synthesis at infrared frequencies as high as 10^{14} Hertz; and a theoretical explanation of its performance based on a model of quantum mechanical barrier penetration by tunneling electrons.

Chapter 1 defines the basic concepts used in IR

frequency synthesis. Chapter 2 reports some successful applications of the synthesis techniques. Any desired frequency below 10^{14} Hz may now be generated or measured. Chapter 3 details the fabrication techniques and performance characteristics of the thin film MDM diode. Chapter 4 deals with the electron tunneling theory.

For consistency, the following discussions will be in the frequency domain with frequencies given in Hz or even THz (10^{12}) when appropriate. Occasionally, the corresponding IR wavelength will be given parenthetically in microns. For example, 100 THz(3μ) = 10^{14} Hz.

2. Detectors and Mixers

Prior to considering the details of the MDM diode and infrared frequency synthesis, a distinction must be drawn between detectors and mixers. The MDM diode is used in both applications, and a clear distinction now may avoid confusion later.

A detector of electromagnetic radiation may be viewed as any device which gives an observable response to incident radiation. At optical frequencies, an interesting variety of bulk material effects are used. The earliest IR detector was a thermometer used by William Herschel (1738 - 1822) to demonstrate the presence of radiation beyond the red end of the visible spectrum.[1] Thermal detectors are currently in very wide use; and, in the very far IR, liquid helium cooled

bolometers are still the most sensitive power detectors available. Other bulk mechanisms in current use involve chemical reactions, color changes, resistance changes, the photoelectric and pyroelectric effects, and stimulated or quenched fluorescence, to name but a few. The choice of detector, of course, depends upon a specific application; and many of these detector types may be used as mixers. The detectors listed above are all power law detectors, a distinction which is very important in some mixer applications.

A mixer is most easily explained in the frequency domain. It is a device with one output and one or more imputs. The frequency of the output is an algebraic linear combination of the frequencies of the inputs.

$$\nu_{out} = n_1\nu_1 + n_2\nu_2 + \ldots + n_i\nu_i \qquad (1)$$

where $n_{1,2,\ldots} = 0, \pm 1, \pm 2, \ldots$ integers.

The order of mixing is here defined as the algebraic sum of the harmonic numbers: $|n_1| + |n_2| + \ldots + |n_i|$. Zero frequency, $\nu_{out} = 0$, is allowed and represents a steady state non-oscillating output.

At radio frequencies, the inputs and output consist usually of oscillating electric currents or voltages. The mixer is a discrete circuit element, usually a diode or a

276<

transistor. At optical frequencies, the inputs are usually propagating electromagnetic radiation or phonons while the output is either a propagating wave or a voltage, depending on its frequency. Optical mixers generally make use of bulk nonlinear effects in a solid, liquid, gas, or plasma.

In general, a mixer is a device which produces an observable response to inputs and which has an output frequency as defined above. A detector is often the special case of a mixer with $\nu_{out} = 0$. Many mixers can be used as detectors, but most simple detectors are not suitable for orders of mixing other than 2.

3. Speed of Response

The human eye is a detector of radiation at 5×10^{14} Hz(.6μ); but it is a slow detector. The response time of the eye to variations in light intensity is about 10^{-1} sec. It is quite sensitive and, within its speed limitations, can be used as a second order mixer. If two incident light sources have frequencies near 5×10^{14} Hz and differ by less than 10 Hz, the eye will mix them producing an output stimulation of the optic nerve at 10 Hz. The observer will see the combination of the two sources as a light blinking on and off.

Similarly, a fast photodiode may have a response of 10^{-9} sec. It could mix two light sources having a difference frequency as high as 1 GHz. The photodiode output would be

277<

a voltage or current with an oscillating component at 1 GHz. For light frequencies differing by much more than 1 GHz, the photodiode output would be simply a DC response depending in a simple way (perhaps linearly) on the sum of the incident light intensities.

If we define the speed of response as the highest possible frequency of a detector output, then the MDM diode is by far the world's fastest detector. It responds from DC to 10^{14} Hz, as will be shown in Chapter 2.

4. High Order Mixing

Power law detectors are generally unsuitable for high order mixing and for sum frequency mixing, as opposed to the second order difference frequency mixing described previously. The reasons may be understood by appealing to a physical description of the phenomenon of mixing.

A radio frequency mixer is a descrete element, usually a semiconductor diode or transistor, with a nonlinear voltage-current governing equation. If a sinusoidal voltage is applied to the device, a highly distorted sinusoidal current will be produced. In the frequency domain, the periodic current may be Fourier analysed as a linear combination of harmonics of the fundamental period of the driving voltage (including,in general, the zeroth harmonic or a DC term).

Consider a simplified (and incorrect) power series expansion for a device where I is the current flowing due to an applied voltage V:

278<

$$I = a_1V + a_2V^2 + \ldots + a_nV^n \qquad (2)$$

The constant coefficient a_i is primarily responsible for the ith order mixing. As an example, consider the second order mixing of the sum of two sinusoidal voltages:

$$a_2V^2 = a_2[\ A\cos\omega_1 t + B\cos\omega_2 t\ ]^2$$

$$= a_2[\ A^2\cos^2\omega_1 t + B^2\cos^2\omega_2 t + 2AB\cos\omega_1 t\cos\omega_2 t\ ]$$

$$= a_2[\ A^2/2\ (1 + \cos2\omega_1 t) + B^2/2\ (1 + \cos2\omega_2 t) + AB\cos(\omega_1+\omega_2)t + AB\cos(\omega_1-\omega_2)t\ ] \qquad (3)$$

Figure 1 shows a frequency domain representation of the Fourier components for this simple case of a strictly square law device.

For frequencies above cutoff, the power series expansion of Eq(2) is no longer valid. Clearly, a bandwidth limited device, as represented by $f(\omega)$ in Fig. 1, cannot be used for sum frequency or harmonic generation to frequencies higher than its cutoff.

The concept of a bandwidth is easily visualized in the frequency domain but is rather complicated in the time domain. A bandwidth implies that the response of a device is not

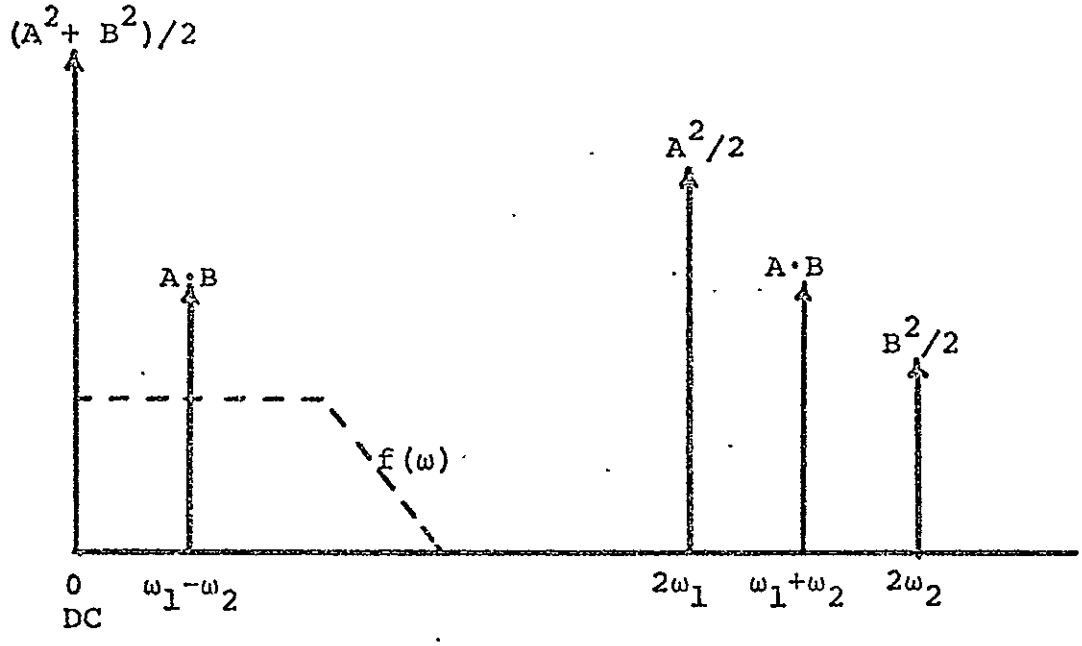

Figure 1.

A frequency domain representation of the Fourier components for second order mixing., The broken curve shows the response of a bandwidth limited detector which would be unsuitable in mixer applications requiring second harmonic generation or sum frequency mixing.

an instantaneous function of its input. Rather, the time domain response depends upon the prior history of the input. Equation (2) must then be replaced by a differential equation, a topic which has been treated extensively in the literature.[2] It will not be further considered here.

A mixer will be distinguished from other detectors in that Eq(2) is assumed valid for a mixer. Of further interest are the magnitudes of the coefficients a_i . For a strictly square law device, only $a_2 \neq 0$. A strictly square law device would not be suitable for any form of 3rd order mixing, for example.

It is important to note that the absence of high order terms does not imply a limit to bandwidth! In Chapter 2, the MDM diode will be compared to a silicon point contact diode. At microwave frequencies, the silicon diode is superior to the MDM diode, especially at high order mixing above about 10 orders. At IR frequencies, however, silicon diodes fail completely while the MDM diode still performs well for mixing orders less than about 10.

5. Discrete and Bulk Circuit Elements

Historically, there have developed two distinct approaches to dealing with electromagnetic radiation. One approach has traditionally been termed "optics" and the other "electronics". Chapter 2 describes the extension of the electronic approach to optical frequencies. Before proceed-

ing, however, it may be helpful to briefly review the differences in the two approaches and to consider their ranges of validity.

Radio frequency circuits usually employ discrete circuit elements and operate by manipulating electric currents. Neither transmitters nor receivers directly interact with electromagnetic radiation. RF wavelengths, being much longer than the typical dimensions of the circuit components, couple only weakly to the circuits. A radio transmitter, for example, is strictly a generator of alternating currents. It is the function of antennas to couple alternating electric currents to electromagnetic radiation.

At optical frequencies, the situation has historically been reversed. Where optical wavelengths are shorter than the circuit dimensions, electromagnetic radiation in waveguides or in free space, rather than electric currents in conductors, constitutes the "working fluid". It is possible to duplicate most of the functions of electronic circuits with optical circuits. Since 1968, interest in integrated optical circuits, which use thin film waveguides integrated with bulk nonlinear circuit elements, has received increasing attention.[3]

In the microwave region, between roughly 10^9 and 10^{12} Hz, both discrete and bulk approaches may be used and are often combined in hybrid circuits. For example, a klystron

oscillator with a coaxial output transmission line may be followed by a waveguide optical isolator which employs Faraday rotation. The isolator in turn may be followed by a waveguide directional coupler and then by a hot carrier diode mixer. The decision to use discrete or bulk effect devices is usually determined by considerations such as device efficiency or power handling capability at the frequency of interest. It is a relatively simple matter to convert between electric currents and electromagnetic radiation with good efficiency.

Given discrete devices of sufficiently high frequency response, such as the MDM diode, the hybrid technology of the microwave region may be directly extended to IR and possibly optical frequencies. The MDM diode has microscopic dimensions; but it comes with "wire leads" and requires an antenna and transmission line to couple it to IR radiation. An upper frequency limit may ultimately be imposed by quantum effects such as the photoelectric effect, where metals no longer act as good conductors. However, that limit clearly lies at frequencies above 10^{14} Hz(3μ) and has not yet been reached experimentally. We may expect in the future to see hybrid integrated optical circuits.

Perhaps the most interesting difference between RF and optical frequency devices is the manifestation of optical quantum effects. Given the existence of fast mixers, it is possible to construct optical frequency heterodyne

receivers; but they will never be more sensitive than existing quantum detectors such as the photomultiplier. Some quantum detectors can actually count individual photons and no higher sensitivity is possible.

Whenever reference is made to the radiation pattern of an antenna or to electric currents flowing at optical frequencies, it is to be understood as the limit of many quanta. Optical heterodyne receivers may have many advantages over wavelength selective devices. Among these are the possibility of extremely narrow bandwidths, precision tuning, or high speed response; but they will not be more sensitive than photon detectors.

Chapter 2

Infrared Frequency Synthesis

1. Precision Frequency Measurements

The development of the mechanically contacted MDM diode has made possible direct frequency measurements (as opposed to wavelength measurements) of laser transitions throughout the IR region. The development followed directly from initial experiments with point contact silicon diodes common to microwave technology. The silicon diodes were used as harmonic mixers to compare klystron harmonics with far IR lasers.

Figure 2 shows a block diagram of the method used to measure the frequency of the 1 THz(300μ) HCN laser transitions.[4] The 12th or 13th harmonic of the V-band klystron can be tuned to zerobeat with the HCN laser or, more conveniently, can be tuned to produce a radio frequency beat signal, which is easier to detect. The beat signal may be observed directly on a radio frequency spectrum analyser.

It is important to take some care in stabilizing the klystrons. When using high order harmonics, moderate short term frequency instabilities in an oscillator will mean very broad bandwidth beat signals. In Fig.2, the V-band klystron is phase locked to the 8th harmonic of a double cavity stabilized X-band klystron. In effect, the experiment makes use of 12 x 8 = 96 harmonics of the X-band source.

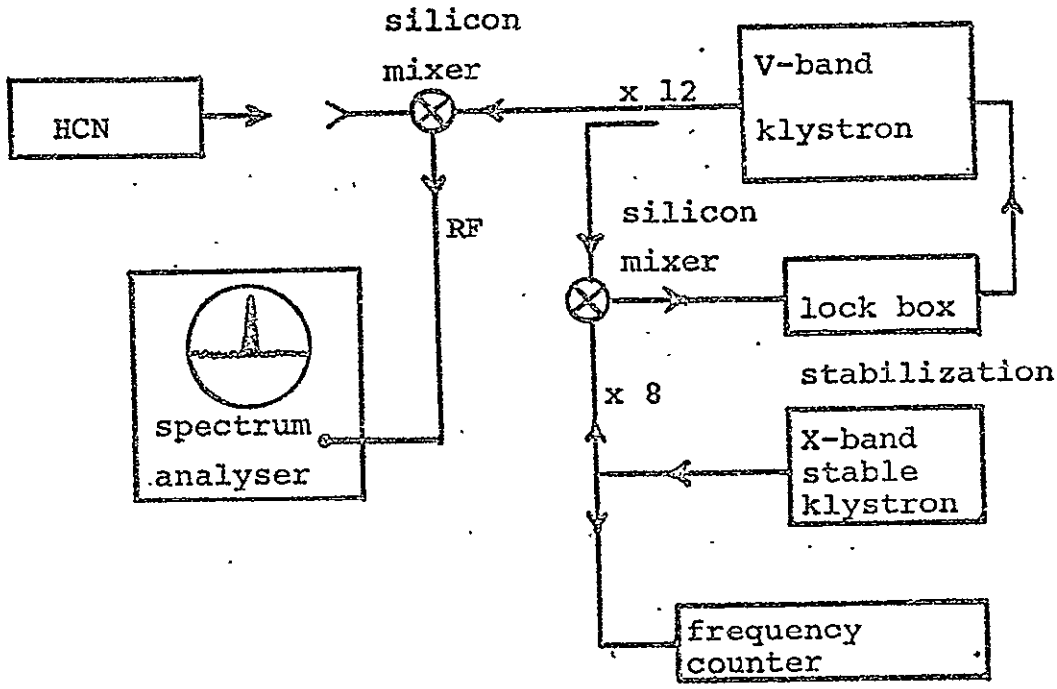

Figure 2

The first laser frequency was measured by comparing the 12 th harmonic of a stabilized V-band (74 GHz) klystron to the frequency of an HCN laser. The frequency mixing was done in a microwave point contact silicon mixer diode.

The experiment of Fig. 2 represented the first direct frequency measurement of a laser. It extended frequency measurement technology by roughly an order of magnitude. In a further extension of the technique, the 23rd harmonic of a klystron was tuned to beat with the 1.5 THz(190μ) DCN laser.[5] Although the signal was observable, it was very weak. Further direct harmonic mixing did not look promising.

Extension of frequency messurements to still higher frequencies was made possible by using harmonics of a laser in addition to klystron harmonics. The 1.5 THz measurement was repeated by mixing the second harmonic of the HCN laser with 3 harmonics of the klystron to produce a beat with the DCN laser.[6] Figure 3 shows the experiment. The order of mixing as defined in Eq.(1) was reduced from 24 to 6 and the observed beat signal was 3 orders of magnitude stronger.

Absolute frequency measurements using laser harmonics and silicon diodes were extended to 3.5 THz(84μ) by this author and others.[7] All attempts at higher frequency measurements, however, failed.

The semiconductor diode is ultimately bandwidth limited by recombination rates of its charge carriers. Heavily doped semiconductors were used in an attempt to increase the upper frequency limit, but diminishing returns are reached at frequencies above about 3 THz. The electron tunneling process of the MDM diode, however, is not subject to the same limitation. A straightforward substitution of

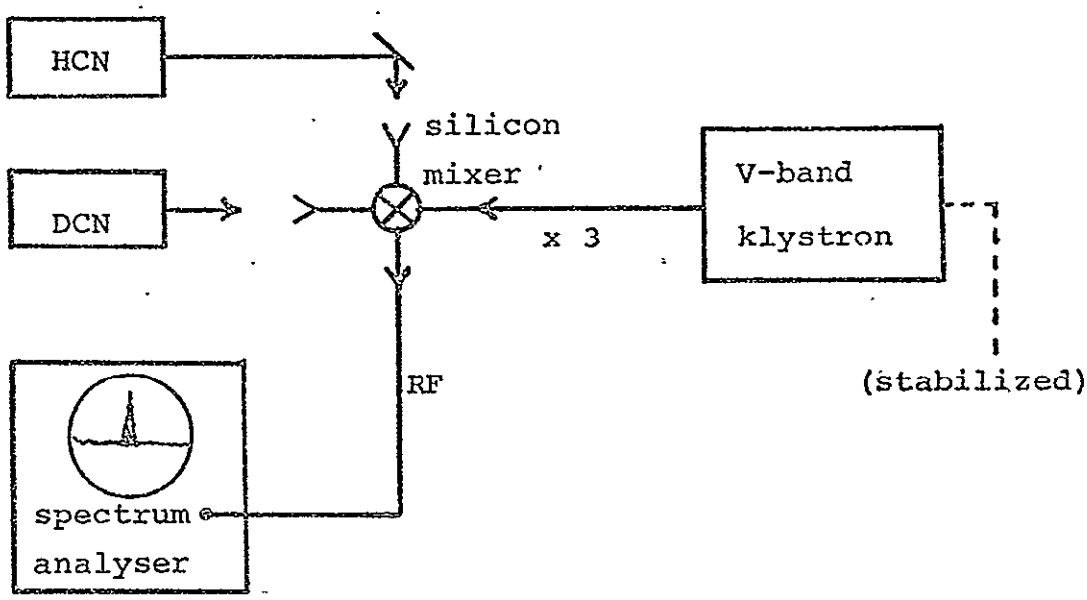

Figure 3

The first laser frequency multiplying chain used the second harmonic of an HCN laser to beat with the fundamental frequency of a DCN laser.

the MDM diode for the silicon mixer of Fig.3 has permitted IR frequency synthesis to be pushed steadily higher to a present limit of about 100 THz.[8-10]

Frequency measurements are presently the most accurate of all physical measurements. The laser frequency measurements described above readily produce 7 digit accuracy. The principle limit to measurement accuracy lies in setting the laser precisely to the center of its gain profile. Using free running lasers, it is possible to make frequency measurements which are an order of magnitude more precise than the best corresponding wavelength measurements which have been made for far IR lasers. Table 1 lists a number of laser transitions which have been measured by harmonic frequency mixing.

2. The Laser Frequency Multiplier Chain

Figure 4 shows two possible chains of laser harmonic multipliers. The difference frequencies shown schematically as mixer outputs may be calculated from the data of Table 1. In each case, the difference frequencies have been observed experimentally by coupling a microwave source of nearby frequency to the mixer and searching for a radio frequency beat.

For IR frequency measurements to the modest accuracy of about one part in 10^7, the lasers of Fig. 4 may be operated without elaborate stabilization measures. Further-

Table I

Precision Frequency Measurements

Laser Type	Wavelength(μ)	Frequency(THz)	Reference
HCN	373	.804 750 9	4
	337	.890 760 550	11,4
	335	.894 414 2	4
	311	.964 313 4	4
	310	.967 965 8	4
DCN	190	1.578 278 7	6
H_2O	118	2.527 954	6
He	95	3.129 791 5	12
D_2O	84	3.557 143	7
H_2O	78	3.821 755	13
	28	10.718 068 6	14,11
CO_2	10.6(P18)	28.359 800	15
	10.6(P20)	28.306 251	15
	10.2(R30)	29.442 483 315	11,15
	9.3(R12)	32.176 062	16
	9.3(R10)	32.134 266 891	11,16
CO	5.2(P13)	58.024 341	17
HeNe	3.39	88.376 181 627	11,18

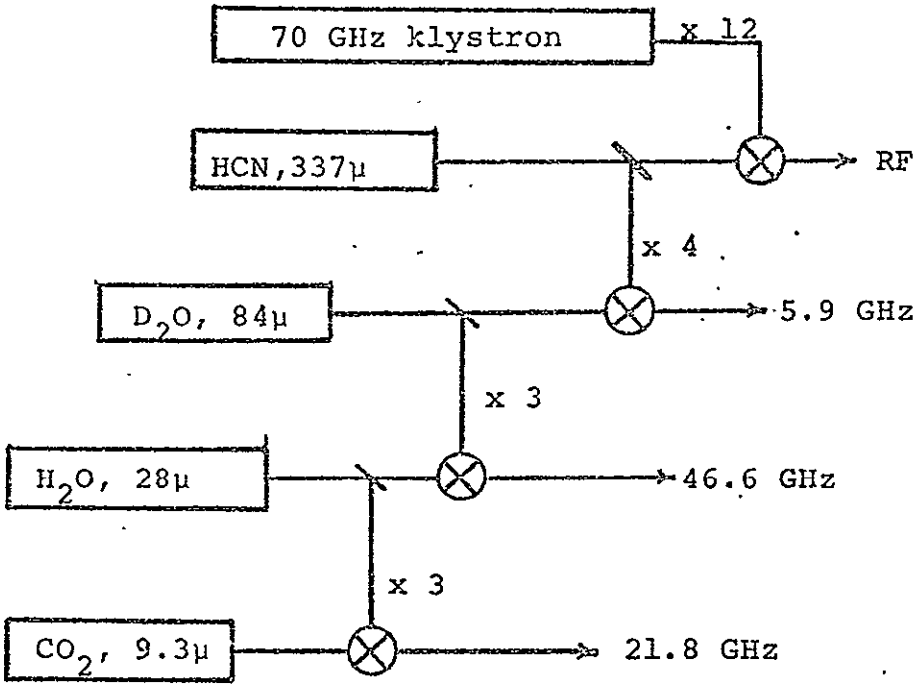

(a)

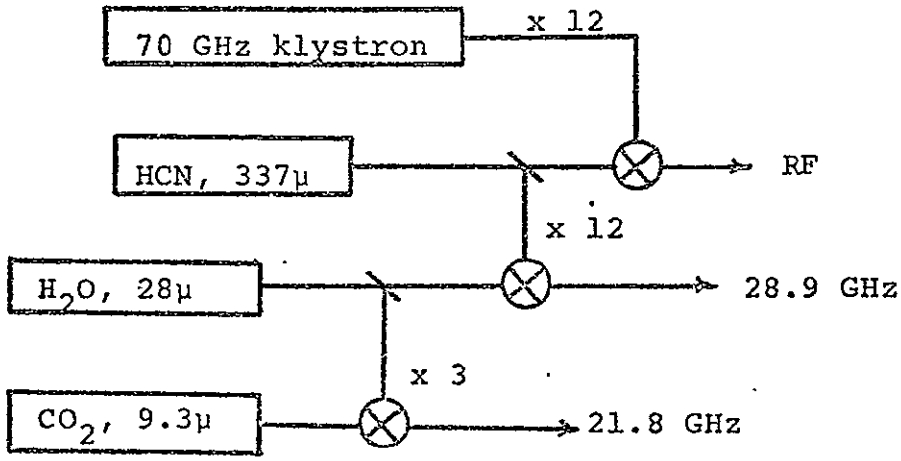

(b)

Figure 4

Laser frequency multiplier chains which can connect microwave measurements to the 30 THz(9.3μ) CO_2 laser are shown. Chain (a) uses one more laser than chain (b) to keep the order of mixing low.

more, the lasers need not all be operating simultaneously. If care is taken to operate the lasers always near the center of their gain curves, each link in the chain need be measured only once. The lasers can then serve as transfer standards of known frequencies throughout the IR.

Higher accuracies , to parts in 10^9, may be achieved by operating all the lasers simultaneously and monitoring the microwave difference frequencies with electronic counters as the lasers drift about their nominal frequencies. Still higher accuracy ; to at least one part in 10^{12}, may be achieved by stabilizing the lasers.

A novel stabilization method makes use of frequency synthesis in the MDM diode. First attempted in 1969,[19] the object is to mix microwave and laser frequencies in the MDM diode. Laser frequency instabilities which would normally show up in the mixer products may be compensated by electronically tuning the microwave oscillator. The mixer product of interest is compared to a harmonic of a lower frequency reference standard in order to derive a correction signal to be applied to the microwave oscillator. The stabilized mixer product , which exists as an oscillating current within the MDM diode, may then be used in harmonic mixing applications, as was demonstrated in the laser frequency multiplier chain.[20]

The use of harmonics of synthesized frequencies works quite nicely. Notice, however, that a frequency multiplier 292<

chain using this type of stabilization will require a higher order of mixing at each link than is required for direct harmonic mixing of lasers.

The laser chain of Fig. 4b requires 14th order mixing in the step between the HCN laser and the H_2O laser: 12 x HCN + 1 x H_2O + 1 x microwave to give an RF beat. The amplitude of the RF beat was marginal. For laser powers of approximately 50 mW and microwave power sufficient to burn out the MDM diode, the observed beat signal was seldom larger than .2 μV. In the chain of Fig. 4a, however, the beats between the HCN and D_2O lasers and between the D_2O and H_2O lasers were approximately 5 μV. The improvement was due primarily to the lower order of mixing. With the stronger intermediate beat signals, harmonics of synthesized frequencies worked well. The electronic tunability of the synthesized frequencies allows them to be phase locked to a microwave standard, thereby achieving at laser frequencies the stability of a standard.

The laser frequency multiplying chain has demonstrated the practicability of synthesizing any desired far infrared frequency. The frequency, existing as an oscillating current in the MDM diode mixer, may be as stable and accurate as the microwave (or laser) reference standard to which it is phase locked.

Presently, several highly stable laser systems are being developed. The systems generally employ an atomic

or molecular optical resonance to which the laser output frequency may be stabilized. The accuracy and stability of systems such as the methane stabilized helium-neon laser at 88 THz(3.39μ) and the iodine stabilized helium-neon laser at 474 THz(.633μ) show promise of eventually rivaling the performance of existing microwave frequency standards such as the hydrogen maser and the cesium atomic beam device.

The great advantage of an optical frequency standard is that a single device can serve both as a standard of frequency and as a standard of length. To be useful as a frequency standard, however, the frequency must be "counted down" or referenced to microwave and radio frequencies. The phase locked laser frequency multiplying chain using the MDM diode has demonstrated that the necessary technology can be developed.

Chapter 3

The Thin Film Diode

1. Review

The frequency synthesis described in Chapter 2 was first made possible by the development of the mechanically contacted MDM diode. In physical appearance, the mechanical MDM diode is identical to the microwave point contact silicon diodes it supersedes. The fabrication techniques for the mechanical MDM diode have been described in detail by Sokoloff[21] and will not be extensively reviewed here.

In its initial applications, the MDM diode was used as a direct replacement for silicon diodes in millimeter wave crossguide mixers. Then, as the MDM diode was applied to problems at progressively shorter wavelengths, the use of waveguides was abandoned. It is not only difficult to fabricate extremely small waveguides, but it is also very difficult to efficiently couple laser power into them.

It was empirically observed that laser power could be more efficiently coupled through a lens to an open structure diode than to a diode inside a waveguide. For an exposed diode in an open structure, the contacting wire serves as a long wire antenna at laser frequencies. Matarrese and Evenson[22] demonstrated that the wire antenna has a radiation pattern identical to the case of a radio

frequency long wire antenna, and it is now standard practice to choose a direction for the incident laser radiation which corresponds to a maximum lobe of the diode. The prefered directions are determined experimentally by rotating the diode structure relative to the direction of the incident radiation until a strong maximum is reached.

Figure 5 shows a schematic representation of the microscopic features of the mechanically contacted MDM diode. A thin tungsten wire, in this case 2.5μ in diameter, is first sharpened by electrochemical etching and then pressed against an oxidized nickel post to form a junction of small area. Electron microscope photographs have shown that the radius of curvature of the wire tip can be as small as 1,000 Å. The frequency response of the device is primarily RC limited where R is an effective series resistance and C is the junction capacitance. For operation at infrared frequencies, it is critical to minimize both, particularly C.

If the output from an IR laser is focused on the diode, a voltage difference will appear between the tungsten wire and the nickel post. The diode is being used as a detector and, in this sense, is by far the world's fastest detector. Usually the nickel post will have positive polarity with respect to the tungsten wire, but not always. The sensitivity and polarity depend upon the contact pressure and localized effects on the oxidized metal

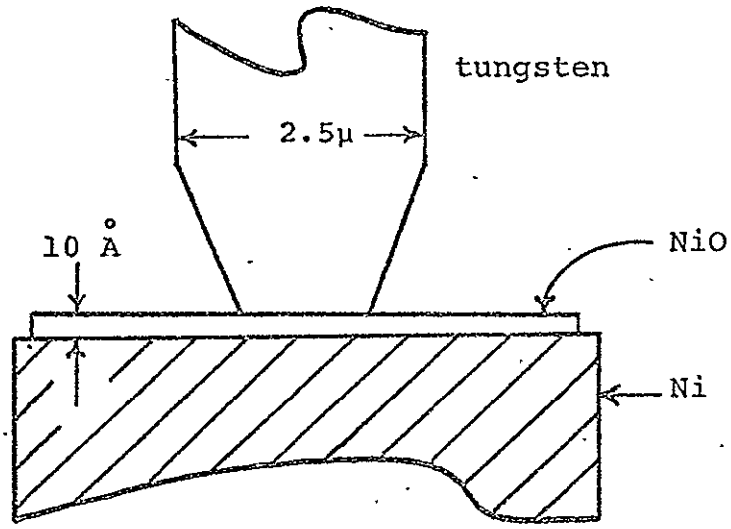

(a)

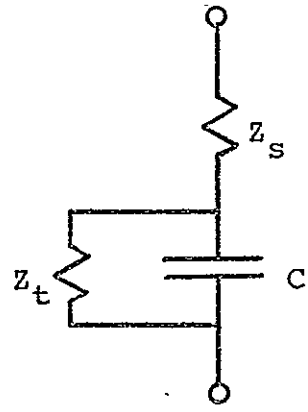

(b)

Figure 5

Shown in (a) is a microscopic representation of a mechanically contacted MDM diode. The tungsten wire acts as an antenna for infrared radiation. The equivalent electric circuit is shown in (b). Z_s represents a series impedance , typically the effective antenna impedance at infrared frequencies. C is the junction capacitance and Z_t represents the impedance due to tunneling electrons.

surface.

The detector sensitivity in the far infrared and microwave regions near 1 THz may be as high as .1 V/Watt. That sensitivity is approximately 10% of a silicon diode at the same frequency range. For the detection of very weak but narrow band signals, a heterodyne detector, using the mechanical MDM diode as the first mixer, is capable of detecting 10^{-13}W/Hz .[10]

When a voltage is applied across the diode, either DC or AC from a microwave of laser source, a current will flow through the junction due to the quantum mechanical tunneling of electrons through the oxide layer. The tunneling impedance is represented in Fig.5b by Z_t. The tunneling impedance is not a constant. It depends in a nonlinear manner on the applied voltage. It is the nonlinearities of the tunneling process which are responsible for the diode's mixer characteristics. The mechanism of electron tunneling is extremely fast and permits the device to be used at IR frequencies.

2. Thin Film Arrays

A very major drawback to the use of mechanically contacted MDM diodes is their extreme sensitivity to mechanical and thermal shock. If the diode is mounted in a rigid inclosed structure, such as a V-band microwave crossguide mixer, it is possible to gently handle the

device without destroying a good contact. It was a rare occasion, however, when such a diode structure would continue to operate after being left overnight.

Mechanical stability and, perhaps, electrical reproducibility can be achieved if the microscopic MDM diode is fabricated with thin metal films firmly bonded to a rigid substrate. Figure 6 shows the first attempt to achieve a "printed" MDM diode on a sapphire substrate. The actual diode junctions are not visible at the scale of Fig.6. The construction of the peacock array is shown schematically in Fig.7 .

Microelectronic techniques which were developed for the manufacture of integrated circuits have currently achieved a resolution control finer than 1μ. All of the thin film structures described here were fabricated with a photolithographic precess capable of achieving .5μ resolution.[23] Other techniques, such as electron beam lithography and X-ray lithography, are currently capable of one order of magnitude finer resolution but have not yet been applied to MDM diodes. The thin film diode fabrication was done in collaboration with F.J. Bachner and D.L. Smythe of the Microelectronics Group 87 of the M.I.T. Lincoln Laboratories.

3. Fabrication

The objective of the thin film structure of Fig.6

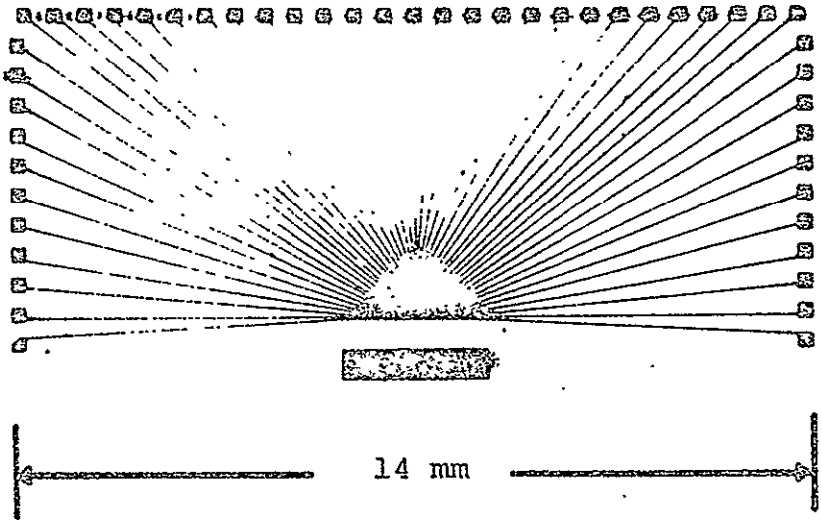

Figure 6

The Peacock Array

The first attempt at printing thin film diodes on a sapphire substrate produced a working device. Shown here in the "peacock array" are 49 diodes. Each diode is connected to the large common contact pad at the bottom and to one of the smaller contact pads at the top. Extending upward from the large contact pad are 49 2.5μ wide conductors not visible at this scale. Details of the diode junctions are shown schematically in Figs. 7 and 8.

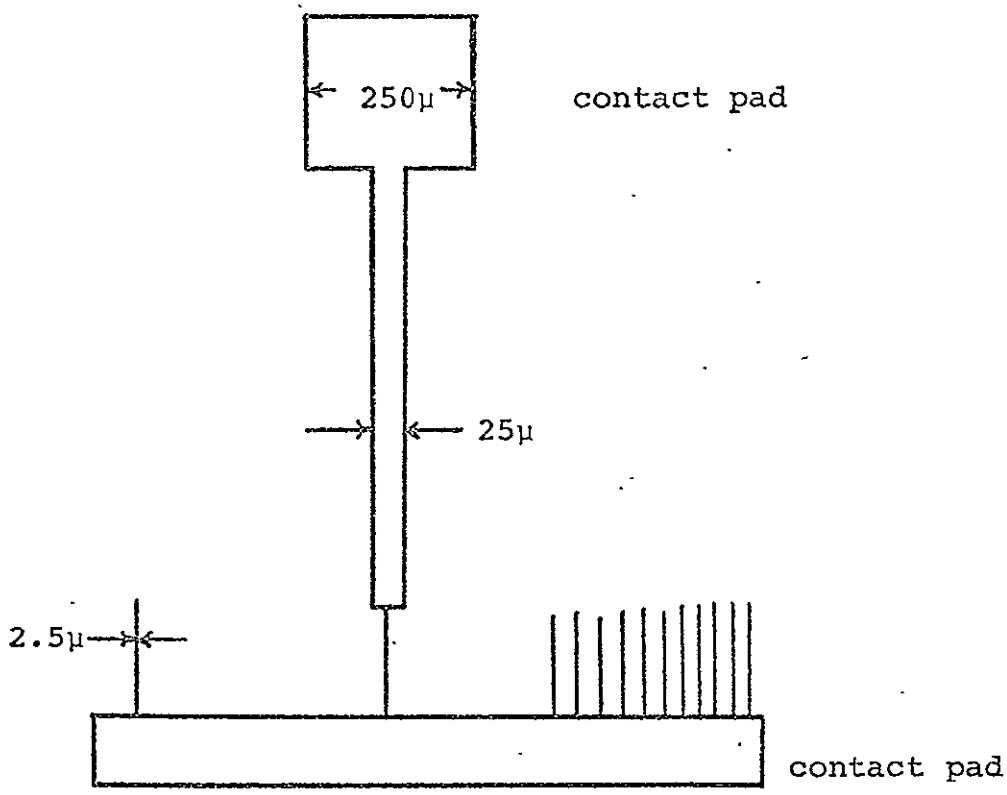

Figure 7.

The Peacock Array.

A schematic representation, not to scale, shows the construction details of the peacock array. The large rectangular contact pad and 49 vertical strips of 2.5μ width are deposited on a sapphire substrate and allowed to oxidize. The remaining 49 square contact pads and 25μ strips are then overlaid to form Metal-Dielectric-Metal junctions. Each junction may be biased and tested separately.

is to approximate the small area mechanically contacted MDM diode. The structure is made in a two step process. First the large rectangular pad and its associated 2.5μ vertical strips are formed on a sapphire substrate.

The desired pattern is formed by coating the sapphire substrate with a light-sensitive resist. The resist is exposed to blue light through a mask of the desired pattern. Unwanted areas of the resist are removed by chemical means. Then metal is vacuum evaporated onto the etched resist. Unwanted metal is removed by chemically removing the remaining underlying resist. The metal films are typically 1,000 Å thick.

After forming the large pad, the entire structure is cleaned by an electric discharge in low pressure helium and oxygen gas, exposed to air, and allowed to naturally oxidize. The gas discharge treatment is a common cleaning technique in thin film operations. It was first done in MDM diode fabrication accidentally but was found to produce, on the average, more successful diodes.

The second step in diode fabrication is to repeat the above process with a second mask. In that manner, a second pattern of metal may be overlaid. Metal-Dielectric-Metal junctions are formed at regions of overlap of the two patterns.

The mask patterns are computer generated and photographically reduced. The second mask is manually registered

with respect to the first pattern by a technician using a microscopel

Figure 8 shows a magnified view of the overlap regions of the array of Fig.6. The MDM diodes are formed where the 25μ strips overlap the previously oxidized 2.5μ strips.

It can be seen that some diodes have relatively large overlaps, some just touch, and some have no overlap at all. Diodes which do not touch show a DC open circuit and are not usable. On any particular substrate, there may be many diodes which have DC continuity but show no observable rectification (less than 1 μV for 30 mW/mm^2 incident laser intensity at .9 THz). That failure mode may be due to diodes of large overlap area where shunt capacitance reduces the frequency response. Doubtless there are other mechanisms, such as pinholes in the oxide layers, which could also produce shorted diodes.

A given substrate may have as high as 80% of its diodes working or as low as zero. The lack of reproducibility form one substrate to the next may be due in part to the manual registration of the two patterns. In an effort to compensate for manual alignment irregularities, the peacock array employs periodically staggered lengths in the 2.5μ strips. The staggering accounts for the open diodes of Fig. 8. The periodic structure was readily apparent in the success of the individual diodes on a single substrate. Indeed, some diodes had too much overlap, some

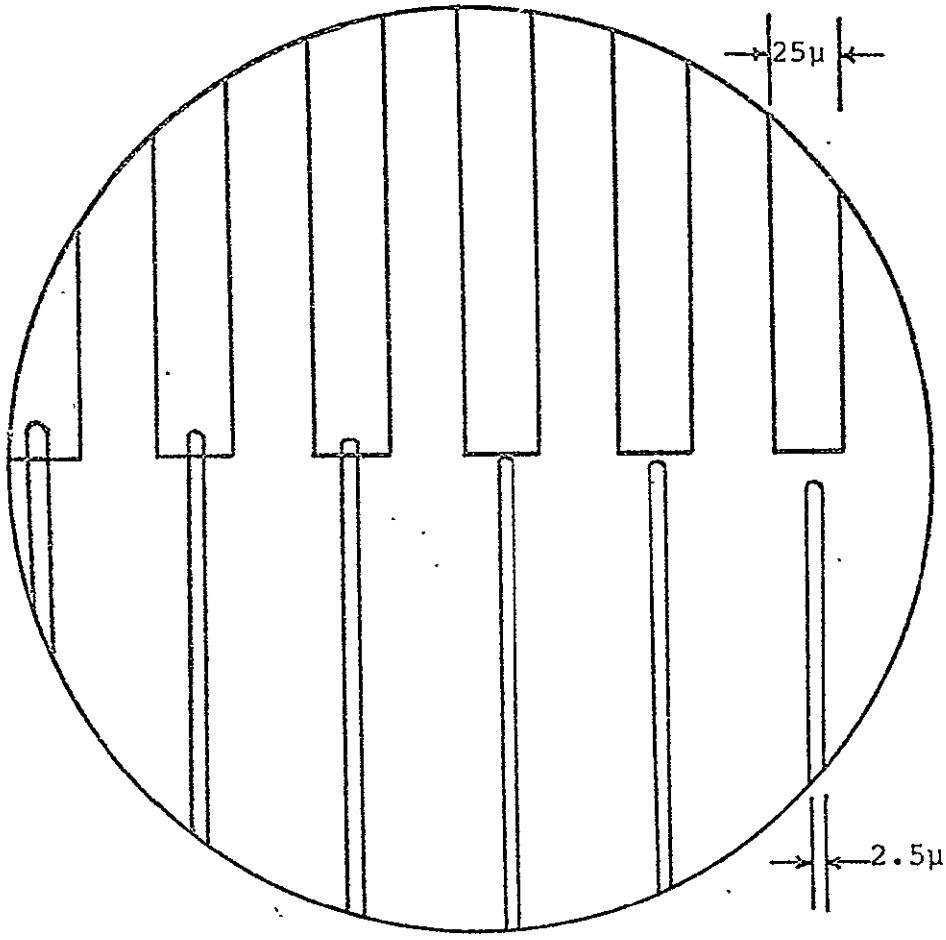

Figure 8.

A magnified view of the diode regions of the peacock array of Fig. 6. Diodes which do not touch exhibit DC open circuits and are not useable. If the overlap area is too large, shunt capacitance reduces the frequency response. The total view shown above is approximately the same size as the period at the end of this sentence.

304<

were open circuits, and some were just right.

4. Materials

In an attempt to duplicate as closely as possible the mechanically contacted diode, the first thin film diode was made from Ni, NiO, and Ni. Conveniently, two of the easiest metals to vacuum evaporate are Ni and Cr. By a great stroke of luck, the first attempt produced a diode capable of rectifying the .9 THz HCN laser.

Figure 9 shows a schematic representation of the experiment. To avoid rectification where the contacting wires of the micromanipulators touch the thin film contact pads, it is necessary to keep the laser focal spot small and away from the wires.

Since that first attempt, two other metals and their oxides have been tried: Cr and Cu., The only successful oxide to date has been NiO. Cu was difficult to fabricate. Its oxide never produced a working diode. However, Cu on NiO produced 6 weakly rectifying junctions on a single substrate. The Cu contact was always positive. The junctions also showed much noise with bias.

The oxide of Cr appears to be too thick. Its diodes show a comparatively high DC resistance (10 kΩ) compared to NiO diodes (10-100 Ω) AND IN NO CASE was laser rectification observed. However, Cr on top of NiO works well.

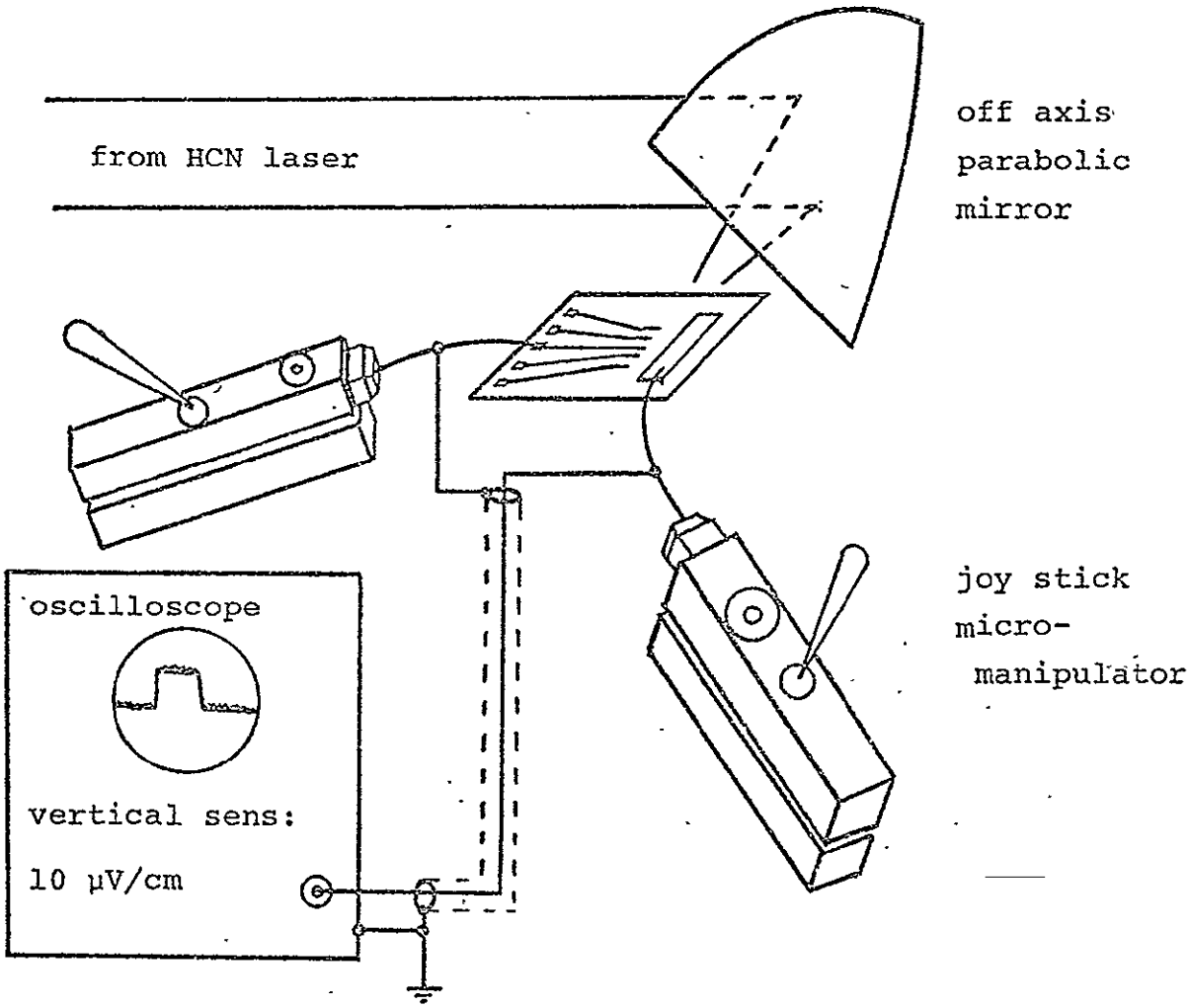

Figure 9.

Rectification of the .9 THz(337μ) HCN laser was observed in the first thin film diode ever fabricated. 30 mW of power focused to a 1 mm diameter spot produced 5 μV of rectified DC. Junctions have now been fabricated with 100 times higher sensitivity. The relative size of the thin film substrate is here greatly exaggerated. A 50x stereoscopic microscope is used to position the contact wires of the micromanipulators.

In an attempt to reduce heating effects in the substrate from a CO_2 laser at 28 THz(10.6μ), the peacock array was also fabricated on a silicon substrate. Two attempts were made and produced no working diodes. In the first attempt, the diodes were fabricated directly on a bare silicon substrate. All of the junctions exhibited DC short circuits due to the finite electrical conductivity of the silicon substrate. A subsequent attempt on an oxidized silicon substrate removed that problem but still produced to operating junctions.

5. Lifting the Symmetry

Unlike the mechanically contacted MDM diode, the thin film version possesses a high degree of spatial symmetry. Instead of a pointed wire touching a flat surface, the thin film diode is much more nearly a sandwich of an insulator between two flat and identical metal surfaces. If the same metal, say Ni, is used for both the upper and lower conductors, there is no particular reason why the device should rectify. Why should a perfectly symmetric device have positive charges building up on one side and negative charges on the other in response to a symmetric sinusoidal excitation? A symmetric diode satisfies the current-voltage condition:

$$J(-V) = -J(V) \qquad (3) .$$

It follows directly that all even order derivatives, $\partial^n J/\partial V^n = 0$ at $V = 0$ for even n.

Sanchez has shown[10] that the symmetry can be upset by making junctions of dissimilar metals with differing work functions. A semiconductor P-N diode may be thought of as the extreme case where the dissimilar metals have charge carriers of opposite sign.

The symmetry can also be upset by application of a DC bias current to the diode. A DC bias may be used to study in detail the various derivatives, $\partial^n J/\partial V^n$, of the diode. Details of the J-V function are discussed in Chapter 4.

Both symmetric and dissimilar metal junctions have been fabricated in the peacock array of Fig. 6. As expected, diodes formed of Cr-NiO-Ni show consistently larger rectified voltages than Ni-NiO-Ni diodes. Furthermore, the Ni side is always positive in the dissimilar metal configuration. With the simmilar metal junctions, the rectified voltage polarity appears to be random even for diodes which were formed simultaneously on the same substrate.

When used as rectifiers at .9 THz, the detectivity of the thin film diodes varies statistically from one junction to the next. It is possible to state, however, that of the several hundred working diodes tested, the use of dissimilar metal Cr-NiO-Ni diodes increases the detectivity by 2 to 5 times over the symmetric devices.

The application of DC bias currents can increase the detected signal by over 2 orders of magnitude. Figure 10 shows the effect of reversing the DC bias current. As expected, the polarity of the detected signal reverses.

It is important to note that a larger detected signal does not necessarily mean a more sensitive detector. The application of a bias current always produces shot noise. As the bias current is turned higher, both detected signal and noise increase. Eventually at high bias the noise increases faster than the signal and masks it.

At zero bias, the principle noise source appears to be thermal or Johnson noise. When using amplifiers of less than perfect noise figure, diode bias may significantly improve the overall system signal to noise ratio. It was found that some diode units performed much better under bias than others. As a general rule in diodes exhibiting a low resistance (10-100 Ω), the detected signal could be increased more than two orders of magnitude before being overtaken by noise. Relatively high impedance diodes (1000 Ω) generally exhibited larger zero bias signals but did not improve with bias. In the best cases with bias, a thin film diode could approach the volts/watt sensitivity of .1 observed with the mechanically contacted versions.

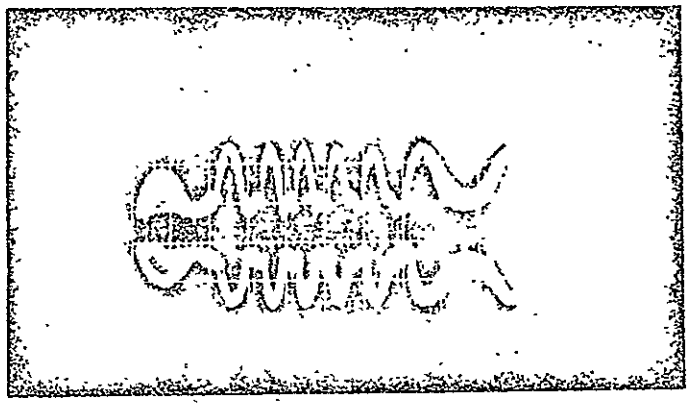

Figure 10.

The application of a DC bias current can increase the detected laser signal by more than two orders of magintude. Here a pulsed .9 THz(337μ) HCN laser is detected with a biased thin film diode similar to Fig. 7. The upper trace shows the detected signal under positive bias of approximately 1 mA and the lower trace under negative bias. The laser is pulsed by changing its resonator cavity length to periodically tune through the HCN molecular resonances.

6. The Series Array

Mechanical and electrical stability was demonstrated in the peacock array. Physical handling of the substrate and bias currents to several mA did not generally damage the thin film devices. Furthermore, temporal stability has been established on a time scale of at least six months. No special storage precautions were used. The substrates were stored in plastic boxes at room temperature and occasionally rinsed with ethanol to remove dust.

To make use of the thin film MDM diode as a fast, room temperature detector of infrared radiation, a series array was fabricated. It is an attempt to make a large area, nonresonant and therefore broadband array of diodes. For optimum sensitivity, dissimilar metal junctions were used, which presents an interesting problem.

If an alternating series of Ni and Cr films are deposited to form an array of Cr-NiO-Ni junctions, it can be seen in Fig.11a that the diode polarities along the string will alternate. Detected voltages will cancel instead of add.

The junctions must be fabricated in the two step process with NiO forming the dielectric in all cases. The solution shown in Fig.11b is to first deposit the Ni and then deposit the Cr making every other junction a large area non-rectifying junction.

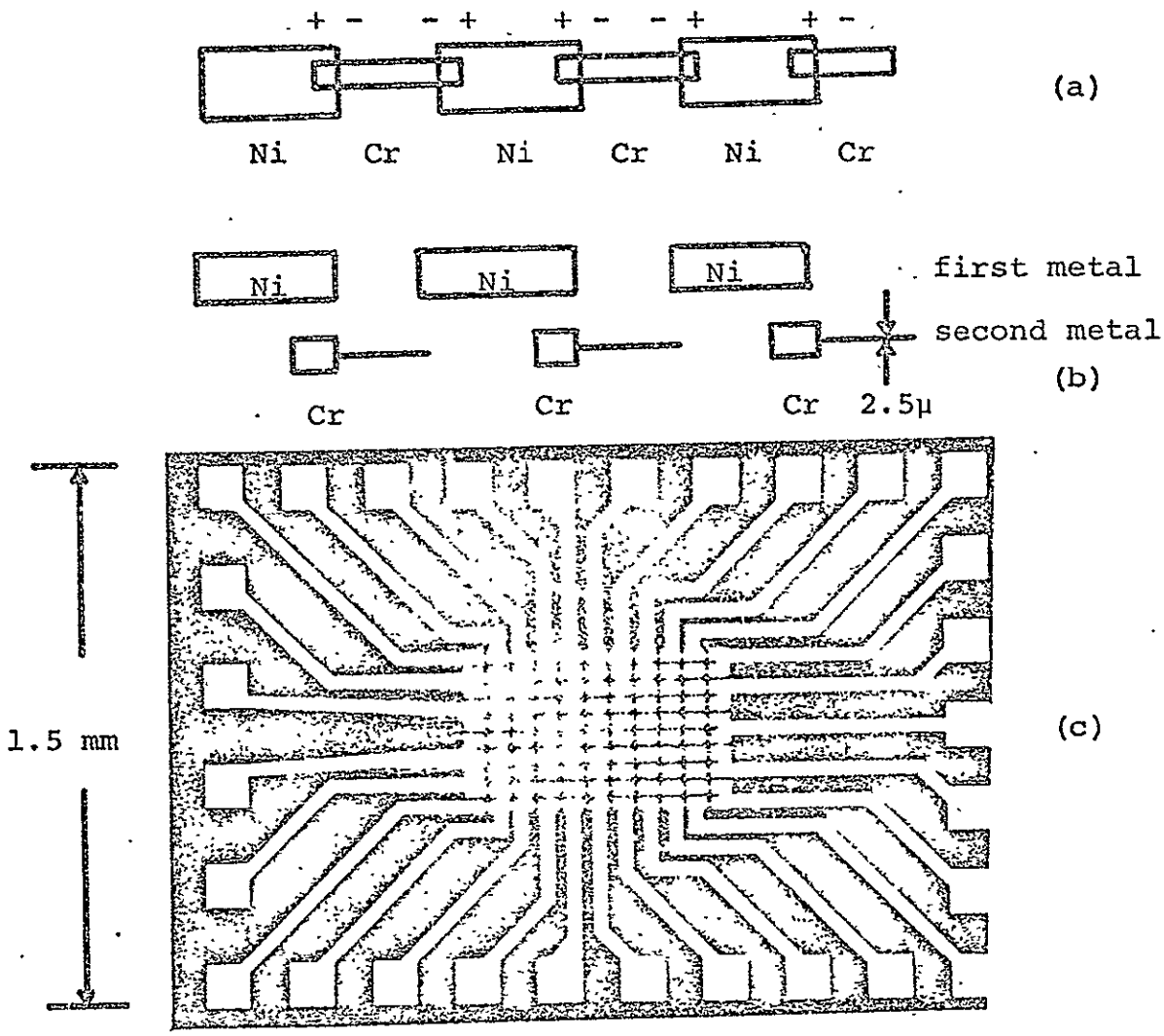

Figure 11.

The series array.

An alternating series of dissimilar metal junctions (a) will produce diodes of alternating polarity and detected signals will not add. In (b) every other junction is made a large area non-rectifying contact. In (c) are 100 diodes in series.

Figure 11c is a photograph of a series string of 100 rectifying junctions alternating with non-rectifying junctions. DC contact pads are provided to test the voltage contributions from individual junctions in the two outer strings and from the entire length of the inner strings.

Note the 1.5 mm scale factor. To the unaided eye, the series array is a fuzzy rectangular spot on the sapphire substrate. The computer generated patterns may be readily stepped and repeated across the substrate. A substrate 2 cm x 2 cm typically held 9 series arrays of 100 diodes each.

As expected, the detected voltages add nicely. It was possible to add algebraically the voltage contributions from as many as 30 diodes in a row before encountering an open circuit junction.

The series array responds to DC bias in a manner similar to the peacock array. In a statistical manner, some junctions have more noise than others under bias. The net result is that the noise due to a string of diodes is always greater than the noise due to the worst diode in the string, which is not a very promising condition for biased detectors. Had bias noise been no major problem, the series string could be made from similar metal junctions. The bias polarity across each junction will

assure that the detected signals add algebraically.

7. Frequency Mixing with Thin Film Antenna Structures

Harmonic frequency synthesis is not possible in either the peacock or series arrays. The restriction follows from the geometry of the arrays. Each of the above designs places many diodes into an area small compared to the wavelength of microwave radiation. No single diode element could be coupled strongly to microwave radiation. Mixing between microwave and laser frequencies was attempted but never observed.

Frequency synthesis at laser frequencies can be used to demonstrate the high speed properties of the diodes. However, a number of slower mechanisms including thermal effects could explain the relatively straightforward detector experiments described above. The antenna arrays described below were developed to demonstrate the faster electron tunneling process.

Figure 12 shows the first thin film MDM diode to be integrated with an antenna system. As always, the structure is fabricated in a two step process. In this instance, the right half of the diode and antenna system was deposited and allowed to oxidize. Next, the left half was deposited with a small area overlap at the center of the smaller dipole to form the tunneling junction. The

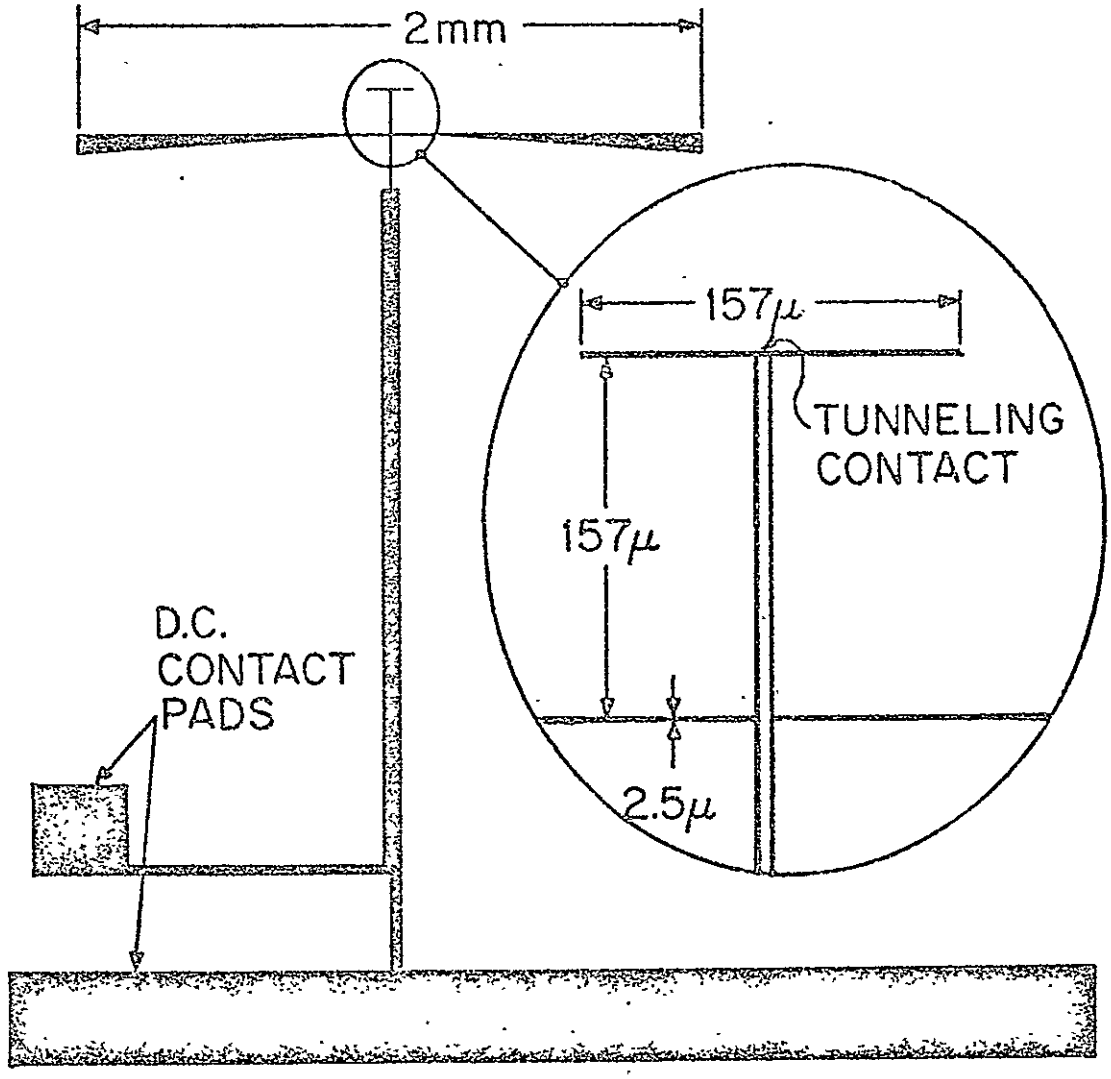

Figure 12

In order to more effectively couple microwave and laser power to the diode, thin film antennas are integrated with the MDM diode. In this structure, laser frequency mixing was first observed in the thin film MDM diode. 315<

DC contact pads are well removed from the diode to prevent microwave pickup and rectification in the micromanipulator contacting wires.

In the figure, the 2 mm cross piece approximates a half wave dipole for 4 mm(75 GHz) klystron radiation. The magnified view at the right shows the half wave dipole for the laser frequency of .9 THz(337μ). The small dipole's length is somewhat shorter than a free space half wavelength in order to compensate for effects due to dielectric loading and finite conductor widths. Also shown in the magnified view is the parallel strip transmission line which connects the diode, antennas, and DC contact pads.

Laser frequency mixing in this structure was successfully demonstrated in an experiment similar to that of Fig.9. The laser output was focused on the substrate as before. Microwave power was coupled to the device from the open end of a V-band (70 GHz) waveguide located under the sapphire substrate directly beneath the 2 mm dipole.

The spacing between the 2mm dipole and the 157μ dipole was chosen to produce a coherent interference structure in the far field radiation pattern at .9 THz. Figure 13 shows the measured laser response at 337μ and 311μ as a function of the angle of the incident radiation.

The radiation pattern was obtained by rotating the antenna structure of Fig.12 about the axis of the 2 mm

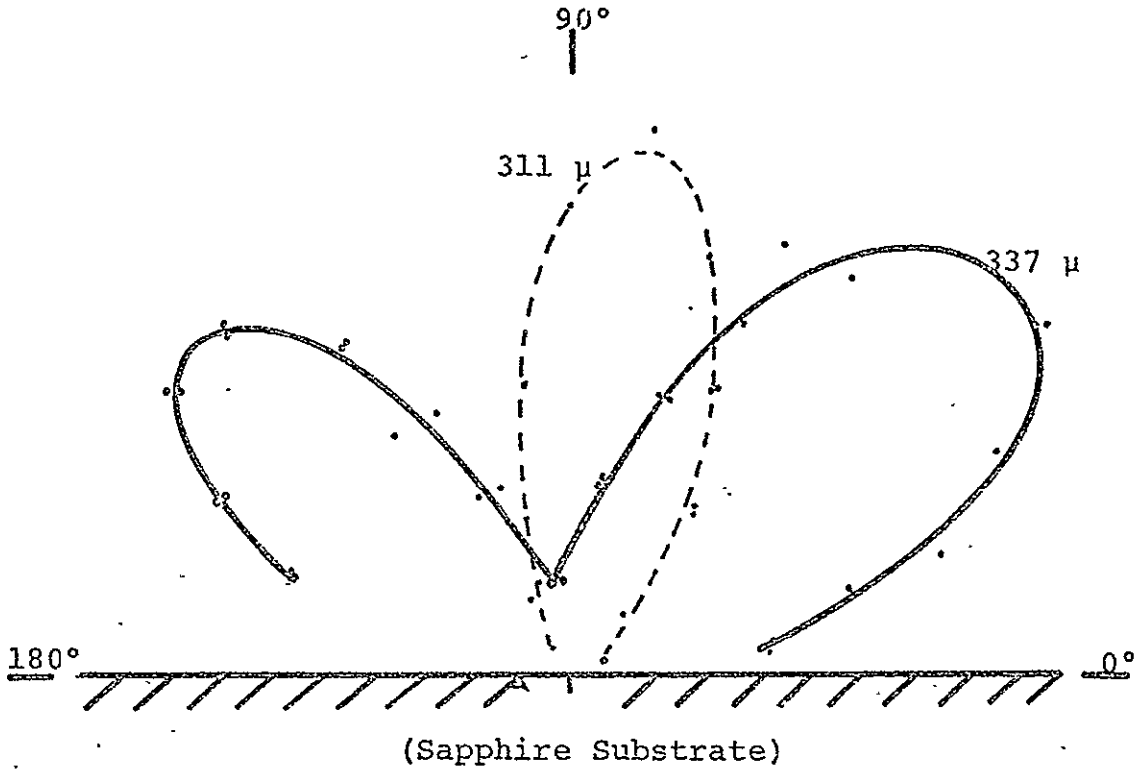

Figure 13

The far field radiation pattern of the antenna structure of Fig. 12 was designed to be strongly wavelength dependent in the region of 1 THz(300μ). Here the pattern is measured for the two strong HCN laser lines at 311 μ and 337 μ. 90° corresponds to laser radiation incident broadside to the array while 0° and 180° are the endfire responses. With the large dipole antenna at the origin, the transmission line and DC contact pads are in the direction of 0° .

317<

dipole. Note that the pattern is highly wavelength sensitive. At 337μ there are two well defined lobes and a sharp broadside null. At 311μ only one strong maximum was observed. The same radiation pattern was measured in several diodes of differing sensitivities but with similar antenna structures.

The structure of Fig.12 may be repeated periodically. A 2 cm x 2 cm substrate held typically 20 diodes and antenna structures. Of approximately 150 diodes fabricated to date, about 10% have shown the characteristics of high speed mixing.

The first verification of high speed performance was a third order mixing experiment between the .890 THz(337μ) and .964 THz(311μ) HCN laser transitions and a 74 GHz microwave source. The laser frequencies are well known from Table 1. After appropriately adjusting the microwave frequency, a relatively strong (10 μV) zero beat signal could be detected across the DC contact pads of the device in Fig.12 in the best case found. See Fig.14. The observed beat signal amplitude is a factor of 5 below the performance of a mechanically contacted MDM diode under similar circumstances.

In mechanical diode mixing, the microwave power is always adjusted for a maximum beat signal. Usually that occurs somewhat below diode burn out. Increasing the

318<

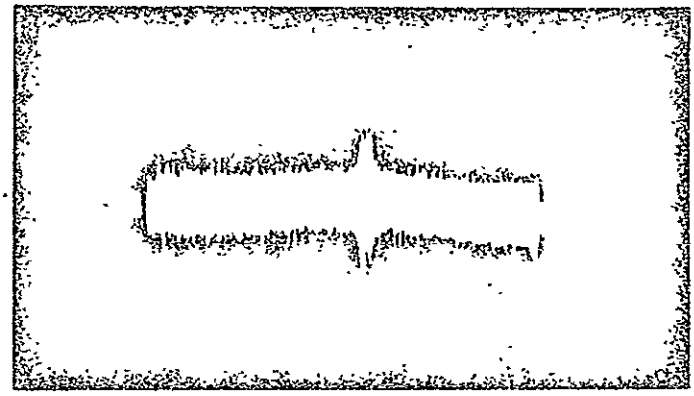

Figure 14

A third order mixing experiment at .9 THz produced this zero beat signal across the DC contact pads of the device in Fig. 11. The vertical scale represents 10 μV/division . The experiment demonstrated that the thin film diode has a frequency response at least as high as the difference frequency between the two HCN laser transitions at .890 THz(337μ) and .964 THz(311μ) ; i.e. 74 GHz .

power further results in less beat signal, probably because of a rectified self biasing effect in the diode.

For the thin film structure of Fig.12, an optimum level of microwave local oscillator could not be reached. The beat signal was still improving when maximum 74 GHz power was applied.

In an attempt to further improve microwave coupling, the antenna structure of Fig. 12 was modified. The 2mm dipole is, at its narrowest point, only 2.5μ wide. Calculations of the resistivity of Ni and Cr thin films indicate that the ohmic resistance from one end of the 2mm dipole to the other should fall in the range of 100 Ω. The tunneling junction appears to have a resistance of about 10 Ω. Therefore, the microwave coupling could be reduced by one order of magnitude due to a simple ohmic voltage devider.

Figure 15 is an antenna design intended to reduce the ohmic losses for microwave coupling. This newer thin film design has been available only recently, but preliminary results indicate improved microwave coupling approximately as expected, one order of magnitude.

The radiation pattern for the antenna of Fig.15 is quite different from the pattern of Fig.13. At 337μ, the newer pattern shows 3 broad overlapping lobes. At 311μ the pattern shows two principle lobes with no sharp nulls.

320<

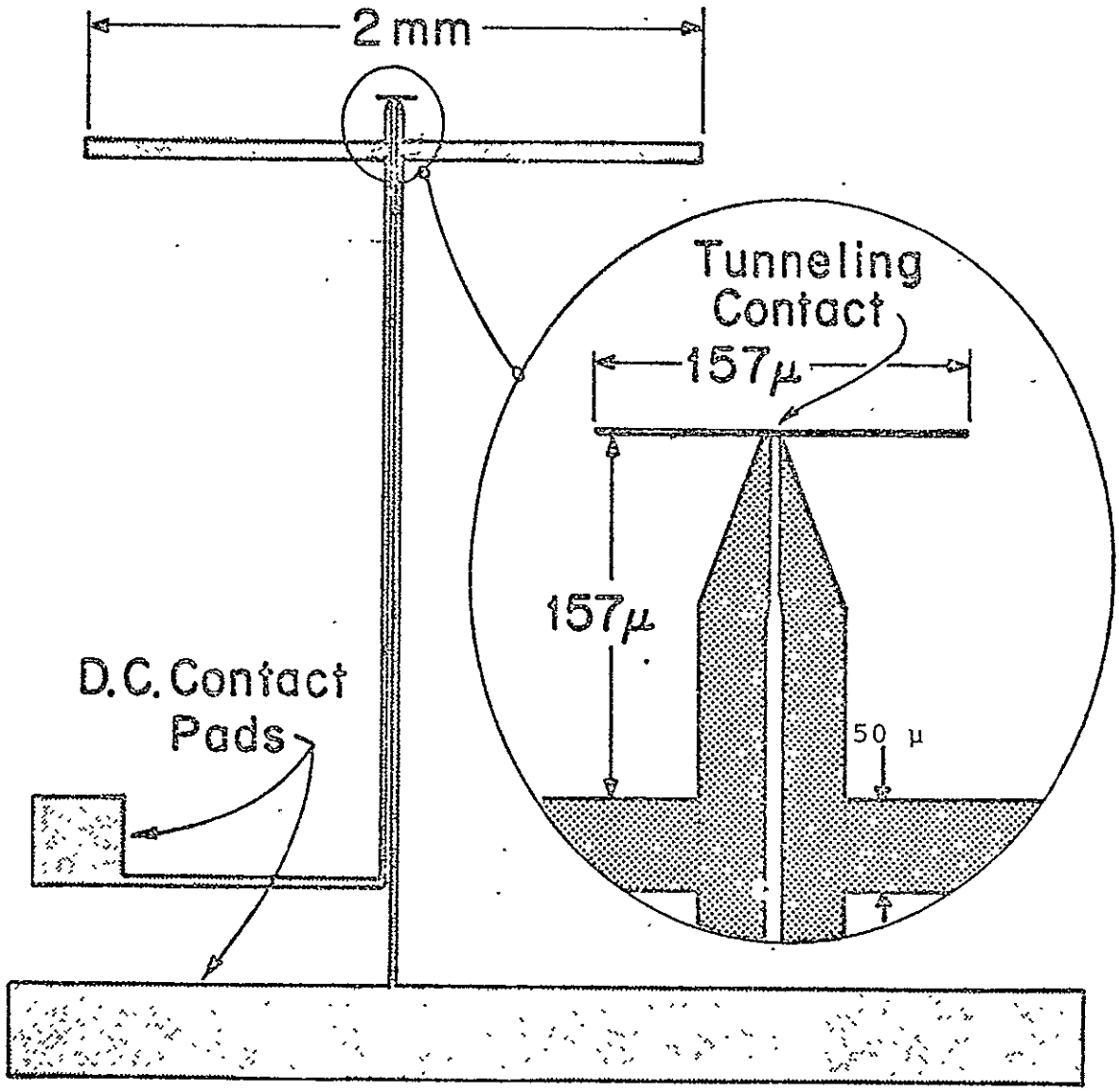

Figure 15

In long thin antennas, the ohmic resistivity of thin metal films may be important. Here the microwave dipole was made wider than that of Fig. 11 to reduce ohmic losses.

321<

In an attempt to push the demonstrated frequency response higher, a 13th order mixing experiment was attempted. The 12th harmonic of a klystron was mixed directly with the .890 THz laser radiation and a search was made for a zero beat.

The search was successful, demonstrating that alternating currents were flowing in the diode at .890 THz. However, the beat signal was very weak and detectable only with a lock-in amplifier and 30 second integration time.

The disappointingly weak performance of the 13th order mixing is most likely due to one of two possibilities. The diode may simply have a cutoff frequency near or below 1 THz , or the high order nonlinear terms in the diode's current-voltage function may not be as large for the nearly symmetric thin film junction as for the mechanically-contacted junction. The following investigations indicate that the second possibility is, in fact, the case.

8. Rectification with DC Bias

The experimental evidence of high speed mixing indicates that the thin film diode responds to frequencies to at least the order of 1 THz. The detected DC signals may then be reasonably expected to arise from the phenomenon of high speed rectification. A detailed theoretical treatment of high speed rectification, as discussed in Chapter 4, substantially confirms the gross features observed

below.

A study was undertaken to determine whether the rectified response as a function of DC bias has a frequency dependence. The response versus bias was initially measured at 10 GHz and .9 THz. Although the magnitudes of the responses may differ according to the relative microwave and laser powers, the shape of the two curves thus obtained is identical. The curve was also measured at 28 THz(10.6μ) and spot checked at frequencies below 10 GHz down to 10 MHz. Figure 16 shows the normalized curves obtained at 10 GHz, .9 THz, and 28 THz.

In addition to the fast "rectified" response at 28 THz, there was also a large thermal response evident. The antenna coupling efficiency and, perhaps, the diode rectification efficiency at that frequency are quite low. Consequently, a rather high laser power density was required to measure the curve. Approximately one watt was focused to a 100μ diameter spot and produced substantial local heating. Under similar conditions, the tungsten wire of a mechanically contacted diode would be heated to visible incandescence. The sapphire substrate of the thin films, however, acts an an efficient heat sink. No damage was noticed from the laser heating.

The thermal response can be separated from the fast response in one of two ways. The laser radiation may be pulsed or chopped periodically. Presumably, any response

323<

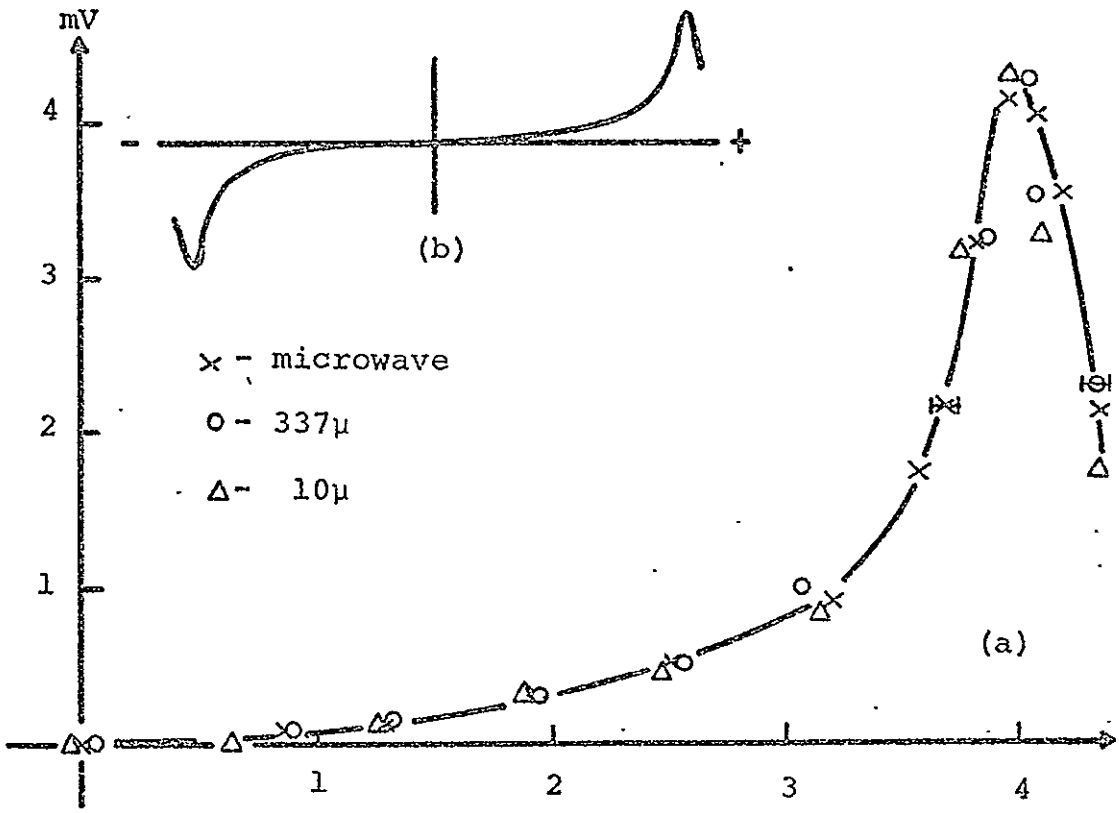

Figure 16

(a) The rectified response as a function of bias current is nearly independent of frequency as shown by measurements at 10 GHz(x-band), .9 THz(337μ) , and 28 THz(10.6μ). THe efficiency of coupling radiation to the MDM diode differs greatly across the frequency range. The incident powers were adjusted to normalize the three curves to the same maximum response. A straight line thermal response in the 28 THz data has also been subtracted. (b) shows, on a reduced scale, that the rectification is antisymmetric with bias reversal. Scatter in the data is not apparent at this scale. Bias currents higher than those shown here can damage the diode.

left immediately after the laser turns off is due to thermal effects. Alternately, the laser radiation may be focused to a spot near the MDM diode but far enough away to simply heat the substrate without exciting alternating currents in the diode.

Both methods for determining the thermal response agree. The thermal response is a linear function of DC bias. When the linear effect is subtracted from the 28 THz data, the agreement with lower frequency data is excellent, as shown in Fig.16.

9. Low Frequency Thermal Effects

The bias curve of Fig.16 remains unchanged from 28 THz to 1 GHz across more than 4 decades of frequency. Below 1 GHz, however, a second thermal effect becomes important.

As in the case of the peacock array at microwave frequencies, the antenna array of Fig.12 is much smaller than the characteristic wavelengths of radio frequencies. The device will not couple efficiently to long wavelength radiation. Instead at radio frequencies, alternating currents must be introduced through the DC contact pads.

A strong DC current flowing through the long thin film transmission line from the contact pads to the tunneling junction might be expected to heat the metal film and raise its resistance. The resistance may not be constant even at

low frequencies due to resistance heating. If the temperature of the thin metal film can change appreciably during the time for one cycle of an alternating current, an additional non-linearity in the current-voltage function will be introduced and a modification of the rectification curve of Fig.16 would be expected.

The time required for a thin metal film to thermally equilibrate with the sapphire substrate may be readily estimated. Consider a short section of the thin film transmission line as shown in Fig.17.

The amount of heat dQ which can flow in time dt through the thickness d across the area A is proportional to the temperature difference ΔT.

$$dQ/dt = -K \cdot A \cdot \Delta T/d \qquad (4)$$

where K is the heat conductivity of the metal.

The change in heat content in the metal is related to the change in temperature, the specific heat σ, the density ρ, and the volume $A \cdot d$.

$$dQ = \sigma \cdot \rho \cdot d \cdot A \cdot \Delta T \qquad (5)$$

Eliminating $A \cdot \Delta T$:

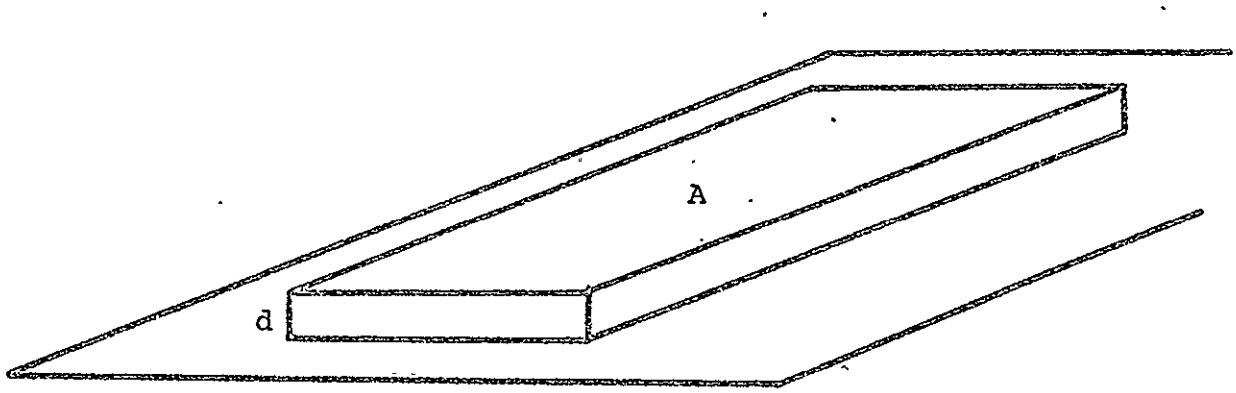

Figure 17

A section of thin film transmission line is in thermal contact with the sapphire substrate. If the metal is suddenly heated by an electric current, a new thermal equilibrium must be established. For a 1000 Å Nickel film, the time to establish equilibrium is of the order of 10^{-9} second.

$$dQ/dt = -K \cdot dQ/\sigma \cdot \rho \cdot d^2$$

$$dQ/Q = -K \cdot dt/\sigma \cdot \rho \cdot d^2$$

$$\ln Q = -K \cdot t/\sigma \cdot \rho \cdot d^2$$

$$Q = C \exp(-t/\tau) + Q_o$$

where $\tau = \sigma \cdot \rho \cdot d^2/K$ (seconds).

For Ni at 18 °C,

$K = .142$ cal sec °C cm

$\sigma = .105$ cal/gm °C

$\rho = 8.7$ gm/cm^3

$d = 1000$ Å $= 10^{-5}$ cm

$$\tau = .6 \times 10^{-9} \text{ sec.}$$

At frequencies below 10^9 Hz, resistance heating can reasonably explain departures from the curve of Fig.16 .

Chapter 4

The Theory of Electron Tunneling

1. Barrier Penetration

The process of electron tunneling through potential barriers has been discussed since the foundation of quantum mechanics. The theory of DC tunneling applied to Metal-Insulator-Metal sandwich structures comprises a very extensive literature[24] which can scarcely be touched in the present discussion.

The development of such a proliferating literature is due to the richness of the quantum theory in its applicability to a host of solid state processes and also due to extreme experimental difficulties in isolating competing effects at a scale of atomic dimensions. Currently, no model has been proposed which can predict both the magnitude and shape of the current-voltage (I-V) tunneling characteristics without resort to adjustable parameters which are experimentally determined from the I-V curves, themselves.[25] The fundamental ideas of electron tunneling, however, are able to qualitatively explain the gross features of DC tunneling and, as will be shown below, of high frequency AC tunneling as well. The intent of this chapter is to explain, at least qualitatively, the data of Fig.16 .

The problem of interest is to calculate a tunneling

current as a function of applied voltage. Of particular concern here are the nonlinearities of the process which are postulated to be responsible for the high speed performance of the MDM diode. It will be seen that high speed mixing and rectification are particularly sensitive probes of the individual nonlinear coefficients as expressed by Eq.(2) of Chapter 1.

2. Interpretation of the Experiment

Figure 18 illustrates the experimental simplicity of measuring bias dependent rectification. If R_s is chosen large compared to R_d, then even large percentage changes in R_d will produce only slight changes in I. $R_s >> R_d$ is the criterion for a constant current source. Typical values are R_d = 10 Ω, R_s = 10 kΩ, V = 20 volts, and I = 2 mA.

In the presence of a DC bias, some MDM diodes produce a positive response to laser or microwave radiation while other diodes produce a negative response. The response polarity depends upon the algebraic sign of the second derivative of the I-V curve. Electron tunneling can be shown to account for either sign by a suitable adjustment of the physical parameters of the potential barrier. Additionally, the detailed shape of the rectification curve with bias, Fig. 16. can yield further qualitative insights on the tunneling

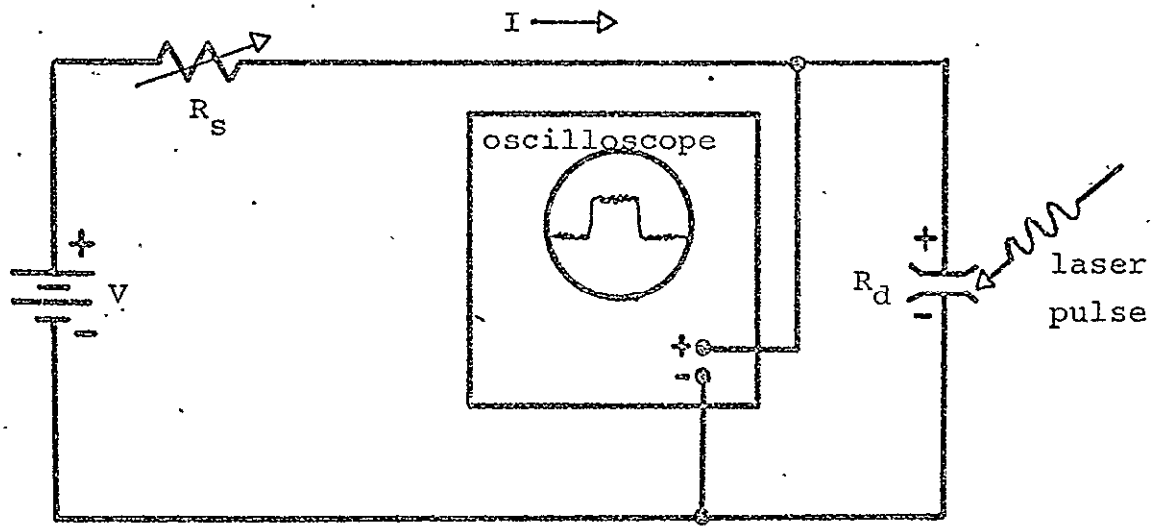

Figure 18

Bias dependent rectification in a thin film diode may be observed by the simple apparatus illustrated here. R_d represents the resistance due to tunneling electrons in the MDM diode. The adjustable series resistance R_s and the voltage source V_s establish a bias current I which is defined positive in the direction shown. For positive bias current, the laser signal is positive in some diodes and negative in others.

331

mechanisms, such as avalanche and saturation effects.

Figure 19 illustrates qualitatively the effect of a nonlinear I-V curve on a sinusoidal modulating voltage. For a positive second derivative, an upward curvature, the current through the diode will exhibit an average increase when a symmetric voltage modulation is applied. An increase of current is the condition for a positive second derivative.

Figure 20 illustrates, in a highly simplified model, that a negative second derivative I-V curve, $\partial^2 I/\partial V^2 < 0$, will produce a positive laser signal. A quantitative treatment of biased rectification can be attempted by considering the more elaborate equivalent circuit of Fig.21.

An MDM diode I-V curve may be constructed from a piecewise linear approximation of ideal diodes in a resistor network. For simplicity, Fig.21 shows a network of only two resistors and one ideal diode; but it will be assumed that the network labeled "MDM diode" instantaneously obeys the power series expansion of Chapter 1:

$$I = a_1 V + a_2 V^2 + \ldots + a_n V^n \qquad (2)$$

The thin film lead resistance, R_l, was found in Chapter 3 to be a function of the temperature and, therefore, of the average current $\bar{I}$. The current dependence of R_l

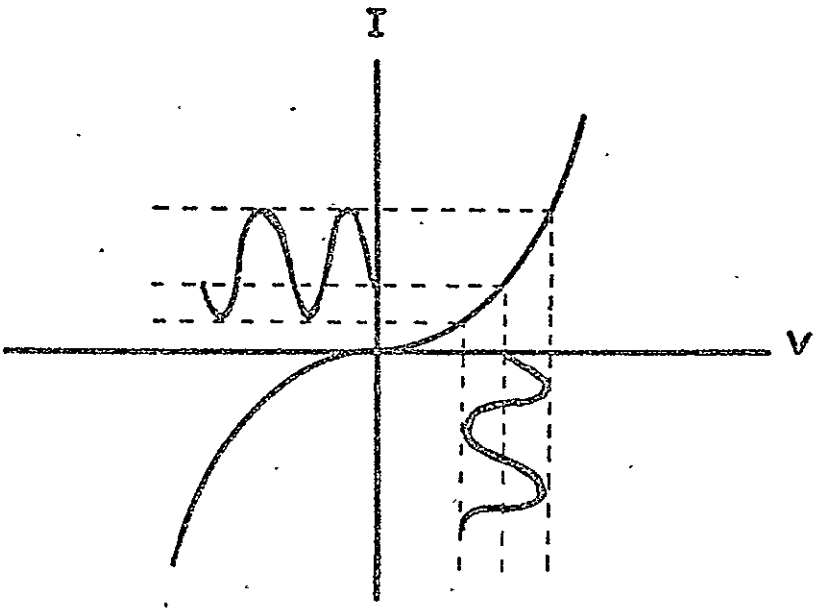

Figure 19

Rectification is primarily determined by the second derivative of I with respect to V. Here $\partial^2 I/\partial V^2 > 0$ for $I > 0$; the right half of the curve has a positive curvature upwards. For a symmetric (sinusoidal) voltage modulation about an equilibrium voltage, the average current increases over the case of no modulation.

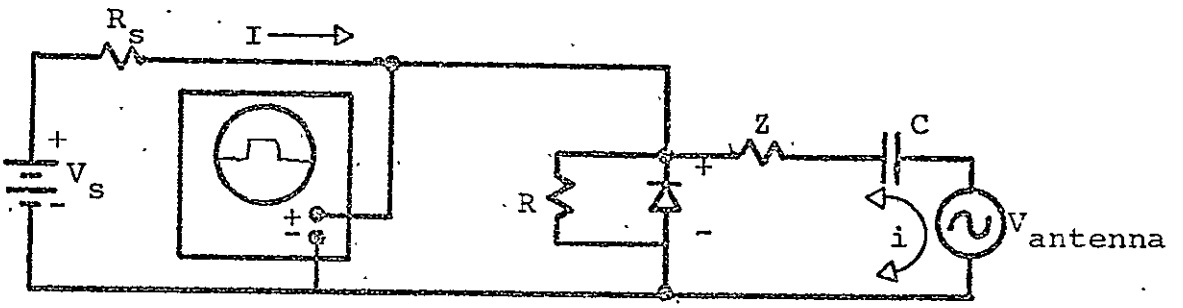

Figure 20

The voltage polarity of the experiment of Fig. 18 may be understood by replacing the MDM diode by an ideal diode and shunt resistor R. Alternating voltages induced in the antenna are represented by an AC voltage source $V_{antenna}$ coupled through a capacitor C and the series antenna impedance Z. For half of the AC cycle the diode is forward biased and shows comparatively little voltage drop. The forward bias current is limited by Z. For the other half cycle, the diode is back biased with the voltage polarity shown. The oscilloscope measures the average voltage across the diode, in this case a positive signal.

For the diode orientation shown above, the I-V curve measured from the oscilloscope will show a strongly negative second derivative. Thus, a negative second derivative produces a positive laser signal and, conversely, a positive second derivative produces a negative signal.

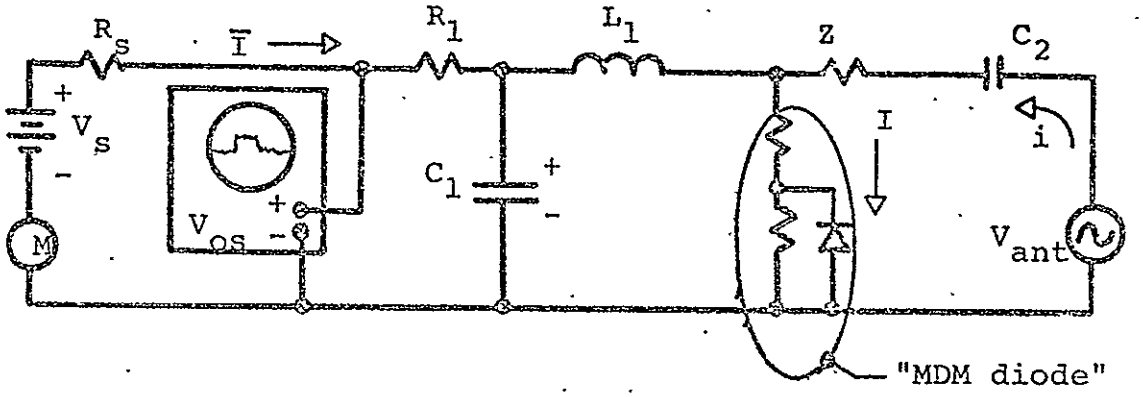

Figure 21

An equivalent circuit for the experiment of Fig. 18 approximates the MDM diode in a piecewise linear fashion by a network of resistors and ideal diodss. Inductance L_1 and capacitance C_1 are due to the thin film connecting leads which form a transmission line low pass filter. Alternating currents in the antenna are thus effectively decoupled from the DC bias source. R_1, the thin film lead resistance, depends upon the magnitude of $\bar{I}$. The oscilloscope measures DC voltages only and is assumed to have negligible effect on the circuit. $\bar{I}$, the average current, is measured by meter M.

prevents a direct determination of the I-V curve of the MDM diode from a source of external DC bias. However, the antenna currents are decoupled from R_1 by the low pass filter L_1 and C_1. High frequency antenna currents can serve as a direct probe of the diode I-V curve.

The voltage measured by the oscilloscope is given simply by:

$$V_o = V_s - R_s\bar{I} \qquad (6).$$

The problem of interest is to relate quantitatively the magnitude of the observed biased rectification signals to the coefficients of the power series expansion, Eq(2). Turning on the antenna voltage must be related to a change in $\bar{I}$. To estimate the rectified voltage developed across the MDM junction, consider first the case of zero bias rectification. Figure 22 defines the voltages and current directions.

3. Zero Bias Rectification

From Kirchhoff's voltage law,

$$V + V_z + V_c = V_a\cos\omega t \qquad (7)$$

$$V_z = iZ \qquad \text{Ohm's law} \qquad (8)$$

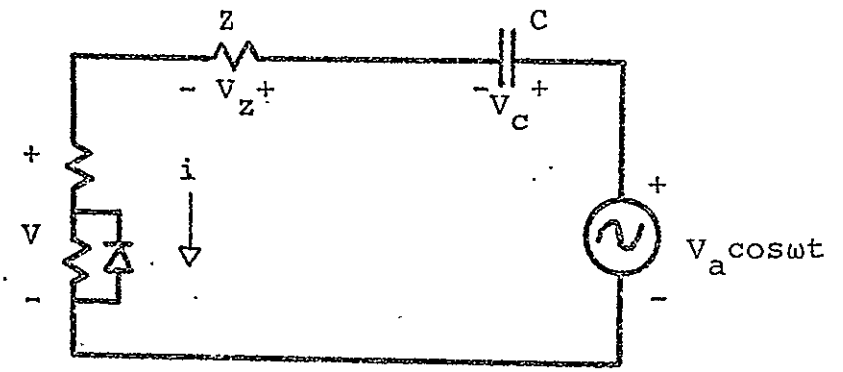

Figure 22

For zero bias rectification, the voltages and current direction are defined above.

$$i = C\,\partial V_c/\partial t \qquad \text{capacitor law} \qquad (9)$$

$$i = a_1 V + a_2 V^2 + \ldots \qquad \text{diode law} \qquad (10).$$

Solve (10) for V ignoring terms above a_2:

$$V = \frac{-a_1 \pm (a_1^2 + 4\,a_2 i)^{1/2}}{2\,a_2}$$

Expand the $(\ldots)^{1/2}$ for $a_2 i < a_1^2$

$$V = \frac{-a_1}{2\,a_2} \pm \frac{a_1}{2\,a_2}\left[1 + 4\frac{a_2 i}{2\,a_1^2} + \frac{(1/2)(-1/2)16}{2\,a_1^4}\,a_2^2 i^2 + \ldots\right]$$

$$V = -a_1/2a_2 \pm \frac{a_1}{2\,a_2}\left(1 + 2\,a_2 i/a_1^2 - 2\,a_2^2 i^2/a_1^4\right) \qquad (11)$$

For I = 0, V = 0. Therefore the (+) sign is correct.

$$V = i/a_1 - a_2 i^2/a_1^3 \qquad (12)$$

Assuming a large capacitor C such that

$$ZC >> 1/\omega$$

there will be no AC voltage drop across the capacitor.

Equation (12) may be solved approximately by using an iteration method. Solve first for i_o with the non-linearity $a_2 = 0$.

For $a_2 = 0$, a completely linear system, we may write by inspection

$$i_0 = V/R$$

$$= V_a \cos\omega t \; / \; (1/a_1 + Z) \qquad (13)$$

Equation (13) may now be substituted into Eq(12) to obtain the instantaneous diode voltage to lowest order in the nonlinearity.

$$V = V_a \cos\omega t/(1 + a_1 Z)$$

$$- \frac{a_2}{a_1^3} \frac{V_a^2 \cos^2 \omega t}{(1/a_1 + Z)^2} \qquad (15)$$

The time average diode voltage:

$$\bar{V} = - \frac{1}{2} \frac{a_2}{a_1^3} \frac{V_a^2}{(1/a_1 + Z)^2} \qquad (16)$$

which is the rectified voltage. Note that for a positive second derivative I-V curve, $a_2 > 0$, the rectified voltage is negative.

4. Biased Rectification

Consider now the complete equivalent circuit of Fig. 21. For rectification in the presence of a DC bias current, the diode law may still be written as a function of the total instantaneous diode voltage. $I = I(V)$. The antenna voltage represents a small deviation from the bias point and the change in I may be written as a Taylor series expansion about I_o .

$$I = I(V_0) + \frac{\partial I(V_0)}{\partial V}(V-V_0) + \frac{1}{2}\frac{\partial^2 I(V_0)}{\partial V^2}(V-V_0)^2 + \cdots \quad (17)$$

$$I - I_0 = \frac{\partial I(V_0)}{\partial V}(V-V_0) + \frac{1}{2}\frac{\partial^2 I(V_0)}{\partial V^2}(V-V_0)^2 + \cdots$$

Define: $$a_1(V_0) \equiv \frac{\partial I(V_0)}{\partial V}$$

$$a_2(V_0) \equiv \frac{1}{2}\frac{\partial^2 I(V_0)}{\partial V^2}$$

then,

$$I - I_0 = a_1(V_0)\cdot(V-V_0) + a_2(V_0)\cdot(V-V_0)^2 + \cdots$$

Change variables

let $$I' = I - I_0$$

$$V' = V - V_0$$

then,

$$I' = a_1(V_0)\,V' + a_2(V_0)\,V'^2 + \cdots \quad (19)$$

which is of the same form as (10).

The low pass filter L_1 and C_1 effectively isolates the high frequency currents from the DC supply. The antenna coupling capacitance C_2 similarly isolates the DC bias current from the antenna circuit. The instantaneous diode voltage may then be written as an algebraic sum of the DC bias voltage

and the voltages of the antenna circuit.

$$V = -V_z - V_c + V_a \cos\omega t + V_0 \qquad (20)$$

where V_0 is the voltage due to the bias current, I_0.

Rewriting (20):

$$V - V_0 = -V_z - V_c + V_a \cos\omega t$$

$$V' + V_z + V_c = V_a \cos\omega t \qquad (21)$$

which is identical in form to (17).

The calculation then proceeds identically to the zero bias case and the answer may be written directly. The instantaneous diode voltage:

$$V' = V_a \cos\omega t \left[\frac{1}{1 + a_1 z} \right] - \frac{a_2}{a_1^3} \frac{V_a^2 \cos^2\omega t}{\left(\frac{1}{a_1} + z\right)}$$

and the time average voltage

$$\overline{V'} = -\frac{1}{2} \frac{a_2(V_0)}{a_1(V_0)^3} \frac{V_a^2}{\left(\frac{1}{a_1(V_0)} + z\right)^2} = \overline{V} - V_0 \qquad (22)$$

where now the coefficients, a_n, are functions of the bias voltage and are given in terms of derivatives of the I-V curve by Eqs. (18).

The oscilloscope voltage, V_{os} of Fig. 21, differs from $\overline{V}$ by a factor depending on the source and lead resistances, R_s and R_1.

$V_{os} = V_s - R_s\bar{I}$ from Ohm's law.

$$\bar{I} = \frac{V_s - \bar{V}}{R_s + R_1}$$

Substituting $\bar{V}$ from Eq.(22),

$$\bar{I} = \frac{V_s - V_0 + \frac{1}{2}\frac{a_2(V_0)}{a_1(V_0)^3}\frac{V_a^2}{(\frac{1}{a_1}+Z)^2}}{R_s + R_1}$$

$$\bar{I} = I_0 + \frac{1}{(R_s+R_1)} \cdot \frac{1}{2} \cdot \frac{a_2 V_a^2}{a_1^3(\frac{1}{a_1}+Z)^2}$$

and

$$V_{os} = V_s - R_s I_1 \frac{-R_s}{(R_s+R_1)} \cdot \frac{1}{2} \cdot \frac{a_2 V_a^2}{a_1^3(\frac{1}{a_1}+Z)^2} \qquad (23).$$

For a positive second derivative , $a_2 > 0$, the rectified response observed at the oscilloscope will be negative going with incident laser power at the antenna.

The intent of the tunneling calculations in the following sections is to relate the coefficients of the I-V power series expansion, Eqs.(18), to physical properties of the MDM diode. A comparison will then be made between the oscilloscope voltages calculated in Eq(23) above and the voltages measured by the data of Fig.16 .

343<

5. The Rectangular Barrier of Constant Height

The simplest case of electron tunneling which exhibits most of the large quantum effects is the case of tunneling through a rectangular barrier. The problem is treated in many quantum mechanics texts,[26,27] but a brief review will illustrate some general limitations.

The calculation raises two fundamental problems: (a) a determination of the barrier penetration probability for a single electron, and (b) a model for the distribution of electron energies. It will be seen that both problems have a strong influence on the nature of the I-V curve and particularly on its second derivative.

The second derivative of the I-V curve is of particular interest. It is the term responsible for video detection and it is the term which was measured by the data of Fig.16. Higher derivatives may, of course, be measured by higher order mixing experiments. Each higher order term becomes more sensitive to changes in the tunneling mechanism.

To calculate the barrier penetration probability, consider the one dimensional barrier of Fig.23. The asymmetry of the potential step, eV, is caused by an external bias voltage V. For the present case, the top of the barrier is assumed to remain flat and at constant height. This assumption is clearly nonphysical, but it will lead to an interesting physical insight. The zero of energy is taken arbitrarily at the bottom of the Fermi sea of the left metal.

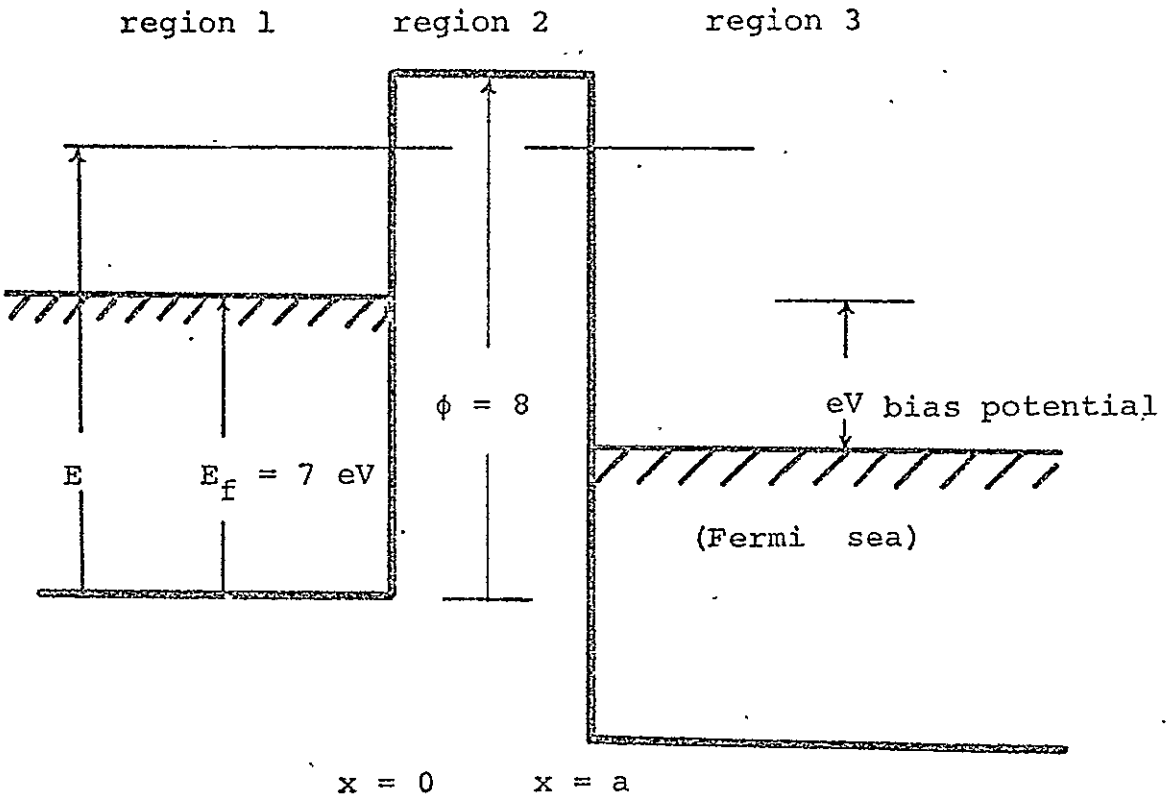

Figure 23

The one dimensional rectangular barrier.

The transmission coefficient, T, for an electron of energy E incident upon the barrier is obtained from a straightforward calculation analagous to the treatment of Eisberg.[26]

From Schrödinger's equation, electron wave functions may be calculated for the three regions of Fig.23. The transmission coefficient T is given by the square of the ratio of the transmitted and incident wave function amplitudes weighted by the transmitted and incident particle velocities.

$$T = \frac{|\psi_3|^2}{|\psi_1|^2} \cdot \frac{v_3}{v_1}$$

The detailed calculations are given in Appendix I.1 and only the results will be presented here.

$$T = \frac{4}{2 + \frac{k_3}{k_1} + \frac{k_1}{k_3} + \left[\frac{k_3}{k_1} + \frac{k_1}{k_3} + \frac{k_2^2}{k_1 k_3} \cdot \frac{k_1 k_3}{k_2^2}\right] \sinh^2 k_2 a} \qquad (24)$$

where $k_1 = \frac{(2mE)^{1/2}}{\hbar}$, $k_2 = \frac{[2m(\phi - E)]^{1/2}}{\hbar}$, $k_3 = \frac{[2m(E + eV)]^{1/2}}{\hbar}$

Note that T is invariant upon interchange of k_1 and k_3. The transmission coefficient for an electron of total energy E is the same when approaching from the right as from the left.

Considering the electrons as a degenerate Fermi gas, their distribution in the Fermi sea as a function of incident energy $E = p_x^2/2m$ is given in the left metal by:

$$F_+(E) = \ln\left[1 + e^{-(E-E_f)/k\theta}\right]$$

(from I.9)

and in the right metal by:

$$F_-(E) = \ln\left[1 + e^{-(E+eV-E_f)/k\theta}\right]$$

where an integration over all y and z components of momenta has been performed in Appendix I.2.

The total tunneling current density is given by the properly normalized integral over energy:

$$J = \frac{4\pi m k\theta e}{h^3}\int_0^\infty dE\,(F_+ T - F_- T) \qquad (25)$$

(from I.10)

$$J = \frac{4\pi m k\theta e}{h^3}\int_0^\infty dE\,\ln\left[\frac{1+e^{-(E-E_f)/k\theta}}{1+e^{-(E+eV-E_f)/k\theta}}\right] T \qquad (26)$$

The constant coefficient of Eq(26) is readily evaluated:

For $m = 9.109 \times 10^{-28}$ gm

$k\theta = 1/40$ electron volt

$e = 1.6023 \times 10^{-19}$ Coulomb

$h = 6.626 \times 10^{-27}$ erg-sec

$$4\pi m k\theta e/h^3 = 4.047 \text{ amp}/\mu^2\text{-ev}$$

Let the supply function F be defined:

$$F = \ln\left[\frac{1+e^{-(E-E_f)/k\theta}}{1+e^{-(E+eV-E_f)/k\theta}}\right] \qquad (27)$$

then

$$J = 4.047 \int_0^\infty dE \; F \cdot T \qquad (\text{amp}/\mu^2) \qquad (28)$$

In general, the integral of Eq(28) cannot be solved in closed form, depending of course on the exact form of T. From Fig.24, graphs of the functions F, T, and F·T are seen to be smoothly varying and lend themselves well to numerical integration. Note that both F and T depend upon the bias voltage V. Integration is with respect to the electron energy E.

The integrals, which are here numerically evaluated, were computed with the use of Simpson's Rule as described

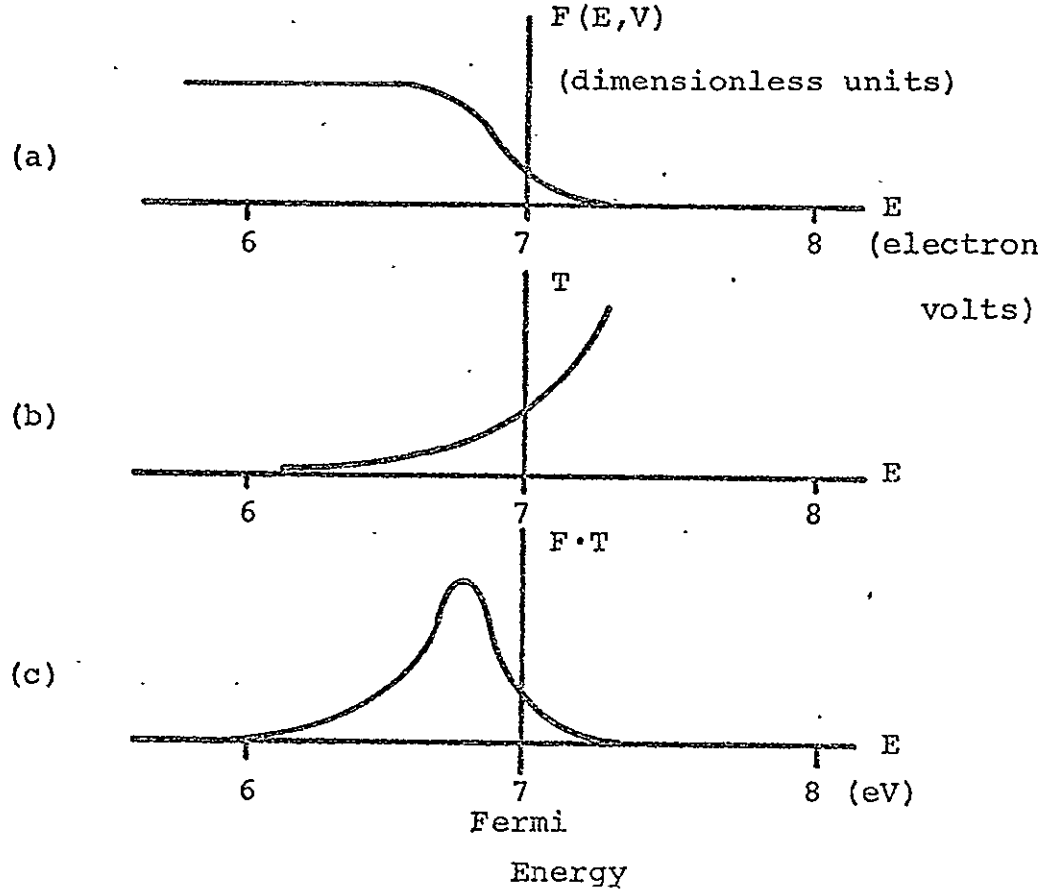

Figure 24

The electron supply function, F, shown in (a) goes rapidly to zero above the Fermi energy. The transmission coefficient, T, drops approximately exponentially at low energies. Their product (c) is a smoothly varying function which contributes significantly to the integrand of Eq(25) over an energy range of less than 2 eV around the Fermi energy for this rectangular barrier. Here $k\theta$ = 1/40 eV, the bias V = .2 volt, and the barrier thickness is 15 Å.

in Appendix I.3. While computing an integral, it is convenient (when using a computer) to plot the integrand values as they are evaluated in addition to plotting the area under the integrand, which is the integral itself.

Figure 25 shows the numerical evaluation of Eq.(26) the tunneling current as a function of bias voltage. Also shown are the integrand curves as they appear for several values of the bias voltage. The computer program is found in Appendix I.4. The range of integration was taken from 5 to 7.4 electron volts as the integrand did not contribute appreciably beyond those limits in this instance. Note that the J-V curve has a downward curvature or negative second derivative. The first and second derivative curves as evaluated by numerical integration are similarly graphed in Fig.26.

In the present case, an increasing bias voltage results in a less than linearly increasing current. It can be seen from the integrand curves at the lower right of Fig.25 that the increase in current is contributed predominately by electrons which lie ever deeper in the Fermi sea. It can also be clearly seen that the range of integration was sufficient to include all appreciable contributions from the integrand.

Of further interest is the relative magnitude of the electron current tunneling to the left "up hill" against the bias voltage. Equation (25) can be readily separated

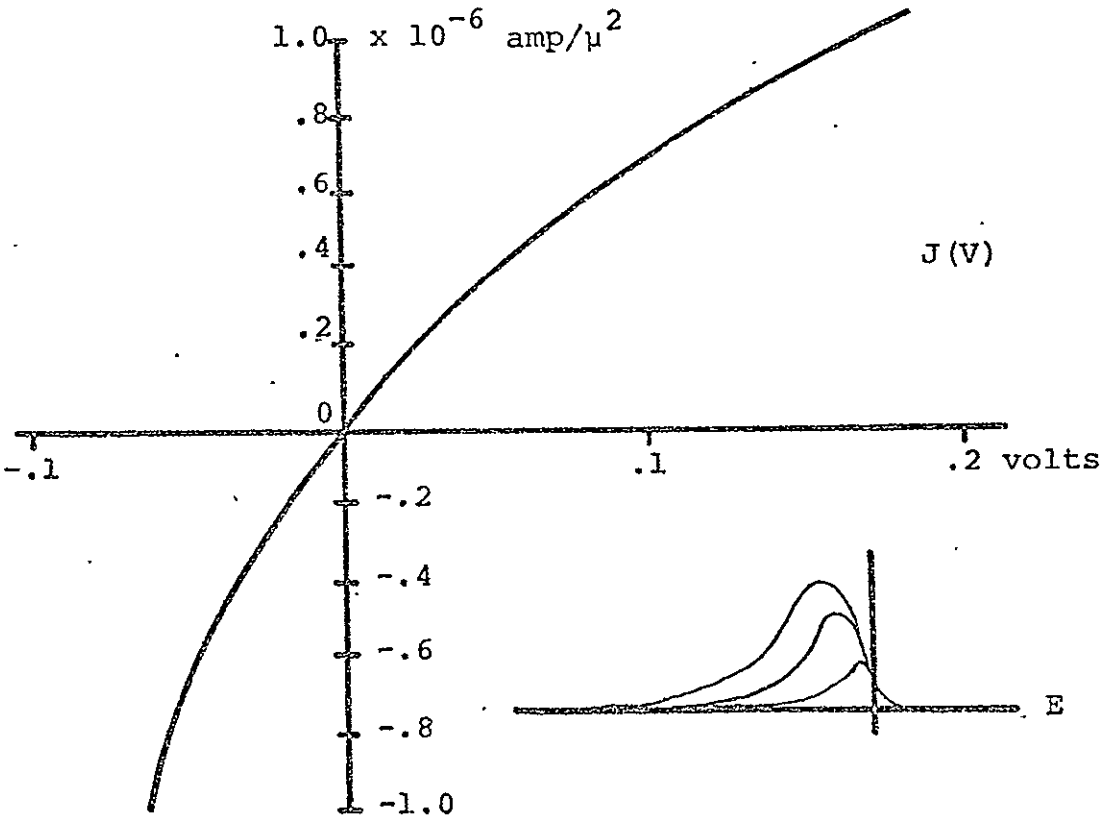

Figure 25

The tunneling current versus bias voltage for the asymmetric rectangular barrier of constant height, Fig. 23 shows a downward curvature, a negative second derivative. The series of curves at the lower right represents the integrands of the current integral for different bias voltages. The integrand curves indicate that, at higher bias voltages, the increase in current is contributed mainly be electrons lying deeper in the Fermi sea.

351<

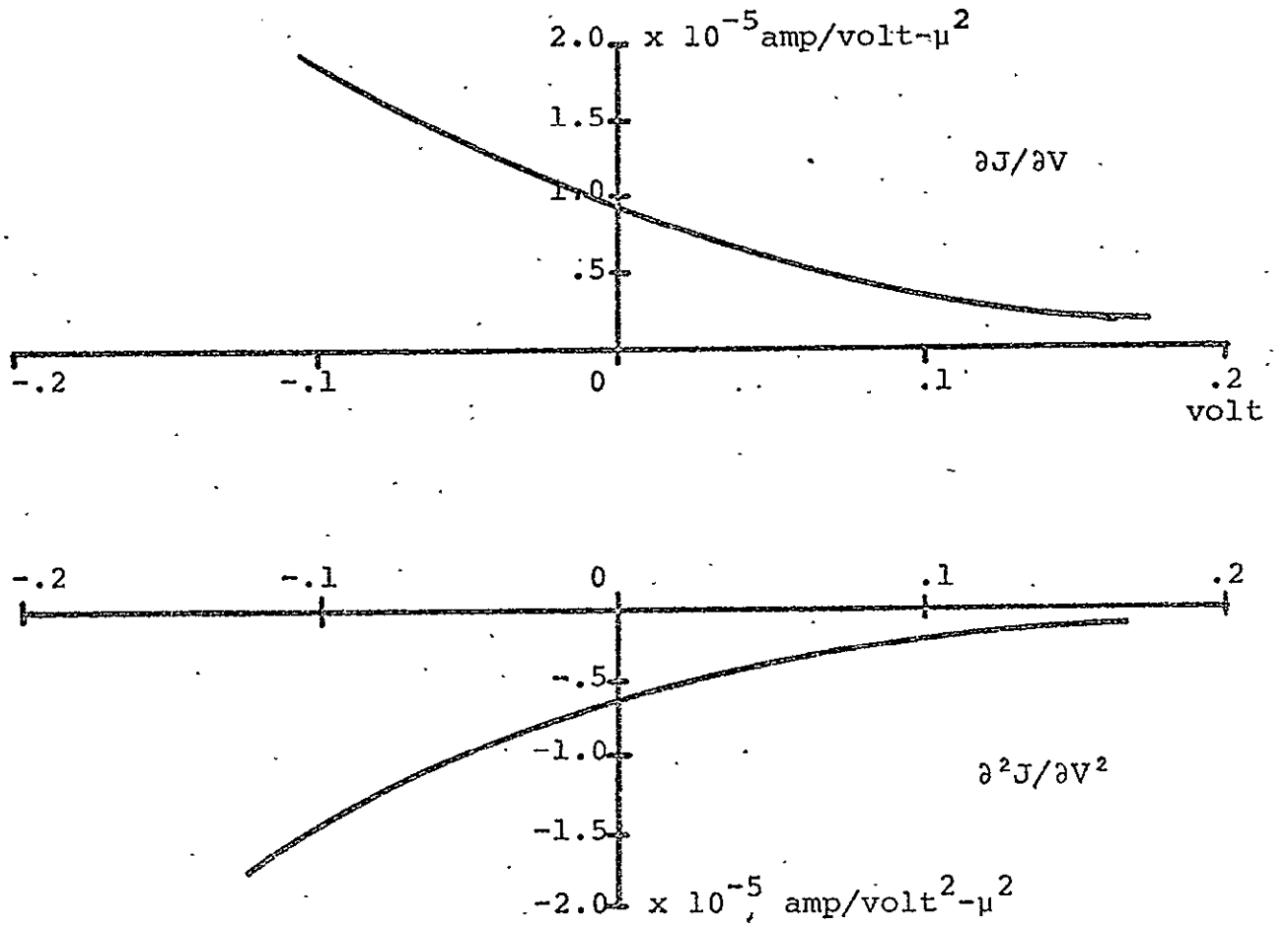

Figure 26

The first and second derivatives of J with respect to V for the asymmetric rectangular barrier of constant height are also evaluated numerically. From these curves, it is possible to read off the magnitudes of the coefficients in the power series expansion for J(V), Eqs(18).

into a term for tunneling to the right minus tunneling to the left. Figure 27 shows the separate integrands for right and left tunneling compared to the total. It can be seen that the number of electrons tunneling up hill is nearly 80% of those tunneling with the bias for a potential drop of 50 mV. Clearly a significant number of electrons tunnel in each direction at zero bias. The program for this calculation is in Appendix I.5.

6. Bias Dependent Potential Barriers

A more subtle attempt to calculate the tunneling current involves choosing a more sophisticated model for the barrier transmission probbility than the simple form of Eq.(23). All models involve simplifying assumptions at some point. It is of interest to investigate the limits of applicability of some of the more common models. The objective will be to develope a model which can adequately describe the high speed rectification data of Fig.16. Note that the rectified signal initially increases with positive curvature with increasing bias and then smoothly but rapidly begins to decrease. It will be particularly interesting to calculate the detailed shape of the second derivative curves and compare them to the strong curvatures seen in the experimental data.

The next simplest potential barrier is the trapezoidal

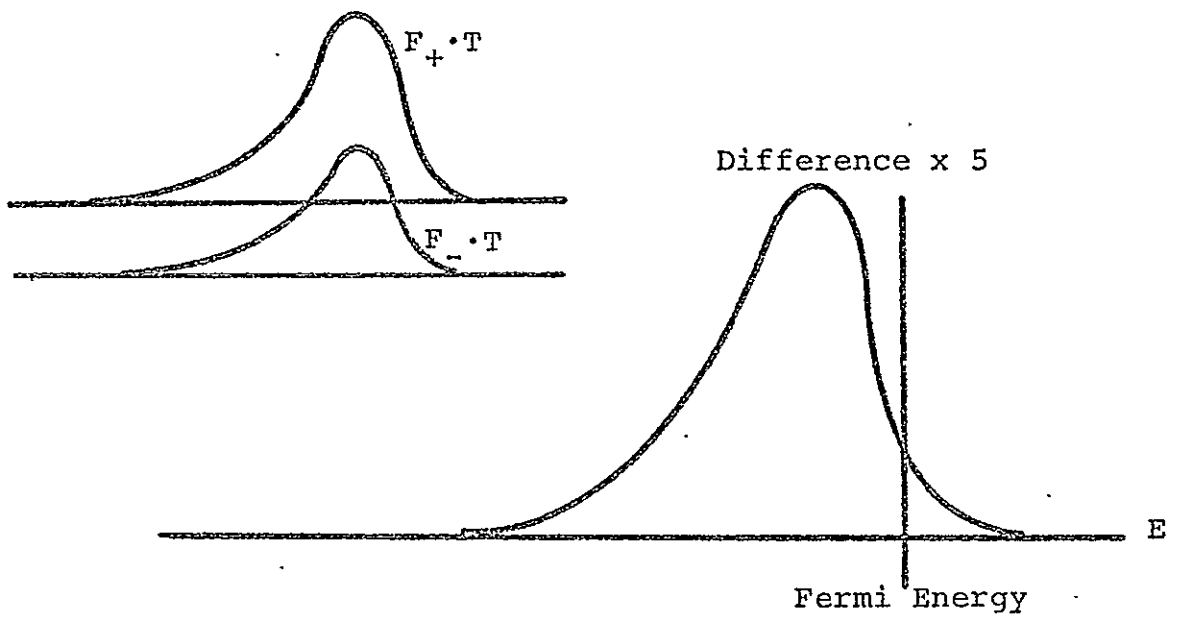

Bias Voltage = 50 mV

Barrier Thickness = 15 Å

Work Function = 1 electron volt

Figure 27

Electrons tunnel through the potential barrier in both directions. Shown here are the integrands of the tunneling current integral Eq(25). The two inset curves at the upper left indicate that electrons tunneling against the bias voltage amount to 80% of those tunneling with the bias. The imbalance is shown at the right where the vertical scale has been magnified 5 times and the horizontal scale twice.

barrier shown in Fig.28. Here the flat top of the rectangular barrier is pulled down by the bias voltage. The effective barrier height is thus reduced, and the tunneling probability is expected to increase more strongly with bias.

The transmission coefficient may be calculated as in the rectangular barrier case of Appendix I.1 by calculating the electron wave functions inside and o utside the barrier and matching boundary conditions. Gundlach has shown[28] that the wave functions in the region between $x = 0$ and $x = a$ have the form of Airy functions of the first and second kind. In matching boundary conditions, only the leading terms in the assymptotic forms of the Airy functions are used. This approximation is roughly equivalent to the case of a thick barrier where reflections of the tunneling electrons upon exiting the barrier are neglected. The model clearly predicts a positive second derivative with bias, but the case for thin barriers, which is of particular interest to thin film diodes, cannot be treated.

Rather than attempting a direct calculation of the exact wave functions for each barrier shape, the WKB method will provide an estimate of the transmission coefficient directly.

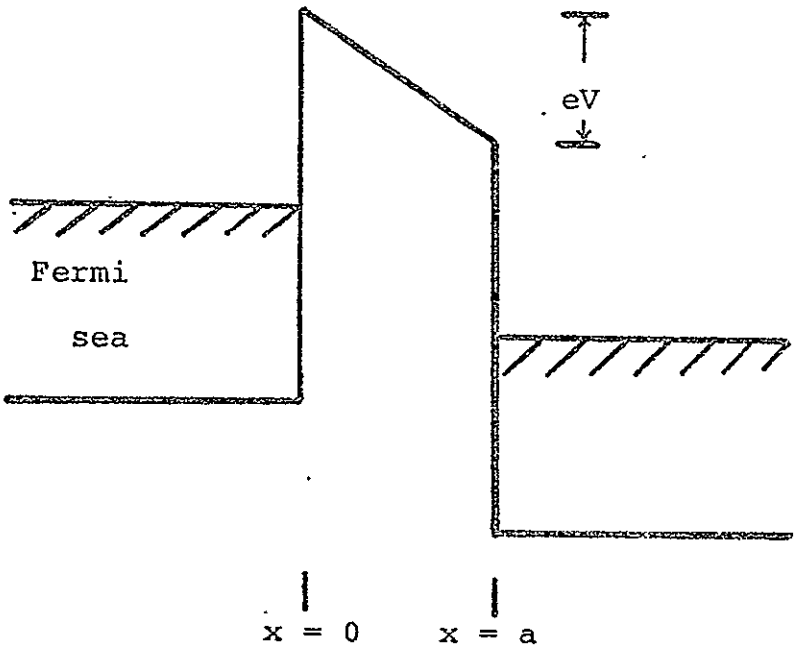

Figure 28

The trapezoidal Barrier.

7. The WKB Approximation

The most widely used approximation in tunneling problems is the WKB method. The method is applicable to potential barriers of arbitrary shape. Barrier penetration calculations using the method are described in most general texts on quantum mechanics.[29] Transmission formulas derived by the WKB method depend solely upon an integral over the potential function. Any details of the spatial structure in the potential barrier are averaged out by the integral, but the effective change in height due to bias is preserved.

Figure 29 shows a smooth, bias dependent, parabolic shaped barrier. The calculation of the tunneling current for this barrier according to the WKB method is given in Appendix I. 6.

A parametric study was made of the J-V curves given by the WKB method. Curves for both the parabolic barrier and the trapezoidal barrier, as described in Appendix I. 7, were computed for barrier thicknesses ranging from 20 Å down to 3 Å. Over the range of bias voltages employed in the thin film diodes, below 200 mV, all of the J-V curves were qualitatively the same. Figures 30,31, and 32 show a series of curves for different barrier thicknesses. All exhibit an upward curvature (second derivative positive) over the range of interest.

It may be generally concluded that the WKB approximation, when applied to potential barriers of simple shape, gives rise

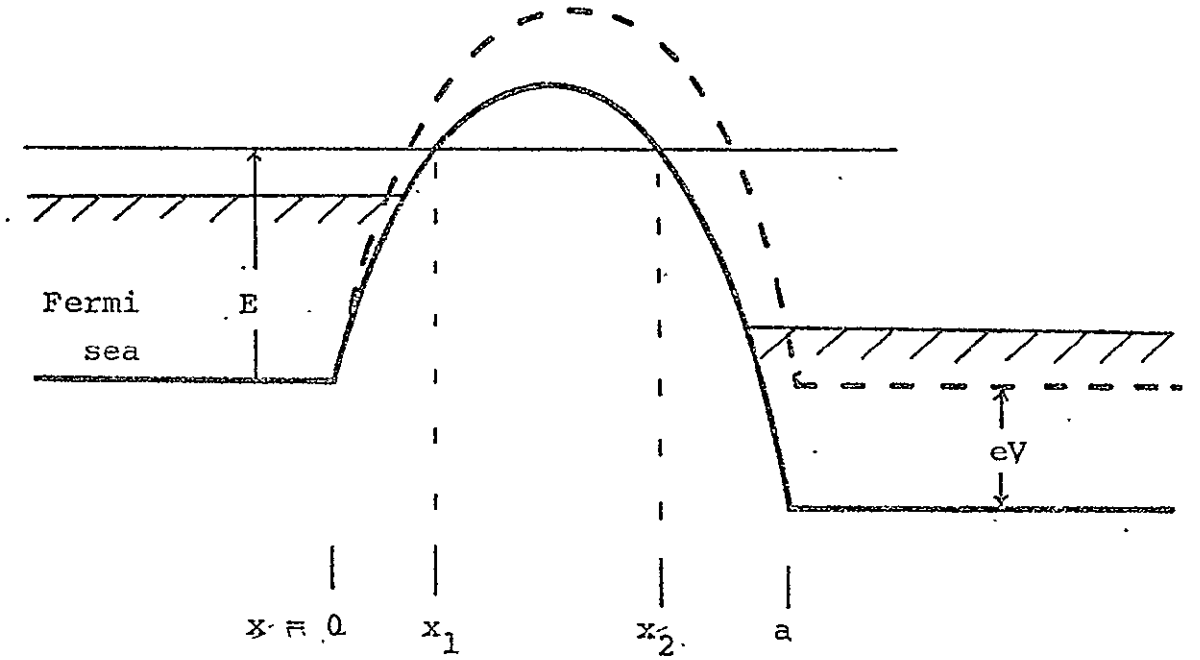

Figure 29

The tunneling current due to a bias-dependent parabolic barrier may be computed by means of the WKB approximation. The transmission coefficient thus obtained depends on an integral over the potential function. Details of the shape of the potential barrier are averaged out by the integral, but the effective change in height due to bias is preserved.

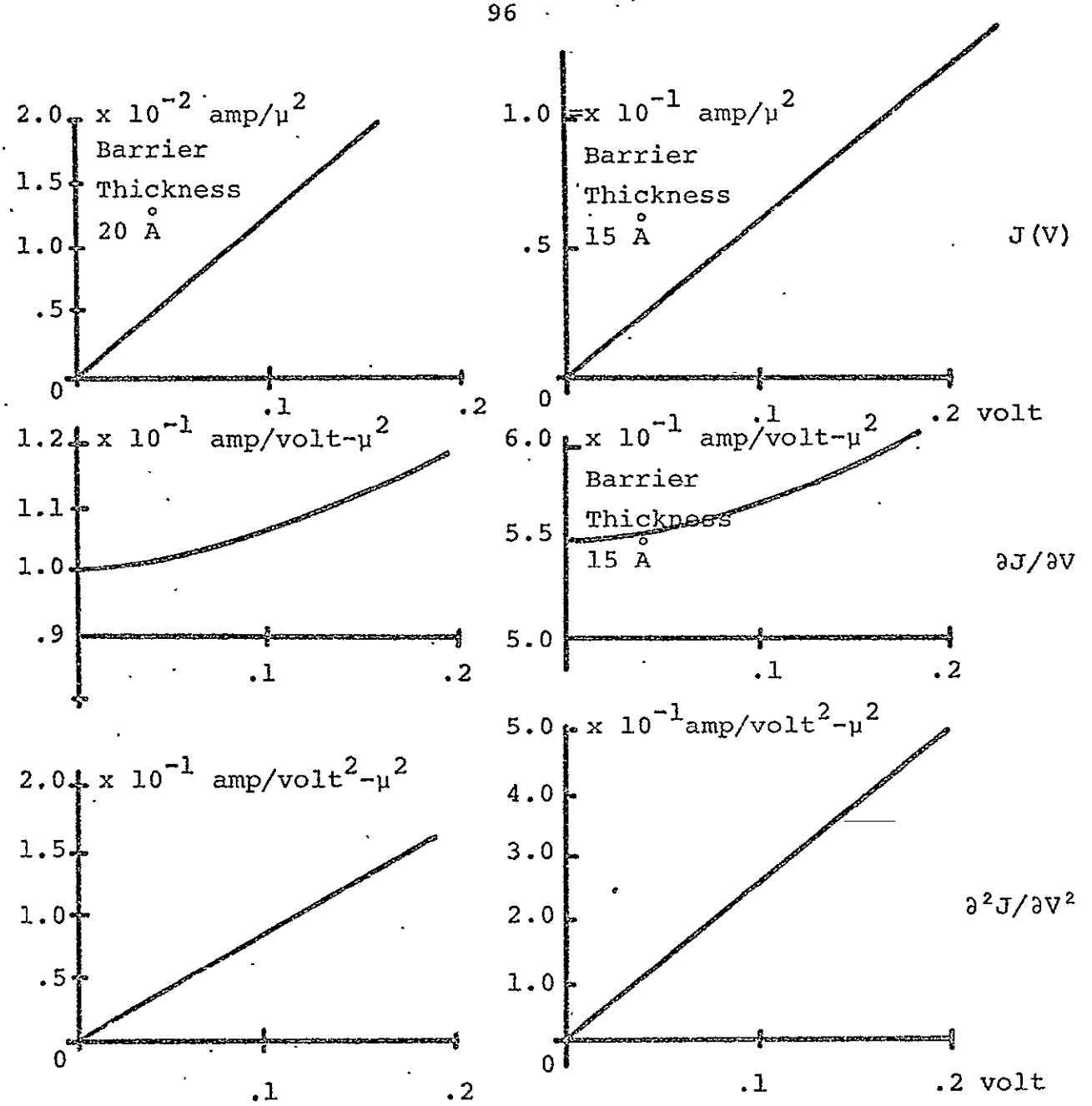

Figure 30

Shown at left and right are the J-V curves and first and second derivatives for parabolic barriers of 20 Å and 15 Å thicknesses computed by means of the WKB approximation. The J-V curves appear to be linear but actually exhibit a slight upward curvature not visible at this scale. The second derivatives likewise have slight upward curvature.

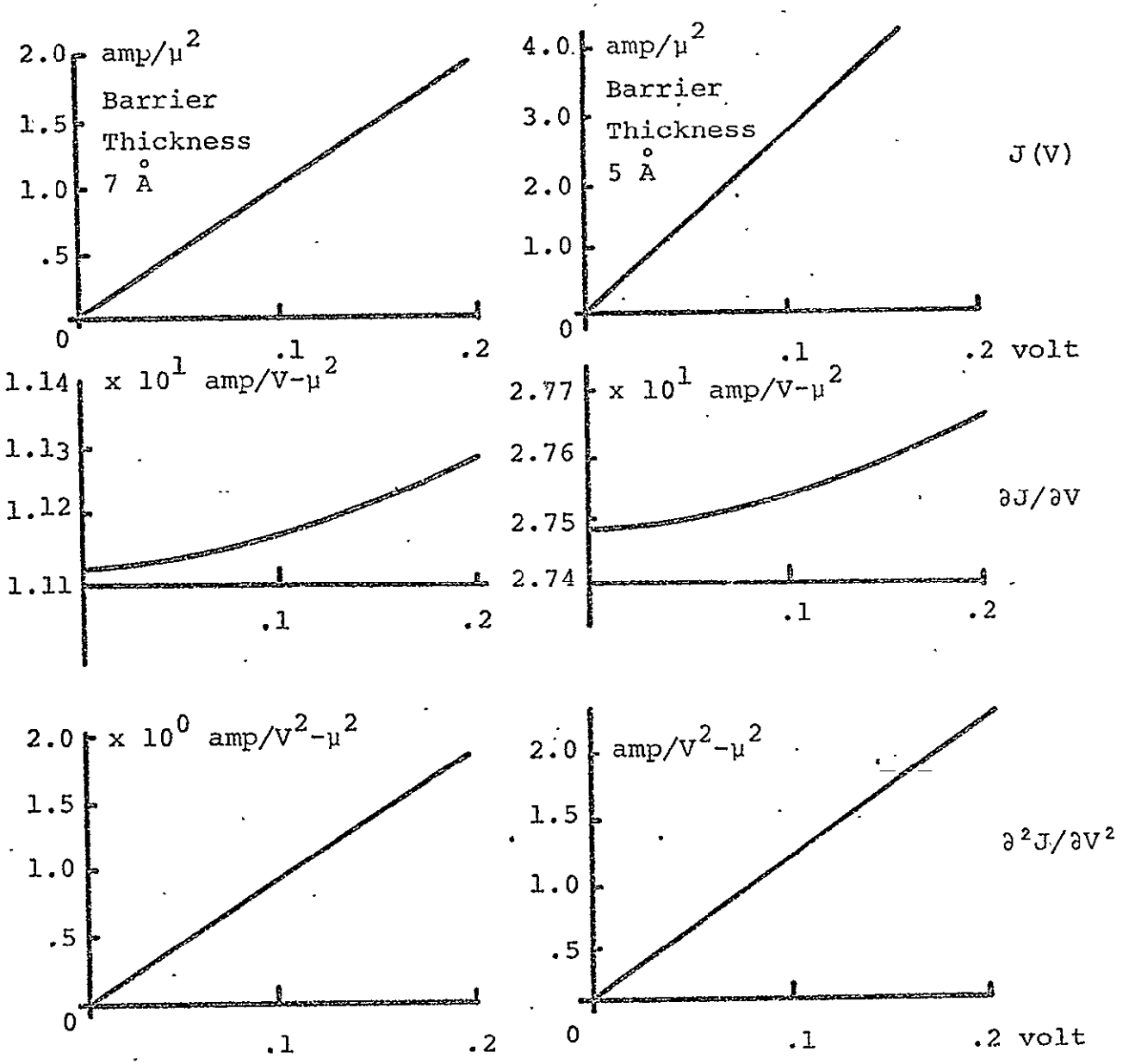

Figure 31

The J-V curves for parabolic barriers of 7 Å and 5 Å thicknesses are shown. Here the second derivative curves again appear linear but actually have slight downward curvature not visible at this scale.

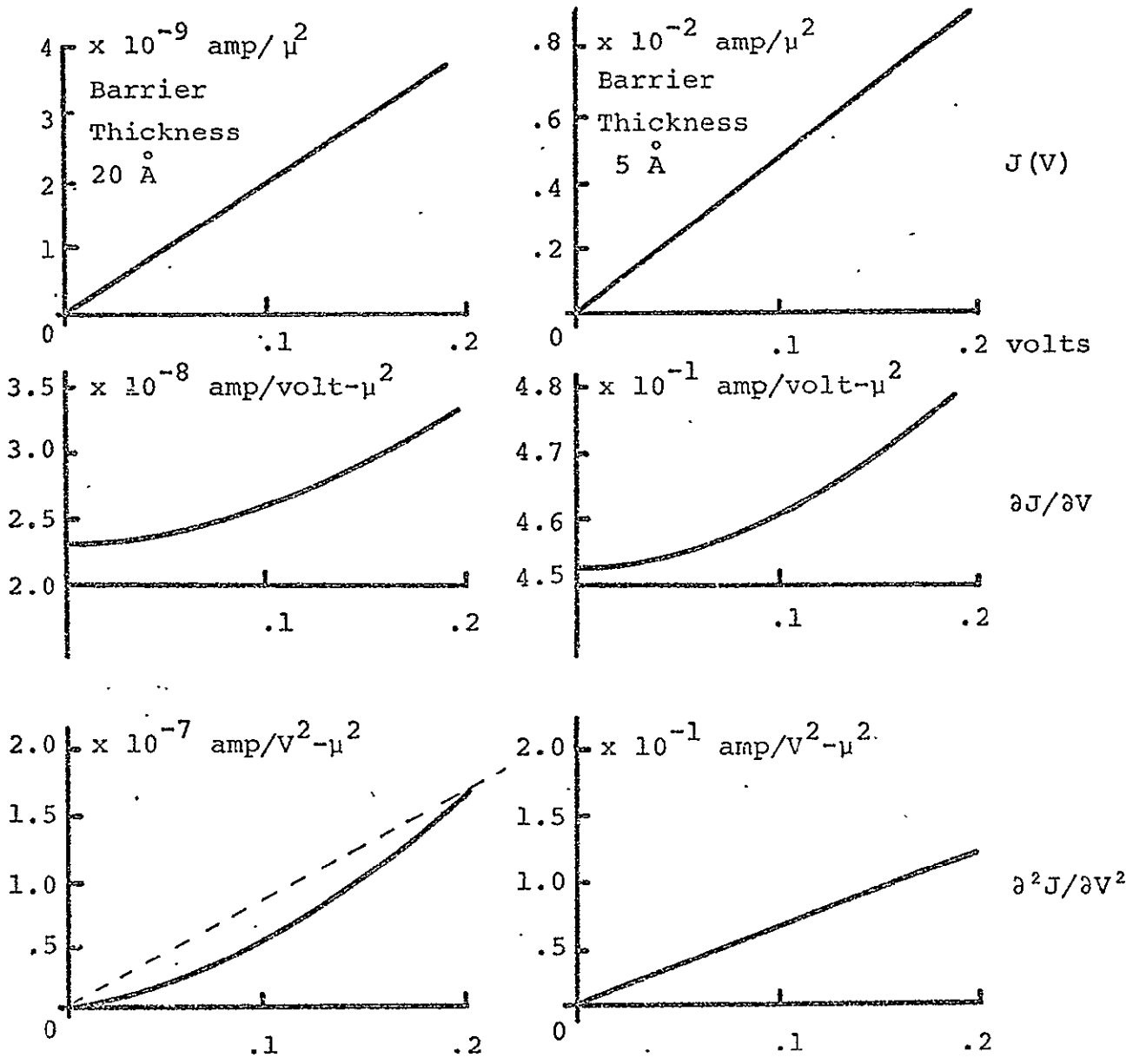

Figure 32

The J-V curves for trapezoidal barriers of 20 Å and 5 Å thickness are shown. Note that the second derivative curve for the 20 Å barrier shows a pronounced upward curvature compared to the broken straight line.

361<

to current-voltage curves of almost linearly increasing positive second derivatives. It must be noted that the WKB approximation applies only to relatively thick barriers. Also, the range of bias voltages investigated here is assumed to remain substantially below the work function of the metals, thus ruling out strongly nonlinear avalanche effects.

It is interesting to observe that the WKB approximation predicts second derivative curves which go smoothly to zero at zero bias voltage, as must be the case for completely symmetric similar metal junctions. By contrast, the calculation for the rectangular barrier of constant height treats the two metals in a most unsymmetric fashion with respect to the height of the potential barrier and gives a nonzero second derivative at zero bias. See Fig.26.

A comprehensive tunneling theory must also predict negative second derivatives for some barrier configurations in order to explain diode rectifications with bias of positive sign. Since the WKB method does not apply to very thin barriers where such effects might be expected to arise, alternative approaches must also be investigated.

8. Electron Tunneling in Thin Barriers

For barriers which have a thickness of the order of the electron wavelength, the tunneling current would not be expected to depend on the exact shape of the barrier. Whether

trapezoidal, parabolic, or a more complicated shape incorporating image force effects, all should reduce to the same J-V curve in the thin limit. In that limit, multiple reflections of the wave function within the barrier will be important.

The Delta Function Barrier

The delta function barrier satisfies the thin barrier criteria and is easily calculated without resort to additional mathematical approximations. Consider the potential diagram of Fig.33. Note that the zero of energy has been chosen to symmetrize the electron supply functions.

The transmission coefficients for electrons tunneling to the right and left, T_r and T_L, are derived in Appendix I.9.

$$T_r = \frac{4(E+eV/2)^{1/2}/(E-eV/2)^{1/2}}{\left[1+\chi\frac{(E+eV/2)^{1/2}}{(E-eV/2)^{1/2}}+\frac{(E+eV/2)}{(E-eV/2)}+\frac{A^2}{(E-eV/2)}\right]} \quad (29)$$

$$T_L = \frac{4(E-eV/2)^{1/2}/(E+eV/2)^{1/2}}{\left[1+\chi\frac{(E-eV/2)^{1/2}}{(E+eV/2)^{1/2}}+\frac{(E-eV/2)}{(E+eV/2)}+\frac{A^2}{(E+eV/2)}\right]} \quad (30)$$

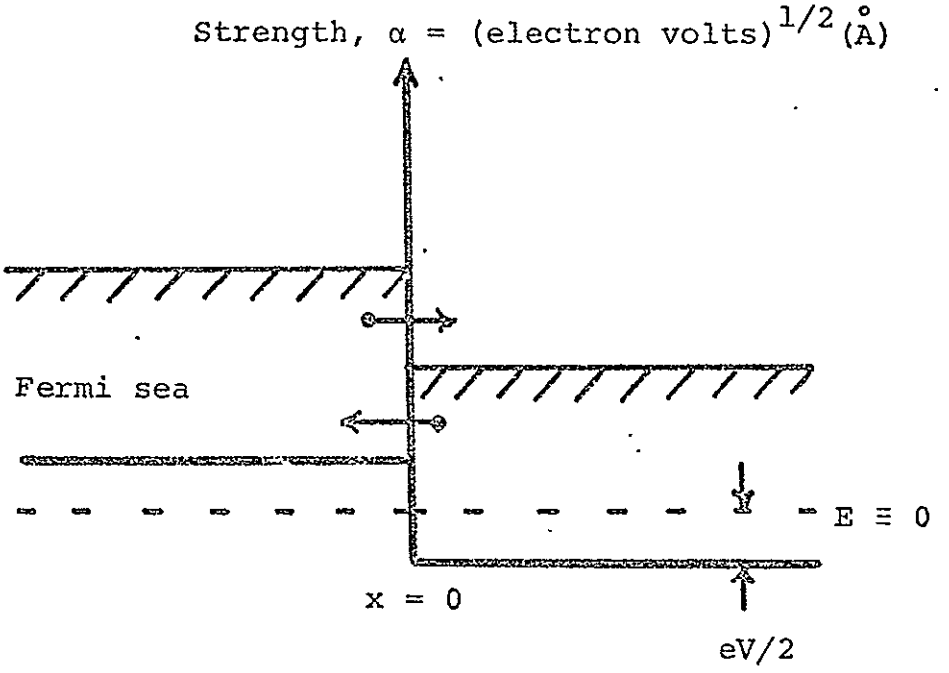

Figure 33

The delta function barrier is the limiting case of a thin barrier of any shape. Here the zero of energy has been chosen to symmetrize the electron supply function.

As usual it may be verified by direct algebraic manipulation that $T_r \equiv T_L$. The constant A^2 is related to the barrier strength:

$$A^2 = 2m\alpha^2/\hbar^2$$

The range of integration is taken for $E > eV/2$.

The tunneling current density is given by:

$$J = \frac{4\pi m k\Theta e}{h^3}\int_{+eV/2}^{\infty} dE\ \ln\left[1+e^{-(E-eV/2-E_f)/k\Theta}\right] T_L\left[1-\frac{\ln\left[1+e^{-(E+\frac{eV}{2}-E_f)/k\Theta}\right]}{\ln\left[1+e^{E_f/k\Theta}\right]}\right]$$

$$-\frac{4\pi m k\Theta e}{h^3}\int_{+\frac{eV}{2}}^{\infty} dE\ \ln\left[1+e^{-(E+\frac{eV}{2}-E_f)/k\Theta}\right] T_L\left[1-\frac{\ln\left[1+e^{-(E-\frac{eV}{2}-E_f)/k\Theta}\right]}{\ln\left[1+e^{E_f/k\Theta}\right]}\right] \qquad (31)$$

Note that the lower limit of all integrations is +eV/2. In the lift metal there exist no electrons below that level. Electrons in the right metal tunneling to the left have no place to go if their energies are less that the bottom of the Fermi sea in the left metal.

Each integrand consists of a product of three terms: the electron supply function, the transmission coefficient, and a term reflecting the density of final states that a tunneling electron may occupy. This last term may be quite important in thin barriers but may be neglected for thick

365<

barrier problems. Note that Eq(31) satisfies the symmetry condition of Chapter 3:

$$J(-V) = -J(V) \qquad (3) .$$

The density of final states term is peculiar to the thin barrier case. For very high thin barriers, the transmission coefficients, Eq(29) and Eq(30), depend only weakly on electron energies E. An electron at the bottom of the Fermi sea is only slightly less likely to tunnel than an electron near the top since both are almost equally far below the actual barrier height. At zero temperature, electrons can tunnel only to the right because both Fermi seas are packed full. Electrons traveling to the left could never find a hole. At elevated temperatures, there are vacancies throughout the Fermi sea but mostly near the top, as expressed by the density of final states term.

If $T_r = T_L$ and if the metals are identical (have the same Fermi energy), the density of states term may be eliminated. Let $f_L(E,V)$ be the electron supply function for the left metal ant f_r for the right metal. Let $f_L(0)$ be the density at the bottom of the Fermi sea in the left metal and $f_r(0)$ stand for the right metal. Then,

$$J(V) = \int_{eV/2}^{\infty} dE \left[f_L \cdot T \cdot \left(1 - \frac{f_R}{f_R(0)}\right) - f_R \cdot T \cdot \left(1 - \frac{f_L}{f_L(0)}\right) \right]$$

366

$$J(V) = \int dE \left[f_L\left(1 - \frac{f_L}{f_L(0)}\right) - f_R\left(1 - \frac{f_L}{f_L(0)}\right) \right] \cdot T$$

If: $f_L(0) = f_R(0)$

$$J(V) = \int dE \; (f_L - f_R) \cdot T$$ which reduces to the thick barrier case of the previous section. The density of final states term must be included for dissimilar metal junctions or for calculating the relative forward and reverse contributions to the total tunneling current.

Figure 34 shows the J-V curve ane its derivatives as computed from Eq(31). The detailed calculations are given in Appendix I.8. Unlike the previous WKB treatments, it is clear from Fig.34 that the second derivative is negative and a nearly linearly decreasing function of bias voltage. Changing the strength of the delta function changes the magnitude of the tunneling current but not the shape of the curve or its derivatives. The shape of the curves in this limit is primarily determined by the details of the electron supply function.

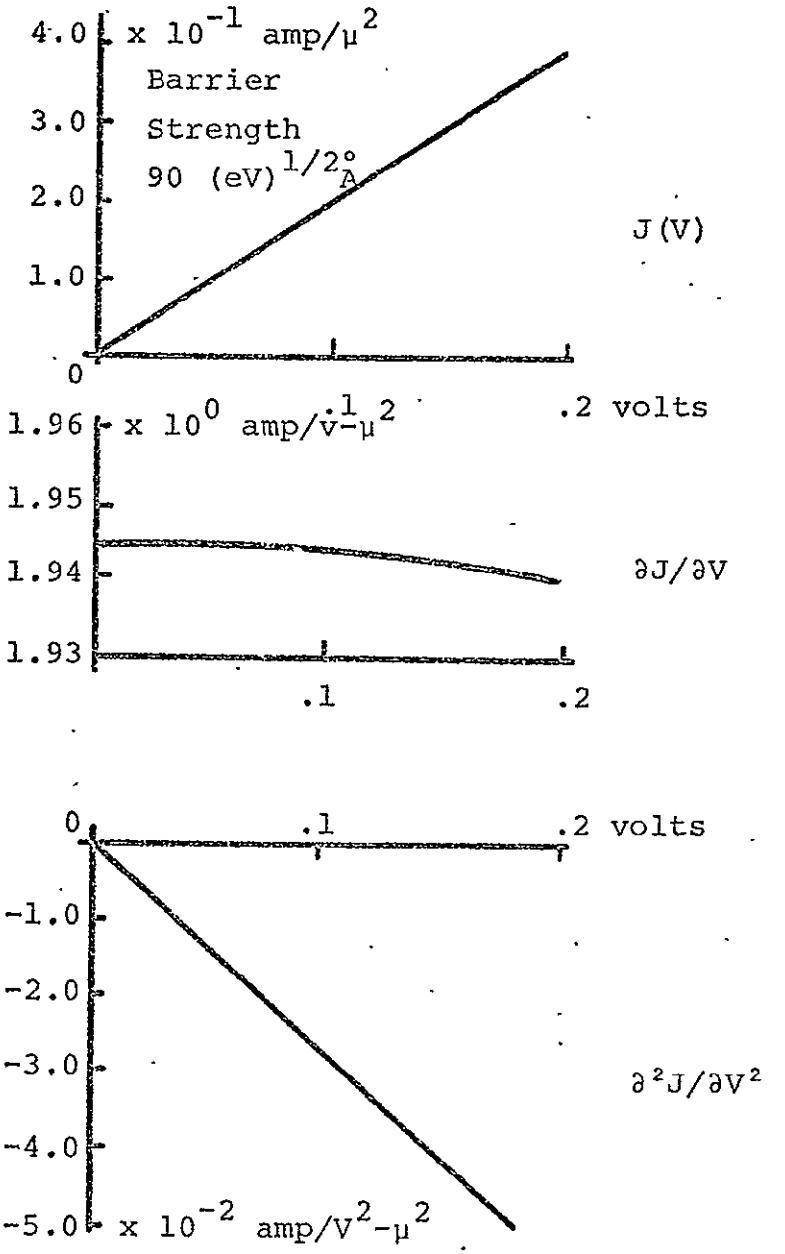

Figure 34

Unlike the WKB approximation calculations, the delta function barrier produces a J-V curve with a nearly linearly decreasing negative second derivative.

368<

The Adjustable Height Rectangular Barrier

Flat topped barriers are particularly easy to calculate because the electron wave functions are simple exponential forms. Duke has suggested[25] using an "effective height" rectangular barrier of bias dependent height to calculate tunneling currents.

The calculations for the rectangular barrier of Fig. 23 may be readily modified. The expression for the transmission coefficient, Eq(24), already includes the effects of multiple reflections of the electron wave functions and will, therefore, be accurate for thin barriers.

As can be seen in the trapezoidal barrier of Fig. 28, the effect of a bias voltage is to lower and modify the barrier shape . Equation (24) need be modified only by substituting a voltage dependent barrier height, $\phi(V)$. The exact functional form of $\phi(V)$ will depend in general on the details of the barrier shape which is to be approximated. A reasonable first approximation is to take

$$\phi(V) = \phi_o - eV/2 \qquad (32) .$$

The current density-voltage curves for this case are shown in Fig .35 for 15 Å and 7 Å barriers. The curves are qualitatively similar to the WKB curves in that they demonstrate positive and nearly linearly increasing second derivatives. Note that the second derivative curves now to to zero for zero bias unlike the curve for the constant height

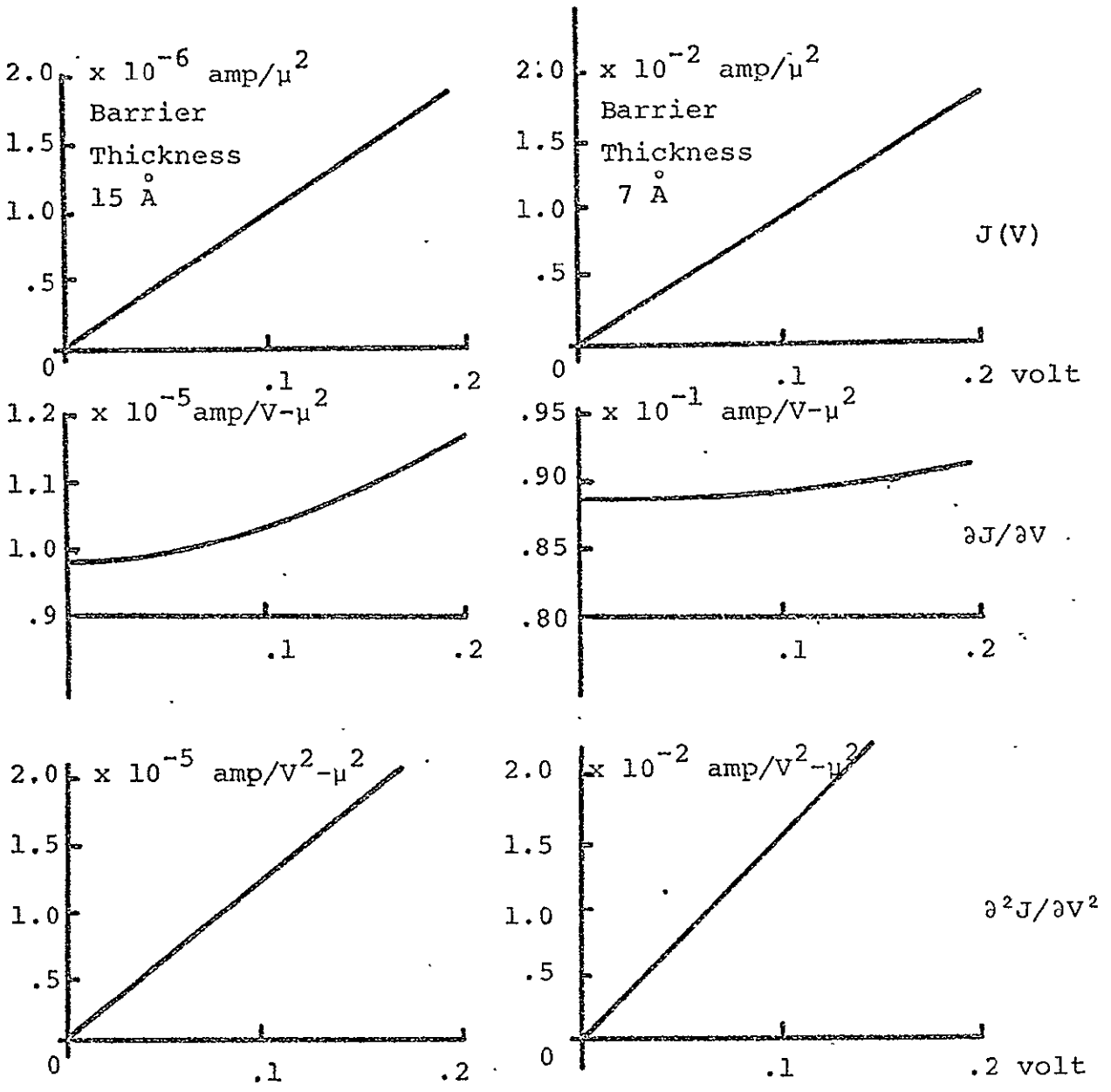

Figure 35

The current density - voltage curves for the adjustable height rectangular barrier are qualitatively similar to the WKB curves.

barrier in Fig. 26.

A higher order modification to Eq(32) which can yield negative second derivatives is suggested by the work of Lewicki and Mead.[30] In their experiments, the peak of the potential barrier in an MDM tunneling junction was measured directly as a function of bias voltage. They observed the photoelectric effect while illuminating the tunneling barrier with a beam of light from a monochromator. One of the junction electrodes was made sufficiently thin to be transparent to the light.

The data of Lewicki and Mead is not explainable by a simple model of image forces which modify the shape of the potential barrier for tunneling electrons. Simmons[31] has proposed a simplified model of electron trapping within the dielectric barrier to fit the data. The resulting charge buildup modifies the potential barrier height in a bias dependent manner.

$$\phi = \phi_0 - \frac{eV}{2} + \frac{(eV)^2}{2(a\beta)^2} \frac{\coth a\beta/2}{(E_f - E_t)} \qquad (33)$$

where a is the barrier thickness

$\beta^2 = e^2 N_t / K\varepsilon_0$ is a constant of the dielectric.

$\varepsilon_0 = 8.85 \times 10^{-12}$ farad/meter $= 1.4 \times 10^{-32}$ Coulomb^2/ev-cm

371<

e is the electronic charge

K the dielectric constant

N_t the number of electron traps per unit volume per unit energy within the insulator

E_f the electrode Fermi energy

E_t is an adjustable parameter related to the lowest energy at which electrons can be trapped within the insulator.

Simmons estimates:

$N_t = 10^{20}\ cm^{-3} ev^{-1}$

$K = 10$

$E_f - E_t = 3$ electron volts.

Equation (33) , due to Simmons, fits the data of Lewicki and Mead fairly well for barrier thicknesses of 50 and 90 Å but shows significant discrepancies at 67 Å. Undoubtedly, the addition of still higher order terms by a more complicated model would produce a better fit.

The work of Simmons suggests that the functional form of Eq(32) for the bias dependent barrier height be modified as follows:

$$\phi = \phi_0 - \frac{eV}{2} + B\,\frac{(eV)^2}{a^2} \qquad (34)$$

Figure 36 shows the results of tunneling calculations for 15 and 7 Å barriers with the coefficient $B = 10\,(Å)^2/ev$ For barrier thicknesses below about 10 Å , the second

372<

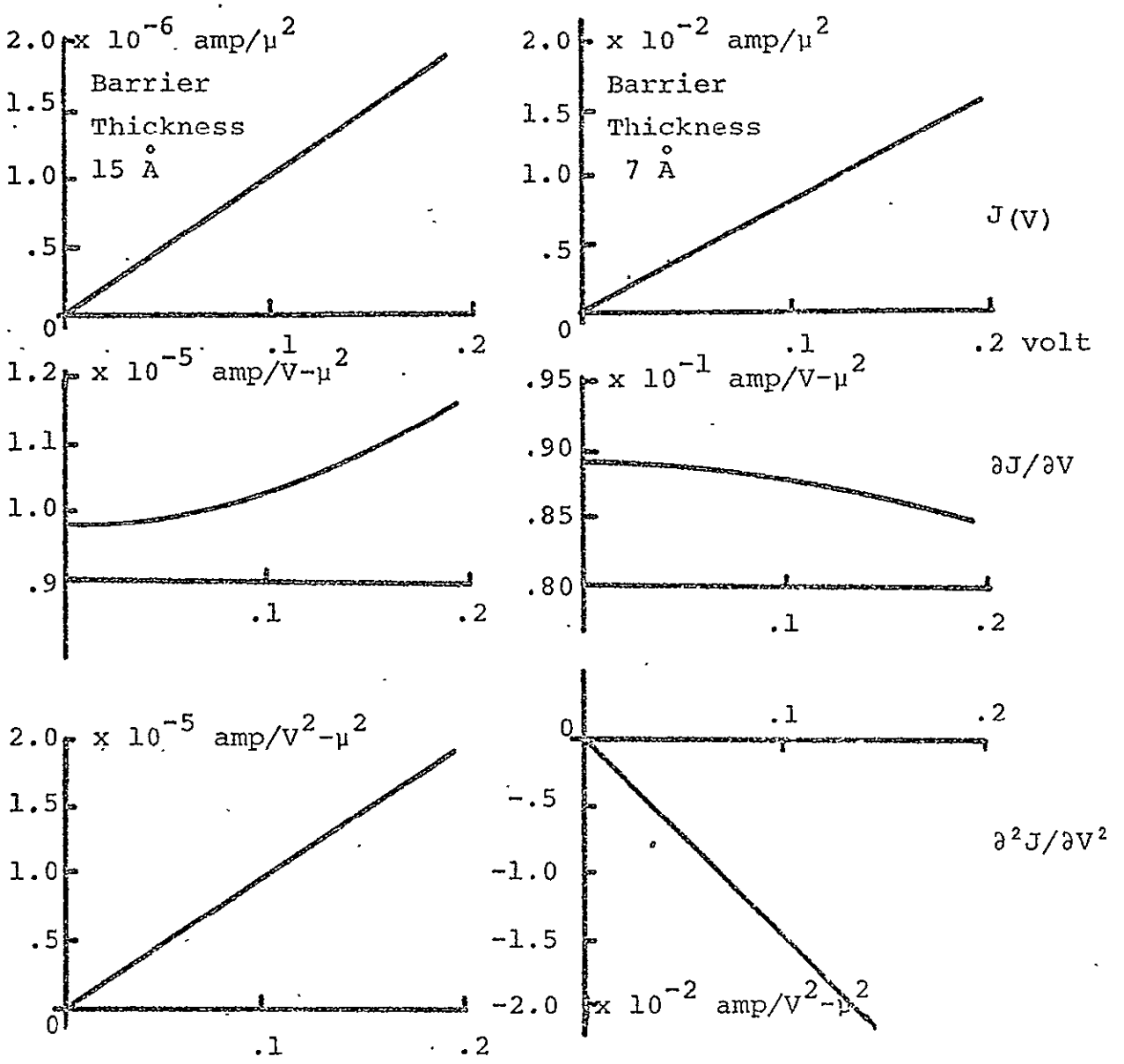

Figure 36

The adjustable height rectangular barrier can produce positive or negative second derivative curves when the barrier height includes an effect due to the buildup of electric charge in the tunneling barrier.

derivative curve can finally be made negative.

To estimate whether B = 10 is a reasonable number, the coefficient of $(eV)^2/a^2$ from Eq(33) may be evaluated using the constants determined by Simmons from the tunneling data at 50 and 90 Å.

For a = 15 Å,

$$B = \frac{\cosh a\beta/2}{2\beta^2(E_f - E_t)} = 12.06$$

and for a = 7 Å, B = 2.1 . The previous choice for B = 10 was of the proper order of magnitude.

9. Second Derivative Curvature

A Higher Order Shape Factor

The WKB method, the delta function barrier, and the adjustable height rectangular barrier have been shown to predict either positive or negative second derivative curves. In all cases, however, the second derivatives are very nearly linear with bias voltage and simply do not show the strong curvatures of the experimental biased rectification curves.

Strong curvatures in the second derivative curves may be obtained by adding higher order terms to the bias dependence of the barrier height. The next higher order term in bias dependence of the barrier height may be written in the form

$$\phi = \phi_0 - \frac{eV}{2} + B\frac{(eV)^2}{2} + C(eV)^3 \qquad (35)$$

374<

Figure 37 shows the result of computer calculations for the 15 Å and 7 Å barrier cases. For C = +.4 $(ev)^{-2}$, the positive second derivative curve of the 15 Å barrier can be made to turn smoothly downward. For C = -.2, the negative second derivative curve of the 7 Å barrier can be made to turn smoothly upward. The computer program for this case is found in Appendix I.10.

As yet, the choice of a magnitude for the coefficient C has not been given physical significance. C is simply a parameter which has been adjusted to produce second derivative curves which have sufficient departure from linearity to qualitatively fit the experimental observations. It is apparent that such a parameter is necessary, and it may indicate that additional physical processes influence the tunneling current. The above straightforward treatments by the WKB method, the delta function method, and the adjustable height barrier do not, in themselves, contain sufficient degrees of freedom to describe strong curvatures in the second derivatives. Perhaps a treatment to higher order of the electron trapping theory of Simmons will account for such a term. Perhaps an additional physical mechanism must be introduced to the model of electron tunneling. Such further treatment must remain beyond the scope of this present work.

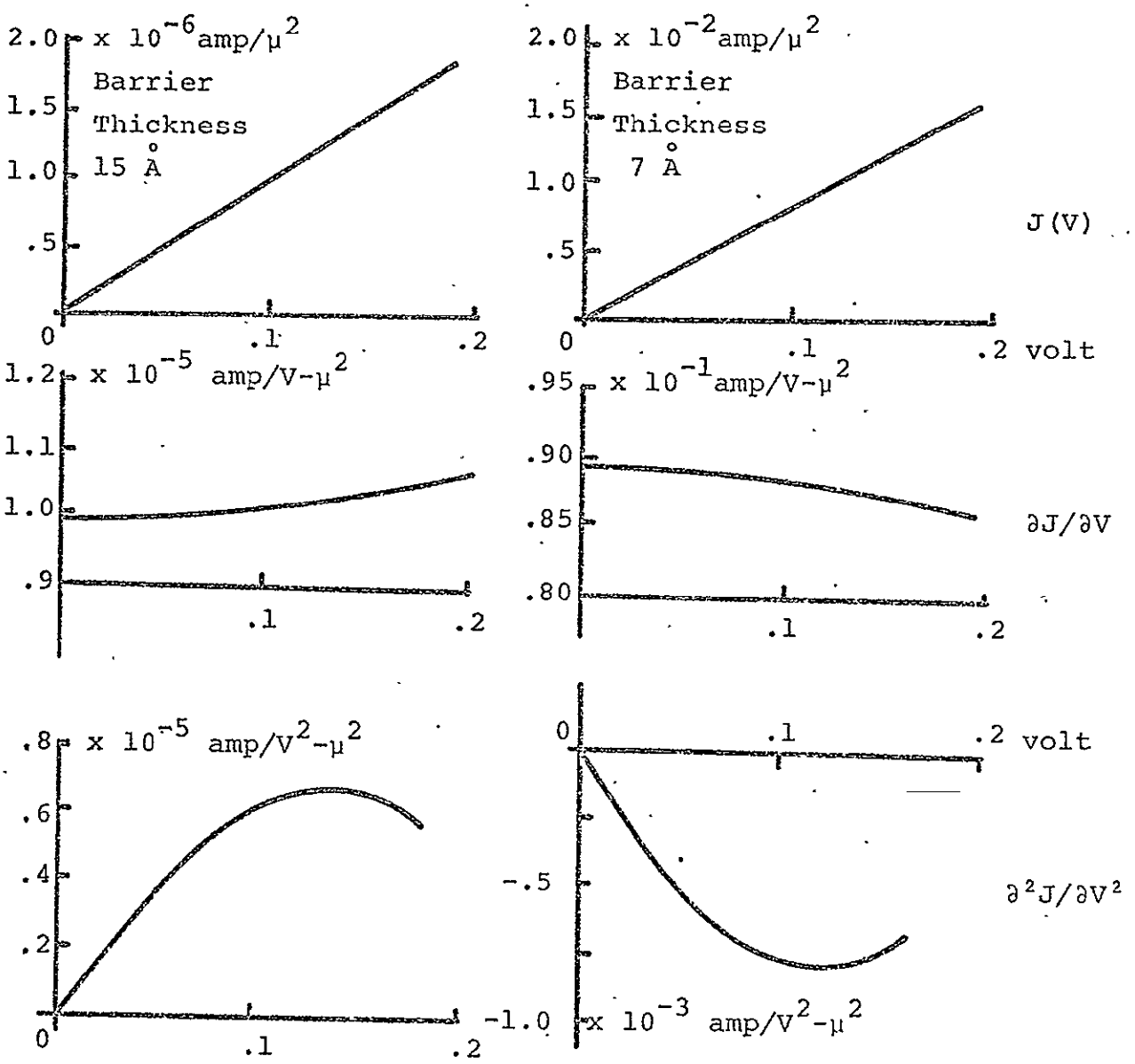

Figure 37

The addition of a higher order effect in the dependence of barrier height with bias is required to produce strong curvature in the second derivatives. Here a term in the third power of the bias voltage has been included.

376<

A Current Dependent Saturation

A physical mechanism which tends to limit high currents will contribute to a negative term in the second derivative. The first example of the rectangular barrier of constant height produced such a curve. See Fig. 26. A weak saturating mechanism will tend to round off and curve positive second derivatives downward. A stronger saturation can change the positive derivatives to negative second derivatives. For a second derivative which is already negative before including a saturation effect, the curvature of the derivative is affected in a more complicated manner. It may then curve either way depending upon the strength of the saturating effect. Any number of saturation mechanisms at high bias currents might be postulated.

The junction area for the device of Fig. 16 can be roughly estimated. It is surely no more than one square micron and, perhaps, an order of magnitude less. At a bias current of 4 mA, the current density is, therefore, greater than 4×10^5 amperes/cm^2. Assume it is 10^6 amp/cm^2.

Substantial local heating can be expected at such high current densities, and a rise in temperature will modify both the electron distribution functions and the barrier height and thickness. Notice, however, that in Chapter 3 low frequency (below 1 GHz) heating nonlinearities were observed to be quite distinct from the fast tunneling curve.

377-

Current in a conductor is carried by the average drift velocity of the electron gas. Normally the drift velocity

is quite low. The current density J is given by:

$$J = ne\,\partial v$$

where n is the number of charge carriers per unit volume

e is the charge per carrier

∂v is the drift velocity.

The number of charge carriers per atom may be estimated from the Hall coefficient for the metal in question. The Hall coefficients for a number of common metals are given below[32] in normalized units.

If the charge carriers are negative, the coefficient is negative. The magnitude indicates the number of atoms/charge carrier. Thus -4 indicates negative charge carriers (electrons) with an average of one electron for every 4 atoms in the metal.

Na = -.9	Au = -.7
K = -.9	Ni = -4
Cu = -.8	Bi = -5000
Ag = -.8	

The atomic weight of Ni = 58.71. The specific gravity is 8.902 gm/cm^3. The number of atoms/cm^3 = .913 x 10^{23}. At one ampere/cm^2, the drift velocity for Ni is:

$$\partial v = J/n = 2.74 \times 10^{-4} \text{ cm/sec.}$$

At 10^6 amperes/cm^2 the electron drift velocity is up to 2.7 meters per second. The unusually high drift velocities at high currents might contribute to a departure from the thermodynamic equilibrium and thus change the functional form of the electron distribution functions. It should be noted, however, that even these high drift velocities are still small compared to the electron microscopic velocities which are typically of the order of 10^5 meters per second .

A topic suitable for a further investigation might be to measure the nonlinearities in an MDM junction made from Bi, which has a drift velocity three orders of magnitude higher than Ni.

To estimate the effect of a current dependent saturation effect, consider a current dependent modification to the tunneling current expression in Eq(26):

$$J = \frac{4\pi m k\theta e}{h^3} \int_0^\infty dE \ln\left[\frac{1+e^{-(E-\xi_f)/k\theta}}{1+e^{-(E+eV-\xi_f)/k\theta}}\right] S(J)\cdot T \qquad (36)$$

S(J) must reduce to unity for $J \to 0$. The above equation is an integral equation in the current density J. It can be solved by numerical iteration. If S(J) is not a function of E, it can be factored out of the integral and, in principle,

J(V) could be solved directly.

The simplest form for S(J) is linear in J

$$S(J) = 1 - B\,J$$

where B is the saturation strength. This form was found to be too weak to give qualitative agreement with the experimental data. The sign of the second derivative could be changed by adjusting B, but no strong curvature was obtained. A somewhat stronger form produced the desired results:

$$S(J) = 1 - B\,J^2$$

Figure 38 shows the results of the computer analysis. The program is given in Appendix I.9 . A saturation parameter of $B = 2\ \mu^4/amp^2$ produces an effect similar to the higher order effect in the adjustable height barrier calculation of Fig.37 . The integral equation Eq(36) was iterated three times. As above, stronger saturation parameters , on the order of $3.5\ \mu^4/amp^2$, can also produce a change in algebraic sign as well as introduce curvature.

The J^2 saturation dependence is a very reasonable form to expect. In conductors, heating effects are proportional to J^2 .

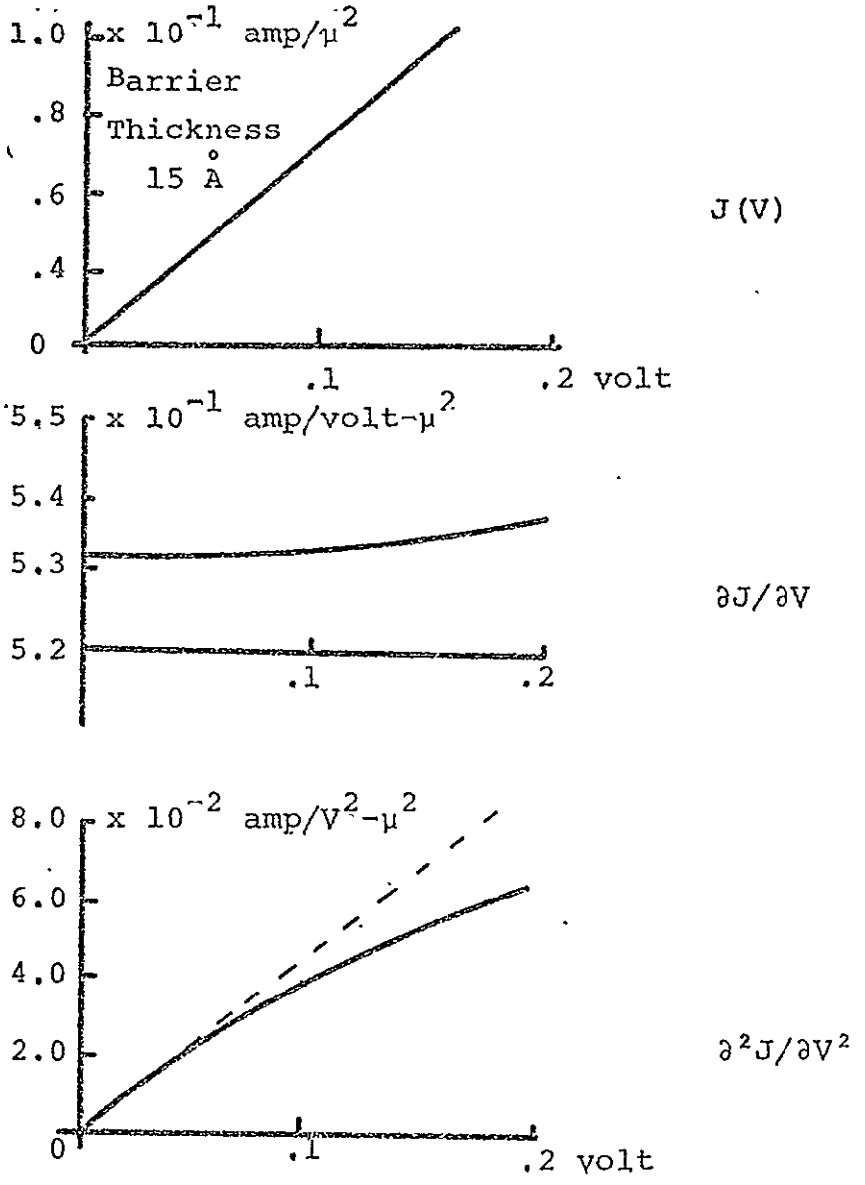

Figure 38

A current dependent saturation mechanism can contribute to downward curvature in positive going second derivatives. Here a weak saturation has been applied to the WKB calculations for the bias dependent parabolic barrier.

381<

10. An Estimate of the Rectified Voltage Magnitude

From Eq(23) the rectified signal with bias is expected to be of the order of

$$\Delta\overline{V}_{os} = -\frac{a_2}{2a_1^3}\frac{V_a^2}{(1/a_1 + Z)^2} \qquad (37)$$

A positive signal corresponding to the data of Fig. 16 must have a negative second derivative. The adjustable height rectangular barrier calculations predicted such an effect for a barrier thickness of 7 Å. From Fig. 36 the magnitudes of the a_1 and a_2 coefficients may be read directly from the graphs of the computer calculations.

For V = .2 volt,

$$a_1 \simeq .8 \times 10^{-1} \text{ amp/v-}\mu^2$$

$$a_2 \simeq -2 \times 10^{-2} \text{ amp/v}^2\text{-}\mu^2$$

assume: $Z = 100\ \Omega$, and, $R_s >> R_1$

then $\Delta V_{os} = 5 \times 10^{-3} V_a^2$ volts (38)

V_a^2 may be estimated by estimating the energy captured from the incident laser radiation. The incident power density at .9 THz is approximately 30 mW/mm^2. Assume that the capture area or antenna cross section is proportional to the square of the wavelength. For an efficient antenna system, the proportionality constant is near unity. Here assume 10^{-1}. Then the power captured is given by:

382<

$$P = .1 \times (30\ mW/mm^2) \times .1\ mm^2 = 3 \times 10^{-4} watt.$$

If this power is dissipated in the diode resistance and antenna ohmic losses, then

$$P = V_a^2/R$$

$$V_a^2 = P\ R$$

Resistivity calculations for the thin film antenna indicates that the small laser frequency dipole has a resistance of approximately 20 ohms from tip to tip. Similarly, the diode resistance = $1/a_1$ = 10 ohms . For an order of magnitude estimate, choose R = 30 ohms.

Then $V_a^2 = 3 \times 10^{-4} \times 3 \times 10^{1} = 9 \times 10^{-3} volts^2$.

For $V_a^2 = 10^{-2} volts^2$, Eq(38) gives an estimate of the magnitude of the rectified signal:

$$\Delta V_{os} = 5 \times 10^{-5}\ volt$$

$$= .05\ mV.$$

Thus, the theory predicts nonlinearities which should produce a rectified voltage two orders of magnitude less than is actually observed in Fig. 16 under the assumption of a 1 μ^2 junction area. Note, however, that a_1 and a_2 are proportional to area. From Eq(37), ΔV_{os} is proportional to $(1/area^2)$ if one can neglect $1/a_1$ compared to Z. Then an area of .1 μ^2 will give ΔV_{os} which is of the same order as the experimentally observed voltages.

11. Theoretical Conclusions

The experimental evidence shows both negative and positive rectification with bias; i.e. both positive and negative second derivatives. Simple WKB electron tunneling models predict only positive second derivatives.

Negative second derivative curves are predicted in the limit of very thin barriers by the delta function model of electron tunneling. The effect of charge buildup within the dielectric barrier can contribute to negative second derivatives for thin barriers but not for thick barriers. Also, strong current dependent saturation effects can change positive second derivative curves to negative curves.

The experimental data shows strong curvature in the rectified responses. A curvature in the second derivative curve reflects the algebraic sign of the 4th derivative.

The simple electron tunneling models predict only weak curvatures in the second derivative curves, and higher order effects must be included to qualitatively fit the experimental evidence. In the WKB models, a current dependent saturation effect can produce sufficiently strong curvatures, but cannot alone explain the detailed form of the rectified signal with its inflection points between regions of positive and negative curvature. In the adjustable height rectangular barrier model, a higher order dependence than that indicated by a simple electron trapping mechanism is needed to introduce curvature. A possible higher order mechanism beyond current dependent

saturation has not yet been identified.

Future investigations into possible saturation mechanisms might inc lude diodes fabricated from Bismuth or other semi-metals which have anomalously high electron drift velocities. An investigation of other types of dielectric barriers is also required.

The higher order mechanisms strongly effect the 4 th derivative curves. Therefore, 4th order mixing experiments might prove useful as direct experimental probes of the higher order tunneling mechanisms.

This report is the substance of the work performed by James G. Small under NASA sponsorship in partial fulfillment of the requirements for the degree of Doctor of Philosophy at the Massachusetts Institute of Technology.

APPENDIX I

Electron Tunneling Calculations and Sample Computer Programs

1. The Asymmetric Rectangular Barrier

Refering to the three regions of the rectangular barrier diagram of Fig. 23, Schrödinger's equation may be written:

$$-\frac{\hbar^2}{2m}\frac{\partial^2\Psi}{\partial x^2} + \phi(x)\,\Psi = E\,\Psi$$

The wave functions for the three regions which satisfy the wave equation may be written:

$$\Psi_1 = A e^{ik_1 x} + B e^{-ik_1 x}$$

$$\Psi_2 = F e^{-k_2 x} + G e^{+k_2 x}$$

$$\Psi_3 = C e^{ik_3 x}$$

where:

$$k_1 = \frac{(2mE)^{1/2}}{\hbar}$$

$$k_2 = \frac{[2m(\phi - E)]^{1/2}}{\hbar}$$

$$k_3 = \frac{[2m(E + eV)]^{1/2}}{\hbar}$$

The transmission coefficient for tunneling to the right is given by:

$$T_+ = \frac{|C|^2}{|A|^2}\cdot\frac{k_3}{k_1}$$

From the continuity of ψ at the barrier boundaries:

at x = 0 $\quad A + B = F + G$ (I.1)

at x = a $\quad F e^{-k_2 a} + G e^{k_2 a} = C e^{i k_3 a}$ (I.2)

From the continuity of the derivatives of ψ:

at x = 0 $\quad i k_1 A - i k_1 B = -k_2 F + k_2 G$ (I.3)

at x = a $\quad -k_2 F e^{-k_2 a} + k_2 G e^{k_2 a} = i k_3 e^{i k_3 a}$ (I.4)

(I.4) $\div k_2$ $\quad -F e^{-k_2 a} + G e^{k_2 a} = i \frac{k_3}{k_2} C e^{i k_3 a}$

add (I.2) $\quad G = \frac{1}{2}\left(1 + i \frac{k_3}{k_2}\right) e^{-k_2 a} e^{i k_3 a}$

(I.5)

and subtract (I.2)

$$F = \frac{1}{2}\left(1 - i \frac{k_3}{k_2}\right) e^{k_2 a} C e^{i k_3 a} \qquad \text{(I.6)}$$

(I.3) ÷ i k_1 $\qquad A - B = i \frac{k_2}{k_1} F - i \frac{k_2}{k_1} G$

adding (I.1) gives: $2A = \left(1 + i\frac{k_2}{k_1}\right)F + \left(1 - i\frac{k_2}{k_1}\right)G$

Now substitute (I.5) and (I.6) and solve for A/C

$$2\frac{A}{C} e^{-ik_3 a} = \left(1 + \frac{k_3}{k_1}\right)\cosh k_2 a + i\left(\frac{k_2}{k_1} - \frac{k_3}{k_2}\right)\sinh k_2 a$$

$$4\frac{|A|^2}{|C|^2} = \left(1 + \frac{k_3}{k_1}\right)^2 (1 + \sinh^2 k_2 a) + \left(\frac{k_2}{k_1} - \frac{k_3}{k_2}\right)\sinh^2 k_2 a$$

$$T_+ = \frac{|C|^2}{|A|^2} \cdot \frac{k_3}{k_1}$$

$$T_+ = \frac{4 k_3/k_1}{\left(1 + \frac{k_3}{k_1}\right)^2 + \left[\left(1 + \frac{k_3}{k_1}\right)^2 + \left(\frac{k_2}{k_1} - \frac{k_3}{k_2}\right)^2\right]\sinh^2 k_2 a} \qquad \text{(I.7)}$$

For electrons tunneling to the left, the transmission coefficient is of the same form with k_1 and k_3 interchanged.

$$T_- = \frac{4 k_1/k_3}{\left(1 + \frac{k_1}{k_3}\right)^2 + \left[\left(1 + \frac{k_1}{k_3}\right)^2 + \left(\frac{k_2}{k_3} - \frac{k_1}{k_2}\right)^2\right]\sinh^2 k_2 a}$$

It can be seen that $T_+ = T_-$ by a straightforward algebraic manipulation. Multiply (I.7) numerator and deonminator by k_1/k_3 :

$$T_+ = \frac{4\,k_3/k_1}{1 + 2\frac{k_3}{k_1} + \frac{k_3^2}{k_1^2} + \left(1 + 2\frac{k_3}{k_1} + \frac{k_3^2}{k_1^2} + \frac{k_2^2}{k_1^2} - 2\frac{k_3}{k_1} + \frac{k_3^2}{k_2^2}\right)\sinh^2 k_2 a}$$

$$= \frac{4}{\frac{k_1}{k_3} + 2 + \frac{k_3}{k_1} + \left(\frac{k_1}{k_3} + \frac{k_3}{k_1} + \frac{k_2^2}{k_1 k_3} + \frac{k_1 k_3}{k_2^2}\right)\sinh^2 k_2 a}$$

$$= \frac{4}{\frac{k_1}{k_3} + 2 + \frac{k_3}{k_1} + \left(\frac{k_1}{k_3} + \frac{k_3}{k_1} + \frac{k_2^2}{k_1 k_3} + \frac{k_1 k_3}{k_2^2}\right)\sinh^2 k_2 a}$$

$$= T_-$$

T_+ can be reduced to a form that is invariant upon interchange of k_1 and k_3 and, therefore, equals identically T_-. This invariance of the transmission coefficient for tunneling in either direction is true of most barrier penetration calculations.

2. The Electron Supply Function for a Degenerate Fermi Gas

The momentum distribution for electrons in a slightly warm metal (lim T → 0) may be approximated by:

$$dN = (2\cdot 4\cdot 1)\cdot \frac{1}{e^{(p^2/2m - E_f)/kT} + 1}\cdot \frac{dP_x\, dP_y\, dP_z}{h^3}\, V$$

Evaluating E_f:

at T = 0, $E_f > p^2/2m \Rightarrow e^{(p^2/2m - E_f)/kT} \to e^{-\infty} \to 0$

$$dN = (2)\cdot 1\cdot \frac{dP_x\, dP_y\, dP_z}{h^3}\, V$$

$$N = \frac{2V}{h^3}\iiint dp^3 = \frac{2V}{h^3}\int_0^{P_f} 4\pi p^2\, dp = \frac{8\pi V}{h^3}\cdot\frac{P_f^3}{3}$$

$$P_f^3 = \frac{3Nh^3}{8\pi V}\quad,\quad P_f = \frac{h}{2}\left(\frac{3}{\pi}\frac{N}{V}\right)^{1/3}$$

$$E_f = \frac{h^2}{8m}\left(\frac{3}{\pi}\frac{N}{V}\right)^{2/3}$$ which agrees with Eisberg[27].

A typical value for E_f is 7 electron volts.

The distribution of electrons with momentum p_x independent of p_y and p_z is given by:

$$dN_x = \frac{2V}{h^3}\left[\iint \frac{dP_y\, dP_z}{e^{(E - E_f)/kT} + 1}\right] dP_x$$

390<

$$E = \frac{p_x^2 + p_y^2 + p_z^2}{2m} = \frac{p_x^2}{2m} + \frac{p_r^2}{2m}$$ integrate by changing variables.

$$p_r^2 = p_y^2 + p_z^2 \quad ; \quad dp_y\, dp_z = p_r\, d\theta\, dp_r$$

$$dN_x = \frac{2V}{h^3} \cdot 2\pi \left[\int_0^\infty \frac{p_r\, dp_r}{e^{\left(\frac{p_x^2}{2m} - E_f\right)/kT} \cdot e^{\frac{p_r^2}{2mkT}} + 1} \right] dp_x$$

$$dN_x = \frac{4\pi V}{h^3} \left[\int_0^\infty \frac{mkT\, dx}{a e^x + 1} \right] dp_x$$

$$x = \frac{p_r^2}{2mkT}; \quad dx = \frac{p_r\, dp_r}{mkT}$$

$$a = e^{\left(\frac{p_x^2}{2m} - E_f\right)/kT}$$

$$dN_x = \frac{4\pi V mkT}{h^3} \ln\left[1 + e^{\left(E_f - \frac{p_x^2}{2m}\right)/kT} \right] dp_x$$

The volume:

$$V = A v_x\, dt$$

$$dN_x = \frac{4\pi m kT}{h^3} \ln[\ \ldots\ ]\, \underbrace{v_x\, dp_x}_{dE} \cdot A$$

The current density:

$$dJ_x = \frac{dN_x}{A\,dt} \cdot e = \frac{4\pi m kT e}{h^3} \ln\left[1 + e^{-(E - E_f)/kT} \right] dE$$

(I.10)

3. Simpson's Rule Applied to Numerical Integration

Consider a function, f(x) , which is smoothly varying:

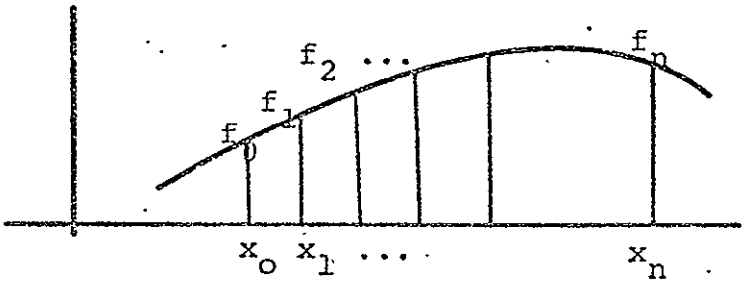

The samples $f_0(x_o)$ to $f_n(x_n)$ represent discrete samples of the function f(x) at equally spaced intervals, h. Simpson's Rule connects the discrete samples with a parabola and computes the area under each parabolic section. The result:[33]

$$\int_{x_0}^{x_m} f(x)\,dx \simeq \frac{1}{3} h\left(f_0 + 4f_1 + 2f_2 + 4f_3 + 2f_4 + \cdots + 2f_{n-2} + 4f_{n-1} + f_n\right)$$

$$h = \frac{x_n - x_o}{n} = \text{the step size}$$

n is even. For n steps there are n + 1 samples taken.

4. Program for Rectangular Barrier Tunneling Currents

For constant height barriers, modify statement 04.04 to read: S EW = EP. This program calculates the curves for Fig. 25 and Fig 26.

```
C-8K FOCAL 01969

01.10 C RECTANGULAR BARRIER
01.12 C USE FOCAL4W
01.14 S B1=0;S B2=0;S D1=0;S D2=0
01.15 T %;T !;W 4.04
01.16 W 1.5
01.17 W 4.05
01.20 T !!,"   I(AMP)                1ST D(AMP/VOLT)"
01.21 T "      2ND D(AMP/VOLT↑2)",!
01.50 S EP=8;S A=15;S B=0;S N=160;S JM=8;S C=.0
01.70 F J=0,JM;S EV=J*.2/JM;DO 2
01.90 Q

02.30 F I=2,2,N;DO 4
02.40 S B2=4*B1;S B1=0
02.50 F I=3,2,N-1;DO 4
02.60 S B2=2*B1+B2;S B1=0
02.70 S I=1;DO 4;S B2=B1+B2;S B1=0
02.80 S I=N+1;DO 4;S B2=B1+B2
02.90 S B2=4.047*B2*4.4/(N*3)
02.94 T !,B2,"     ",(B2-D1)*JM/.2
02.95 T "     ",(B2-D1-D2)*JM*JM/.04
02.96 S D2=B2-D1;S D1=B2

04.04 S EW=EP-.5*EV+B*EV*EV/(A*A)+C*EV*EV*EV
04.05 S EN=3+4.4*I/N
04.10 S S=.51166*A*FSQT(EW-EN)
04.15 S S=FEXP(S)-FEXP(-S);S S=(S/2)↑2
04.20 S E1=FEXP(-43*EN+283)
04.22 S E2=FEXP(-40*EN-40*EV+280)
04.30 S D=1+EV/EN+EV/EN+(EN+EV)/(EW-EN)
04.32 S L=D*S
04.34 S D=(1+FSQT(1+EV/EN))↑2+D
04.36 S T=4*FSQT(1+EV/EN)/D
04.40 S G1=T*FLOG((1+E1)/(1+E2))
04.60 S B1=G1+B1
*
```

5. Program to Display Tunneling Current Integrands

This program calculates the curves of Fig. 27

```
*W A
C FOCAL-12

01.10 C ASYMMETRIC RECTANGULAR BARRIER
01.11 C OF CONSTANT HEIGHT
01.20 C USE FOCAL-12

02.10 S A=15;S EV=.05;S EW=5
02.15 O 0;O S
02.20 F I=1,200;D 4.
02.30 F I=15,1,60;S Z=FDIS(I/50,.1);O D
02.40 F I=1,60;S Z=FDIS(33/75,I/60);O D
02.50 T "ASSYM RECT BARRIER",!!!!!!!!!!!!!!!!!,"+X",!!!,"-X"
02.60 O T
02.70 Q

04.05 S EN=5+2.4*I/220
04.10 S S=.51163*A*FSQT(EW-EA)
04.15 S S=FEXP(S)-FEXP(-S);S S=(S/2)↑2
04.20 S E1=FEXP(-A)*EV-A*EA+200)
04.25 S E2=FSQT(EA/(EV+EA))
04.30 S E3=(1+E2)↑2*(1+EW/(EV+EA)+EA/(EW-EA))*S
04.40 S G1=(1+1/E2)↑2*(1+(EW+EV)/EA*(EA+EV)/(EW-EA))*S
04.45 S G1=.83*10↑7*FLOG(1+FEXP(-43*A+2*C))/G1
04.50 S G2=.89*10↑7*FLOG(1+E1)/E3
04.60 S Z=FDIS(I/300,G1/5+.43)
04.70 S Z=FDIS(I/300,G2/5+.46)
04.80 S Z=FDIS(I/150,G1-G2+.1);O D
*
```

6. Program for Parabolic Barrier WKB Approximation

This program calculates the curves for Figs. 30 and 31.

```
C-8( FOCAL @1969

01.10 C PARABOLIC BARRIER, WKB
01.12 C USE FOCAL4V
01.14 S B1=0;S B2=0;S D1=0;S D2=0
01.15 T %;T !
01.16 V 1.5
01.17 W 4.05.
01.20 T !!,"   I(AMP)                1ST D(AMP/VOLT)"
01.21 T "       2ND D(AMP/VOLT↑2)",!
01.50 S EP=8;S A=0;S B=0;S N=300;S JM=8;S C=0
01.70 F J=0,JM;S EV=J*.2/JM;DO 2
01.99 Q

02.30 F I=2,2,N;DO 4
02.40 S B2=A*B1;S B1=0
02.50 F I=3,2,N-1;DO 4
02.60 S B2=2*B1+B2;S B1=0
02.70 S I=1;DO 4;S B2=B1+B2;S B1=0
02.80 S I=N+1;DO 4;S B2=B1+B2
02.90 S B2=4.047*B2*7.4/(A*3)
02.94 T !,B2,"    ",(B2-B1)*JM/.2,"
02.95 T (B2-D1-D2)*JM*JM/.04
02.96 S D2=B2-D1;S D1=B2

04.05 S EN=7.4*I/N
04.20 S E1=FEXP(-40*EN+880)
04.22 S E2=FEXP(-40*EN-40*EV+280)
04.30 S E3=(1-EV/(4*EP))↑2
04.32 S D=A*(E3-EN/EP)*3.14159/4
04.33 S B=-1.02466*D*FSQT(EP)
04.34 S T=FEXP(B)
04.40 S C1=T*FLOG((1+E1)/(1+E2))
04.60 S B1=C1+B1
*
```

7. Program for Trapezoidal Barrier WKB Approximation

This program calculates the curves of Fig.32 .

```
*W 4.
C-8I  FOCAL, 01969

01.10 C  TRAPEZOIDAL BARRIER,WKB
01.12 C  USE FOCAL4W
01.14 S B1=0;S B2=0;S D1=0;S D2=0
01.15 T %;T !
01.16 W 1.5
01.17 W 4.05
01.20 T !!,"   I(AMP)              1ST D(AMP/VOLT)"
01.21 T " ..     2ND D(AMP/VOLT^2)",!
01.50 S EP=8;S A=5;S B=0;S N=300;S JM=8;S C=0
01.70 F J=0,.4;S EV=.001+J*.2/JM;DO 2
01.90 Q

02.30 F I=2,2,N;DO 4
02.40 S BP=4*B1;S B1=0
02.50 F I=3,2,N-1;DO 4
02.60 S B2=2*B1+B2;S B1=0
02.70 S I=1;DO 4;S B2=B1+B2
02.80 S I=N+1;DO 4;S B2=B1+B2
02.90 S B2=4.047*B2*7.4/(N*3)
02.94 T !,B2,"    ",(B2-D1)*JM/.2,"
02.95 T (B2-D1-D2)*JM*J/.04
02.96 S D2=B2-D1;S D1=B2

04.25 S EN=7.4*I/N
04.20 S E1=FEXP(-40*EN+280)
04.22 S E2=FEXP(-43*EN-40*EV+280)
04.30 S E3=FSQT(EP-EN-EV)
04.31 S E4=FSQT(EP-EN)
04.32 S D=.66666*A*(E4^3-E3^3)/EV
04.35 S T=FEXP(-1.02466*D)
04.40 S G1=T*FLOG((1+E1)/(1+E2))
04.60 S B1=G1+B1
```

8. Program for Delta Function Barrier

This program calculates the curves of Fig.34.

```
C-8K FOCAL 01969
01.10 C SYMMETRIZED DELTA FCTN BARRIER
01.12 C USE FOCAL4W
01.14 S B1=0;S B2=0;S D1=0;S D2=0
01.15 T %;T !
01.16 W 1.5.
01.17 W 4.05
01.20 T !!,"    I(AMP)              1ST D(AMP/VOLT)"
01.21 T !"      2ND D(AMP/VOLT↑2)",!
01.50 S EP=8;S A=15;S B=0;S N=300;S JM=3;S C=0
01.70 F J=0,.1;S EV=J*.2/.4;DO 2
01.90 Q

02.30 F I=2,2,N;DO 4
02.40 S B2=4*B1;S B1=0
02.50 F I=3,2,N-1;DO 4
02.60 S B2=2*B1+B2;S B1=0
02.70 S I=1;DO 4;S B2=B1+B2;S B1=0
02.80 S I=N+1;DO 4;S B2=B1+B2
02.90 S B2=4.047*B2*7.4/(N*3)
02.94 T !,B2,"    ",(B2-D1)*JM/.2,"    "
02.95 T (B2-D1-D2)*JM*JM/.04
02.96 S D2=B2-D1;S D1=B2

04.04 S EN=EP
04.05 S EN=EV/2+.00001+7.4*I/N
04.20 S E1=FEXP(-40*EN+20*EV+280)
04.22 S E2=FEXP(-40*EN-20*EV+280)
04.30 S E3=FSQT((EN+EV/2)/(EN-EV/2))
04.32 S D=(1+E3)↑2+A*A/(EN-EV/2)
04.34 S T=4*E3/D
04.40 S C1=T*FLOG((1+E1)/(1+E2))
04.60 S B1=C1+B1
```

ORIGINAL PAGE IS
OF POOR QUALITY

9. Program for Current Dependent Saturation

This program iterates three times and calculates Fig.38.

```
C-64 FOCAL 01069

01.10 C PARABOLIC BARRIER W/ SATURATION
01.12 C USE FOCAL.4w
01.15 T %;T !
01.16 S B1=0;S B2=0;S D1=0;S D2=0
01.18 S EP=3;S A=15;S N=302;S DJ=3;S B=2
01.20 T !,"      I(AMP)                  1ST D(AMP/VOLT)"
01.21 T "      2ND D(AMP/VOLT^2)"
01.30 F I=0,DJ;S U(I)=0

02.10 S EV=0;D 4;T !
02.20 F J=1,DJ;S EV=J*.2/DJ;T !;DO 3
02.90 Q

03.20 S BJ=0;D 4;S BJ=B2
03.22 D 4;S BJ=B2
03.24 D 4;S BJ=B2
03.25 S U(J)=B2

04.30 F I=2,2,N;DO 6
04.40 S B2=4*B1;S B1=0
04.50 F I=3,2,N-1;DO 6
04.60 S B2=2*B1+B2;S B1=B
04.70 S I=1;DO 6;S B2=B1+B2;S B1=0
04.80 S I=N+1;DO 6;S B2=B1+B2
04.90 S B2=4.047*B2*7.4/(N*3)
04.94 T !,B2,"     ",(B2-U(J-1))*DJ/.2
04.95 T "     ",(B2-2*U(J-1)+U(J-2))*DJ*DJ/.04

06.05 S EN=7.4*I/A
06.20 S E1=FEXP(-40*EN+280)
06.22 S E2=FEXP(-40*EN-40*EV+280)
06.30 S E3=(1-EV/(4*EP))^2
06.32 S D=A*(E3-EN/EP)*3.14159/4
06.33 S D=-1.02406*D*FSQT(EP)
06.34 S T=(1-B+B.)*BJ)*FEXP(D)
06.40 S G1=T*FLOG((1+E1)/(1+E2))
06.60 S B1=G1+B1

07.10 C RUNNING TIME = 1 HR 15 MINUTES
```

APPENDIX II

ELECTROMECHANICAL MIRROR TRANSDUCER FOR INFRARED LASERS

A practical laser mirror transducer must be capable of changing the length of a laser oscillator cavity by at least half a wavelength and preferably by several wavelengths. For optical and infrared lasers with wavelengths shorter than about 20 microns, piezoelectric transducers are quite satisfactory for frequency tuning and compensating thermal drifts. However, for a large class of lasers with wavelengths between about 20 and 400 microns, the piezoelectric effect does not provide adequate motion.

Far infrared gas lasers, such as He, H_2O, HCN, and CH_3F have relatively narrow Doppler and collision broadened bandwidths (typically 5 to 30 MHz). The frequency spacing between laser cavity modes, $\Delta\nu = c/2L$, is greater than those bandwidths for all but the longest cavities. For these lasers, the cavity length must be adjusted to resonate with the laser transition before any oscillation is possible. Mechanical adjusting screws and translating tables have been employed.[34]

A further consideration with far infrared gas lasers is high voltage insulation of the mirror mounts. Since low loss windows are not available, the mirrors must be mounted internally and allowed to float at the potential of the neighboring plasma, which may be as high as tens of kilovolts.

The design of Figure 39 provides ample length of travel, electronic tuning, and adequate high voltage insulation. It is

an outgrowth of the idea of mounting a mirror on a loudspeaker cone.

The transducer consists of an electromagnet with one moving and one fixed pole piece. The moving pole is spring loaded at each end and rides on 9.52 mm (3/8 inch) linear ball bushings.[35] It is allowed to pass inside the fixed pole thereby producing a stable mechanical equilibrium. The moving pole is well polished. Its ride on the linear ball bushings is surprisingly smooth and completely adequate for laser wavelengths as short as 10 microns.

All moving parts are under vacuum and float at the potential of the attached mirror. The transducer is bolted to an existing mirror mount for angular adjustment. The various parts are threaded into each other and the vacuum is sealed by O-rings at the joints.

The magnet coil is wound on a lucite form for high voltage insulation and slipped over the outside of the vacuum enclosure. It is operated at atmospheric pressure and ground potential. In an earlier design, the magnet coil was placed inside the vacuum enclosure. The driving power supply must then float at the mirror potential, 10 kilovolts in our case, and was rather difficult to construct. With the coil outside the vacuum, a simple transistor circuit or low voltage power supply is adequate to drive the coil. A mild steel jacket (not shown) over the coil serves to confine the

magnetic field. When wound with approximately 250 meters of 0.5 mm diameter enameled wire, the coil resistance is about 20 ohms and one ampere will produce 1 mm of motion.

When driven by the circuit of Figure 40, this transducer is capable of moving a 10 cm diamter by 1 cm thick glass mirror a distance of 1.5 mm at a repetition rate of 60 Hz. The far infrared lasers mentioned above may now be tuned as easily as a klystron. Features such as Q-switching, saturation dips, and competition and cascade effects between coupled atomic transitions are readily seen. Also, swept operation of the mirror in an otherwise CW laser has eliminated most of the needs for a mechanical chopper on the experiment table.

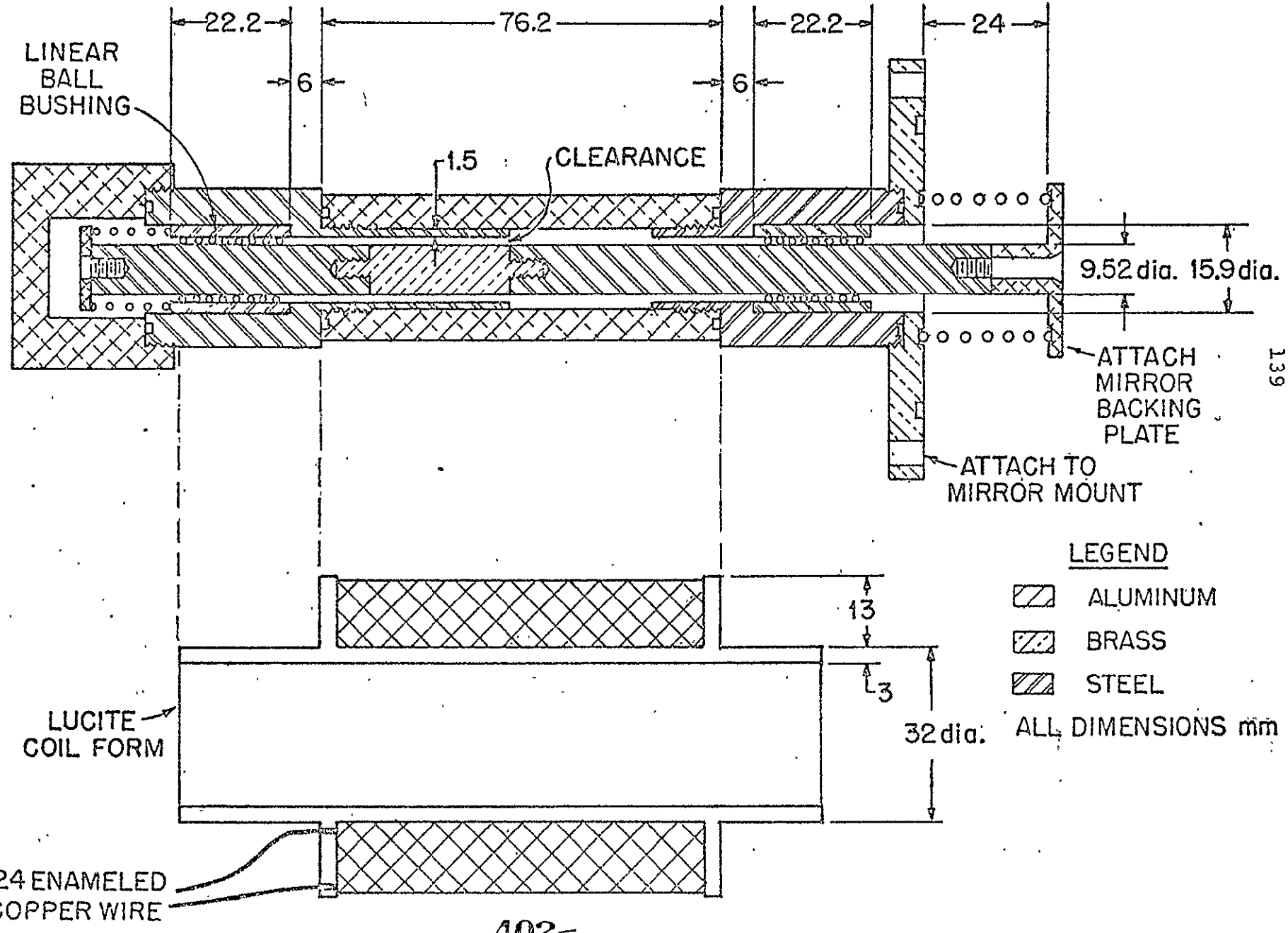

Figure 39

139

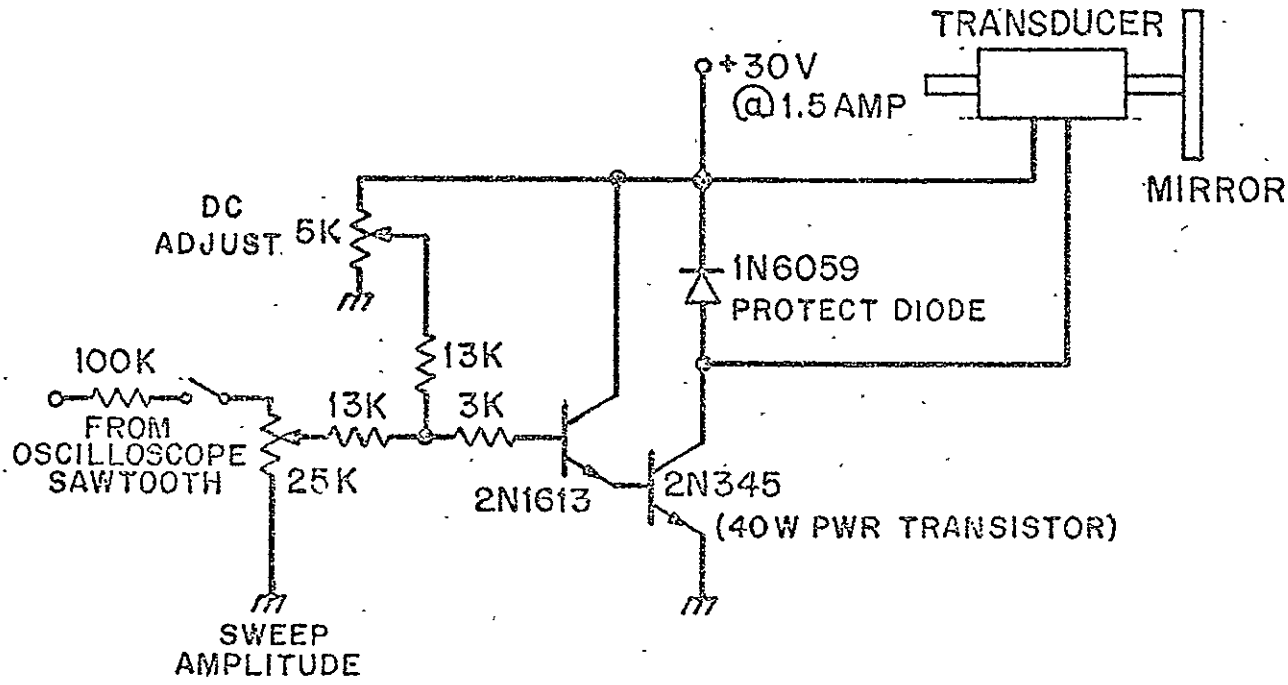
TRANSDUCER
+30V
@1.5 AMP
MIRROR
DC
ADJUST 5K
1N6059
PROTECT DIODE
100K
13K
13K
3K
FROM
OSCILLOSCOPE
SAWTOOTH
25K
2N1613
2N345
(40W PWR TRANSISTOR)
SWEEP
AMPLITUDE

Figure 40

REFERENCES

1. V. Ronchi, The Nature of Light, an Historical Survey, Harvard Univ. Press, Cambridge (1970), P.274.

2. J. Klapper and J. T. Frankle, Phase-Locked and Frequency-Feedback Systems, Academic Press, New York (1972), P.7.

3. P. K. Tien, Scientific American 230, No.4, 28 (April 1974).

4. L. O. Hocker and A. Javan, Phys. Letters 25A, 489 (1967).

5. L. O. Hocker, D. Ramachandra Rao and A. Javan, Phys. Letters 24A, 12 (1967).

6. L. O. Hocker and A. Javan, Phys. Letters 26A, 255 (1967).

7. L. O. Hocker, J. G. Small and A. Javan, Phys. Letters 29A, 321 (1969).

8. V. Daneu, D. Sokoloff, A. Sanchez and A. Javan, Appl. Phys. Lett. 15, 398 (1969).

9. K. M. Evenson, G. W. Day, J. S. Wells and L. O. Mullen, Appl. Phys. Lett. 20, 133 (1972).

10. A. Sanchez, Ph.D. Thesis, M.I.T. (1973).

11. Wherever possible, the most recent measurements from the National Bureau of Standards are given. See K. M. Evenson, J. S. Wells, F. R. Petersen, B. L. Danielson and G. W. Day, Appl. Phys. Lett. 22, 192 (1973). Also referenced are the first reported (and less accurate) measurements.

12. J. S. Levine, Ph.D. Thesis, M.I.T. (1971).

13. K. M. Evenson, J. S. Wells, L. M. Matarrese and L. B. Elwell, Appl. Phys. Lett. 16, 159 (1970).

14. K. M. Evenson, private communication. This number updates a previous measurement reported in reference 12.

15. K. M. Evenson, J. S. Wells and L. M. Matarrese, Appl. Phys. Lett. 16, 251 (1970).

16. See reference 8.

17. D. R. Sokoloff, A. Sanchez, R. M. Osgood and A. Javan, Appl. Phys. Lett. 17, 257 (1970).

18. K. M. Evenson, G. W. Day, J. S. Wells and L. O. Mullen, Appl. Phys. Lett. 20, 133 (1972).

19. L. O. Hocker, J. G. Small and A. Javan, Quarterly Progress Report, AFCRL Contract F19628-68-C-0204, Project #80950, Jan. 22, 1969; A. Javan, Bull. Am. Phys. Soc. 14, 32 (1969); A. Javan, Proceedings of the Esfahan Symposium on Fundamental and Applied Laser Physics.

20. J. G. Small, J.P. Monchalin, M. J. Kelly, F. Keilmann, A. Sanchez, S. K. Singh, N. A. Kurnit, A. Javan and F. Zernike, Proceedings of the 26th Annual Symposium on Frequency Control, U.S. Army Electronics Command, Fort Monmouth, N. J., pp. 248-9, June 1972. Copies available from Electronics Industries Assoc., 2001 Eye Street, N.W., Washington, D.C. 20006.

21. D. R. Sokoloff, Ph.D. Thesis, M.I.T. (1972).

22. L. M. Matarrese and K. M. Evenson, Appl. Phys. Lett. 17, 8 (1970).

23. H. I. Smith, F. J. Bachner and N. Efremow, J. Electrochem. Soc. 118, 821 (1971).

24. For a review of the tunneling literature see C. B. Duke, Tunneling in Solids, Academic Press, New York (1969).

25. C. B. Duke, Tunneling Phenomena in Solids, edited by E. Burstein and S. Lundqvist, Plenum Press, New York (1969).

26. L. I. Schiff, Quantum Mechanics, McGraw Hill, New York (1968).

27. R. M. Eisberg, Fundamentals of Modern Physics, Wiley, New York (1961).

28. K. H. Gundlach, Solid State Electronics, 9, 949 (1966).

29. See for example, E. Merzbacher, Quantum Mechanics, Wiley, New York (1970), or reference 26 or 27.

30. G. W. Lewicki and C. A. Mead, Appl. Phys. Lett. 8, 98 (1966).

31. J. G. Simmons, Phys. Rev. Lett. 23, 297 (1969).

32. J. M. Ziman, Electrons and Phonons - The Theory of Transport Phenomena in Solids, Oxford Clarendon Press (1960), p. 487.

33. M. L. James, G. M. Smith and J. C. Wolford, Applied Numerical Methods for Digital Computation with FORTRAN, International Textbook Company, Scranton (1968).

34. M. Gundersen, H. B. Lloyd and B. W. Poarch, Rev. Sci. Instruments 43, 333 (1972).

35. Linear ball bushings are manufactured by Thomson Industries, Inc., Manhasset, New York.